

# Fluxon Dynamics in Annular Josephson Junctions: From Relativistic Strings to Quantum Particles.

Den Naturwissenschaftlichen Fakultäten der  
Friedrich-Alexander-Universität Erlangen-Nürnberg  
zur  
Erlangung des Doktorgrades

vorgelegt von

Andreas Wallraff  
aus Bonn

July 18, 2000



Als Dissertation genehmigt von den  
Naturwissenschaftlichen Fakultäten der  
Friedrich-Alexander-Universität Erlangen-Nürnberg

Tag der mündlichen Prüfung:

Vorsitzender der Promotionskommission: Prof. Dr. W. Buggisch

Erstberichterstatter: Prof. Dr. A. V. Ustinov

Zweitberichterstatter: Prof. Dr. M. Cirillo



# Preface

In this thesis, the results of three years of research on the nonlinear electrodynamics of long Josephson junctions performed in the group of Prof. Alexey Ustinov at the University of Erlangen-Nürnberg are reported. This thesis is the result of the work which I did in collaboration with a considerable number of people, who all contributed in different ways.

Most of all, I want to thank you, Alexey Ustinov, my supervisor, for the excellent and inspiring time I had in your group. I enjoyed very much being one of the first members of your new group in Erlangen, with all the opportunities and all the duties that were associated with that. I am glad to have spent the time of my graduate research with one of the most enthusiastic and motivated and, at the same time, one of the most demanding persons I got to know during my physics research and education. I have profited a lot from the stimulating physics discussions with you, steering my research activities in the good directions. I also thank you for granting me the opportunity to attend a number of meetings, summer schools and conferences during the past years and also for supporting the publication of the results of my work.

Furthermore, I want to thank the undergraduate students who decided to do their Master's thesis in collaboration with me on different subjects. The joined work with Andreas Franz has resulted in interesting experimental results on annular junctions with large idle region, some of which are in the process of being published [WFU<sup>+</sup>00, FWU00b, FWU00a]. Sascha Lebeda is the one who realized our ambitions to start up the sub-micron size aluminum junction technology, which will hopefully open the door to a new direction of research in the group. He also shared the burden with me spending the nights with an old dilution refrigerator that needed more time and care than we had expected. Lately, I have benefited from Alexander Kemp joining the small quantum computation team and contributing with new ideas and a lot of motivation.

Among my senior collaborators is Vladislav Kurin, who helped a lot to answer the question 'How one-dimensional is an annular junction?'. His insight into the theory of the relativistic motion of vortex strings in annular junctions triggered our discovery of the 'whispering vortices' [WUK<sup>+</sup>00, WBK<sup>+</sup>97, WFU<sup>+</sup>00]. I have also enjoyed the critic and stimulating discussion with Dietmar Kruse about his low temperature scanning electron microscope measurements of whispering gallery modes. I have benefited a lot from the collaboration with Misha Fistul, who has provided theoretical solutions [KWF<sup>+</sup>99, WKL<sup>+</sup>00, FCC<sup>+</sup>00] to problems which would have taken ages for myself to solve. I thank Lilly Caputo for her long lasting company in our group. She has initiated myself to the secrets of sample design and has provided space for my samples on her chips. (My junctions seem to work best, when one of Lilly's arrays with a fin-line antenna is near by.) I thank Edward Goldobin for the inspiring collaboration with him since my first days in the world of Josephson junctions. Our joint work on simulations and measurements of stacked Josephson junctions continues to reveal interesting physics [GWTU98, GWU00]. I am grateful to Yuri Koval for fabricat-

ing the most narrow long Josephson junctions [KWF<sup>+</sup>99] which will hopefully allow us to observe quantum properties of Josephson vortices in the near future [WKL<sup>+</sup>00]. I have profited from the productivity of Norbert Thyssen, whose samples are still alive, and also from the work of Maxim Levitchev who inherited the machine for fabricating Nb–Al/AIO<sub>x</sub>–Nb trilayers. A big thank you also to Gena Logvenov who guided my way through the secrets of cryogenics, dilution refrigerators and leak testing. The efforts he put into reanimating our old dilution refrigerator will hopefully pay off soon. Peter Binder has supported my quest in the secrets of electronics by helpful explanations of electronic circuitry. Also, I thank him for sharing some of the administrative duties in our international group. The other colleagues who made my time in Erlangen enjoyable are Dima Abraimov and Jan Zitzmann. Also, the support and help of my colleagues in the ‘higher temperature’ part of the institute is acknowledged. A special thank you to the head of our institute Prof. Paul Müller for providing an excellent environment to perform this research.

My work has been supported by a number of summer students, Bernd Bayerlein and Marcus Schuster, who implemented many of my ideas to do computer-controlled measurements. A very big thank you to Konrad Urlichs, who explored the secrets of LabView. As a result I can perform hours of switching-current measurements with automatic control of all experimental parameters. His efforts in experimental work in the lab will hopefully contribute further to our plans of observing quantum properties of vortices.

I am indebted to Matteo Cirillo for the enjoyable time I had in Rome working on a common project. I express my gratitude to Marc Feldmann for supporting my stay at Rochester University, New York, during which I got to know the secrets about their quantum computation project. I also enjoyed fruitful discussions about quantum vortices with Takeo Kato, Alexander Shnirman, Yuri Makhlin and Thorsten Dröse. I am grateful to Caspar van der Wal and the Delft group for having had the opportunity to spy on a number of the Delft secrets of performing successful experiments with nano-scale electronic circuits.

Experimental research is not possible without technical support. Special thanks to our excellent mechanical workshop headed by G. Muhr and G. Heimpel, also to the electronics workshop headed by G. Merkel did provide useful support, to our in-house technical support managed by D. Harrer, J. Wissenz and to E. Peetz for caring for the liters and liters of helium which I have used for performing measurements. Thanks also to Christa Metze who has taken care of a lot of the administrative work related to the projects I have been working on. I acknowledge the financial support of our quantum vortices project by ‘Deutsche Forschungsgemeinschaft’ within the framework ‘Quanteninformationsverarbeitung’. I am also grateful to Jamie Peterson at Wolfram Research, Inc. for providing complementary copies of Mathematica to me, which I have used as a major tool for data analysis and evaluation.

Finally, I would like to thank my family and the friends who have accompanied and supported me during the years of my PhD. And most important of all, ‘des gros bisous’ for my little princess Katia Sourbelle who has suffered most from the nights which I have spent at the side of cold cryostats rather than being with her.

Andreas Wallraff  
June, 2000







# Contents

<b>I</b>	<b>INTRODUCTION</b>	<b>1</b>
<b>1</b>	<b>Basic Properties of Josephson Junctions</b>	<b>4</b>
1.1	The Josephson junction . . . . .	4
1.2	The Josephson effect . . . . .	5
1.3	Static phase distribution of a small junction . . . . .	8
1.4	Dynamics of a small junction . . . . .	8
<b>2</b>	<b>The Physics of Long Josephson Junctions</b>	<b>10</b>
2.1	The sine-Gordon model . . . . .	10
2.1.1	The wave equation . . . . .	10
2.1.2	Lagrangian and hamiltonian functions . . . . .	13
2.2	Excitations of the sine-Gordon system . . . . .	15
2.2.1	Linear long Josephson junctions . . . . .	15
2.2.2	Linear long Josephson junctions in external magnetic field . . . . .	18
2.2.3	Annular long Josephson junctions . . . . .	19
2.3	Basic experimental techniques . . . . .	20
2.3.1	Sample preparation . . . . .	20
2.3.2	Typical junction parameters . . . . .	22
2.3.3	Basic measurement technique . . . . .	22
<b>II</b>	<b>TWO-DIMENSIONAL ANNULAR JOSEPHSON JUNCTIONS</b>	<b>25</b>
<b>3</b>	<b>Critical-Current Diffraction Patterns</b>	<b>26</b>
3.1	State of the art . . . . .	27
3.2	Experimental results and comparison with theory . . . . .	29
3.2.1	Diffraction patterns without trapped fluxons . . . . .	29
3.2.2	Diffraction patterns with trapped fluxons . . . . .	33
3.3	Conclusion . . . . .	34
<b>4</b>	<b>Whispering Gallery Resonances</b>	<b>35</b>
4.1	The idea and the model . . . . .	36
4.2	The samples . . . . .	38
4.3	Single-vortex resonances . . . . .	40
4.3.1	Normalization . . . . .	41
4.3.2	The fine structure . . . . .	44
4.4	Resonance interaction . . . . .	44

4.5	The plasmon spectrum of an annular junction . . . . .	46
4.5.1	The circular resonator approximation . . . . .	47
4.5.2	Exact annular resonator spectrum . . . . .	50
4.6	Numerical calculations . . . . .	52
4.7	Quantitative comparison and discussion of results . . . . .	54
4.8	Conclusion and outlook . . . . .	56
<b>5</b>	<b>Annular Junctions with Idle Region</b>	<b>58</b>
5.1	The model . . . . .	60
5.2	Critical-current diffraction patterns . . . . .	61
5.3	Whispering gallery modes . . . . .	64
5.3.1	Experimental observation . . . . .	65
5.3.2	Whispering gallery modes in the presence of an idle region . . . . .	66
5.3.3	Results and discussion . . . . .	69
 <b>III CLASSICAL AND QUANTUM PARTICLE PROPERTIES OF JOSEPHSON VORTICES</b>		 <b>71</b>
<b>6</b>	<b>Thermal Activation of Josephson Vortices</b>	<b>74</b>
6.1	Introduction . . . . .	75
6.1.1	Fundamentals of thermal activation . . . . .	75
6.1.2	Activation of the phase in a small junction . . . . .	77
6.1.3	Activation of a vortex in a long junction . . . . .	79
6.2	Vortex pinning potentials . . . . .	81
6.2.1	Magnetic-field induced potential . . . . .	82
6.2.2	Microresistor (microshort) potential . . . . .	86
6.2.3	Scaling of parameters . . . . .	89
6.3	Experimental technique . . . . .	92
6.3.1	Measurement method . . . . .	92
6.3.2	Experimental setup and data acquisition . . . . .	94
6.3.3	Data evaluation: probability distributions, activation rates and es- cape temperature . . . . .	95
6.4	Experimental results . . . . .	98
6.4.1	Small junction . . . . .	98
6.4.2	Magnetic-field induced vortex potential . . . . .	103
6.4.3	Vortex in a microresistor potential . . . . .	109
6.5	Summary and conclusion . . . . .	115
<b>7</b>	<b>Quantum Tunneling</b>	<b>117</b>
7.1	Macroscopic quantum tunneling . . . . .	117
7.1.1	Calculated switching-current distributions . . . . .	119
7.1.2	Experimental requirements . . . . .	123
7.2	Energy level quantization . . . . .	125
7.3	Summary and conclusion . . . . .	127

<b>8</b>	<b>A Vortex in a Double-Well Potential</b>	<b>128</b>
8.1	Introduction . . . . .	128
8.2	Engineering the vortex potential . . . . .	130
8.3	A Fluxon in a double-well potential . . . . .	133
8.4	Manipulation of a fluxon in a double-well . . . . .	136
8.5	A macroscopic quantum coherence experiment . . . . .	139
8.6	Quantum computation using the vortex-qubit . . . . .	140
8.7	Decoherence . . . . .	142
8.8	Summary and conclusions . . . . .	143
<b>A</b>	<b>Numerical solution of the stationary Schrödinger equation</b>	<b>145</b>
<b>B</b>	<b>List of symbols</b>	<b>146</b>
	<b>Bibliography</b>	<b>151</b>
	<b>Summary</b>	<b>163</b>
	<b>Curriculum Vitae</b>	<b>165</b>
	<b>List of Publications</b>	<b>166</b>



# Part I

## INTRODUCTION

Since the theoretical prediction of the Josephson effect in 1962 and its first experimental observation by Anderson and Rowell in 1963, the physics of Josephson junctions has stimulated a large amount of experimental and theoretical research, both due to their fascinating basic physical properties and the wide range of existing and prospective applications.

One of the most intriguing properties of Josephson junctions arises from the fact that the dynamics of the charge carriers and the electromagnetic fields in the junction is governed by the quantum mechanical phase difference between the macroscopic wave functions describing the superconducting electrons in each of the junction electrodes. In the limit of high temperatures and large damping, the electrodynamics of the junction are purely classical. However, at low temperatures and small damping, the quantum dynamics of the phase difference is revealed. The classical and quantum mechanical properties of Josephson junctions are examined experimentally by measuring macroscopic quantities, such as the superconducting and normal tunnel currents flowing across the junction barrier and the voltage drop appearing across the junction.

A major field in Josephson physics is concerned with the classical non-linear electro-dynamics of small junctions, arrays of small junctions and extended junctions. The non-linear properties of these systems arise due to the Josephson current which depends on the sine of the phase difference across the junction. In extended junctions, the phase difference may vary both in space and time, giving rise to the existence of collective non-linear excitations like solitons and breathers. Of particular interest is the investigation of soliton dynamics in quasi-one-dimensional long Josephson junctions. In such systems, one dimension is much larger than the characteristic spatial scale of changes in the phase difference whereas the other one is much smaller. Long junctions are excellent models to investigate soliton dynamics both theoretically and experimentally. They are a forerunner in the field of soliton research and receive a lot of attention in a wide range of other fields like non-linear optics, laser and plasma physics.

In long Josephson junctions, solitons are created due to the quantized penetration of magnetic flux into the junction. A flux quantum threading the junction is associated with a vortex of the superconducting screening current and thus is frequently called a Josephson vortex. Under certain conditions, a flux quantum behaves as a particle-like object with an effective mass and a coordinate. Therefore it is often called fluxon. The dynamics of fluxons – and the dynamics of the phase difference in long junctions in general – is accurately described by the perturbed sine-Gordon equation. In nature, a large variety of phenomena in different physical systems can be modeled using the sine-Gordon equation, for example the dynamics of dislocations (crystal defects) or the dynamics of domain walls in magnetic materials.

This thesis is devoted to the investigation of the statics and dynamics of the phase difference in annular long Josephson junctions. In particular the classical wave and par-

title properties of Josephson vortices in wide and narrow annular junctions are studied experimentally. Also the feasibility to observe quantum properties of Josephson vortices, including energy level quantization, macroscopic quantum tunneling and quantum coherence is investigated.

In the first chapter of the introductory part of this thesis, the Josephson effect and the basic properties of small Josephson tunnel junctions are introduced. The fundamentals of the physics of long Josephson junctions are reviewed in Chapter 2. The sine-Gordon equation governing the electrodynamics of a long junction is derived and the energetics of the junction are discussed in terms of the lagrangian and hamiltonian functions. The fundamental electromagnetic excitations of the junction, i.e. fluxons and plasmons, are introduced. Finally, the basics of junction fabrication and the experimental techniques used for measurements are presented.

In Part II, experiments investigating the classical properties of wide annular Josephson junctions are reported. The results are interpreted in terms of the spatial and temporal evolution of the phase difference across the two-dimensional junction.

In Chapter 3, the static phase distribution of annular junctions with different inner and outer radii is investigated experimentally by measuring their critical current in dependence on the externally applied magnetic field. The experimental data are analyzed using existing theory which considers a linear gradient of phase across the junction induced by the external field. The data are interpreted in terms of the phase-dependent interference of the supercurrent flowing across the junction barrier. The characteristic dependence of the critical current on the field is used to uniquely identify the number of Josephson vortices topologically trapped in the annular junction.

The dynamics of a single Josephson vortex in a wide annular junction is investigated in Chapter 4. Experiments proving the theoretically predicted excitation of whispering gallery-type plasmon modes by a vortex propagating at relativistic velocities along the junction are presented. It is shown that the vortex interacts resonantly with the linear modes of the junction giving rise to a characteristic fine structure on the single-vortex resonance. The resonance condition is interpreted in terms of Cherenkov radiation generated by the vortex moving with a group velocity which is larger than the phase velocity of the plasmon modes. The exact voltage positions of the fine structure are used to identify the characteristic frequencies of the whispering gallery modes. The experimental data are compared to numerical simulations and finally the results are discussed.

The electromagnetic environment in which a Josephson junction is embedded substantially modifies its static and dynamic properties. The junction characteristics in presence of the environment, which is also frequently called idle or passive region, is investigated experimentally in Chapter 5. The static properties are probed in measurements of the critical current versus field pattern in dependence on the width of the idle region. The results are interpreted in terms of a renormalization of the magnetic properties of the junction induced by the inductance of the idle region. In experiments similar to those presented in Chapter 4, the effect of the idle region on the whispering gallery mode spectrum is investigated. The spectrum of the junction is shown to depend sensitively on the electrical parameters and the size of the idle region coupled to it. The measured resonances in the current-voltage characteristic are compared to resonance frequencies calculated considering the electrical and geometrical properties of the junction and the idle region.

In Part III, the fluctuation-induced escape of a Josephson vortex from a metastable state

is investigated. The observed effects are explained considering the vortex as a collective particle-like excitation with an effective mass and a generalized center of mass coordinate. The observed effects are similar to the escape of the phase in small junctions. However, they are special in the sense that the particle-like excitation is a soliton and the relevant generalized coordinate has a spatial character.

In Chapter 6, the thermal escape of a Josephson vortex from a metastable state is investigated experimentally. The metastable state is realized by spatially localizing the vortex in a magnetic field induced potential well. Applying a bias current to the junction, the height of the barrier separating the metastable localized state from the propagating state is controlled. To analyze the thermal escape process, the distribution of the vortex depinning currents is measured. The data are interpreted in terms of a particle which is activated from a potential well due to thermal fluctuations. A similar experiment is performed considering a pinning potential induced by a microresistor implemented into the junction barrier. The results of both experiments are well explained within the model.

The prospects of observing quantum properties of Josephson vortices by performing measurements of the depinning current distribution are analyzed in Chapter 7. In particular, the magnetic field induced potential well – the depth of which can be varied in situ – is considered. The cross-over temperature below which quantum tunneling dominates thermal activation is evaluated. The requirements on the experimental setup and on the measurement accuracy for the observation of this macroscopic quantum phenomenon are analyzed quantitatively. The possibility to observe the energy level quantization of a quantum vortex in a potential well is also examined.

Finally, in Chapter 8, our proposal to modify the shape of an annular junction in order to design interesting types of magnetic-field induced vortex potentials is discussed. In particular, a heart-shaped junction is suggested to be used to form a double-well potential for a vortex. A method to classically determine the state of the vortex by manipulating fields and bias currents applied to the junction is presented. We suggest that a macroscopic quantum coherence experiment can be performed using a vortex in a double-well potential. A successful experiment of this type would encourage the use of vortex states in shaped junctions as qubits in quantum computers. Possibilities to manipulate the quantum states of a vortex to perform single-qubit and two-qubit operations necessary for quantum computation are indicated and decoherence is briefly considered.

# Chapter 1

## Basic Properties of Josephson Junctions

In this introductory chapter the basic properties of Josephson junctions are briefly reviewed. The Josephson effect is introduced and the dynamics of the charges and the electromagnetic fields in the junction are related to the phase difference between the order parameters describing the superconducting condensate in each electrode. As an introduction to the electrostatics of Josephson junctions, the statics and dynamics of the phase difference in a single small junction are discussed.

### 1.1 The Josephson junction

Josephson junctions are systems in which two superconductors are weakly coupled to one another, see Fig. 1.1. In each of the two superconductors<sup>1</sup> the conduction electrons are interacting with phonons of the crystal lattice. At low temperatures this effect gives rise to an effective attractive interaction between the electrons which then form pairs of opposite spin and angular momentum. Such pairs are called Cooper pairs and are the carriers of the charge in the superconductor. Due to the anti-parallel combination of the spins and the angular momenta of the electrons in each pair, the total angular momentum vanishes and the Cooper pairs have boson character. At zero temperature, all Cooper pairs are Bose-condensed into the electronic ground state of the superconductor. All excited quasiparticle states (i.e. single electron states) are separated by an energy gap  $\Delta$ , which is proportional to the effective binding energy of the Cooper pair, from the superconducting ground state, see Fig. 1.2b. The superconducting state can be described by an effective macroscopic wave function with an amplitude proportional to the density of Cooper pairs  $n_i^{\text{CP}}$  and a phase  $\theta_i$

$$\Psi_i = \sqrt{n_i^{\text{CP}}(\vec{r}, t)} \exp(i\theta_i). \quad (1.1)$$

$\Psi$  is also frequently called the superconducting order parameter.

In the region of the weak link, the amplitude of the wave function of each superconductor is reduced from its bulk value. The two superconductors are then weakly coupled with one another due to the small overlap of the macroscopic wave functions, see Fig.1.1b. Different types of weak links providing the coupling between the superconductors are discussed in

---

<sup>1</sup>A general introduction to superconductivity and the physics of Josephson junction can be found in a number of text books. See for example Refs. [Tin96, PJFC95, Lik86, VDT81].



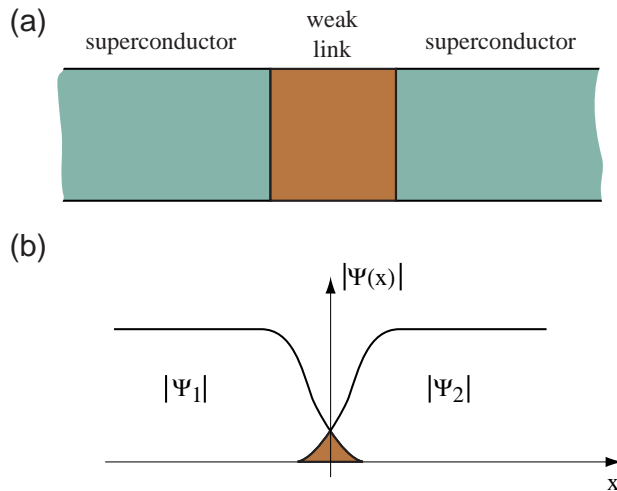


Figure 1.1: (a) Two superconductors weakly coupled to one another. (b) Amplitude of the macroscopic wave function (order parameter) of the two superconductors.

detail in the literature [Lik79]. Here, I consider the coupling of two superconductors via a thin insulating barrier. Such a system is called a superconductor–insulator–superconductor (SIS) tunnel junction. This realization of a Josephson weak link is the one most commonly used in basic research and applications because its electrical properties can be well controlled.

A typical tunneling current-voltage characteristic of an SIS Josephson tunnel junction is depicted in Fig. 1.2a. Four different tunneling regimes can be observed in this characteristic, see Fig. 1.2a-e. At zero voltage, Cooper pairs tunnel through the barrier ( $S \rightarrow S$ ), giving rise to a non-dissipative current. At voltages  $0 < V < 2\Delta/e$ , quasiparticles tunnel through the barrier giving rise to the quasiparticle subgap current ( $Q \rightarrow Q$ ). The voltage  $V_g = 2\Delta/e$  is called the gap voltage. At voltages  $V \geq 2\Delta/e$  Cooper pairs are broken up and quasiparticles tunnel ( $S \rightarrow Q$ ). All three processes follow the linear branch of normal electron tunneling ( $n \rightarrow n$ ) at voltages  $V > V_g$ .<sup>2</sup>

## 1.2 The Josephson effect

The tunneling of Cooper pairs through the insulating barrier of an SIS type junction was predicted by B. D. Josephson [Jos62] in 1962 and experimentally observed for the first time by Anderson and Rowell [AR63] in 1963. Solving the quantum mechanical problem of the tunneling of Cooper pairs across a potential barrier in a point like junction, Josephson found that the local superconducting tunnel current density at zero voltage is given by

$$j = j_c \sin(\phi), \quad (1.2)$$

where  $\phi = \theta_1 - \theta_2$  is the difference in phase between the order parameters of the two superconducting junction electrodes. The maximum supercurrent density  $j_c$  sustained by the junction, calculated from microscopic theory by Ambegaokar and Baratoff [AB63a, AB63b], is given by

$$j_c = \frac{\pi}{4} \frac{2\Delta(T)}{\rho e} \tanh\left(\frac{\Delta(T)}{2k_b T}\right), \quad (1.3)$$

where  $\Delta(T)$  is the temperature dependent energy gap of the superconductor and  $\rho$  is the normal tunnel resistance of the junction per unit area. The electron charge is denoted

<sup>2</sup>A good description of the relevant tunneling processes is given in Ref. [PJFC95].

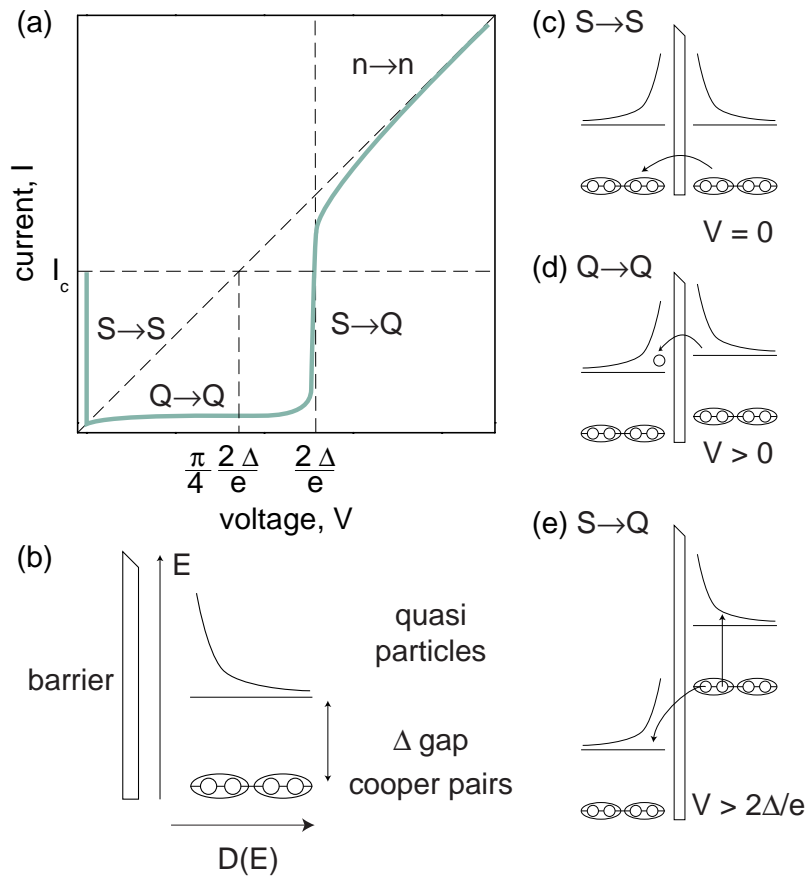


Figure 1.2: (a) Current-voltage characteristic of a Josephson tunnel junction. Different tunneling regimes are indicated. (b) Bose representation of the electron density of states of the superconductor;  $\Delta$  is the energy gap between quasiparticle states and Cooper pair states. (c) Josephson tunneling process  $S \rightarrow S$ . (d) Quasiparticle tunneling process  $Q \rightarrow Q$ . (e) Cooper pair dissociation and tunneling into quasiparticle states  $S \rightarrow Q$ . Regular single electron tunneling is indicated by  $n \rightarrow n$ .

as  $e$  and the Boltzmann constant as  $k_b$ . Equation (1.2) is called *dc Josephson equation*.<sup>3</sup> Applying a constant dc voltage to the tunnel junction, the phase difference  $\phi$  evolves in time according to the *ac Josephson equation*

$$V = \frac{\Phi_0}{2\pi} \frac{d\phi}{dt}, \quad (1.4)$$

where  $\Phi_0$  is the *flux quantum*

$$\Phi_0 = \frac{h}{2e} = 2.07 \cdot 10^{-15} \text{ Wb}. \quad (1.5)$$

At the constant voltage  $V$  the supercurrent through the junction oscillates with the characteristic frequency

$$\frac{d\phi}{dt} \frac{1}{2\pi V} = \frac{1}{\Phi_0} = 483.6 \text{ MHz}/\mu\text{V}. \quad (1.6)$$

<sup>3</sup>An elegant derivation of the Josephson equations in the Schrödinger picture can be found in the Feynman lectures [FLS65].

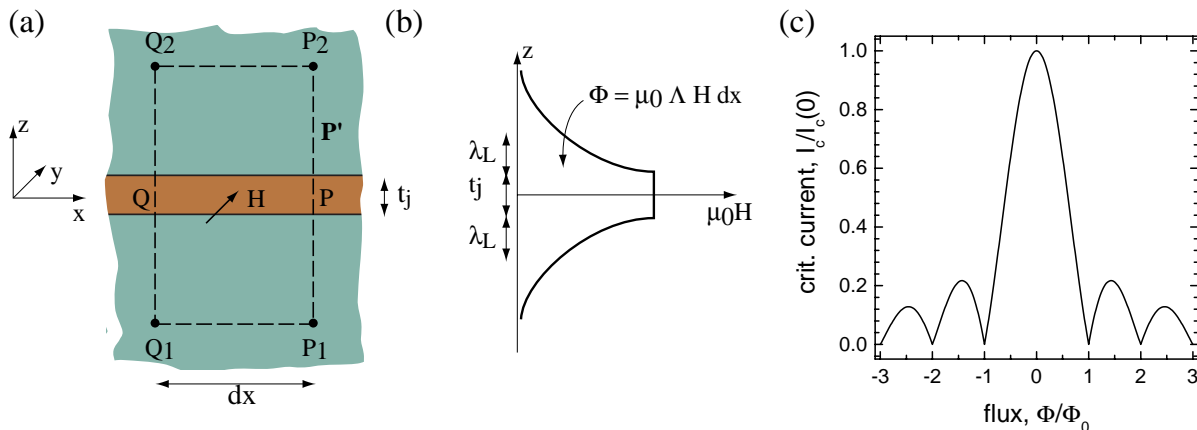


Figure 1.3: a) Closed path across the barrier of a Josephson tunnel junction. b) Magnetic field (thick line) penetration into the superconductor according to London equations. The flux  $\Phi = \mu_0 H \Lambda dx$  per unit length of the junction is given by the area under the curve. c) Critical-current diffraction pattern of a small rectangular junction.

The Josephson equations govern the electrodynamics of Josephson junctions. In particular, the dc-Josephson equation gives rise to the non-linear current flow across the junction barrier and the ac Josephson equation relates the electric field in the junction to the evolution of phase in time.

The magnetic field  $\vec{H}$  in a Josephson junction can be related to the gauge invariant phase difference  $\phi$  which is defined as (see for example Ref. [VDT81])

$$\phi = \theta_2 - \theta_1 + \frac{2\pi}{\Phi_0} \int \vec{A} d\vec{l}, \quad (1.7)$$

where  $\vec{A}$  is the electromagnetic vector potential. Considering an extended Josephson junction as shown in Fig. 1.3a, the difference in phase  $\phi$  between the two coordinates  $P$  and  $Q$  chosen at different points along the junction is given by

$$\phi(Q) - \phi(P) = \frac{2\pi}{\Phi_0} \left[ \int_{P_1}^{P_2} \vec{A}(P) d\vec{l} - \int_{Q_1}^{Q_2} \vec{A}(Q) d\vec{l} \right]. \quad (1.8)$$

If an external magnetic field  $\vec{H}$  is applied in the plain of the junction the flux enclosed in the path  $P' = Q_1 Q_2 P_2 P_1$  (see Fig. 1.3) is given by

$$\Phi = \int_S \mu_0 \vec{H} d\vec{S} = \oint \vec{A} d\vec{l} \quad (1.9)$$

$$= \int_{Q_2}^{Q_1} \vec{A} d\vec{l} + \int_{Q_1}^{P_1} \vec{A} d\vec{l} + \int_{P_1}^{P_2} \vec{A} d\vec{l} + \int_{P_2}^{Q_2} \vec{A} d\vec{l}. \quad (1.10)$$

The second and fourth terms in Eq. (1.10) vanish if the horizontal parts of the path are chosen considerably deeper in the superconductor than the *London penetration depth*  $\lambda_L$ , which is the characteristic screening length of the magnetic field in a superconductor. Thus, equating (1.10) and (1.8) and considering the flux enclosed in the differentially small section  $dx$  of the junction we find

$$\frac{\phi(Q) - \phi(P)}{dx} = \frac{2\pi}{\Phi_0} \Lambda \mu_0 H, \quad (1.11)$$

where  $\mu_0$  is the vacuum permeability.  $\Lambda = t_j + 2\lambda_L$  is the *magnetic thickness* of the junction with the thickness of the tunnel barrier given by  $t_j$ .  $\Lambda\mu_0 H$  is the magnetic flux per unit length penetrating into a junction taking into account the screening of the magnetic field due the superconductors. Thus, the gradient of  $\phi$  can be expressed as

$$\nabla\phi = \frac{2\pi}{\Phi_0}\Lambda\mu_0\vec{H} \times \hat{z}, \quad (1.12)$$

where  $\hat{z}$  is the normal vector perpendicular to the junction plane.

### 1.3 Static phase distribution of a small junction

The total supercurrent supported by a Josephson junction depends on the applied external magnetic field  $H$ . According to Eq. (1.12), the field induces a constant gradient of the phase difference across the junction. Thus, the local Josephson current oscillates sinusoidally with the coordinate perpendicular to the field. The total supercurrent that can flow through the junction is given by the integral

$$I_c = \int_A j_c \sin\left(2\pi\frac{\mu_0\Lambda Hx}{\Phi_0}\right) dA \quad (1.13)$$

over the junction area  $A$ , where we assume a spatially homogeneous critical-current density  $j_c$ . If a rectangular junction is considered the integral (1.13) can be solved explicitly yielding a critical current of

$$I_c(H) = I_c(0) \frac{\sin(\pi\Phi/\Phi_0)}{\pi\Phi/\Phi_0}, \quad (1.14)$$

where  $\Phi = \mu_0\Lambda Hw$  is the total flux threading the junction of length  $w$ . The expression (1.14) is frequently referred to as the *critical-current diffraction pattern* of a rectangular junction, because it resembles the Fraunhofer diffraction pattern of light passing through a narrow rectangular slit. The sinc-type critical current diffraction pattern (1.14) of a small rectangular junction is plotted in Fig. 1.3c.

### 1.4 Dynamics of a small junction

The electrodynamics of a small Josephson junction can be accurately described neglecting the variation of the phase difference across the junction area. This approximation is valid, if the lateral junction dimensions are smaller than the characteristic length scale  $\lambda_J$  of the variation of  $\phi$  (see next chapter). In this regime, a small junction like the one shown in Fig. 1.4a is accurately described by the lumped circuit model depicted in Fig. 1.4b. The junction is modeled by a parallel connection of an ideal Josephson junction, a resistor and a capacitor accounting for the Cooper pair, the quasiparticle and the capacitive contribution to the total current [Ste68, McC68]. Using the Kirchoff laws, the total current through the junction is given by

$$I = I_c \sin\phi + \frac{V}{R} + C\frac{dV}{dt}. \quad (1.15)$$

This model is called the resistively, capacitively shunted junction (RCSJ) model. Eq. (1.15) can be rewritten in terms of the superconducting phase difference  $\phi$  using the Josephson

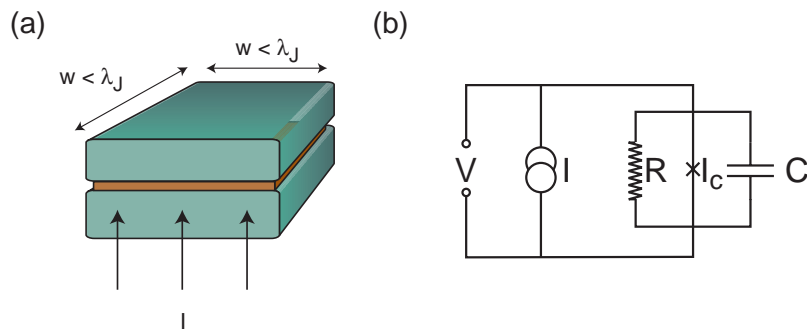


Figure 1.4: (a) Sketch of a small Josephson junction with lateral dimensions  $w \times w$ . (b) Lumped circuit model of a small junction.

equations (1.2) and (1.4)

$$I = I_c \sin \phi + \frac{\Phi_0}{2\pi R} \frac{d\phi}{dt} + \frac{\Phi_0 C}{2\pi} \frac{d^2 \phi}{dt^2}. \quad (1.16)$$

It is important to note that this equation maps to the one describing a driven and damped pendulum or equivalently the viscous motion of a particle in a tilted sinusoidal potential, which is also called a *washboard potential*. The rich dynamics of such a system can be investigated using Josephson junctions. If the junction is driven by the external bias current  $I$  and damped by the resistance  $R$ , the phase  $\phi$  can have a complex time dependent behavior. The time average of the evolution of phase can be monitored by measuring the dc voltage

$$V = \langle V \rangle = \left\langle \frac{d\phi}{dt} \right\rangle \frac{\Phi_0}{2\pi} \quad (1.17)$$

across the junction. Depending on the bias conditions and the damping, the phase can either oscillate with small amplitude  $\phi < 2\pi$ , or it can rotate over  $2\pi$ . If the phase rotates a dc-voltage drop across the junction appears, whereas the average voltage for small oscillations of the phase is zero. The dynamics of small junctions and arrays of small junctions is a topic of current research [GT95].

It is important to point out that the Josephson junction is an outstanding example of a macroscopic physical system, the dynamics of which is governed by the underlying quantum mechanical phenomena of tunneling of Cooper pairs and quasiparticles across a tunnel barrier. The macroscopic dynamics of the junction is fully described in terms of the phase difference  $\phi$ . It has been rigorously shown that the dynamics of *all* microscopic degrees of freedom (charges and quantized fields) is described by a single collective variable which is the phase  $\phi$  across the junction [AES82, ESA84, SZ90]. At high temperatures and high damping, the dynamics of the phase is purely classical. At low temperatures however, the quantum nature of the dynamics of the phase becomes apparent and macroscopic quantum phenomena can be observed. This issue is discussed in more detail in Part III of this thesis.

# Chapter 2

## The Physics of Long Josephson Junctions

In a large area Josephson junction, the phase difference  $\phi$  between the top and the bottom electrode may vary in space. Therefore, the dynamics of a large junction is much more rich and diverse than the dynamics of a single small junction. The spatial extension of the junction gives rise to the existence of solitons, breathers and other interesting non-linear and linear phenomena. The characteristic length scale of the spatial variation of  $\phi$  is called the *Josephson length*  $\lambda_J$ . If one dimension of a junction is much larger than  $\lambda_J$  while the other dimension is much smaller than  $\lambda_J$ , the system is called a long Josephson junction. A sketch of such a junction with length  $l$  and width  $w$  is depicted in Fig. 2.1a.

In the first section of this introductory chapter, the wave equation describing the electromagnetic properties of a long Josephson junction is introduced. The hamiltonian and lagrangian functions governing the energetics of the junction are also presented. In section 2.2, the important electromagnetic excitations of a long junction are reviewed, with particularly focus on solitary waves. In the last section, the procedure used for junction fabrication is described and the basic measurement techniques employed for the experimental investigation of long Josephson junctions are discussed.

### 2.1 The sine-Gordon model

Long Josephson junctions possess an extremely rich spectrum of linear and non-linear electromagnetic excitations. Their physics is very attractive and exciting because the dynamics of a long junction can be investigated experimentally in great detail. At the same time many of the observed effects can be analyzed theoretically considering the junction as a non-linear waveguide described by the *sine-Gordon equation*. The long Josephson junction is one of the few outstanding physical systems that enable us to investigate the interesting and diverse sine-Gordon physics.

#### 2.1.1 The wave equation

The wave equation governing the electrodynamics of an ideal long Josephson junction can be derived starting from the lumped circuit model shown in Fig. 2.1b. In this model, the junction is described by a parallel connection of small RCSJ-like Josephson junctions interconnected by a parallel connection of an inductance and a resistance. An external bias

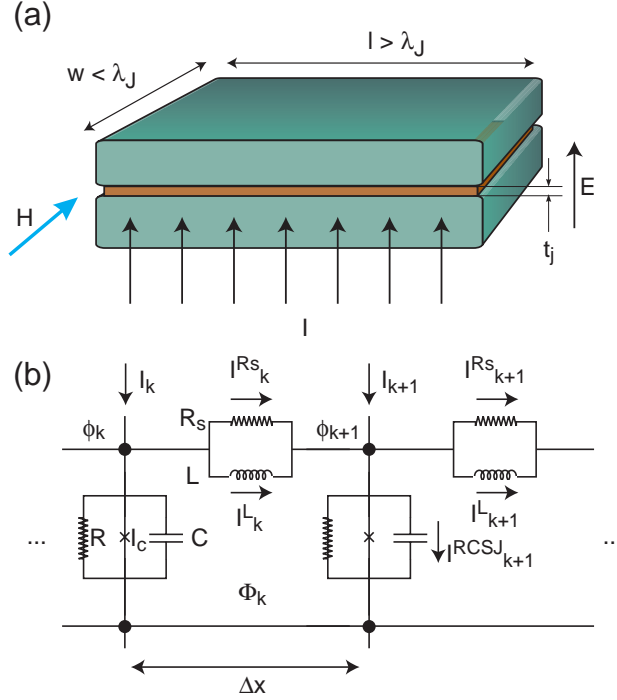


Figure 2.1: (a) Sketch of a long Josephson junction. Two planar superconducting films of dimensions  $l$  and  $w$  are separated by a tunnel barrier of thickness  $t_j$ . The directions of the electromagnetic fields in the junction are indicated. (b) The lumped circuit model of a long Josephson junction. The phase difference across the junction at node  $k$  is given by  $\phi_k$ . The current through the RCSJ type junction is  $I^{RCSJ}$ .  $I^L$  and  $I^{R_s}$  model the inductive and resistive components of the surface currents in the electrodes.  $\Phi_k$  is the total flux enclosed in one cell.

current  $I_k$  is injected in each node  $k$  and the external flux  $\Phi_{\text{ext}}$  threading each cell is taken into account. In this model, the wave equation is derived considering the flux quantization

$$\phi_{k+1} - \phi_k = \frac{2\pi}{\Phi_0} (\Phi_{\text{ext}} - LI_k^L), \quad (2.1)$$

where the flux threading the loop  $k$  due to an externally applied field can be expressed as  $\Phi_{\text{ext}} = \mu_0 H \Lambda \Delta x$ . The Kirchoff law at the node  $k+1$  is given by

$$I_k^{R_s} + I_k^L + I_{k+1} = I_{k+1}^L + I_{k+1}^{R_s} + I_{k+1}^{RCSJ}. \quad (2.2)$$

Thus, considering a small section  $\Delta x$  of the long junction we can write down the continuous limit of the Eqs. (2.1) and (2.2)

$$\frac{\phi_{k+1} - \phi_k}{\Delta x} = \frac{\partial \phi}{\partial x} = \frac{2\pi}{\Phi_0} (\mu_0 \Lambda H - L^* I^L) \quad (2.3)$$

and

$$\frac{\partial I^L}{\partial x} = j - j^{RCSJ} - \frac{\partial I^{R_s}}{\partial x}, \quad (2.4)$$

with  $L^* = L/\Delta x$ ,  $j = I/\Delta x$  and  $j^{RCSJ} = I^{RCSJ}/\Delta x$ . Differentiating Eq. (2.3) with respect to space we find

$$\frac{\partial^2 \phi}{\partial x^2} = \frac{2\pi}{\Phi_0} \left( \mu_0 \Lambda \frac{\partial H}{\partial x} - L^* \frac{\partial I^L}{\partial x} \right). \quad (2.5)$$

Substituting Eq. (2.4) with  $I^{R_s} = -1/\rho_s \partial V/\partial x$  and the RCSJ current density (1.15) into Eq. (2.5) and considering a homogeneous external magnetic field ( $\partial H/\partial x = 0$ ), we calculate the equation

$$\frac{\Phi_0}{2\pi L^*} \frac{\partial^2 \phi}{\partial x^2} = -j + j_c \sin(\phi) + \frac{V}{\rho} + C^* \frac{\partial V}{\partial t} - \frac{1}{\rho_s} \frac{\partial^2 V}{\partial x^2}, \quad (2.6)$$

where  $C^* = C/\Delta x$ ,  $\rho = R\Delta x$  and  $\rho_s = R_s\Delta x$ . Now we can express all voltages in Eq.(2.6) via the phase as  $V = \Phi_0/2\pi \partial\phi/\partial t$  using the ac Josephson relation. The resulting one-dimensional wave equation for the superconducting phase difference  $\phi(x, t)$  is called the *perturbed sine-Gordon equation* (PSGE)

$$\frac{\Phi_0}{2\pi} \frac{1}{L^*} \frac{\partial^2 \phi}{\partial x^2} - \frac{\Phi_0}{2\pi} C^* \frac{\partial^2 \phi}{\partial t^2} - j_c \sin(\phi) = -j + \frac{\Phi_0}{2\pi} \frac{1}{\rho} \frac{\partial \phi}{\partial t} - \frac{\Phi_0}{2\pi} \frac{1}{\rho_s} \frac{\partial^3 \phi}{\partial x^2 \partial t}, \quad (2.7)$$

where  $\Phi_0$  is the magnetic flux quantum,  $L^*$  the specific inductance of the junction,  $C^*$  the specific capacitance,  $j_c$  the critical-current density,  $j$  the bias current density,  $\rho$  the quasiparticle resistance per unit length, and  $\rho_s$  the surface resistance of the superconducting electrodes per unit length. The electric and magnetic fields are related to the phase differences  $\phi$  in the following way:

$$E = \frac{V}{t_j} = \frac{1}{t_j} \frac{\Phi_0}{2\pi} \frac{\partial \phi}{\partial t}, \quad (2.8)$$

$$H = \frac{1}{L^*} \frac{\Phi_0}{2\pi} \frac{\partial \phi}{\partial x}. \quad (2.9)$$

The specific inductance and capacitance of the junction are given by

$$L^* = \mu_0 d', \quad (2.10)$$

$$C^* = \frac{\epsilon_0 \epsilon_j}{t_j}, \quad (2.11)$$

where  $\epsilon_j$  is the relative dielectric constant of the junction barrier,  $t_j$  is its thickness and  $d'$  the magnetic thickness. In the limit of thick electrodes ( $d > \lambda_L$ ),  $d'$  is given by [Wei69]

$$d' = 2\lambda_L + t_j. \quad (2.12)$$

Dividing Eq.(2.7) by  $j_c$  and introducing the *Josephson length*  $\lambda_J$  and the *plasma frequency*  $\omega_p$

$$\lambda_J = \sqrt{\frac{\Phi_0}{2\pi L^* j_c}}, \quad (2.13)$$

$$\omega_p = \sqrt{\frac{2\pi j_c}{\Phi_0 C^*}}, \quad (2.14)$$

Eq. (2.7) can be expressed as

$$\lambda_J^2 \phi_{xx} - \frac{1}{\omega_p^2} \phi_{tt} - \sin(\phi) = -\frac{j}{j_c} + \frac{1}{\omega_p^2 C^* \rho} \phi_t - \frac{\lambda_J^2 L^*}{\rho_s} \phi_{xxt}, \quad (2.15)$$

where the short notation  $\phi_\xi$  has been used for the partial derivative  $\partial\phi/\partial\xi$ . From the first two terms of the wave equation (2.15), it is easy to see that the phase velocity of linear waves in this system is given by

$$c_0 = \omega_p \lambda_J = c \sqrt{\frac{t_j}{\epsilon_j d'}}. \quad (2.16)$$

$c_0$  is termed the Swihart velocity [Swi61] and  $c$  is the velocity of light in vacuum. In long Josephson junctions the Swihart velocity is typically only a few percent of  $c$  because the



magnetic field penetrates into the superconductor on a length scale  $d'$ , whereas the electric field is localized only in the junction barrier of thickness  $t_j \ll d'$ .

It is often useful to express the sine-Gordon equation in coordinates normalized with respect to the characteristic time and space scales  $\omega_p$  and  $\lambda_J$  according to

$$\tilde{t} = \omega_p t, \quad (2.17)$$

$$\tilde{x} = \frac{1}{\lambda_J} x. \quad (2.18)$$

In the normalized perturbed sine-Gordon equation

$$\phi_{\tilde{x}\tilde{x}} - \phi_{\tilde{t}\tilde{t}} - \sin \phi = -\gamma + \alpha \phi_{\tilde{t}} - \beta \phi_{\tilde{x}\tilde{x}\tilde{t}}. \quad (2.19)$$

all physical quantities are of order 1. In particular the Swihart velocity is equal to unity. The perturbation terms on the right hand side of Eq. (2.19) are defined as

$$\gamma = \frac{j}{j_c}, \quad (2.20)$$

$$\alpha = \sqrt{\frac{\Phi_0}{2\pi j_c \rho^2 C^*}} = \frac{1}{\rho C^* \omega_p}, \quad (2.21)$$

$$\beta = \sqrt{\frac{2\pi j_c L^{*2}}{\Phi_0 C^* \rho_s^2}} = \frac{\omega_p L^*}{\rho_s}, \quad (2.22)$$

where the first term is the normalized bias current, the second is the damping term due to quasiparticle resistance and the third term corresponds to the damping due to the surface impedance of the superconducting electrodes.

### Limitations of the 1D description

As mentioned in the introduction to this section, a long Josephson junction is considered quasi-one-dimensional if its width  $w$  is less than  $\lambda_J$ . If  $w < \lambda_L$  however, non-local effects may become important [IS90, Gur92]. The non-local dependence of the magnetic field on the phase in very narrow junctions made of thin films is actively discussed in literature [AS93a, AS93b, GV95, Alf95, AOSU95, Min97] and contains interesting physics by itself. For Josephson junctions prepared in Nb/Al-AlO<sub>x</sub>/Nb technology, non-local effects are only relevant for the most narrow long Josephson junctions [KWF<sup>+</sup>99] fabricated until now. On the other hand, long Josephson junctions may display two-dimensional properties even though their width is less or equal to  $\lambda_J$ . These effects are frequently neglected. One of the main aims of this work is to investigate *both* the properties of effectively two-dimensional and narrow long Josephson junctions and to discuss their intriguing physics.

### 2.1.2 Lagrangian and hamiltonian functions

Having established a wave equation which describes the dynamics of a long Josephson junction, it is useful to introduce the lagrangian and hamiltonian functions to calculate its energy. To determine the lagrangian, the energies of the electromagnetic fields and the Josephson coupling are to be considered. For now the contribution of the perturbations to the total energy of the junction are neglected. Combining the kinetic energy  $T_{\text{kin}}$  associated

with the energy density of the electric field and the potential energy  $U_{\text{pot}}$  associated with the energy density of the magnetic field and the Josephson coupling, we obtain the lagrangian  $\mathcal{L} = T_{\text{kin}} - U_{\text{pot}}$  by integrating over the junction volume  $V$

$$\mathcal{L} = \int_V \left[ \frac{1}{2} \epsilon_0 \epsilon_j E^2 - \frac{1}{2} \mu_0 \mu_r H^2 - \delta(z) \frac{\Phi_0}{2\pi} j_c (1 - \cos \phi) \right] dV. \quad (2.23)$$

Expressing the electromagnetic fields by the phase difference  $\phi$  according to Eqs. (2.8) and (2.9) and rewriting their coefficients in terms of  $\lambda_J$  and  $\omega_p$  we find

$$\begin{aligned} \mathcal{L} = & \int_0^l \int_0^w \left\{ \int_{-t_j/2}^{t_j/2} \left[ \frac{1}{2} \frac{j_c^2}{\epsilon_0 \epsilon_j} \left( \frac{1}{\omega_p^2} \phi_t \right)^2 \right] dz - \int_{-d'/2}^{d'/2} \left[ \frac{1}{2} \mu_0 \mu_r j_c^2 (\lambda_J^2 \phi_x)^2 \right] dz \right. \\ & \left. - \frac{\Phi_0}{2\pi} j_c (1 - \cos \phi) \right\} dy dx. \end{aligned} \quad (2.24)$$

Upon rearranging the coefficients and performing the integration over the width of the junction  $w$  ( $y$ -coordinate) and perpendicular to the junction plane ( $z$ -coordinate) and considering the different penetration depths of the electric and magnetic fields into the junction barrier, we find the lagrangian

$$\mathcal{L} = \frac{\Phi_0}{2\pi} j_c w \int_0^l \left[ \frac{1}{2} \frac{1}{\omega_p^2} \phi_t^2 - \frac{1}{2} \lambda_J^2 \phi_x^2 - (1 - \cos \phi) \right] dx. \quad (2.25)$$

The normalized lagrangian

$$\tilde{\mathcal{L}} = \frac{\mathcal{L}}{\mathcal{E}_0} = \int_0^\ell \left[ \frac{1}{2} \phi_t^2 - \frac{1}{2} \phi_x^2 - (1 - \cos \phi) \right] d\tilde{x}, \quad (2.26)$$

with the characteristic energy scale of the Josephson junction

$$\mathcal{E}_0 = \frac{\Phi_0}{2\pi} j_c w \lambda_J \quad (2.27)$$

is found by introducing the normalizations (2.17) and (2.18) for time and space. Here  $\ell = l/\lambda_J$  is the normalized junction length.

Making use of the lagrangian formalism [Gol91], the sine-Gordon equation is obtained by calculating the equation of motion for the continuous variable  $\phi$

$$\frac{d}{dt} \frac{\partial \mathcal{L}}{\partial \phi_t} + \frac{d}{dx} \frac{\partial \mathcal{L}}{\partial \phi_x} - \frac{\partial \mathcal{L}}{\partial \phi}. \quad (2.28)$$

The hamiltonian, determining the total energy of a long Josephson junction, is given by

$$\tilde{\mathcal{H}} = \tilde{\mathcal{H}}^{\text{SG}} + \tilde{\mathcal{H}}^P, \quad (2.29)$$

where

$$\tilde{\mathcal{H}}^{\text{SG}} = \int_0^\ell \left( \frac{1}{2} \phi_x^2 + \frac{1}{2} \phi_t^2 + 1 - \cos \phi \right) d\tilde{x} \quad (2.30)$$

is the unperturbed sine-Gordon energy. Obviously, the sine-Gordon (SG) part of the hamiltonian contains the magnetic field energy ( $\propto \phi_x^2$ ), the electric field energy ( $\propto \phi_t^2$ ) and the Josephson coupling energy ( $\propto 1 - \cos \phi$ ). The contributions of the different perturbations  $\tilde{\mathcal{H}}^P$ , i.e. bias current, microresistors and microshorts, external magnetic field *etc.*, to the total energy are discussed in Chapter 6.

## 2.2 Fluxons, breathers and plasmons: Excitations of the sine-Gordon system

In a sine-Gordon system, a large variety of linear and in particular non-linear excitations, like plasmons, solitons, anti-solitons and breathers does exist. The long Josephson junction, being well described by the sine-Gordon equation, supports many of these excitations and allows for their detailed experimental investigation. In the following, different Josephson junction geometries and their various excitations are discussed, pointing out those of particular importance for this work.

### 2.2.1 Linear long Josephson junctions

To identify the different types of excitations that exist in long Josephson junctions, I first consider a linear infinitely long quasi-one-dimensional junction. The electrodynamics of such a junction can be modeled by the perturbed sine-Gordon equation (2.15) with the boundary conditions

$$\phi_{\tilde{x}}|_{\tilde{x}=\pm\infty} = 0. \quad (2.31)$$

Using the assumption of an infinite junction, several simple analytic solutions to the sine-Gordon equation can be found. Neglecting all perturbations on the right hand side of Eq.(2.19) the exact solution

$$\phi_f(\tilde{x}, \tilde{t}) = 4 \arctan \left[ \exp \left( \pm \frac{\tilde{x} - u\tilde{t} - \tilde{x}_0}{\sqrt{1-u^2}} \right) \right] \quad (2.32)$$

to the unperturbed sine-Gordon equation

$$\phi_{\tilde{x}\tilde{x}} - \phi_{\tilde{t}\tilde{t}} - \sin \phi = 0 \quad (2.33)$$

is obtained. Depending on the sign ( $\pm$ ),  $\phi_f$  describes a *kink* (or *anti-kink*) in the phase difference  $\phi$  moving at a normalized velocity  $0 \leq u \leq 1$ . For illustration, the phase distribution (2.32) is plotted in Fig. 2.2b. The kink corresponds to a jump of  $\phi$  from  $0$  to  $2\pi$  (or  $2\pi$  to  $0$ , for an anti-kink). Obviously, the supercurrent distribution ( $\sin \phi$ ) associated with this excitation changes sign around the center of the kink, see Fig. 2.2c. Moreover,  $\phi_f$  is associated with a localized magnetic flux distribution ( $\phi_{\tilde{x}}$ ), as shown in Fig. 2.2d. In this way, the kink in  $\phi$  generates a vortex of the supercurrent creating a flux identical to a single flux quantum  $\Phi_0$ , as indicated in Fig. 2.2d. Therefore, this excitation is called a *Josephson vortex* or *fluxon*.

Kinks in sine-Gordon systems have all properties of solitons. Solitary waves exist in systems in which dispersion, which leads to the spreading of the energy of the waveform in space, and non-linear effects compensate each other. As a result, a stable solitary wave may propagate in a non-linear medium while its energy remains localized in space.<sup>1</sup> The kink in a sine-Gordon system is a *topological soliton*. There are no dynamical restrictions on its existence. This is in contrast to *dynamical solitons*, which have to have a certain energy for the dispersion to be balanced with the non-linearity. Hence there are dynamical restrictions on the existence of this type of solitons. An example are light pulses propagating in glass fibers, which only display solitary properties if their intensity is sufficiently high to stimulate non-linear effects in the fiber.

---

<sup>1</sup>For a review on different types of solitons in various physical systems, see Refs. [KM89, Abd94].

In a long Josephson junction, the Josephson vortex (i.e. the kink) can be driven by external forces, for example by a bias current applied to the junction. The bias current gives rise to a Lorentz-Magnus force acting on the charge carriers of the vortex, resulting in the propagation of the vortex along the junction. Due to the presence of dissipation, the driving force and the damping forces are balanced for a certain vortex velocity, leading to a steady motion of the kink. In the fundamental work by McLaughlin and Scott, it was pointed out that in this case the dynamics of the vortex can be described in lowest order perturbation theory [MS78]. In this approximation, the effect of the perturbations is assumed to influence only the dynamics of the center of mass coordinate  $q(t)$  of the vortex, but not its shape  $\phi_f$ . Hence, an equation of motion is derived considering the balance between the energy gain of the vortex due to the bias current and the loss due to damping.

Substituting  $\phi_f$  into the sine-Gordon hamiltonian (2.30), we find the normalized energy of a vortex propagating at velocity  $u$

$$\tilde{\mathcal{H}}^{SG}(\phi_f) = \frac{8}{\sqrt{1-u^2}}. \quad (2.34)$$

At  $u = 0$ , the rest energy equals to 8, which is identified with the normalized rest mass  $\tilde{m}_f$  of the vortex. The change of the vortex energy with time is given by

$$\frac{d}{dt}\tilde{\mathcal{H}}^{SG}(\phi_f) = \tilde{m}_f \frac{u}{(1-u^2)^{3/2}} \frac{du}{dt}. \quad (2.35)$$

The rate of energy supplied to or extracted from the junction due to the perturbations is identical to

$$\frac{d}{dt}\tilde{\mathcal{H}}^P(\phi) = - \int_{-\infty}^{\infty} (\gamma\phi_{\tilde{t}} + \alpha\phi_{\tilde{x}}^2 + \beta\phi_{\tilde{x}\tilde{t}}^2) d\tilde{x}, \quad (2.36)$$

where the first term in Eq. (2.36) corresponds to the power supplied to the junction through the bias current ( $\gamma\phi_{\tilde{t}} \propto IV$ ), the second and third terms correspond to the power extracted from the system due to the quasiparticle losses ( $\alpha\phi_{\tilde{x}}^2 \propto V^2/R$ ) and the surface impedance losses ( $\beta\phi_{\tilde{x}\tilde{t}}^2 \propto I_s^2 R_s$ ). Substituting  $\phi_f$  into Eq. (2.36), we calculate the change of vortex energy per unit time in dependence on the vortex velocity

$$\frac{d}{dt}\tilde{\mathcal{H}}^P(\phi_f) = 2\pi\gamma u - \tilde{m}_f\alpha \frac{u^2}{\sqrt{1-u^2}} - \tilde{m}_f\frac{\beta}{3} \frac{u^2}{(1-u^2)^{3/2}}. \quad (2.37)$$

Finally calculating the energy balance by equating Eqs.(2.35) and (2.37), we find the equation of motion for the vortex in presence of bias current and damping

$$\tilde{m}_f \frac{du}{dt} + \tilde{m}_f\alpha u(1-u^2) + \tilde{m}_f\frac{1}{3}\beta u + 2\pi\gamma(1-u^2)^{3/2} = 0. \quad (2.38)$$

Because of the ac Josephson effect (1.4), the motion of the vortex, being associated with a change of the phase difference  $\phi$  in time, generates a voltage drop across the junction, which is proportional to the vortex velocity  $u$ . This mechanism allows the experimental investigation of kink dynamics in long Josephson junctions by means of electrical transport measurements. Neglecting the surface damping ( $\beta = 0$ ), we find the solution

$$u = \left[ 1 + \left( \frac{4\alpha}{\pi\gamma} \right)^2 \right]^{-1/2}, \quad (2.39)$$

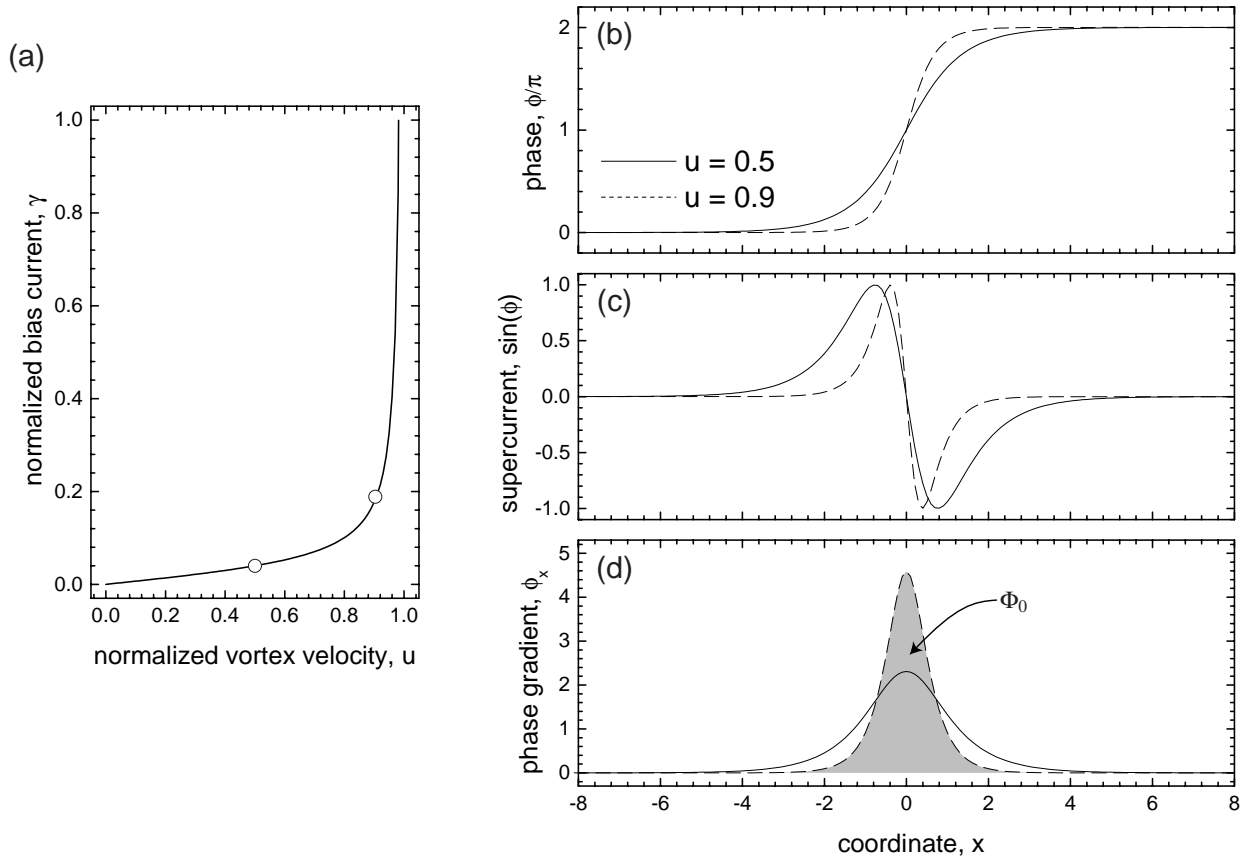


Figure 2.2: (a) Normalized bias current - vortex velocity ( $\gamma$ - $u$ ) dependence. Indicated are the two bias points, for which plots (b-d) are presented. (b) Phase distribution of a kink centered at  $\tilde{x}_0 = 0$  for two different kink velocities  $u$ . (c) Sine of the phase being proportional to the supercurrent across the junction. (d) Gradient of the phase being proportional to the magnetic field threading the junction. The total flux (shaded area) associated with the kink in the phase is identical to  $\Phi_0$ .

to the equation of motion (2.38) which determines the vortex velocity in dependence on the bias current and damping. In Fig. 2.2a, a typical normalized current-voltage (driving force - vortex velocity) characteristic is plotted. The characteristic is linear for small bias currents. Further increasing the current, the vortex velocity approaches the maximum velocity of light in the junction.<sup>2</sup> Thus, by means of the bias current, the Josephson vortex can be accelerated to velocities close to the maximum velocity and relativistic effects are observed, e.g. the Lorentz-contraction of the vortex. This effect is illustrated in Fig.2.2d, where the reduction in the width of the flux distribution with increasing vortex velocity is depicted. This phenomenon is understood noting that the sine-Gordon equation is Lorentz-invariant. The relativistic contraction of the Josephson vortex has been experimentally verified in long Josephson junctions [LDL<sup>+</sup>95].

By now we have identified the Josephson vortex as an excitation of an infinite long Josephson junction, but did not consider how it is created. Since kinks are topological excitations, it is important to note that in an infinite system, only pairs of vortices and anti-vortices may be created and annihilated if the required energy is supplied. In junctions

<sup>2</sup>In normalized units, this velocity is unity.

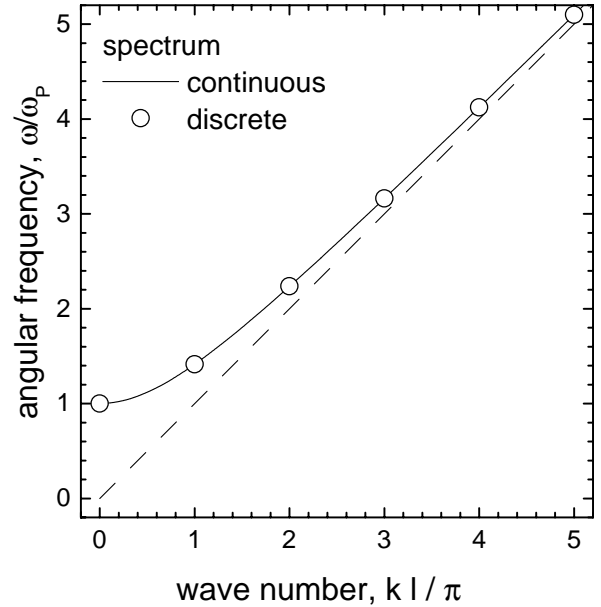


Figure 2.3: Normalized continuous (discrete) plasmon spectrum for an infinite (finite length) sine-Gordon system. The dashed line corresponds to  $\omega/\omega_p = kl/\pi$ , i.e. a mode spectrum with linear dispersion and hence constant phase velocity.

of finite size these excitation may also be generated at the boundary, as discussed later. The nucleation and annihilation of kinks in sine-Gordon systems with large damping have been investigated in detail theoretically and discussed quite controversially in literature [BL79, BL81, BHL83, Büt89, HMS88, BC95, CB98]. One of the few systems in which these processes may be investigated experimentally is the long Josephson junction.

Under certain conditions kinks and anti-kinks may form bound pairs, so called *breathers*. Breathers are unstable with respect to perturbations and decay after some transient time. This type of excitation in continuous long Josephson junctions with open boundary conditions is discussed in Ref. [CPS<sup>+</sup>78].

In a long Josephson junction also linear, small amplitude excitations of  $\phi$  do exist. These can be modeled by the linearized sine-Gordon equation (2.33)

$$\phi_{\tilde{x}\tilde{x}} - \phi_{\tilde{t}\tilde{t}} - \phi = 0 \quad (2.40)$$

which has linear wave solutions of the form

$$\phi = \phi_0 \exp(i\tilde{k}\tilde{x} - i\tilde{\omega}\tilde{t}) \quad (2.41)$$

with a spectrum

$$\tilde{\omega}(\tilde{k}) = \sqrt{1 + \tilde{k}^2}, \quad (2.42)$$

where  $\tilde{k}$  is the wave number of the mode and  $\tilde{\omega}$  is its frequency. The continuous spectrum (2.42) for an infinite length junction is plotted in Fig. 2.3. Obviously, there is a gap of  $\Delta\tilde{\omega} = 1$  (corresponding to the plasma frequency  $\omega_p$  in SI units) in the excitation spectrum. These linear excitations of the long Josephson junction are called *plasmons*.

## 2.2.2 Linear long Josephson junctions in external magnetic field

A Josephson junction of normalized length  $\ell = l/\lambda_J$ , subject to a homogeneous external magnetic field  $H$  applied in the plane of the tunnel barrier and perpendicular to the long

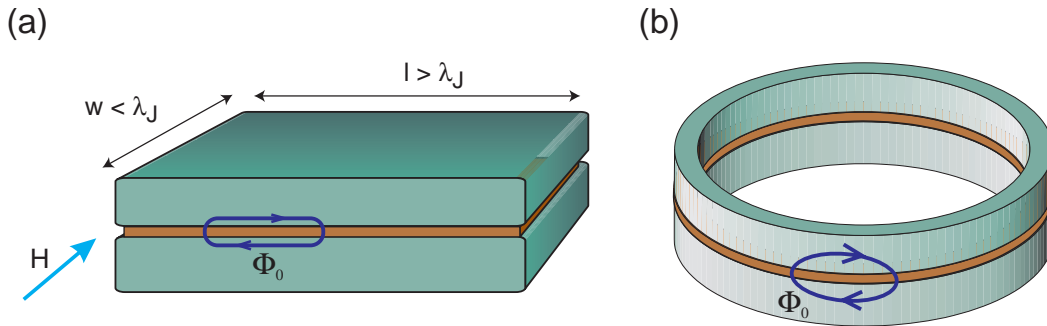


Figure 2.4: (a) Sketch of a linear long Josephson junction and (b) an annular long Josephson junction. The current distribution associated with a Josephson vortex is indicated by arrows.

dimension of the junction (see Fig. 2.4a) is described by the perturbed sine-Gordon equation with the boundary condition

$$\phi_{\tilde{x}}|_{\tilde{x}=0,\ell} = \tilde{H} . \quad (2.43)$$

Equation (2.43) is deduced from the dependence (2.3) of the phase gradient on the normalized magnetic field  $\tilde{H} = H 2\pi\mu_0\Lambda\lambda_J/\Phi_0$ . In this system, all of the linear and non-linear excitations discussed in the previous section can be studied. Additionally, the dependence of the boundary conditions on the external magnetic field allows to control the nucleation of vortices at the boundaries. The interaction of vortices with the boundaries excites plasmons in the junction. As shown in Fig 2.3, the plasmon spectrum of the junction is discrete due to its finite length.

In linear long Josephson junctions, three major regimes of fluxon motion can be observed.

*Zero-Field Resonances.* In zero external magnetic field, Josephson vortices are nucleated at the boundary of the junction. An applied bias current drives the vortices through the junction, which are reflected under a change of polarity (fluxon  $\leftrightarrow$  anti-fluxon) at its ends. This process gives rise to so-called zero-field steps in the current-voltage characteristic of the junction. A detailed discussion of zero-field resonances can be found in Ref. [Ped82].

*Fiske Resonances.* At magnetic fields larger than a certain threshold value, vortices nucleate at one end of a long current biased junction and annihilate at the other end. In the process of annihilation, plasmons are emitted, which resonate with the junction cavity. This process gives rise to so-called Fiske resonances [Fis64, Kul67, GJC94].

*Flux-Flow Resonance.* In high magnetic fields, vortices are nucleated at a high rate at one end of the junction and flow viscously in a dense chain to the other end, where they leave the junction. This process is termed flux-flow [NEIY83, NEYI84, NEYI85].

A more detailed discussion of these dynamical regimes is found in the vast literature on long junctions. A good starting point are the reviews [Ust98, PU95, Par93].

### 2.2.3 Annular long Josephson junctions

The annular geometry is of particular importance for the experimental and theoretical investigation of non-linear properties of long Josephson junctions. An annular Josephson tunnel junction is formed by two ring shaped superconducting electrodes separated by a thin tunnel barrier, as shown in Fig. 2.4b. The electrostatics of a junction with circumference

$\ell$  is described by the perturbed sine-Gordon equation with the periodic boundary conditions

$$\phi(\tilde{x} = 0) = \phi(\tilde{x} = \ell) - 2\pi n, \quad (2.44)$$

$$\frac{\partial\phi}{\partial\tilde{x}}(\tilde{x} = 0) = \frac{\partial\phi}{\partial\tilde{x}}(\tilde{x} = \ell). \quad (2.45)$$

The number of kinks  $n$  initially present in the annular junction is conserved due to the closed topology, which is expressed by the boundary condition (2.44). The condition (2.45) enforces the continuity of the magnetic field along the junction. Similar to the infinite system, kink excitations can only be nucleated in pairs of kinks and anti-kinks. Due to the finite length of the annular junction, the plasmon excitation spectrum is discrete.

Experimentally, annular junctions are prepared in states with  $n$  topologically trapped Josephson vortices by cooling the junction from the normal to the superconducting state in a small applied field. The required magnetic field can be generated either by using an external coil or by biasing the junction with a small current. Alternatively, vortices may be trapped in the junction by locally heating up one of its electrodes in an external field using an electron or laser beam in a low temperature scanning microscope [UDH<sup>+</sup>92]. Dynamic states of an annular junction with  $n$  vortices trapped are called  $n$ -vortex states. In an  $n$ -vortex state, all flux quanta thread one junction loop and the junction barrier, but not the other. Additional vortex anti-vortex pairs can be nucleated in the junction under the appropriate bias conditions. These states are called  $n + \bar{n}$ -vortex states, where  $\bar{n}$  is the total number of anti-vortices. The different states can be clearly identified by the dependence of the critical current of the junction on the external field (see Chapter 3) and by their current-voltage characteristics (see Chapter 4).

## 2.3 Basic experimental techniques

Long Josephson junctions are almost ideal physical realizations of a sine-Gordon system. They can be fabricated with high quality and high reproducibility. Their non-linear and linear excitations can be studied experimentally in great detail and with a good accuracy by performing electrical transport measurements at low temperatures.

### 2.3.1 Sample preparation

Josephson tunnel junctions are formed by bringing two superconducting films into contact via a thin insulating tunnel barrier. The most reliable and widespread fabrication technology for high quality junctions is based on niobium (Nb) as the superconductor and aluminum oxide ( $\text{AlO}_x$ ) to form the tunnel barrier. These materials are employed in the so-called Nb–Al/ $\text{AlO}_x$ –Nb trilayer technology [KHN<sup>+</sup>97] to form tunnel junctions for both basic research and applications. The experiments presented in this work were done with samples prepared using techniques identical or similar to the ones described in the following paragraphs.

Nb–Al/ $\text{AlO}_x$ –Nb trilayer tunnel junctions are typically fabricated on thermally oxidized silicon (Si) wafers. Each wafer can carry a number of chips, typically of size 0.25 to 1 cm<sup>2</sup>, with a number of tunnel junctions on each chip. In a first step, the Si wafer is coated with a thin film (about 1.5  $\mu\text{m}$ ) of photoresist which is subsequently exposed using optical lithography to define the areas of the chip on which the trilayer is to be deposited. After development of the photoresist (PR), the first Nb layer is sputtered onto the wafer. In



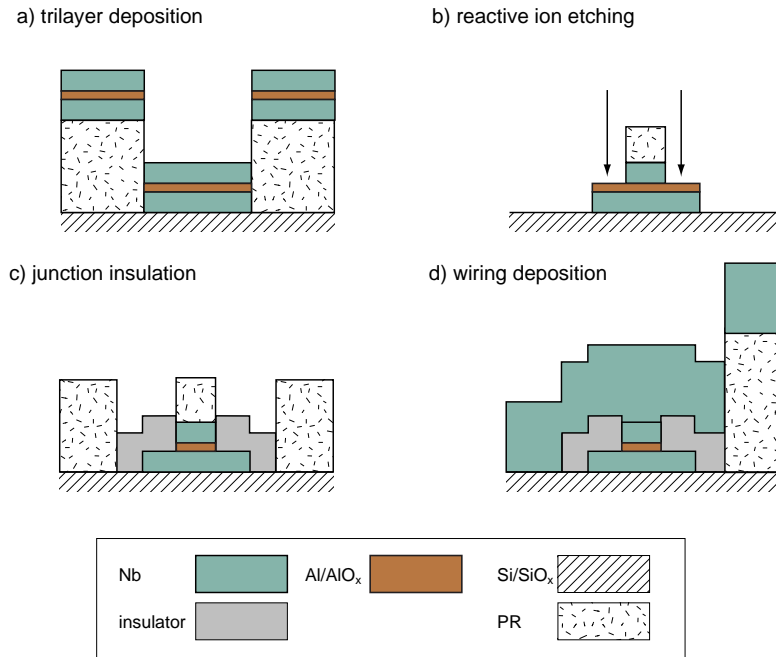


Figure 2.5: Selected fabrication steps of a Josephson junction (cross-sectional view). (a) Trilayer deposition. (b) Reactive ion etching for definition of junction area. (c) Junction insulation by deposition of insulator. (d) Deposition of wiring layer.

the sputter process, a polycrystalline Nb film of several tens to some hundreds of nm is deposited in a plasma discharge glowing between the sample and the target in the vacuum chamber of the deposition system. Next a thin film (3–5 nm) of aluminum is sputtered onto the wafer and subsequently oxidized in an oxygen atmosphere within the sputter chamber to form an AlO<sub>x</sub> tunnel barrier of 2–3 nm thickness. The thickness and the morphology of the aluminium oxide layer crucially determine the critical-current density, the quasiparticle resistivity and the specific capacitance of the junction. The trilayer is completed by the deposition of the niobium film forming the top electrode of the junction. In Fig. 2.5a, a cross-section through the junction area at this stage of fabrication is shown.

After the deposition of the trilayer a lift-off [YKN87], removing the trilayer from the parts of the wafer covered with photoresist, is performed. The effective junction area is defined by reactive ion etching (RIE) through a mask of photoresist defined in a second photolithographic process. The etching process is stopped at the AlO<sub>x</sub> tunnel barrier, see Fig. 2.5b. The sides of the Josephson junction are subsequently electrically insulated by deposition of silicon oxide (SiO<sub>x</sub>) to avoid shorting out the tunnel junction by a direct contact between the top and bottom electrodes, see Fig. 2.5c. Alternatively, the junction can also be insulated using anodic oxidization of the junction edges [HG85, KGS91]. In the final lithographic step, the top electrode of the junction is contacted by depositing a film of Nb (see Fig. 2.5d) onto a mask of photoresist and performing a lift-off. The bottom electrode of the sample is contacted using a part of the bottom Nb film which extends outside the junction area.

With standard photolithographic techniques, Josephson junctions of sizes of approximately  $3 \times 3 \mu\text{m}^2$  are prepared regularly. With extra effort, sizes down to  $1 \times 1 \mu\text{m}^2$  can be reached. If smaller sample features are required, electron beam lithography techniques have to be employed and the fabrication process has to be optimized to provide the necessary accuracy in alignment and junction insulation. Recently, we have developed techniques [KWF<sup>+</sup>99] to prepare Josephson junction based on the trilayer technology with feature sizes down to smaller than  $0.3 \mu\text{m}$ . Independently similar techniques have been elaborated by other groups.

### 2.3.2 Typical junction parameters

The material properties of sputtered polycrystalline niobium and aluminum films can be rather well controlled and reproduced. A few important characteristic properties of high quality films are listed in Table 2.1. These parameters are rather constant and can hardly be modified to influence the junction parameters. Instead the thickness  $t_j$  and the properties of the tunnel barrier can be very well controlled in order to change the critical-current density  $j_c \propto \exp(-t_j)$ , the quasiparticle tunnel resistance  $\rho \propto \exp(-t_j)$  per unit area and the specific capacitance  $C^* \propto 1/t_j$  of the junction. Obviously these parameters cannot be changed independently. The range of attainable electrical parameters is quoted in Table 2.1.

The electrical properties of a Josephson tunnel junction are not solely depending on the properties of the tunnel barrier itself, but are also influenced by the electrical properties of the surrounding area. Of particular importance is the region in which the top and bottom junction electrodes overlap outside of the tunnel barrier, see Section 2.3.1. This part of the junction is often called *idle region* or window, to contrast it to the (active) tunnel region of the junction. As pointed out in later chapters, this idle region needs to be considered to quantitatively understand the static and the dynamic properties of the long annular Josephson junctions which have been examined experimentally in this work.

### 2.3.3 Basic measurement technique

Josephson tunnel junctions are cooled below their critical temperature  $T_c$  to investigate their superconducting properties. By immersing the sample directly into liquid helium or into the vapor above the helium surface, temperatures down to 4.2 K can be reached. To achieve lower temperatures and/or better temperature stabilization, the sample is mounted in the vacuum chamber of a cryostat. Depending on the lowest temperatures that are required, either a pumped  $^4\text{He}$  (down to 1.4 K), a pumped  $^3\text{He}$  cryostat (down to 260 mK) or a  $^3\text{He}$ - $^4\text{He}$  dilution refrigerator (down to 10 mK) is used [Pob95].

Since the spatial distribution of the phase of a long Josephson junction depends sensitively on the magnetic field, the sample is magnetically shielded in a cylindrical high permeability container. Magnetic fields up to 40 gauss can be applied in the plane of the junction barrier, using a cylindrical superconducting coil which is energized with currents up to 100 mA.

The sample is current biased using a custom-made battery-powered analog current source with current ranges adjustable between 100 mA and 100 nA. Likewise, the volt-

Table 2.1: Characteristic electrical parameters of Josephson junctions fabricated in Nb–Al/ $\text{AlO}_x$ –Nb trilayer technology.

quantity	unit	value	meaning
$T_c$ Nb	[K]	9.2	critical temperature
$\lambda_L$ Nb	[nm]	90	London penetration depth
$T_c$ Al	[K]	1.2	critical temperature
$\lambda_L$ Al	[nm]	50	London penetration depth
$j_c$	[A/cm <sup>2</sup> ]	10 – 5000	critical-current density
$C^*$	[fF/ $\mu\text{m}^2$ ]	10 – 100	specific capacitance
$\rho$	[ $k\Omega\mu\text{m}^2$ ]	0.01 – 10	quasiparticle sheet resistance

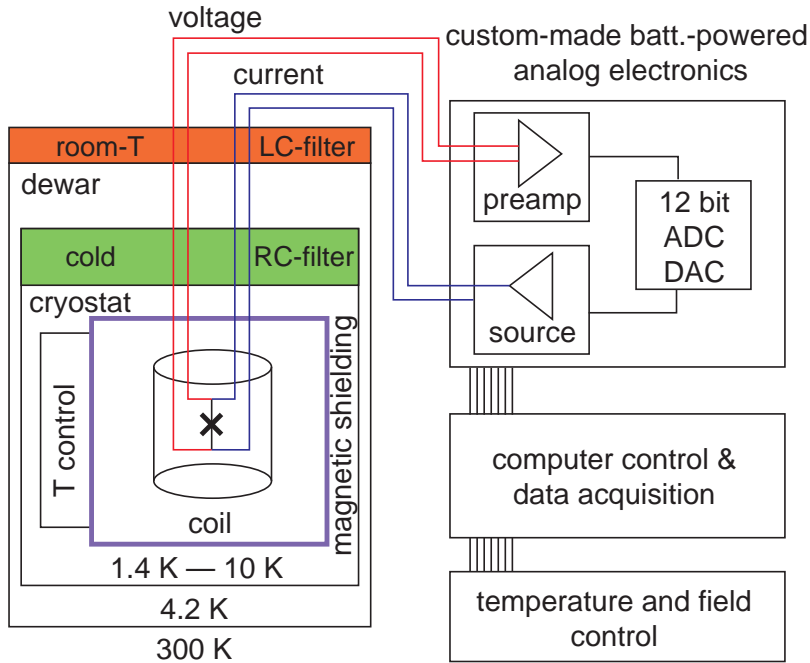


Figure 2.6: Schematic of the basic measurement setup containing temperature control, analog and digital electronics, and electromagnetic shielding and filtering.

age across the junction is measured using a custom-made battery-powered bipolar or FET preamplifier circuit with adjustable low-pass filters. The sample is connected to the analog electronics using shielded and/or twisted pairs of wires. The wires are filtered with commercial  $\pi$ -type LC filters at room temperature and cold RC filters at liquid helium temperature to avoid interference due to electromagnetic pick up from the environment. A four-point measurement technique is employed to avoid wiring and contact resistances in the measurements.

The bias current through the sample and the coil are controlled using 12-bit D/A converters. The voltage across the sample is monitored using 12-bit A/D converters. All elements of the data-acquisition are software controlled. The software Gold-exi [Gol] is used to measure the current-voltage characteristics and the dependence of the critical current on the external magnetic field. A schematic layout of a typical measurement setup is shown in Fig. 2.6.

In addition to dc measurements, the electromagnetic radiation emitted from a Josephson junction can be measured to gain information about the temporal evolution of the electromagnetic fields inside the junction [KSF<sup>+</sup>96, KSF<sup>+</sup>97]. Spatially resolved but time averaged electromagnetic properties of junctions can be measured using low temperature scanning electron microscopy [GK94] or low temperature scanning laser microscopy [SZTD96, SZT<sup>+</sup>94].



## Part II

# TWO-DIMENSIONAL ANNULAR JOSEPHSON JUNCTIONS

The annular Josephson junction is ideal to investigate the dynamics of solitons in a quasi-one-dimensional sine-Gordon system. Due to the periodic boundary conditions, the dynamics of the fluxon is not perturbed by collisions with the junction ends. The first measurements of single fluxons in annular junctions were reported by Davidson *et al.* [DDKP85]. Using perturbation theory [MS78], the fluxon dynamics in the annular junction was analyzed quantitatively, allowing the determination of the losses in the junction [DPP86, UDH<sup>+</sup>92].

Initially, the controlled trapping of single and multiple vortices in the junction became possible using a low temperature scanning electron microscope (LTSEM) [UDH<sup>+</sup>92]. Imaging the collisions between a vortex and an anti-vortex trapped in an annular junction using the LTSEM, the Lorentz contraction of the vortex was verified [LDL<sup>+</sup>95]. The static properties of annular junctions in the presence of an external field were investigated both theoretically and experimentally [MMS, MM96b, MM96a]. In the initial works, the junction was considered as quasi-one-dimensional. The finite width of the junction was first taken into account theoretically in Ref. [Nap97]. The bunching of multiple vortices was examined [VLS<sup>+</sup>96] and the dynamics of vortex–anti-vortex pairs was investigated [MSM96]. The pinning of fluxons by an external magnetic field applied in the plane of the junction was analyzed experimentally, measuring critical current versus field patterns [VKT<sup>+</sup>97, VKT<sup>+</sup>96] and by imaging spatially the static vortex configuration in the junction [KVL<sup>+</sup>96]. The dynamics of the vortex in a field-induced harmonic potential well was analyzed [UT97, Ust99], also considering the depinning from the potential well and the re-trapping into the well [UMT97]. Later it was found that the vortex may experience pinning also at the junction leads [MDP<sup>+</sup>98]. Recently, we have started to investigate the process of the vortex escape from such pinning potentials in more detail. We have examined the thermal activation of the vortex [WKL<sup>+</sup>00, FCC<sup>+</sup>00] and are planning to observe quantum tunneling [KI96, WKL<sup>+</sup>00].

Recently, large area annular junctions have been proposed as radiation and particle detectors [NC97]. In these junctions, vortices may be used to effectively suppress the critical current [NCL98, CEF<sup>+</sup>99] which is required to operate the junction as detector.

In this part of the thesis, I consider the static and dynamic properties of *wide* annular Josephson junctions. The observed effects are analyzed and explained specifically considering the junction width and the idle region coupled to it. First, the static phase distribution of annular junctions subject to an external field is examined by measuring their critical current. In particular, the dependence of the critical-current diffraction pattern on the inner and outer junction radius is considered [FWU00b]. Then, I present experiments, proving the theoretically predicted [KYSV98] excitation of whispering gallery modes by a vortex propagating at relativistic velocities in a wide annular junction [WUK<sup>+</sup>00]. Finally, the effect of the electromagnetic environment on the static and dynamic properties of annular junctions which are embedded in striplines of various widths is investigated by measuring the critical current versus field patterns [FWU00a] and single vortex resonances [WFU<sup>+</sup>00].

## Chapter 3

# Critical-Current Diffraction Patterns in Annular Josephson Junctions

Systematic measurements of the critical current versus magnetic field patterns of annular Josephson junctions in a wide magnetic field range are reported. A modulation of the envelope of the pattern, which depends on the junction width, is observed. The data are compared with theory and good agreement is found.<sup>1</sup>

Large area Josephson junctions are intriguing objects for performing experiments on non-linear electrodynamics. In particular, the propagation of solitons, also called Josephson vortices or fluxons, in long Josephson junctions has attracted a lot of attention and has been studied in detail [Ust98]. In an annular Josephson junction, magnetic flux quanta threading one superconducting loop but not the other, can be trapped and stored in the junction due to the fluxoid quantization [DDKP85]. This property of the system offers the unique possibility to study fluxon dynamics in the absence of collisions with boundaries [MS78]. The number and the configuration of Josephson vortices trapped in an annular junction can be determined accurately by measuring the dependence of its critical current on the external field, which is related to the static spatial distribution of the phase difference in the junction. The detailed knowledge of the static phase configuration in annular Josephson junctions with and without trapped vortices is important both for the basic understanding of the vortex states of the junction and for their use in applications.

Recently large area Josephson junctions have been proposed as efficient radiation and particle detectors [EFPB96, NC97, CEF<sup>+</sup>99]. The detection mechanism relies on the excitation of quasiparticles in the superconductor by the incoming electromagnetic radiation or particles. Such detectors have a high energy resolution due to the small energy gap  $\Delta$  of the superconductor resulting in a large number  $n = E/\Delta$  of quasiparticles generated per incident particle of energy  $E$ . To effectively detect these quasiparticles, the junction is biased in the subgap region. To do so, the critical current is suppressed either by an external magnetic field or more efficiently by trapping Josephson vortices in an annular

---

<sup>1</sup>Parts of this chapter have been accepted for publication in ‘Physical Review B’.

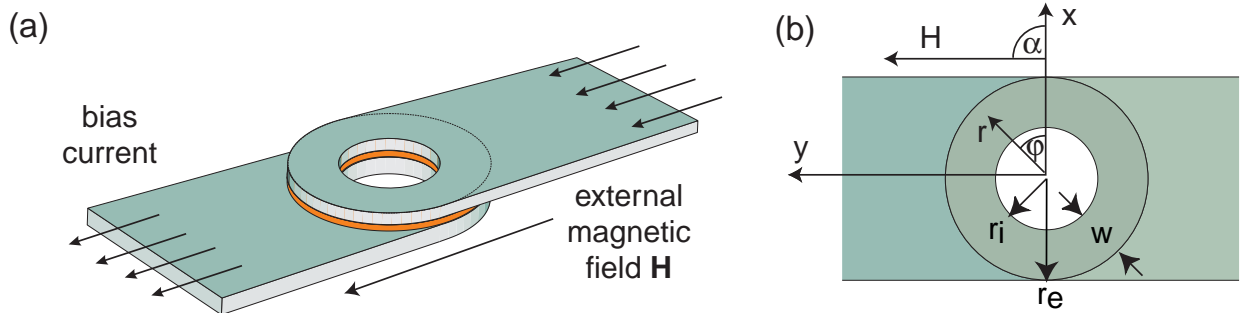


Figure 3.1: (a) Schematic drawing of the annular Josephson junction biased in the Lyngby-geometry [DDKP85]. The wide leads attached to the junction shall guarantee a homogeneous distribution of the bias current. (b) The junction dimensions: inner radius  $r_i$ , outer radius  $r_e$ , junction width  $w$ . The external field  $H$  is applied at an angle  $\alpha$  with respect to the  $x$ -axis. The phase difference is expressed in polar coordinates  $\phi(r, \varphi)$ .

junction as proposed in Refs. [NC97, CEF<sup>+</sup>99].

Here, I present systematic measurements of the critical current of annular Josephson junctions in dependence on the externally applied in-plane magnetic field (see Fig. 3.1). The critical current  $I_c$  of a junction without trapped fluxons is at maximum in zero field. In the presence of a magnetic field, the critical current is reduced. Magnetic fields can be due to the bias current applied to the junction (self-fields), due to flux trapped in the junction itself or its leads (Josephson or Abrikosov vortices, respectively), or they can be applied externally. The modulation of the critical current with the external field is often called a *critical-current diffraction pattern* [MBCF85]. We investigate these patterns for annular junctions of various dimensions in a wide range of magnetic fields.

### 3.1 State of the art

Critical-current diffraction patterns of annular junctions have been actively investigated experimentally and theoretically [MM96a, MM96b, Nap97]. The qualitative understanding of their features is rather complete, however a number of open problems remain. In this chapter, I address the field dependence of the critical current on the exact junction geometry. In particular, new results in the large-field regime are presented allowing a more precise comparison between theory and experiment.

Several theoretical approaches to predict and explain the critical current diffraction patterns of annular Josephson junctions can be found in literature [KVL<sup>+</sup>96, MM96a, MM96b, VKT<sup>+</sup>96, VKT<sup>+</sup>97, Nap97]. Mainly, two different cases have been considered so far, i.e. the long annular Josephson junction with a circumference  $2\pi\bar{r}$  larger than the Josephson length  $\lambda_J$  and the small annular Josephson junction with  $2\pi\bar{r} < \lambda_J$ . Here  $\bar{r} = (r_i + r_e)/2$  is the mean radius of the junction. In these approaches, the dependence of the pattern on the junction geometry is treated approximately, which results in quantitatively inaccurate interpretation of experimental data.

The most complete and mathematically exact analytical description of the critical-current diffraction pattern  $I_c(H)$  of a small annular junction with arbitrary number of trapped fluxons  $n$  is presented by Nappi in Ref. [Nap97]. In this work the finite width of the junction is considered exactly. Using the results of Nappi and the results of our measure-

ments in the high-field limit, the quantitative understanding of experimental critical-current diffraction patterns can be improved.

In Ref. [Nap97] the critical-current diffraction pattern of a small annular junction is calculated from the dependence of the phase  $\phi$  on the external field (see Section 1.2)

$$\left( \vec{n}_r \frac{\partial}{\partial r} + \vec{n}_\varphi \frac{1}{r} \frac{\partial}{\partial \varphi} \right) \phi = \frac{2\pi\mu_0\Lambda}{\Phi_0} \vec{H} \times \vec{n}_z. \quad (3.1)$$

In Eq. (3.1)  $(\vec{n}_r \partial/\partial r + \vec{n}_\varphi 1/r \partial/\partial \varphi)$  is the gradient in polar coordinates (see Fig. 3.1b) and  $\Lambda$  is the magnetic thickness of the junction. With the external magnetic field expressed in polar coordinates

$$\begin{aligned} H_r(\varphi) &= H \cos(\alpha - \varphi), \\ H_\varphi(\varphi) &= H \sin(\alpha - \varphi) \end{aligned}$$

Eq. (3.1) separates into two differential equations for the coordinates  $r$  and  $\varphi$ . Both equations can be integrated yielding the same result

$$\phi(r, \varphi) = \frac{2\pi}{\Phi_0} r \mu_0 \Lambda H \sin(\alpha - \varphi) + \phi_0, \quad (3.2)$$

where  $\phi_0$  is the phase difference in the junction along the direction of the magnetic field ( $\varphi = \alpha$ ). The critical current  $I_c$  of the junction at the field  $H$  is found by integrating the Josephson current density over the junction area

$$I_c(H) = j_c \max_{\phi_0} \left[ \int_0^{2\pi} \int_{r_i}^{r_e} \sin \left( \frac{2\pi}{\Phi_0} r \mu_0 \Lambda H \sin(\alpha - \varphi) + \phi_0 \right) dr d\varphi \right] \quad (3.3)$$

and maximizing the expression with respect to  $\phi_0$ . Here  $j_c$  is assumed to be homogeneous across the whole junction.

In Ref. [Nap97], the critical current is also calculated for vortices being trapped in the junction. Assuming that the field generated by  $n$  vortices is distributed homogeneously along the junction length, the field

$$H = n \frac{\Phi_0}{2\pi r \mu_0 \Lambda} \quad (3.4)$$

is to be added to the radial component of  $H$ . This additional field gives rise to an extra term  $-n\varphi$  in the equation for the 2D phase distribution (3.2). Hence, the dependence of the critical current  $I_c$  on the magnetic field  $H$  (3.3) for an arbitrary number  $n$  of trapped vortices is calculated as

$$I_c(H) = I_c(0) \left| \frac{2}{1 - \delta^2} \int_\delta^1 x J_n \left( x \frac{H}{H_0} \right) dx \right|, \quad (3.5)$$

where  $J_n$  is the  $n$ -th Bessel function of integer order.  $\delta = r_i/r_e$  is the ratio of the inner junction radius  $r_i$  to the outer radius  $r_e$  and  $I_c(0) = j_c \pi (r_e^2 - r_i^2)$  is the maximum superconducting current at zero field. The characteristic magnetic field

$$H_0 = \Phi_0 / (2\pi r_e \mu_0 \Lambda) \quad (3.6)$$

is proportional to the field at which one flux quantum penetrates the magnetic cross-section  $2r_e \Lambda$  of the junction.



Maximizing the critical current (3.3), the phase  $\phi_0$  for an odd number  $n$  of vortices is found to be

$$\phi_0 = \begin{cases} 0 & \text{for } \int_{\delta}^1 x J_n \left( x \frac{H}{H_0} \right) dx \geq 0 \\ \pi & \text{for } \int_{\delta}^1 x J_n \left( x \frac{H}{H_0} \right) dx \leq 0 \end{cases} \quad (3.7)$$

and

$$\phi_0 = \begin{cases} \frac{\pi}{2} & \text{for } \int_{\delta}^1 x J_n \left( x \frac{H}{H_0} \right) dx \geq 0 \\ -\frac{\pi}{2} & \text{for } \int_{\delta}^1 x J_n \left( x \frac{H}{H_0} \right) dx \leq 0 \end{cases} \quad (3.8)$$

for zero or an even number of vortices trapped in the junction.

For  $n = 0$ , the two extreme cases  $\delta \rightarrow 1$  (see Ref. [MM96a]) and  $\delta \rightarrow 0$  (see Ref. [BP82]) of Eq. (3.5) have been discussed in the literature. The predictions of Eq. (3.5) have also been compared to experiments in a relatively small magnetic field range [CEF<sup>+</sup>99, MM96b, NCL98]. To our knowledge, there has been no systematic comparison of this theory with experimental data for different junction widths in a large field range. The intention here is to perform such a comparison.

## 3.2 Experimental results and comparison with theory

Experimental data on five annular Josephson junctions with the same external radius  $r_e = 50 \mu\text{m}$  but different inner radii  $r_i$  ranging from 30 to 47  $\mu\text{m}$  are presented. Their width  $w = r_e - r_i$  varies between 3 and 20  $\mu\text{m}$ . The junction geometry is shown in Fig. 3.1b and the sample dimensions are listed in the second and third columns of Table 3.1. All junctions have been prepared on the same chip using Hypres technology [Hyp] with a nominal critical-current density of  $j_c = 100 \text{ A/cm}^2$ . Accordingly, the Josephson length is approximately 30  $\mu\text{m}$  at 4.2 K.

### 3.2.1 Diffraction patterns without trapped fluxons

In Fig. 3.2 the critical-current diffraction patterns of the two junctions  $B$  and  $D$ , being representative for the set of measured samples, are shown. A strong dependence of the pattern on the junction width is clearly observed. As expected, the critical current at zero field scales with the junction size as  $I_c = j_c \pi (r_e^2 - r_i^2)$ . Measuring the diffraction patterns in a wide range of magnetic field, two characteristic modulation scales of the critical current are observed. The pattern, having a small magnetic field period  $\Delta H$ , has an envelope of the larger period  $\Delta H'$  which depends strongly on the junction width, compare Figs. 3.2a and b.

The observed patterns can be qualitatively understood in the following way: the modulation of the critical current with the period  $\Delta H$  is due to the penetration of magnetic flux into the junction in the direction perpendicular to the external magnetic field. This period is inversely proportional to the junction diameter  $\Delta H \propto 1/(2r_e)$  [compare to the characteristic field (3.6)]. This is analogous to the standard linear junction case, where  $\Delta H$  is proportional to the reciprocal junction length in the direction perpendicular to the magnetic field [BP82]. The minima of the modulation with the period  $\Delta H'$  occur when the magnetic flux penetrates the junction strongly also along the *width* of the junction. Therefore, the period  $\Delta H'$  of the second modulation is proportional to  $1/w$ . Calculating the ratio

$$\frac{\Delta H'}{\Delta H} = \frac{2r_e}{w} \quad (3.9)$$

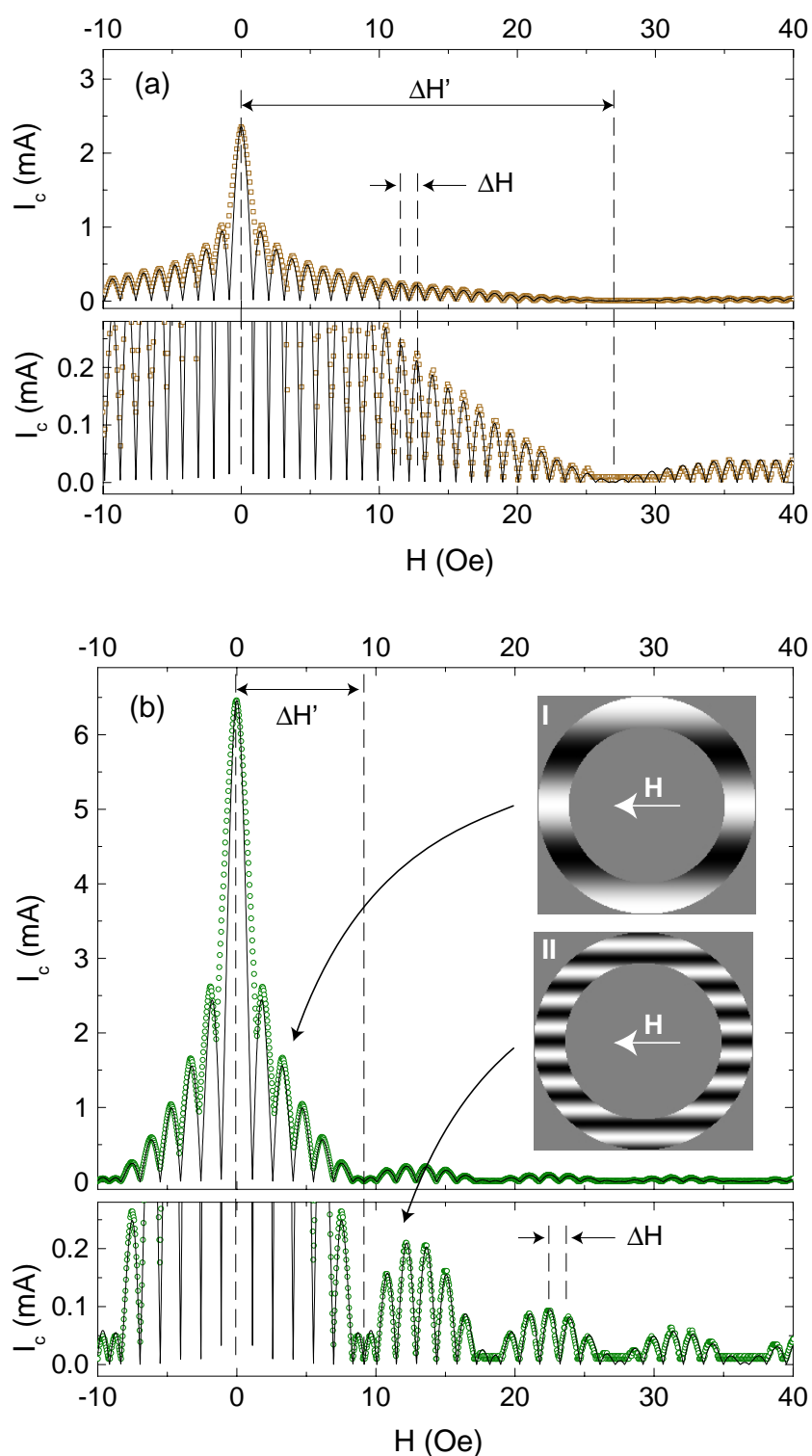


Figure 3.2: Critical-current diffraction patterns of (a) junction  $B$  and (b) junction  $D$  at 4.2 K. Dots are experimental data, the solid line is theory according to Eq. (3.5). For better visibility the low current region is also plotted on an enlarged scale. The two field modulation periods  $\Delta H$  and  $\Delta H'$  are indicated in each plot. The insets  $I$  and  $II$  of plot (b) display the supercurrent distribution in junction  $D$  at the magnetic fields indicated by arrows; light (dark) regions correspond to current in positive (negative) direction.

Table 3.1: Geometrical parameters and fitted values of the measured annular Josephson junctions.

#	$r_i$ [ $\mu\text{m}$ ]	$\delta = r_i/r_e$	$\Delta H'/\Delta H$	$2r_e/w$	$\delta$	$\Delta r$ [ $\mu\text{m}$ ]	$\tilde{H}_0$ [Oe]	$\tilde{H}_0/H_0$	$\Lambda$ [nm]
A	47	0.94	-	-	0.96	0.5	0.319	0.65	208
B	45	0.9	22.9	20.0	0.92	0.5	0.346	0.703	193
C	42	0.84	13.2	12.5	0.88	1.0	0.321	0.646	210
D	35	0.7	6.5	6.7	0.72	0.6	0.405	0.821	165
E	30	0.6	4.8	5.0	0.62	0.5	0.376	0.765	177

for the different junctions, this simple prediction is quantitatively compared with experiment. As can be seen from the forth and fifth columns of Table 3.1, Eq. (3.9) is quite accurately fulfilled for our junctions.<sup>2</sup>

The described effect is illustrated in Fig. 3.2b by plotting the supercurrent density  $j_s = j_c \sin(\phi)$  at different magnetic fields versus the junction coordinates using Eq. (3.2) and taking into account  $\phi_0$  as given by Eq. (3.8). At  $H = 3.25$  Oe  $< \Delta H'$ , approximately two and a half flux quanta have penetrated into the junction cross section  $2r_e$ , as shown in the inset I of Fig. 3.2b. At the larger field  $H = 12.2$  Oe  $> \Delta H'$ , more than one flux quantum threads the width cross section of the junction (see inset II). Thus, after each period  $\Delta H'$ , one additional flux quantum is threading the width of the junction. We note here that the spatial distribution of the supercurrent density can also be measured in experiment [KVL<sup>+</sup>96].

In Fig. 3.2, the experimental data are fitted to Eq. (3.5). In the fitting procedure the values of both  $H_0$  and  $\delta$  are determined. Subsequently, the quantities acquired from the fits are labeled by a tilde ( $\tilde{H}_0$ ,  $\tilde{\delta}$ ). For the fit, the initial value of  $\tilde{\delta}$  is calculated from the designed geometry of the junction; the initial  $\tilde{H}_0$  is calculated according to Eq. (3.6) assuming the reasonable value of 200 nm for the magnetic thickness  $\Lambda$ . Then, the best fit is found by iteratively adjusting  $\tilde{H}_0$  and  $\tilde{\delta}$ . The value of  $\tilde{H}_0$  predominantly determines the small period of the critical-current modulation  $\Delta H$ , whereas  $\tilde{\delta}$  determines the large modulation scale  $\Delta H'$ . This fact is in agreement with the qualitative discussion above. As can be seen from Fig. 3.2, excellent agreement between theory and experiment is found. The parameters  $\tilde{\delta}$  and  $\tilde{H}_0$  determined from the best fits to the data of junctions A to E are quoted in Table 3.1.

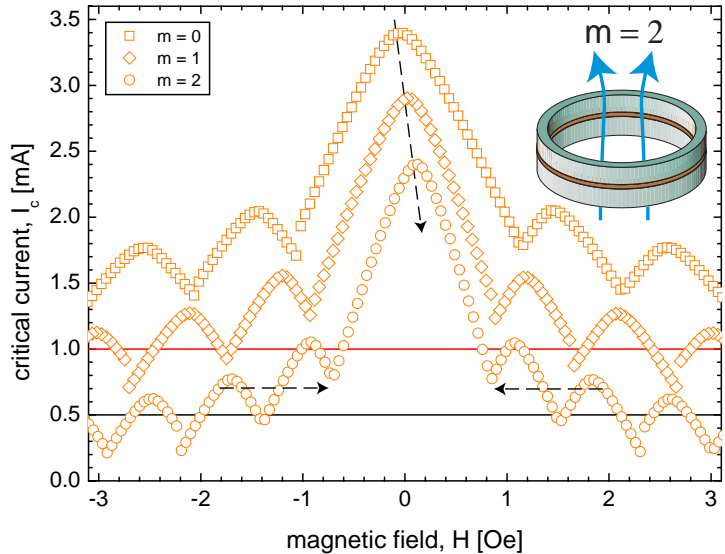
Comparing the values of  $\delta$  and  $\tilde{\delta}$  in Table 3.1, we find that  $\tilde{\delta} > \delta$  for all junctions. The small but systematic difference can be explained by considering a symmetric deviation  $\Delta r$  of the junction radii from their designed dimensions, e.g. due to the photolithographic procedure during the preparation. Using this assumption,  $\tilde{\delta}$  can be expressed as

$$\tilde{\delta} = \frac{r_i + \Delta r}{r_e - \Delta r}. \quad (3.10)$$

From the fits we find that  $\Delta r$  varies between 0.5 and 1.0  $\mu\text{m}$ , see Table 3.1. This size correction can also be explained as due to a slight over-etching of the trilayer during sample fabrication, which results in a small reduction of the junction size. The obtained values of  $\Delta r$  agree with the size tolerance quoted by Hypres [Hyp].

<sup>2</sup>For junction A,  $\Delta H'$  could not be evaluated due to its small width. The field necessary to observe the first minimum of the envelope of the diffraction pattern was above the maximum range of our experimental setup.

Figure 3.3: Critical-current diffraction patterns of junction  $B$  at 4.2 K. The qualitatively similar curves correspond to different number  $m$  of flux quanta threading both junction loops, see inset. Arrows indicate the tendencies in the offset and in the rescaling in  $H$  for patterns with different  $m$ . For better visibility each curve is offset by 0.5 mA with respect to the other.



According to the theory, the quantity  $H_0$  depends only on the outer junction radius  $r_e$  and hence should be identical for all junctions measured. From the fits however, we find values of  $\tilde{H}_0$  that slightly differ from junction to junction, see Table 3.1. Using Eq. (3.6), the magnetic thickness  $\tilde{\Lambda}$  is calculated from  $\tilde{H}_0$  for each junction, see last column of Table 3.1. The average magnetic thickness is  $\tilde{\Lambda} = 191 \pm 18$  nm, yielding a London penetration depth of  $\lambda_L \approx 95$  nm which is in good agreement with typical values of  $\lambda_L (\approx \tilde{\Lambda}/2)$  found for niobium films.

The scatter observed in  $\tilde{H}_0$  (or, equivalently, in  $\tilde{\Lambda}$ ) may be due to a small number  $m$  of flux quanta threading the holes of both junction electrodes simultaneously, see inset of Fig.3.3. Cooling the junction a large number of times from the normal to the superconducting state in a small residual magnetic field and measuring the resulting critical current versus magnetic field, we find different diffraction patterns. Focusing on the low field range, three such reproducibly generated diffraction patterns labeled by different  $m$  are shown in Fig. 3.3. The patterns are very similar in their qualitative features, but differ quantitatively depending on  $m$ . They show a slight offset in field and a large rescaling in the low field range depending on the index  $m$ , see arrows in Fig.3.3. These effects may be due to self-fields generated by the trapped flux-induced screening currents circulating in the junction loops. For a perfectly symmetric junction (i.e. one without bias leads), the screening currents should not contribute to the pattern, but for the junction geometry used here (see Fig. 3.1) they may not be negligible. In this particular measurement, we have only observed three different diffraction patterns, despite repeating the described procedure a large number of times. This strongly suggests that quantized magnetic flux is threading the junction loop perpendicular to the substrate.

The effective local field at the junction may be slightly different from the externally applied field because of a small misalignment between the junction and the field. This misalignment may vary between different measurement runs. Moreover, the superconducting environment of the junction, due to the presence of other circuits on the same chip, may change the effective local fields. Both effects may give rise to small variations of the characteristic field values  $H_0$  found in experiment.

At small fields, we observe a systematic deviation of the calculated patterns from the experimental ones. In particular, the first minimum of the critical current appears at larger

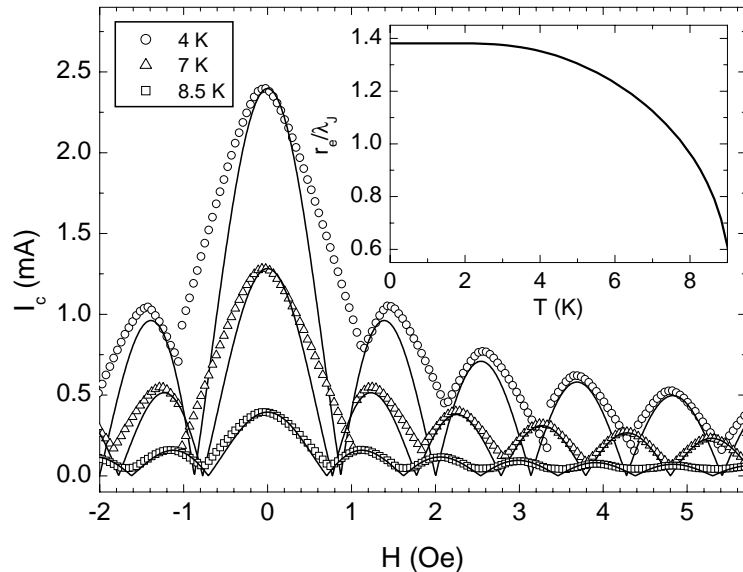


Figure 3.4: Critical-current diffraction patterns of junction  $B$  at temperatures between 4 K and 8.5 K. Dots are experimental data, solid line is theory. In the inset the normalized external junction radius  $r_e/\lambda_J$  is plotted versus temperature.

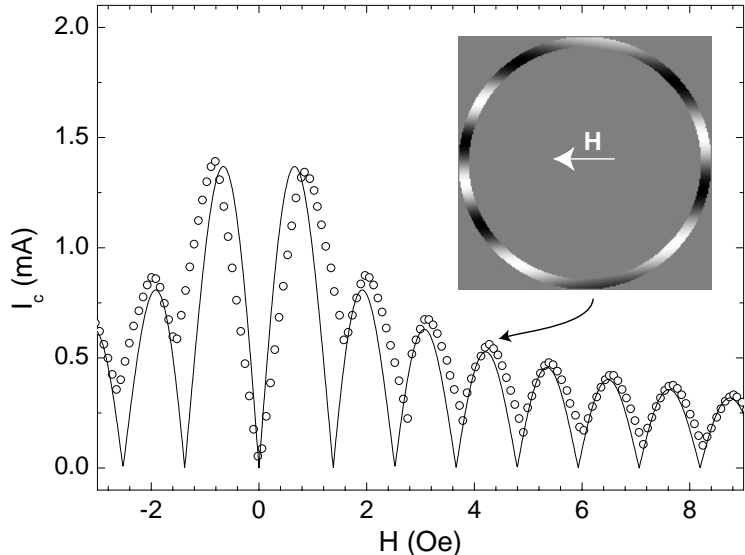
field than predicted by the theory. Moreover, the critical current at the first minimum does not fall to zero. Both facts are to be expected for junctions that are not really small in comparison with  $\lambda_J$ . Indeed, the dimensions of our junctions are slightly larger than  $\lambda_J$ . This leads to a nonlinear penetration of the magnetic field into the junction at low fields, resulting in an increase of the field at which the first minimum of the pattern is observed. The analogous effect is observed in conventional long Josephson junctions [BP82, PRS91].

At higher temperatures, the Josephson length  $\lambda_J$  increases [BP82] and, hence, the effective size of the junction decreases. In the inset of Fig. 3.4, the normalized external junction radius  $r_e/\lambda_J$  is plotted versus temperature, taking into account the temperature dependence of both the critical-current density  $j_c(T)$  and the London penetration depth  $\lambda_L(T)$  [BP82]. At  $T > 7.8$  K the normalized radius drops below unity. Therefore, at higher temperatures, a better agreement between experimental data at low fields and theory is expected. This is illustrated in Fig. 3.4, where the experimental critical-current diffraction pattern of junction  $B$  is plotted together with a fit for the temperatures  $T = 4.0, 7.0, 8.5$  K. The data are fitted keeping  $\tilde{\delta}$  constant for all  $T$  and adjusting  $\tilde{H}_0$ . At elevated temperatures, both the position of the first minimum and the modulation depth of the critical current at small fields show better agreement with the theoretical prediction.

### 3.2.2 Diffraction patterns with trapped fluxons

We have also measured all junctions with a single vortex trapped in the junction barrier. As an example, the critical-current diffraction pattern of junction  $B$  at 4.2 K with  $n = 1$  is shown in Fig. 3.5. The most prominent feature of the pattern is the strong suppression of the critical current at small fields. The zero field value of the critical current in this state is reduced by more than a factor of 100 in comparison with the flux-free junction. Taking the same fitting parameters as for  $n = 0$ , we find as good agreement between the theory and the experimental data. The high-field part of the patterns show the same geometry dependence as without trapped vortices. The slight differences between the fit and the experimental data at low fields are, again, due to the dimensions ( $r_e > \lambda_J$ ) of the junction. Moreover, the assumption that the magnetic field associated with the vortex is homogeneously spread along the junction circumference is not good enough to describe the low field features of the

Figure 3.5: Diffraction pattern of junction  $B$  with one trapped fluxon at 4.2K. Dots are experimental data, solid line is theory. The inset displays the supercurrent distribution in the junction at the magnetic field indicated by the arrow.



pattern correctly. In the inset of Fig. 3.5, the supercurrent distribution in junction  $B$  at  $H = 4.21$  Oe calculated according to Eq. (3.5) is shown. Evidently, at this field a number of vortex anti-vortex pairs have penetrated into the junction but the width of the junction is not fully penetrated, compare Fig. 3.2b, inset II. Also note that the symmetry of the current distribution in the junction is broken due to the presence of the trapped vortex. Similar current distributions in the presence of trapped vortices have also been observed in experiment [KVL<sup>+</sup>96].

### 3.3 Conclusion

We have systematically measured the critical-current diffraction patterns of a number of annular junctions of different width, with and without trapped fluxons, in a wide magnetic field range and at different temperatures. The experimental data show a pronounced width dependence that is explained accurately using the existing theory. In particular, a modulation of the envelope of the critical-current diffraction pattern is observed for junctions of large width. The period of this modulation depends very sensitively on the normalized junction size described by the parameter  $\delta$ . Analyzing the experimental data at large fields, it is possible to determine the contribution of the geometry dependent parameter  $\delta$  and the magnetic field penetration dependent parameter  $H_0$  independently and consistently, allowing for a quantitatively accurate comparison between experiment and theory. The data analysis is accurate enough to detect a small reduction of the junction size due to the fabrication process. The dependence of the critical current on the field in the low field range can be used as one of the important characteristic criteria to determine the number of Josephson vortices trapped in the junction.

It is worth pointing out that good agreement between theory and experiment in the large field range is found for junctions of a diameter substantially larger than  $\lambda_J$ . At low fields, the theory [Nap97] describes well the experiments for  $r_e < \lambda_J$ , as confirmed by our measurements at high temperatures. Thus, the magnetic properties of the junction are determined rather by the junction radius than by the junction circumference, as already pointed out in Ref. [MMK<sup>+</sup>98].

## Chapter 4

# Whispering Gallery Resonances in Annular Long Josephson Junctions

Experiments indicating the excitation of whispering-gallery-type electromagnetic modes by a vortex moving in an annular Josephson junction are reported. At relativistic velocities the Josephson vortex interacts with the modes of the superconducting stripline resonator giving rise to novel resonances on the current-voltage characteristic of the junction. The experimental data are in good agreement with analysis and numerical calculations based on the two-dimensional sine-Gordon model.<sup>1</sup>

Whispering gallery modes are universal linear excitations of circular and annular resonators. They have first been observed in form of a sound wave traveling along the outer wall of a walkway in the circular dome of St. Paul's Cathedral in London, see Fig 4.1, and were investigated by Lord Rayleigh [Ray14] and others [Wal78]. In the 2 meter wide walkway, which forms a circular gallery of 38 meter diameter about 40 meters above the ground of the cathedral, the whispering of a person can be transmitted along the wall to another person listening to the sound on the other side of the dome. The investigations by Rayleigh led to the conclusion that the whisper of a person excites acoustic eigenmodes of the circular dome which can be described using high order Bessel functions. This acoustic phenomenon lends its name “whispering gallery mode” to a number of similar, mostly electromagnetic excitations in circular resonators. Whispering gallery modes are of strong interest in microresonators used for ultra small lasers [MLS<sup>+</sup>91]. Most recently, circular resonators with small deformations, in which chaotic whispering gallery modes were observed, attracted a lot of attention [GCN<sup>+</sup>98]. Here, we describe the experimental observation of electromagnetic whispering gallery modes excited by a vortex moving in an annular Josephson junction with a diameter of about 100  $\mu\text{m}$ .

Annular long Josephson junctions are intriguing systems for the experimental study of

---

<sup>1</sup>Parts of this chapter have been published in ‘Physical Review Letters **84**, 151 (2000)’.

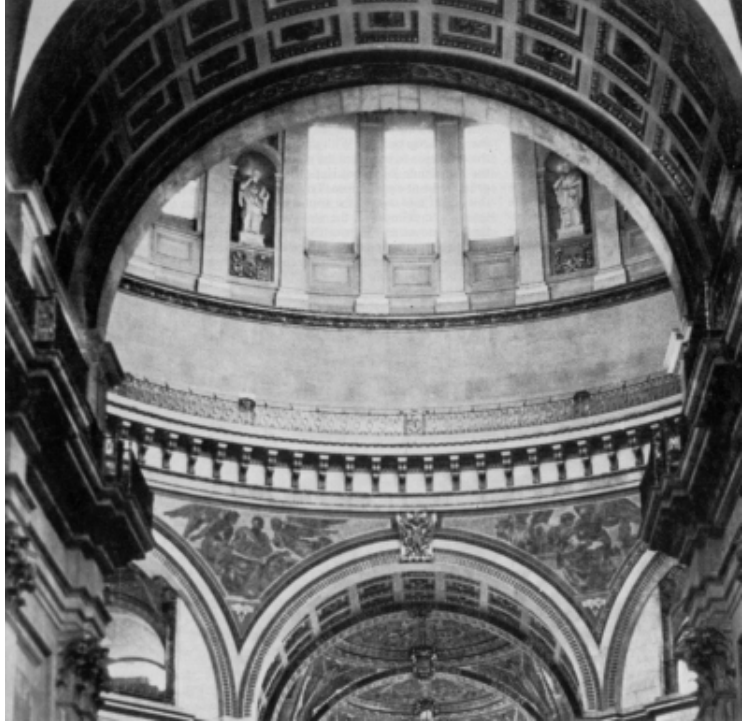


Figure 4.1: Whispering gallery of St. Pauls cathedral, London, Great Britain.

solitons. The interest in this particular system stems from the possibility to fabricate annular junctions of width  $w < \lambda_J$  and consider their dynamics as quasi-one-dimensional with periodic boundary conditions, which allows their description by an 1D sine-Gordon model. Only recently, the relevance of the finite width of the junction for its static [Nap97, MM96a] and dynamic properties [WBK<sup>+</sup>97, KYSV98, NCL98] was started to be considered in experimental and theoretical work. The detailed theoretical consideration of the dynamics of Josephson vortices in effectively two-dimensional annular junctions and the prediction of new physical phenomena by Kurin *et al.* [KYSV98] stimulated the work presented here.

In the first section, I introduce the basic idea of the generation of whispering gallery type plasmon modes by a vortex moving in a wide annular junction. This system is modeled by the 2-D sine-Gordon equation in polar coordinates. The geometry and the basic properties of the annular junctions used for experiments in this work are presented in Section 4.2. The measured single vortex resonances indicating the resonant interaction between the vortex and the junction plasmon modes are presented in Section 4.3. The renormalization of the resonance voltages due to the idle region is considered specifically. In Section 4.4, the resonance condition between the vortex motion and the whispering gallery modes, the spectrum of which is calculated in Section 4.5, is derived. The experimental results are compared qualitatively and quantitatively to results of numerical simulations in Sections 4.6 and 4.7. Finally, I conclude and point out possible directions for future work on the investigation of whispering gallery type plasma modes in annular junctions.

## 4.1 The idea and the model

In Reference [KYSV98] Kurin considers the Josephson vortex trapped in a wide annular Josephson junction as a *soliton string* that propagates along the junction with an angular velocity  $\Omega$  under the action of the external bias current, as shown in Fig 4.2. Because the



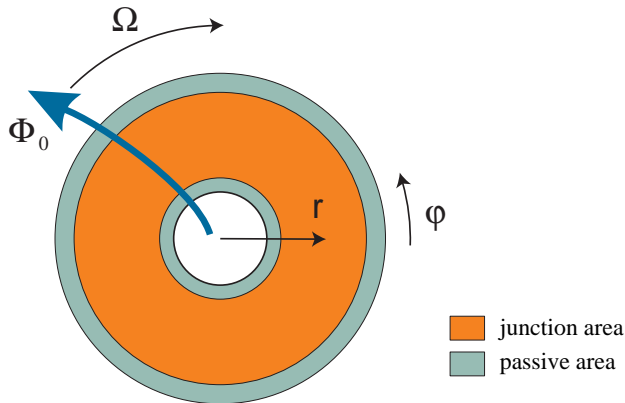


Figure 4.2: Top view of an annular junction with large width. The Josephson vortex string (indicated by a large arrow) moves at the average angular velocity  $\Omega$ . The angular coordinates  $r$  and  $\varphi$  are also indicated.

Josephson vortex is a topological soliton, the vortex string moves (almost) rigidly along the junction. Obviously, the linear velocity  $v = v_e = \Omega r_e$  of the string at the outer edge of the junction is higher than at the inner edge  $v = v_i = \Omega r_i$ . At a certain threshold value  $\Omega_{\text{thr}}$ , the velocity  $v_e$  of the vortex at the outer junction edge exceeds the (Swihart) velocity of light  $c_0$  of the junction. For  $\Omega > \Omega_{\text{thr}}$ , an outer fraction of the rigid vortex string moves at a velocity larger than the phase velocity of linear waves  $c_0$ . This effect gives rise to a *Cherenkov-like* interaction between the string and the linear electromagnetic modes of the junction [KM88]. Due to the annular junction geometry, the traveling linear waves are predicted to be Bessel-type eigenmodes of the resonator, which are also termed *whispering gallery modes*.

The Cherenkov effect is not observed in homogeneous, one-dimensional junctions because the vortex always moves at velocities smaller than the linear mode phase velocity  $c_0$ . However, if the junction is effectively two-dimensional, contains inhomogeneities or is coupled to other stripline resonators, the linear wave spectrum can be changed, such that the vortex group velocity may be higher than the phase velocity of the lowest linear mode. Similar effects have recently been observed experimentally in artificially and intrinsically stacked Josephson junctions [HKUM97, GWTU98, GWU00].

Theoretically, the electrodynamics of a wide annular Josephson junction is described by the perturbed sine-Gordon equation (PSGE) for the superconducting phase difference  $\phi$ , see Section 2.1.1. The Josephson vortex string corresponds to a twist over  $2\pi$  in  $\phi$ , which is localized in space. The vortex carries a magnetic flux equal to the magnetic flux quantum  $\Phi_0 = h/2e = 2.07 \cdot 10^{-15}$  Vs. Physically, this flux is induced by a vortex of the screening current flowing across the junction barrier. The linear excitations in this system are Josephson plasma waves that account for small amplitude oscillations in  $\phi$  (see Section 2.2). The maximum phase velocity of electromagnetic waves in such a junction is the Swihart velocity given by  $c_0 = \lambda_J \omega_p$ , where  $\lambda_J$  is the Josephson length and  $\omega_p$  the plasma frequency (see Section 2.1.1). In zero external magnetic field, the normalized PSGE for an annular Josephson junction of width  $w < \lambda_J$  is found by extending Eq. (2.19) to two dimensions and using the polar coordinates  $(\tilde{r}, \varphi)$

$$\left( \tilde{\nabla}^2 - \frac{\partial^2}{\partial \tilde{t}^2} \right) \phi - \sin \phi = -\gamma + \alpha \frac{\partial \phi}{\partial \tilde{t}} - \beta \tilde{\nabla}^2 \frac{\partial \phi}{\partial \tilde{t}}. \quad (4.1)$$

In Eq. (4.1),  $\tilde{\nabla}^2 - \partial^2/\partial \tilde{t}^2$  is the D'Alembert wave operator,  $\sin \phi$  is the non-linear term due to the phase-dependent Josephson current and  $\gamma$  is the normalized bias current. The damping terms  $\alpha \partial \phi / \partial \tilde{t}$  and  $\beta \tilde{\nabla}^2 \partial \phi / \partial \tilde{t}$  are inversely proportional to the quasiparticle resistance

across the junction barrier and to the quasiparticle impedance of the electrodes, respectively. The boundary conditions are fixed by the continuity of the phase in the junction Eq. (2.45) and by the radial  $\tilde{H}_{\tilde{r}}$  and tangential components  $\tilde{H}_{\tilde{\varphi}}$  of the normalized external magnetic field

$$\begin{aligned}\tilde{H}_{\tilde{\varphi}} &= \frac{\partial\phi}{\partial\tilde{r}}, \\ \tilde{H}_{\tilde{r}} &= \frac{1}{\tilde{r}} \left( \frac{\partial\phi}{\partial\tilde{\varphi}} + n \right),\end{aligned}$$

where  $\tilde{H}$  is normalized to the characteristic field  $H_0 = \Phi_0/(2\pi r_e \mu_0 \Lambda)$  and  $n$  is the number of vortices trapped in the junction (also see Chapter 3). The zero field boundary conditions ( $\tilde{H}_{\tilde{\varphi}} = \tilde{H}_{\tilde{r}} = 0$ ) are appropriate if no external magnetic field is applied and the self-field of the bias current can be neglected. For the junctions of width  $w < \lambda_J$  considered here, a homogeneously distributed bias current  $\gamma$  as in Eq. (4.1) is justified. In contrast, for junctions with  $w > \lambda_J$ , the bias current may contribute to the boundary conditions of Eq. (4.1) [MM96a].

Solving Eq. (4.1) in a perturbation approach, assuming negligible curvature of the vortex string and small linear wave amplitudes, Kurin predicted in Ref. [KYSV98] that the vortex interacts resonantly with the whispering gallery modes of the junction. If the group velocity of the vortex coincides with the phase velocity of the linear mode, the resonance condition is fulfilled. These predictions have been verified in numerical simulations [KYSV98]. In the original work however, Kurin *et al.* did not observe any indication for the excitation of whispering gallery modes on the current-voltage characteristic of the junction. The interpretation of their results relied on the analysis of the spatial distribution of the electromagnetic fields in the junction.

In the experiments presented here, we make use of the same Josephson vortex for both exciting and detecting the whispering gallery mode. This is possible because the vortex, steadily moving at a velocity  $u$  driven by the Lorentz force due to the bias current  $\gamma$ , generates a voltage  $V \propto u$  across the Josephson junction. At low damping the resonant interaction between the vortex moving at relativistic velocities and the whispering gallery modes results in a novel fine structure on the current-voltage characteristic of the junction. Our experiments are consistent with the theory developed by Kurin *et al.* [KYSV98]. Numerical calculations based on the 2D sine-Gordon model considering the experimental junction parameters show good agreement with experiments.

## 4.2 The samples

In contrast to many experiments focusing on quasi-one-dimensional annular Josephson junctions, we investigate comparatively wide, effectively two-dimensional junctions. We have prepared a set of 5 annular Josephson junctions ( $A \dots E$ ) with the ratio  $\delta = r_i/r_e$  between the inner radius  $r_i$  and the fixed outer radius  $r_e = 50 \mu\text{m}$  being varied between  $\delta = 0.94$  and  $\delta = 0.60$ , see Fig. 4.3b and Table 4.1.

The junctions have been fabricated at Hypres Inc. [Hyp] using Nb-Al/ $\text{AlO}_x$ -Nb trilayer technology with a nominal critical-current density of  $j_c = 100 \text{ A/cm}^2$ . The junction is formed using a trilayer of thickness  $d_{tri} \approx 200 \text{ nm}$ . The top and bottom electrodes are of identical thickness  $d_{tj} = d_{bj} \approx 100 \text{ nm}$  separated by an  $\text{AlO}_x$  tunnel barrier of thickness

Table 4.1: Geometrical parameters of the annular Josephson junctions used in experiment. The outer radius of every junction is  $r_e = 50 \mu\text{m}$ .  $w_j = r_e - r_i$  is the junction width.

junction	A	B	C	D	E
$r_i$ [ $\mu\text{m}$ ]	47	45	42	35	30
$w_j$ [ $\mu\text{m}$ ]	3	5	8	15	20
$\delta = r_i/r_e$	0.94	0.90	0.84	0.70	0.60
$\xi = c_0/\bar{c}_0$	0.70	0.78	0.85	0.91	0.94

$t_j \approx 2 \text{ nm}$ . The dielectric constant of this barrier is typically  $\epsilon_j \approx 10$ . The junction is defined in an etching process after which the bottom electrode extends about  $w_p \approx 2 \mu\text{m}$  outside of the active Josephson tunneling region, see Fig. 4.3c. The junction is insulated by a  $t_p = 200 \text{ nm}$  thick  $\text{SiO}_x$  layer which has a dielectric constant of  $\epsilon_p \approx 4$ . The electrical contact to the top electrode is made by etching through the insulating  $\text{SiO}_x$  layer with a minimum distance of approximately  $0.5 \mu\text{m}$  from the junction edge. For the wiring a  $d_w \approx 300 \text{ nm}$  thick Nb layer is used. This layer also extends outside the junction area forming, in combination with the bottom electrode, a passive region of width  $w_p \approx 2 \mu\text{m}$  around the junction, see Figs. 4.3b, c. This passive region acts as a small stripline in parallel to the junction, but with electrical parameters different from the junction itself.

The passive region has a considerable effect on the phase velocity of electromagnetic waves in the Josephson junction [Lee91, LB92, TUK<sup>+</sup>95], which is frequently neglected in the discussion of experimental results obtained with long junctions. Most Josephson junctions fabricated in Nb-Al/ $\text{AlO}_x$ -Nb trilayer technology have a passive region, due to the need of insulating the junctions effectively and simultaneously providing a reliable wiring contact. The geometrical parameters and the electrical properties of the passive region might vary considerably depending on the fabrication process. In the evaluation of our experimental data, we take into account the effect of the passive region according to Lee *et al.* [Lee91, LB92].

We use two wide leads attached to the electrodes to apply the bias current homogeneously to the junction, see Fig. 4.3a. This standard biasing scheme is frequently called the Lyngby geometry [DDKP85]. All presented measurements have been done using a well shielded low noise measurement setup. Measurements at  $T = 4.2 \text{ K}$  are done by immersing the sample stage of a dipstick into the liquid helium bath of a storage dewar, measurements at all other temperatures are performed in a temperature-controlled sample in vacuum cryostat. The sample is electrically connected to a current source and a preamplifier using twisted pairs which are fed through high frequency filters at room temperature. The sample was mounted in a cryoperm magnetic shield and a coil was used to apply a magnetic field of up to 40 gauss at 100 mA coil current in the plane of the junction, see Section 2.3.3 for more details.

In a first set of measurements, the current-voltage characteristics of all samples were acquired up to about twice the gap voltage and the critical-current diffraction patterns were measured with the magnetic field applied in parallel to the bias leads. All junctions were typically found in a state with no trapped fluxons and free of parasitic flux in the superconducting electrodes, which could be inferred from the modulation of the critical current with the magnetic field (see Chapter 3). All samples have a homogeneous bias current distribution, inferred from the large value of the vortex-free critical current at zero

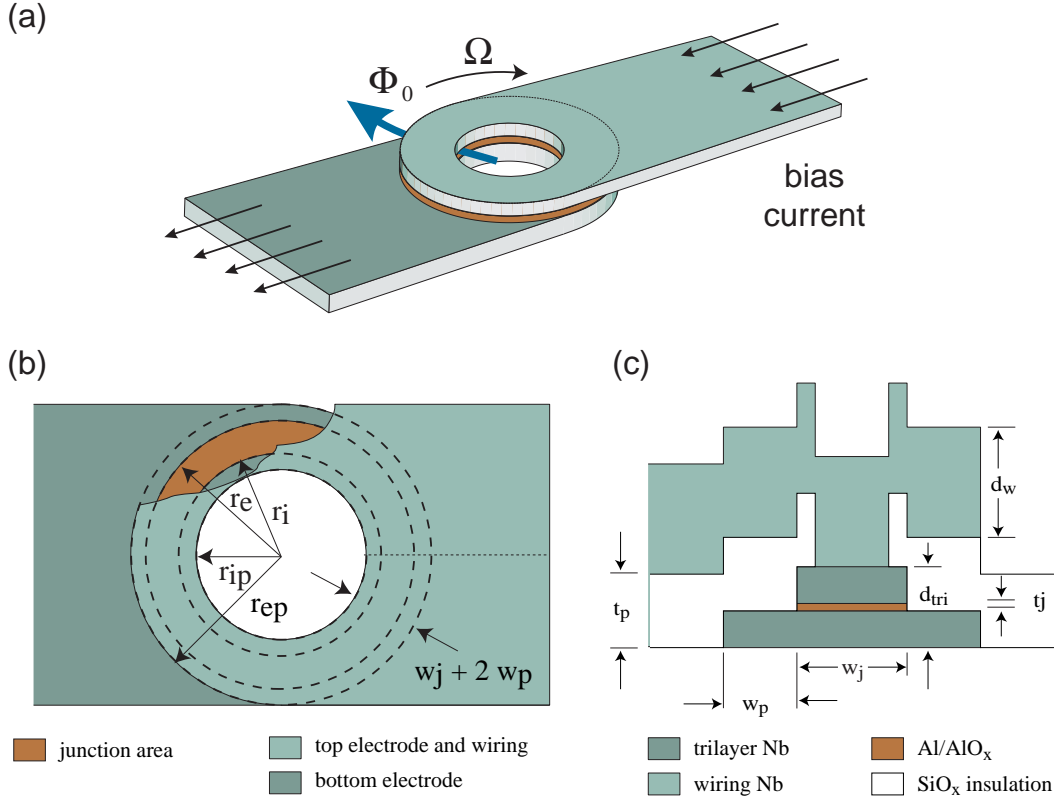


Figure 4.3: (a) Three-dimensional sketch of the annular Josephson junction. The direction of the angular velocity  $\Omega$  of the vortex ( $\Phi_0$ ) under the action of the bias current is indicated. (b) Top view of the junction. The active junction region (inner radius  $r_i$ , outer radius  $r_e$ ) and the passive region (inner radius  $r_{ip} = r_i - w_p$ , outer radius  $r_{ep} = r_e + w_p$ ) are indicated. (c) Cross-sectional view of the junction along the dashed line in Fig. (b). Layer thicknesses and overlap between electrodes are indicated.

field, which is close to the theoretical Ambegaokar-Baratoff limit [AB63a, AB63b]. The critical-current density is  $j_c \approx 160 \text{ A/cm}^2$  (deviating somewhat from the projected value of  $100 \text{ A/cm}^2$ ) and the London penetration depth is determined as  $\lambda_L \approx 95 \text{ nm}$  at  $4.2 \text{ K}$ , see Chapter 3. Using the magnetic field penetration depth  $\Lambda \approx 2\lambda_L + t_j$ , the characteristic parameters are estimated as  $\lambda_J \approx 30 \mu\text{m}$  and  $\nu_p = \omega_p/2\pi \approx 50 \text{ GHz}$ .

### 4.3 Single-vortex resonances

We could realize single and multiple vortex states reproducibly in any of the junctions. Vortices were trapped by applying a small bias current during cooling down from the normal to the superconducting state.<sup>2</sup> Single-vortex states are identified as the lowest quantized voltage step observed on the current-voltage characteristic. Also, a characteristic change of the critical-current modulation with magnetic field, as discussed in some detail in Chapter 3

<sup>2</sup>We achieved good results by choosing the current such that the voltage drop across the junction in the resistive state was about the voltage of the fluxon resonance to be observed in the superconducting state. Usually several (about 2 to 5) cycles of cooling were sufficient to prepare the junction in the wanted state. The current applied to the junction was chosen large enough to generate a flux threading the junction loop that is close to one flux quantum.

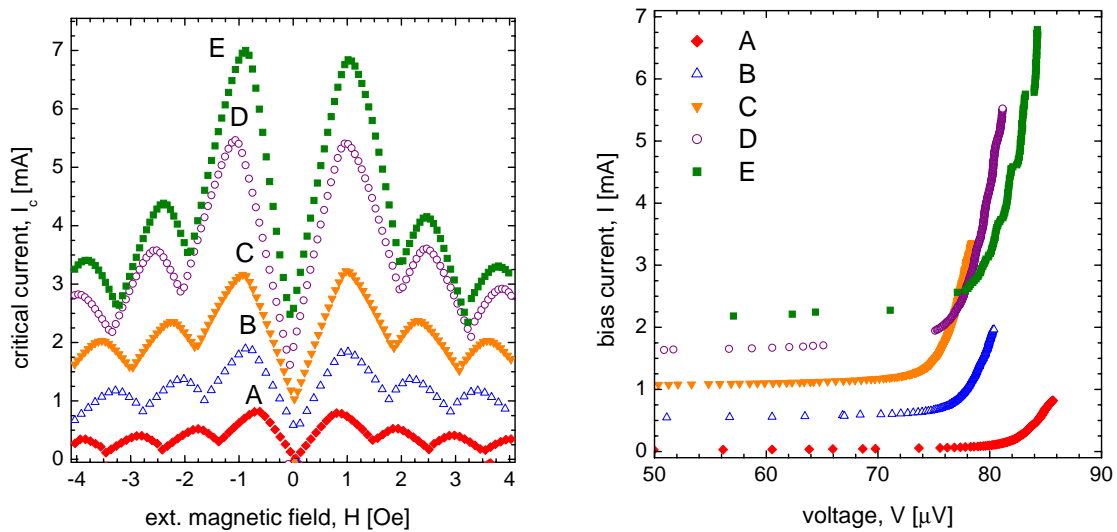


Figure 4.4: (a) Critical-current diffraction patterns of junctions  $A$  through  $E$  with a single fluxon trapped. (b) Current-voltage characteristics of single fluxon states in junctions  $A$  through  $E$ . In both plots each characteristic is offset by  $\Delta I = 0.5$  mA for better visibility.

and reported earlier [VKT<sup>+</sup>97], was observed when a vortex was trapped in the junction, see Fig. 4.4a. At zero field, the critical current is suppressed by a factor of more than 100 if a vortex is present in the junction.

The low voltage part of the current-voltage characteristics of junctions  $A$  to  $E$  with a single trapped fluxon are plotted in Fig. 4.4b. Each curve is offset by 0.5 mA in current with respect to the other, else the resonances are plotted as acquired. The most important and initially unexpected feature of the characteristics is a fine structure on the resonances of the widest junctions  $D$  and  $E$ , which is not observed for the more narrow junctions  $A$ ,  $B$  and  $C$ . Such width-dependent features have not been noticed on the single-vortex characteristics of annular Josephson junctions before.<sup>3</sup>

Before focusing on the fine structure, some general properties of the samples characteristics are discussed and the raw data are normalized according to those results. Then, in the remainder of this chapter, I analyze these data and explain their features using the model discussed in Section 4.1.

### 4.3.1 Normalization

In Fig. 4.4b, different maximum currents (step heights) of the single-vortex resonances of different junctions are observed. This feature is well accounted for by the distinct critical currents, due to the differing junction areas. Dividing the current scale of each individual resonance by the critical current of the corresponding junction results in an almost equal step height of all resonances, as shown in Fig. 4.6.

More important, we observe a strong non-monotonic dependence of the maximum voltage of the resonances on the junction width  $w$ . From very general assumptions, we would

<sup>3</sup>A similar fine structure has been observed independently in low temperature measurements of very long annular Josephson junctions by Martucciello et al. [MMK<sup>+</sup>98], though no convincing explanation of its origin was presented.

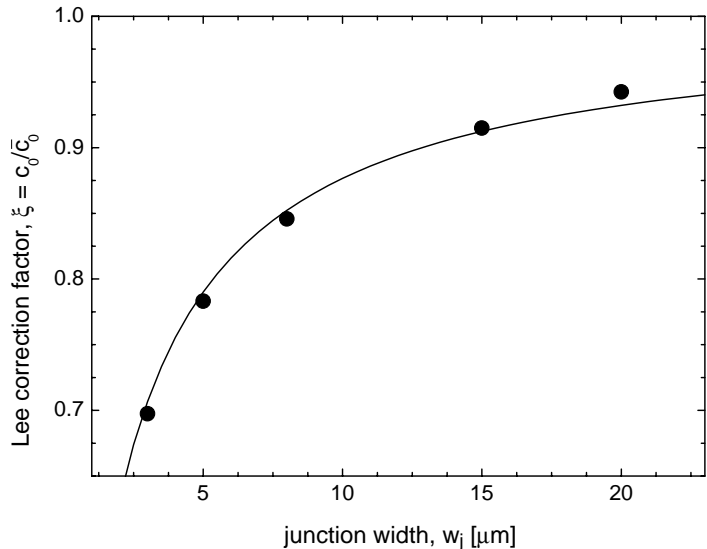


Figure 4.5: The normalized velocity of light  $c_0/\bar{c}_0$  [see Eq. (4.6)] in our junctions with a fixed width of passive region  $w_p$  and identical electrical parameters vs. the junction width  $w_j$ .

expect a scaling of the maximum fluxon step voltage  $V_{\max}$  with an effective junction length  $L_{\text{eff}}$  according to

$$V_{\max} = \Phi_0 \frac{v_{\max}}{L_{\text{eff}}}, \quad (4.2)$$

where  $v_{\max}$  is the maximum velocity of the vortex. The effective length of an annular junction is usually estimated from its mean radius

$$L_{\text{eff}} = 2\pi \frac{r_e + r_i}{2}. \quad (4.3)$$

For junctions of finite width, there are corrections to be taken into account [WBK+97], which are usually neglected in literature. Based on these simple assumptions,  $V_{\max}$  should monotonically increase with the decrease of  $L_{\text{eff}}$ , i.e. with a decrease of the inner radius  $r_i$  at a fixed external junction radius  $r_e$ . Our junctions obey this geometrical property, but the experimental results differ strongly from that expectation.

This feature of our experimental data can be explained by taking into account the passive region enclosing the junction. This region, which is directly connected in parallel to the common electrodes of the Josephson junction, acts as a transmission line with a specific inductance and capacitance different from the junction itself. In the limit of a small idle region, this effect can be taken into account by introducing an effective capacitance and an effective inductance for the whole system, i.e. the Josephson junction coupled to the stripline.

Accordingly, the phase velocity  $\bar{c}_0$  of a long Josephson junction with a stripline coupled in parallel was first calculated by Lee *et al.* [Lee91, LB92]

$$\bar{c}_0 = c \left( \frac{\frac{w_j \epsilon_j}{t_j} + \frac{2w_p \epsilon_p}{t_p}}{\frac{w_j}{\Lambda_j} + \frac{2w_p}{\Lambda_p}} \right)^{-1/2}, \quad (4.4)$$

where  $c$  is the velocity of light in vacuum and  $\Lambda_{j,p}$  are the magnetic thicknesses of the junction in the active Josephson (j) and in the passive insulation region (p) respectively. The other parameters are the width  $w_{j,p}$ , the thickness  $t_{j,p}$  and the dielectric constant  $\epsilon_{j,p}$  of

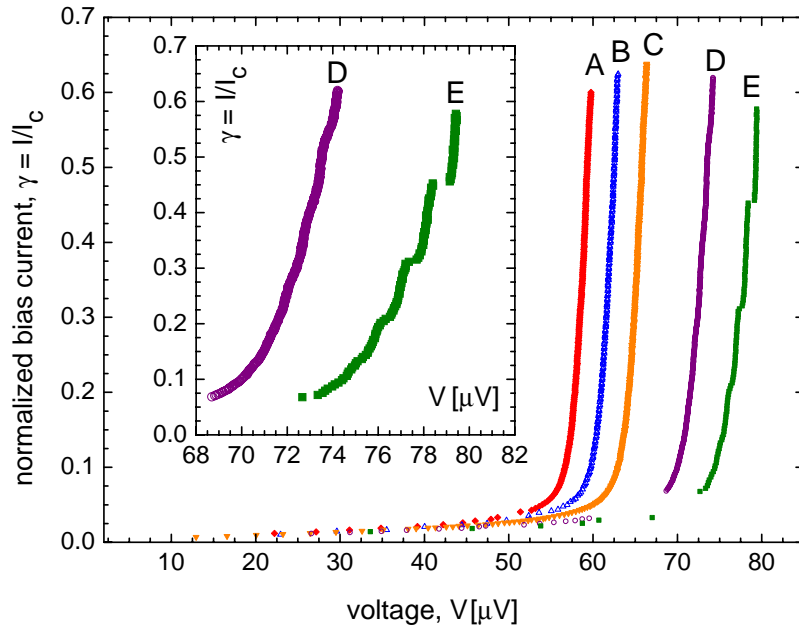


Figure 4.6: Experimental normalized current-voltage characteristics of single-vortex states in junctions *A* to *E*. An enlargement of the high voltage region of the resonances in junctions *D* and *E* is shown in the inset.

the barrier. For the samples considered here, the magnetic thickness  $\Lambda_{j,p}$  was approximated in the thick film limit [Wei69] as

$$\Lambda_{j,p} = 2\lambda_L + t_{j,p}. \quad (4.5)$$

Using the geometrical and electrical parameters of the different samples, we have calculated the renormalization factor

$$\xi = \frac{\lim_{w_p \rightarrow 0} \bar{c}_0}{\bar{c}_0} = \frac{c_0}{\bar{c}_0}, \quad (4.6)$$

see Table 4.1. Multiplying the voltage scale of each individual resonance with the respective factor  $\xi$ , we effectively restore the characteristic of a bare junction, i.e. one without idle region. In Fig. 4.5,  $\xi$  is plotted versus the junction width  $w_j$  for fixed width ( $w_p = 2 \mu\text{m}$ ) and electrical parameters of the idle region, see Section 4.2. It is clearly seen from the figure that the increase of the phase velocity in a junction with a low-capacitance and high-inductance stripline coupled to it can be substantial. For the junctions considered here, the correction with respect to the bare junction are as big as 30% for the most narrow junction (*A*). Still, for the widest junction measured (*E*) the correction is bigger than 5% and hence cannot be neglected. The values of  $\xi$  found for the experimental data are shown by solid circles. As an additional check for consistency, we have performed numerical simulations for junctions without idle region but otherwise identical to the geometry used in experiment. The maximum voltages found from simulations have been compared to the renormalized data shown in Fig. 4.6 and excellent agreement has been found.

Using the normalization of both the current and the voltage axis, as discussed above, the single-vortex characteristics of the junctions *A* to *E* are plotted in Fig. 4.6.

### 4.3.2 The fine structure

After understanding the general properties of the single-vortex characteristics, I now focus on the novel feature noticed already in Fig. 4.4b, i.e. the fine structure which appears on the vortex resonance of wide junctions. The fine structure is most clearly visible for the widest junction  $E$  (see inset of Fig. 4.6), where steps well separated in voltage by approximately  $\Delta V \approx 1.0 \mu\text{V}$  are observed. In the more narrow junction  $D$ , a somewhat less pronounced fine structure with a period of about  $\Delta V \approx 0.7 \mu\text{V}$  is observed. However, at  $T = 4.2\text{K}$ , a similar feature is not noticed for any of the more narrow junctions.

The fine structure is reproducible and also robust against small perturbations, for example induced by an external magnetic field. Varying the field between  $H = 0$  and the first maximum of the critical-current diffraction pattern (see Fig. 4.4a), the positions of the fine structure steps in voltage do not change. However, the onset and the current height of individual fine structure steps can be tuned by the field. In the well resolved current-voltage characteristic of junction  $E$ , hysteresis is observed between jumps from one step of the fine structure to the other.

In the following sections, I argue that the observed fine structure is well explained by the resonant interaction of the moving vortex with linear whispering gallery modes [KYSV98].

## 4.4 Resonant interaction between soliton strings and plasmons

As pointed out in the introduction, the Josephson vortex string is predicted to excite plasmon modes of the annular junction by a Cherenkov-radiation-like mechanism if it moves at a velocity higher than a certain threshold value. The vortex is expected to interact resonantly with these self-generated plasmons. The resonance condition for this process can be found by considering the dispersion of the fluxon mode and the dispersion of the linear modes.

Fourier decomposing in time the voltage or magnetic field associated with a fluxon moving in an annular junction at the angular velocity  $\Omega$ , one finds that the spectrum contains only multiples  $m\Omega$  of the fundamental frequency of rotation  $\Omega$ . This is due to the geometric quantization of the electromagnetic waves in the annular system. The same result is found decomposing the fluxon in space, where only multiples  $mk$  of the fundamental spatial Fourier component are found. Considering these two features, it is obvious that the vortex can be represented in a dispersion diagram by a straight line  $\Omega(k) = \Omega k$ . Thus, the angular group velocity of the vortex is given by  $v_g = \partial(\Omega k) / \partial k$  which is identical to its angular velocity  $\Omega$ . Therefore, the vortex shows no dispersion which is a universal property of a soliton. The spectrum of the fluxon, being a non-linear excitation, contains high harmonic Fourier components, the amplitudes of which decrease exponentially with increasing wave number  $k$ . Thus, the high harmonics of the vortex interact with large wave number and high-frequency linear modes  $\omega(k)$  of the resonator. To find the resonance frequencies, the spectrum  $\omega(k)$ , i.e. the dispersion, of the linear modes for a given resonator has to be determined, see Section 4.5.

Plotting both the dispersion of the vortex mode and of the linear modes into a common dispersion diagram (Fig. 4.7), one finds that resonance occurs if the vortex dispersion line crosses one of the discrete modes  $\omega_k$  of the plasmon spectrum. Mathematically this



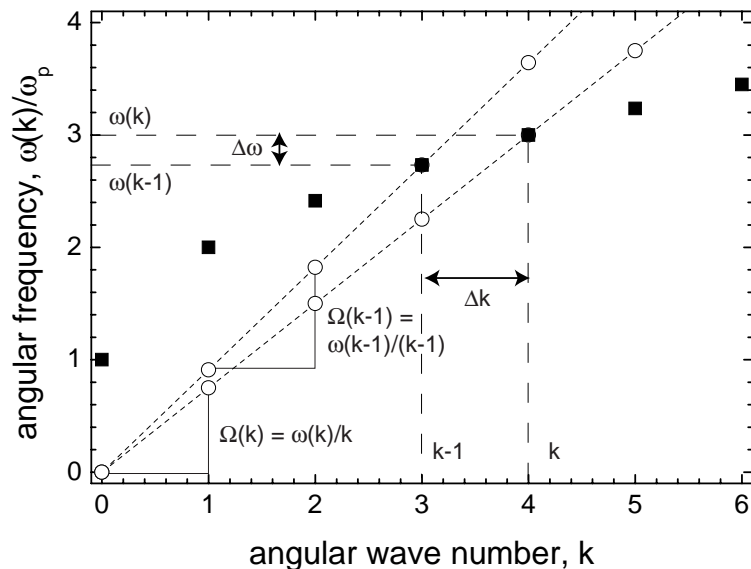


Figure 4.7: Dispersion diagram for two fluxon modes with different resonant angular velocities  $\Omega_k$  and  $\Omega_{k-1}$  (open circles) and linear modes (solid squares) of the annular junction. The difference in frequency  $\Delta\omega$  between two neighboring ( $\Delta k = 1$ ) linear modes and the difference in vortex velocity  $\Delta\Omega = \Omega_{k-1} - \Omega_k$  are indicated.

condition is expressed as

$$\Omega = \frac{\omega_k}{k}, \quad (4.7)$$

which was found in a rigorous calculation in Ref. [KYSV98]. Equation (4.7) states that resonance occurs, if the vortex group velocity  $v_g = \Omega$  is identical to the linear mode phase velocity  $v_{ph} = \omega_k/k$ .

Thus, in an annular junction, a vortex moving at the angular frequency  $\Omega$  may come into resonance with a whispering gallery mode of wave number  $k$ . Alternatively speaking, a harmonic of the vortex-rotation frequency locks to the oscillation frequency of the linear mode. If the spacing in  $\Omega$  between the resonances for different  $k$  is large enough and the width of the resonances is narrow, this effect can be observed as a fine structure on the single-vortex current-voltage characteristic. Since the locking is stable in a certain current range, it leads to step-like resonances. The step height depends on the damping and the frequency separation of different resonances. The strength of the damping ( $\alpha$  and  $\beta$  terms) determines the quality factor  $Q$  of the resonator. The spectral width of the linear modes scales inversely proportional to  $Q$ . Therefore, the resonance condition is not strict but is also fulfilled in a range around the center frequency of the resonance. If the damping is high (e.g. due to large temperature) and the resonances are closely spaced in frequency (e.g. for a narrow junction), the resonances strongly overlap and the individual fine-structure steps cannot be resolved.

The resonant interaction between the vortex and the linear modes can be observed on the current-voltage characteristic because the voltage drop across the junction is proportional to the vortex rotation frequency (see Section 2.2)

$$\langle V \rangle = \frac{\Phi_0}{2\pi} \left\langle \frac{\partial \phi}{\partial t} \right\rangle \quad (4.8)$$

$$= \frac{\Phi_0 n 2\pi v}{2\pi l}, \quad (4.9)$$

where  $n$  is the number of vortices trapped in the junction,  $v$  is the linear vortex velocity and  $l$  is the junction length. Using the fact that  $v = \Omega r$  and  $l = 2\pi r$  for any  $r$ , we can express Eq. (4.9) as

$$V = \frac{\Phi_0}{2\pi} n \Omega, \quad (4.10)$$

which is more appropriate for annular junctions since the linear velocity of the vortex  $v$  as used in Eq. (4.9) is not well defined in this case. Using the resonance condition (4.7) the voltage of a fine structure step is given by

$$V = \frac{\Phi_0}{2\pi} n \frac{\omega_k}{k}. \quad (4.11)$$

Increasing the vortex (angular) velocity  $\Omega$  by increasing the bias current (i.e. increasing the slope of the vortex dispersion line), a resonance with another linear mode of lower  $k$  may be established, see Fig. 4.7. The decrease of the excited wave number  $k$  with increase of the vortex velocity is a characteristic feature of the interaction between the Josephson vortex and the whispering gallery modes of the junction. This property is clearly demonstrated in our numerical calculations presented in Section 4.6.

## 4.5 The plasmon spectrum of an annular junction

The plasmon spectrum of a Josephson junction is determined by both its geometrical and its electrical parameters. If the junction geometry is annular, its eigenmodes are of the whispering gallery type. The plasmon spectrum needs to be known precisely to predict the voltages at which the whispering gallery resonances appear. In normalized units, the linear modes of an annular junction are solutions to the inhomogeneous D'Alembert equation in the polar coordinates  $(\tilde{r}, \varphi)$

$$\left( \frac{1}{\tilde{r}} \frac{\partial}{\partial \tilde{r}} \tilde{r} \frac{\partial}{\partial \tilde{r}} + \frac{1}{\tilde{r}^2} \frac{\partial^2}{\partial \varphi^2} - \frac{\partial^2}{\partial \tilde{t}^2} - 1 \right) \phi^{(\text{lin})} = 0, \quad (4.12)$$

which is found from Eq. (4.1) neglecting all perturbations ( $\gamma$ ,  $\alpha \partial/\partial \tilde{t}$ ,  $\beta \tilde{\nabla}^2 \partial \phi / \partial \tilde{t}$ ) and approximating the non-linearity as  $\sin \phi \approx \phi$  to take into account the gap in the plasmon excitation spectrum. In zero external magnetic field, the solutions to Eq. (4.12) have to fulfill the boundary conditions

$$\frac{\partial \phi^{(\text{lin})}}{\partial \tilde{r}}(\tilde{r} = \tilde{r}_i, \tilde{r}_e) = 0. \quad (4.13)$$

In terms of the electromagnetic waves in the junction, Eq. (4.13) corresponds to a total internal reflection condition.

The partial differential equation (4.12) is separable, therefore its solutions can be expressed in the form

$$\phi^{(\text{lin})} = R(\tilde{r}) \Phi(\varphi) \tau(\tilde{t}), \quad (4.14)$$

where  $R(\tilde{r})$  is the radial component,  $\Phi(\varphi)$  the angular component and  $\tau(\tilde{t})$  the temporal component. The solutions to the temporal and the angular part are obviously given by

$$\tau(\tilde{t}) = \exp(i\tilde{\omega}\tilde{t}), \quad (4.15)$$

$$\Phi(\varphi) = \exp(ik\varphi), \quad (4.16)$$

where  $\bar{\omega} = \sqrt{\bar{\omega}^2 - 1}$ . The general solution to the radial part  $R(\tilde{r})$  of Eq. (4.12) is a linear combination of the Bessel functions of the first ( $J$ ) and second ( $Y$ ) kind

$$R(\tilde{r}) = [A J_k(\bar{\omega}\tilde{r}) + B Y_k(\bar{\omega}\tilde{r})] . \quad (4.17)$$

$k$  is the angular wave number,  $\bar{\omega}$  the angular frequency of the mode, and  $A$  and  $B$  are constants determined by the boundary conditions (4.13). Thus, the general solution to Eq. (4.12) is given by

$$\phi^{(\text{lin})}(\tilde{r}, \varphi, \tilde{t}) = [A J_k(\bar{\omega}_{k,\rho}\tilde{r}) + B Y_k(\bar{\omega}_{k,\rho}\tilde{r})] \exp(ik\varphi) \exp(i\bar{\omega}\tilde{t}) . \quad (4.18)$$

Applying the boundary conditions (4.13) to the solution (4.18), we find a set of equations

$$\begin{aligned} A J'_k(\bar{\omega}\tilde{r}_i) + B Y'_k(\bar{\omega}\tilde{r}_i) &= 0 \\ A J'_k(\bar{\omega}\tilde{r}_e) + B Y'_k(\bar{\omega}\tilde{r}_e) &= 0 \end{aligned} , \quad (4.19)$$

which has non-trivial solutions for

$$\begin{vmatrix} J'_k(\bar{\omega}\tilde{r}_i) & Y'_k(\bar{\omega}\tilde{r}_i) \\ J'_k(\bar{\omega}\tilde{r}_e) & Y'_k(\bar{\omega}\tilde{r}_e) \end{vmatrix} = J'_k(\bar{\omega}\tilde{r}_i)Y'_k(\bar{\omega}\tilde{r}_e) - J'_k(\bar{\omega}\tilde{r}_e)Y'_k(\bar{\omega}\tilde{r}_i) = 0 . \quad (4.20)$$

The set of solutions  $\bar{\omega}(k, \rho) \equiv \bar{\omega}_{k,\rho}$  to Eq. (4.20) is characterized by the angular and radial wave numbers  $k$  and  $\rho$ . They determine the linear mode spectrum, i.e. the dispersion, of the annular resonator. Substituting the characteristic mode frequencies  $\bar{\omega}_{k,\rho}$  into Eq. (4.18), the solution satisfying the boundary conditions (4.13) is of the form

$$\phi_{k,\bar{\omega}_{k,\rho}}(\tilde{r}, \varphi, \tilde{t}) = A \left[ J_k(\bar{\omega}_{k,\rho}\tilde{r}) - Y_k(\bar{\omega}_{k,\rho}\tilde{r}) \frac{J'_k(\bar{\omega}_{k,\rho}\tilde{r}_e)}{Y'_k(\bar{\omega}_{k,\rho}\tilde{r}_e)} \right] \exp(ik\varphi) \exp(i\bar{\omega}_{k,\rho}\tilde{t}) \quad (4.21)$$

with the free amplitude parameter  $A$ .

No exact analytical solutions to Eq. (4.20) determining the mode spectrum  $\bar{\omega}_{k,\rho}$  exist. Therefore, an approximate solution in the limit of vanishing inner junction radius  $\tilde{r}_i$  is discussed first. Then, Eq. (4.20) is solved numerically exact for junctions with finite inner radius. The resulting spectra are discussed.

### 4.5.1 The circular resonator approximation

If the internal radius  $\tilde{r}_i$  of the junction is much smaller than its external radius  $\tilde{r}_e$ , i.e.  $\delta \ll 1$ , the annular junction can be essentially treated as a disc-shaped resonator with respect to its linear modes, as pointed out in Ref. [KYSV98]. Thus, Eq. (4.20) simplifies to the problem of finding  $\bar{\omega} = \bar{\omega}_{k,\rho}$  such that

$$J'_k(\bar{\omega}\tilde{r}_e) = 0 . \quad (4.22)$$

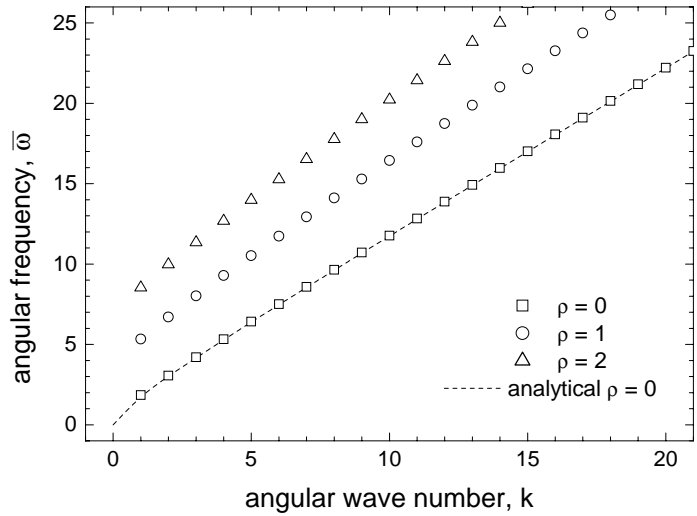
An approximate, but sufficiently accurate, analytical solution to Eq. (4.22) is given by [JEL60]

$$\bar{\omega}_{k,\rho} = \frac{k + \alpha_\rho k^{\frac{1}{3}}}{\tilde{r}_e} , \quad (4.23)$$

where  $\alpha_\rho$  is a numerical constant characterizing the radial mode  $\rho$ .

In Fig. 4.8, the numerical solutions of Eq. (4.22) for the first three radial modes ( $\rho = 0, 1, 2$ ) are plotted together with the analytical approximation (4.23) for  $\rho = 0$  with  $\alpha_0 =$

Figure 4.8: Numerically calculated dispersion (open symbols) for  $\tilde{r}_e = 1$  and  $\tilde{r}_i = 0$ . For comparison the analytical approximation of the fundamental radial mode (dashed line) is also plotted.



0.808. Evidently, for angular wave numbers  $k \gg 1$ , the analytical approximation is accurate. In Fig. 4.8, we also observe that the higher-order radial modes have substantially higher characteristic frequencies. Considering the resonance condition (4.7), it is easy to see that, at a fixed vortex velocity, the wave number of any excited higher-order radial mode is much larger than the one of the fundamental mode  $\rho = 0$ . Since the interaction strength between the vortex and the whispering gallery mode decreases exponentially with increasing  $k$ , the effect of the higher order modes can be safely neglected in this discussion.

In the limit  $\tilde{r}_i \rightarrow 0$ , the solutions (4.21) can be approximated as

$$\phi_{k,\rho}^{(\text{lin})}(\tilde{r}, \varphi, \tilde{t}) = A J_k(\bar{\omega}_{k,\rho} \tilde{r}) \exp(ik\varphi) \exp(i\bar{\omega}_{k,\rho} \tilde{t}), \quad (4.24)$$

where  $\bar{\omega}_{k,\rho}$  is the angular frequency associated with the mode  $k, \rho$  satisfying the boundary condition (4.13) at the external radius only. To visualize the structure of the whispering gallery modes, we plot the spatial part of the solutions  $\phi_k^{(\text{lin})}(\tilde{r}, \varphi, \tilde{t} = 0)$  for the fundamental radial mode ( $\rho = 0$ ) and the angular modes  $k = 13, 7$ , and  $4$  in Fig. 4.9. In each subfigure, the radial and the angular solutions  $R(\tilde{r})$  and  $\Phi(\varphi)$  are plotted. The phase amplitude is normalized, such that the total energy of the electromagnetic field is the same for each mode. The angular part of each mode is a periodic function of  $\varphi$  with the period  $2\pi/k$ . The radial structure of the mode is coupled to the angular wave number  $k$ , and is described by a  $k$ th order Bessel function of the first kind. For increasing  $k$  the radial distribution of the phase  $R(\tilde{r})$  is increasingly peaked at the outer edge of the junction, which is a characteristic feature of the Bessel function.

Additionally, contour plots of the phase  $\phi$  in the respective mode  $k$  are shown in Fig. 4.9. The contours connect points of constant phase. Regions with a high density of contours corresponding to a large gradient of phase are associated with a large magnetic field. The whispering gallery modes are clearly recognized by their large phase gradient at the outer edge, the small phase gradient in the inner part of the junction, and the periodic modulation along the junction circumference. It is evident that the amplitude of the field is increasingly concentrated at the outer junction edge with increasing  $k$ , whereas the fields are almost zero in the center of the junction, see contour plots in Fig. 4.9. Therefore, for large  $k$ , the boundary condition at  $r_i$  does not need to be considered specifically. Thus, the assumption of a disc-shaped resonator works reasonably well for junctions with sufficiently small inner

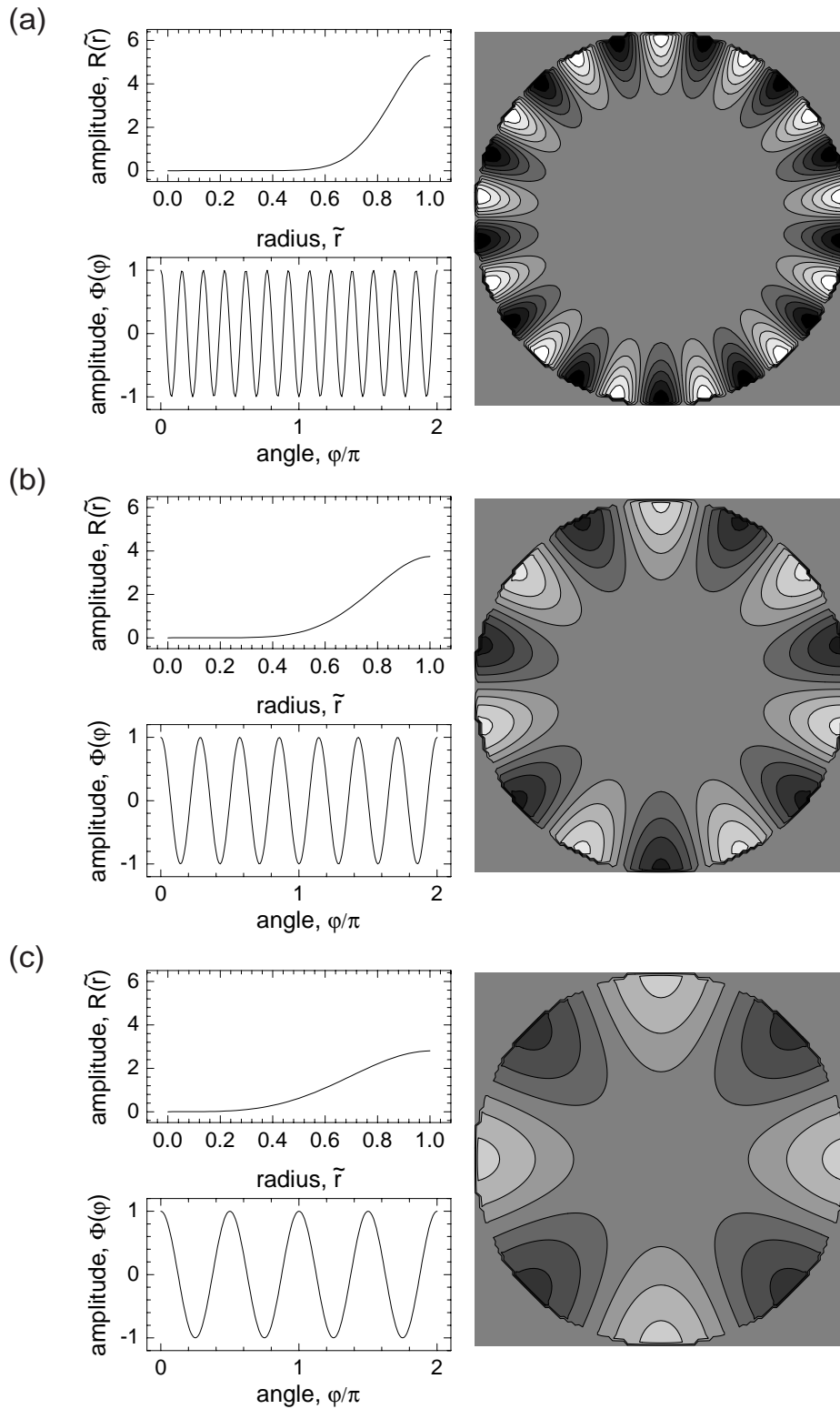


Figure 4.9: Spatial part of the phase distribution  $\phi^{(\text{lin})}$  in arbitrary units for  $\rho = 0$  and (a)  $k = 13$ , (b)  $k = 7$  and (c)  $k = 4$ . In the left part of each figure,  $R(\tilde{r})$  and  $\Phi(\varphi)$  are plotted. On the right hand side the spatial distribution of the phase is shown in a contour plot. The contours indicate lines of constant phase  $\phi$ , light (dark) shades of gray correspond to large (small) values of  $\phi$ .

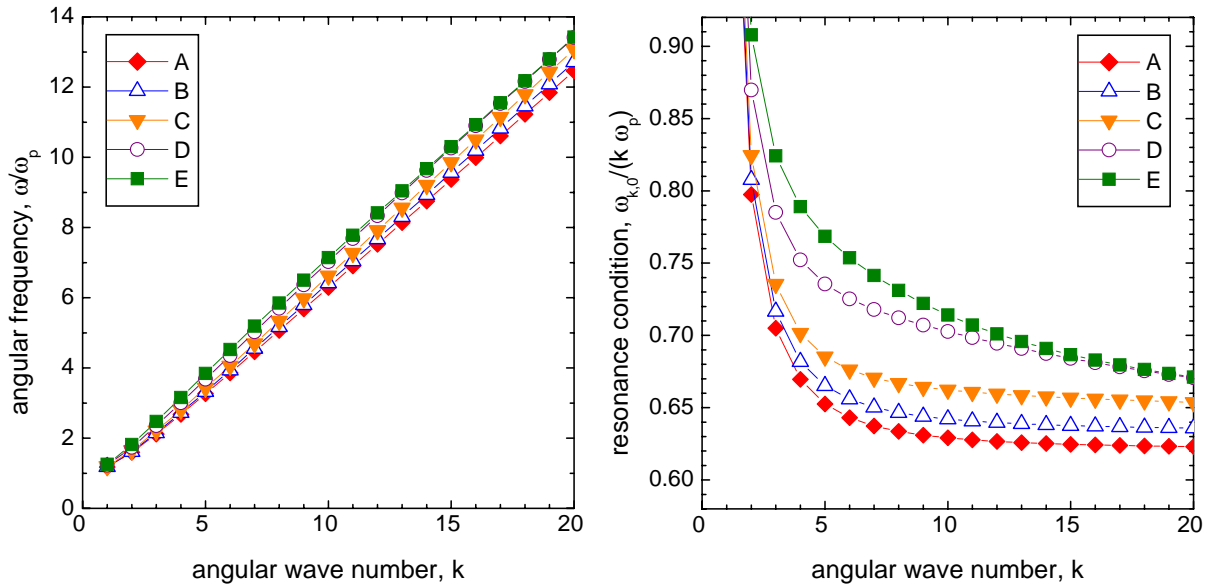


Figure 4.10: (a) Mode spectra for junctions *A* to *E*. The plasmon gap is considered. (b) Resonance conditions for junctions *A* to *E*.

radius.

Therefore, for large  $k$  the boundary condition at the inner junction radius does not need to be considered specifically and the simplified assumption of a disc-shaped resonator works reasonably well, even for some range of junctions with  $\tilde{r}_i \neq 0$ .

## 4.5.2 Exact annular resonator spectrum

If the whispering gallery mode spectrum of an annular junction is to be calculated exactly for any value of  $k$  and  $\delta$ , Eq. (4.20) has to be solved numerically. We have calculated the spectrum  $\tilde{\omega}_{\rho,k}$  for the first 30 radial modes and the first 100 angular modes for the fixed outer radius  $\tilde{r}_e = 1.0$  and the inner radii  $\tilde{r}_i = 0.60, 0.70, 0.84, 0.90, 0.94$ . The spectra have been calculated by finding the zeros of Eq. (4.20) using Newton's method with a guessed initial value. The spectra can be easily rescaled for any junction size by dividing  $\tilde{\omega}_{k,\rho}$  by the external radius  $\tilde{r}_e$ .

Taking into account the common external radius  $\tilde{r}_e = 1.66$  and the plasmon gap, the plasmon mode spectra calculated for junctions *A* to *E* are plotted in Fig. 4.10a. Though the differences in the spectra seem to be small on the first sight, the dispersion of the modes changes significantly with the junction width. The more narrow the junction is, the more closely the spectrum of the fundamental radial mode resembles the one of a narrow quasi-one-dimensional annular resonator with the simple spectrum  $\tilde{\omega}_{k,0} = \sqrt{\tilde{k}^2 + 1}$ . Additionally, we observe that the characteristic frequencies of higher order radial modes are shifted strongly to higher values with decreasing width of the resonator. Therefore, these modes are even less relevant than in the wide junction case.

The effect of the junction width is more apparent when considering the resonance condition, see Fig. 4.10b. Here the resonance frequencies  $\Omega$  and the separation between resonances  $\Delta\Omega$  depend strongly on the junction width. As the most important feature, we observe that the separation in frequency between different resonant modes decreases sig-

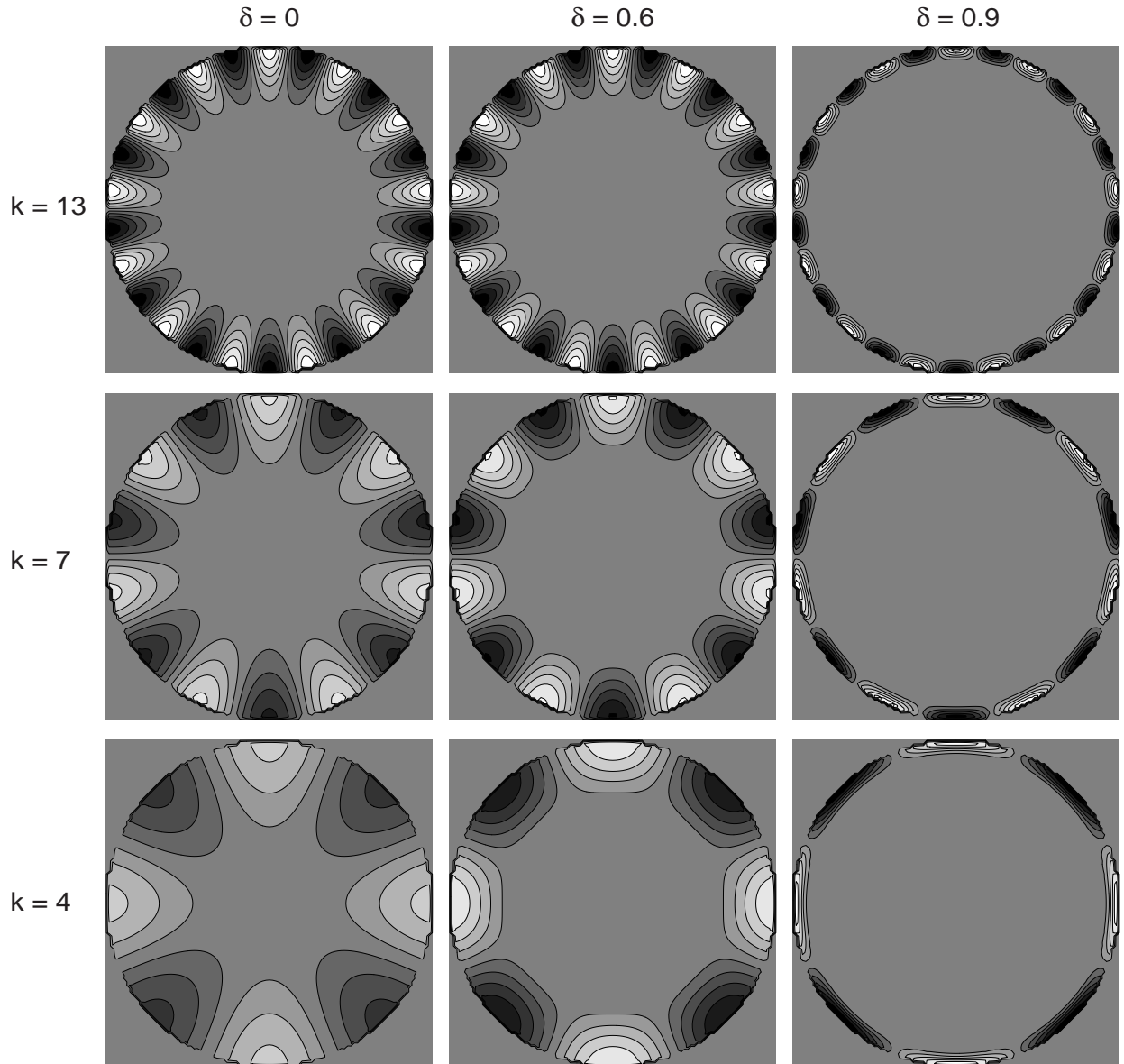


Figure 4.11: Phase profiles for junctions with  $\tilde{r}_e = 1$ ,  $\delta = 0, 0.6, 0.9$  and angular wave numbers  $k = 13, 7, 4$ . Note the squeezing of the spatial structure of the mode with increasing  $\delta$ . The effect is more pronounced for modes with low  $k$  in narrow junctions.

nificantly with decreasing junction width. Therefore, these resonances are not resolved in measurements of the narrow junctions  $A$ ,  $B$ , and  $C$  at  $T = 4.2\text{K}$ , where the damping is relatively high, see Fig. 4.6.

In Fig. 4.11, we compare the phase profiles of the whispering gallery modes with the same angular wave number  $k$  for junctions of different normalized width ( $\delta = 0, 0.6, 0.9$ ). The radial squeezing of the modes in dependence on the junction width is clearly observed. This squeezing leads to the shift of the mode frequencies to higher values. The effect is large for modes with low  $k$ , which have high amplitudes at the inner boundary of the junction. This observation stresses the importance of the finite inner junction radius in particular for modes with low  $k$  and junctions with large  $\delta$ .

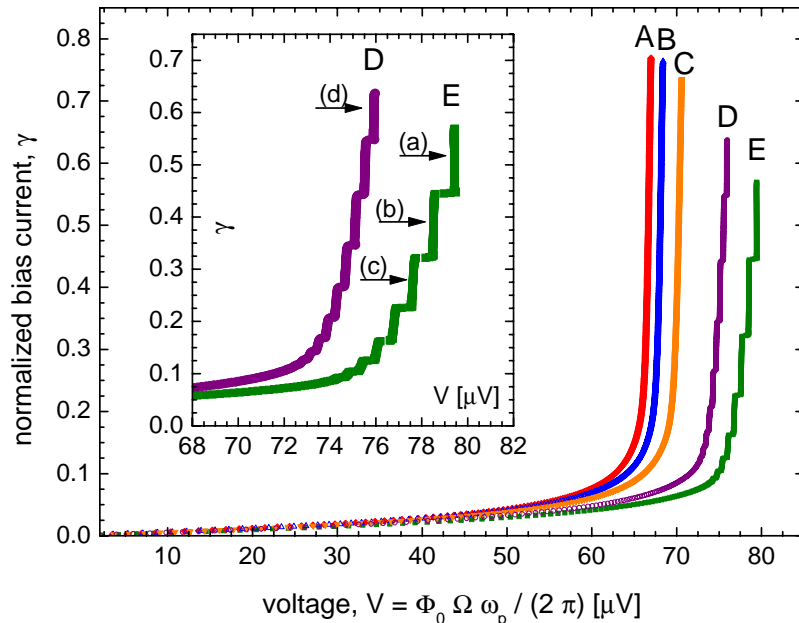


Figure 4.12: Numerically calculated current-voltage characteristics  $V(\gamma)$  for junctions  $A$  to  $E$ . In the inset the characteristics of junctions  $D$  and  $E$  are shown on an enlarged scale. Arrows indicate the bias points used to obtain the phase profiles shown in Fig. 4.13.

## 4.6 Numerical calculations

To confirm the interpretation of our experimental findings, direct numerical simulations of the full 2D perturbed sine-Gordon equation (4.1) in polar coordinates with the boundary conditions (4.13) have been performed for each of the five junctions listed in Table 4.1 [WUK<sup>+</sup>00]. We have calculated both current-voltage characteristics  $V(\gamma)$  and two-dimensional phase profiles  $\phi(\tilde{r}, \varphi, \tilde{t})$ , describing the spatial and temporal field distributions in the junction. The damping parameter  $\alpha = 0.03$  was chosen close to its estimated experimental value at  $T = 4.2$  K, and  $\beta$  was set to 0 for a first qualitative analysis. The calculated  $V(\gamma)$  characteristics for junctions  $A$  to  $E$  are plotted in Fig. 4.12. For comparison with experiment, we converted the calculated normalized vortex rotation frequency  $\tilde{\Omega}$  into voltage units according to

$$V(\gamma) = \frac{\Phi_0}{2\pi} \omega_p \tilde{\Omega}(\gamma) \quad (4.25)$$

using a plasma frequency of  $\omega_p/2\pi = 52.4$  GHz. This value of  $\omega_p$  has been determined from fits to experimental data, which are discussed in Section 4.7. The similarities between the experimental data shown in Fig. 4.6 and the numerical simulations presented in Fig. 4.12 are striking. Clearly, the fine structure on the current-voltage characteristics of the wide junctions  $D$  and  $E$  is very well reproduced in the simulation, see inset of Fig. 4.12. In simulations, the fine structure disappears with decreasing junction width, which is also found in experiment. Additionally, a decrease of the maximum voltage of each individual resonance with increasing inner junction radius, being in accordance with the experimental data, is observed.

It is worth pointing out that in the initial work presented by Kurin *et al.* in Ref. [KYSV98] no peculiarities were observed on the simulated single-vortex current-voltage characteristics. This effect is attributed to the relatively large damping parameter  $\alpha = 0.02$  and the



simultaneously large junction circumference  $\ell = 6\pi$  which were chosen in their calculations ( $\alpha\ell = 0.38$ ). In contrast, the simulations discussed here were done for  $\ell = 3.3\pi$  and  $\alpha = 0.03$  and thus a somewhat smaller effective damping ( $\alpha\ell = 0.31$ ). At the same time, the wave numbers of the excited whispering gallery modes in our simulations are smaller than those discussed in the original paper by Kurin. Moreover, the numerical accuracy of the simulations discussed above was increased in order to explicitly search for the fine structure which was observed in our experiments.

The phase distribution in the junctions at various bias points has been analyzed to further investigate the origin of the fine structure. Fig. 4.13 shows the phase profiles at the bias points on the subsequent fine-structure resonances of junction  $E$  indicated by the arrows in Fig 4.12. As before, the phase profiles are visualized by plotting lines of constant phase. Hence, the vortex position is easily identified by the largest gradient of phase in the position indicated by the arrows in Figs. 4.13a, b, c, and d. Most striking, a clear whispering gallery structure, which resembles closely the analytically calculated modes, is observed in these simulations, e.g. compare Fig.4.13a and Fig. 4.11. The whispering gallery modes are clearly recognized by their large phase gradient at the outer edge and the small phase gradient at the inner edge of the junction and the periodic modulation along the junction circumference. The angular wave number of the mode is identified by the number of periods of the field modulation along the junction perimeter. As expected, only the fundamental radial mode is observed.

From the analysis of the resonance condition (4.7), it has been predicted that the an-

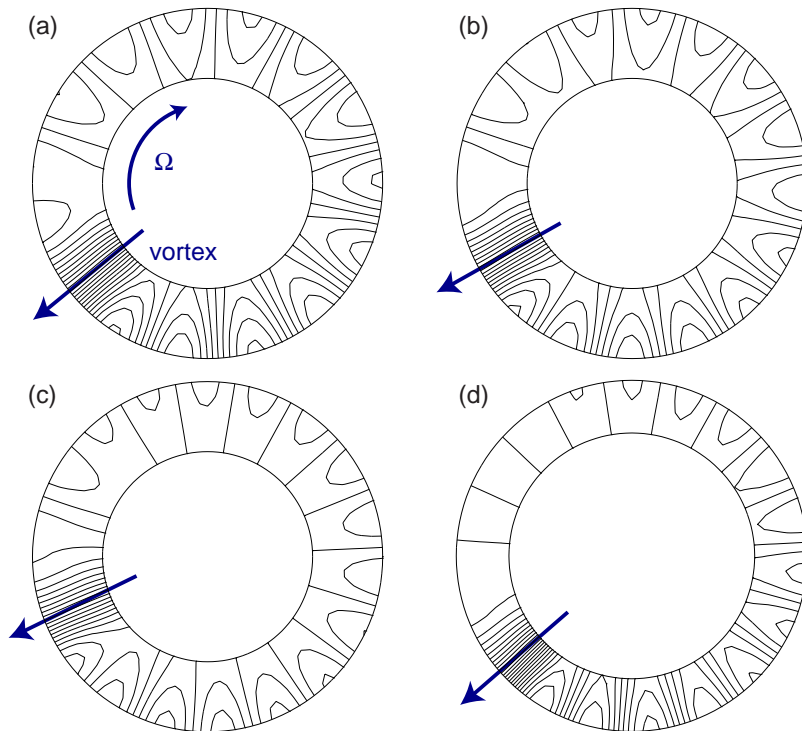


Figure 4.13: Phase profiles  $\phi(\tilde{r}, \varphi)$  at bias  $\gamma$  equal to (a) 0.5, (b) 0.4, (c) 0.3 on the single-vortex resonance of junction  $E$  and (d) at  $\gamma = 0.6$  for junction  $D$ . Plotted are lines of constant phase, their high density corresponds to a large gradient of phase and hence a large magnetic field. The position of the vortex is indicated by an arrow. The whispering gallery modes with angular wave number  $k$  equal to (a) 7, (b) 8, (c) 9 and (d) 9 are observed.

gular wave number of the mode excited by the moving vortex increases from resonance to resonance with decreasing vortex velocity. Precisely this feature is observed in the numerical calculations, see Figs. 4.12 and 4.13.

Considering the resonance condition Eq. (4.7) and the dispersion of the linear modes  $\omega_k$ , we have shown in Section 4.5 that the density of resonances in voltage and the wave number of the lowest excited mode increase with decreasing junction width  $w_j = r_e - r_i$ . This fact has been verified in numerical calculations for junction  $D$ , where the lowest mode number excited at the top of the resonance is  $k = 9$ , see Fig. 4.13d. At comparable bias current, the mode excited in the more narrow junction  $D$  has a notably higher wave number than the one excited in junction  $E$ . For very narrow rings, no fine structure is observed in experiment and in simulation, due to the overlapping of the closely spaced neighboring resonances in the presence of damping.

## 4.7 Quantitative comparison and discussion of results

Using the resonance condition (4.7) and the proportionality between the angular frequency of the vortex  $\Omega$  and the voltage  $V$  [Eq. (4.10)], the fine structure resonances are fitted according to

$$V = \frac{\Phi_0}{2\pi} \omega_p \tilde{\Omega} = \frac{\Phi_0}{2\pi} \omega_p \frac{\tilde{\omega}_k}{k}, \quad (4.26)$$

with the plasma frequency  $\omega_p$  and the mode number  $k$  as parameters. For the fits we use the numerically exact values of  $\tilde{\omega}_{k,0}$  calculated for the specific junction geometry as described in Section 4.5.

The best fit to the experimental data of junction  $E$ , which has the most clearly resolved fine structure at 4.2 K, is found for the plasma frequency  $\omega_p/2\pi = 52.4$  GHz and the wave number  $k_{\min} = 7$  for the highest voltage resonance, see Fig. 4.14a. Both the absolute voltage of the resonance as well as the spacing between different resonances are well explained by the model. The value of  $k_{\min}$  determined from the fit to experimental data is exactly the one found for the highest resonance in numerical simulations, compare Fig. 4.13a. Also, the voltages of the resonances found in simulation (Fig. 4.14b) are in excellent agreement with the ones calculated from the dispersion relation (dotted lines). The agreement between the calculated resonance voltages, the numerical simulations and the experimental data is better than 1 percent, which is near the limit of the voltage resolution of  $0.1 \mu\text{V}$  of our experimental setup.

In the simulations performed with  $\alpha = 0.03$  and  $\beta = 0$ , the differential resistance of the individual steps of the resonances is observed to be smaller than in experiment. The qualitative agreement of the shape of the resonances is significantly improved, by considering a non-zero surface damping and somewhat reduced quasiparticle damping in the simulation. The simulated current-voltage characteristic of junction  $E$  with the damping parameters  $\alpha = 0.02$  and  $\beta = 0.0012$  is presented in Fig. 4.14b (open squares). Clearly, taking into account the quasiparticle surface losses ( $\propto \beta$ ) leads to a larger differential resistance of the resonance, which closely resembles the experimental data in Fig. 4.14a. In contrast to simulation, the upper step with the wave number  $k = 6$  is not present in the experimental curve. A possible reason may be the reduced stability of the step in the presence of thermal fluctuations or small current fluctuations induced by residual electromagnetic noise in the experimental setup.

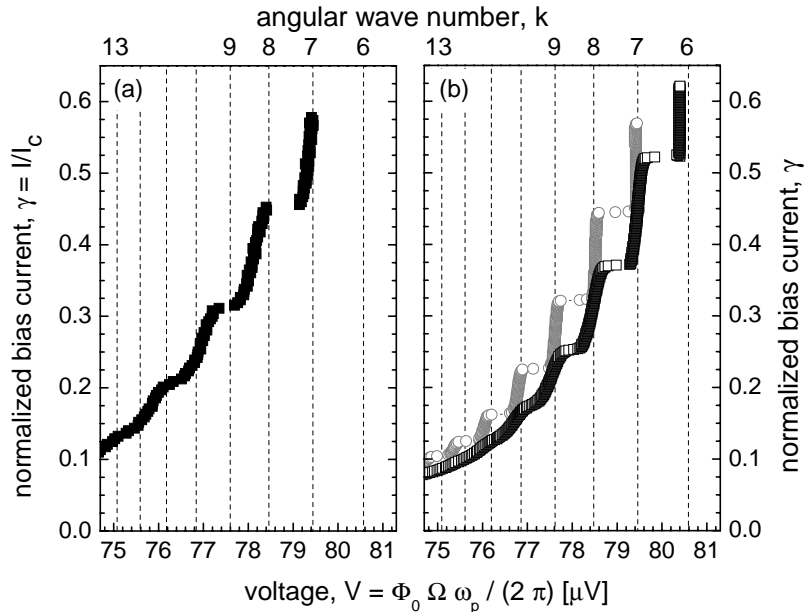


Figure 4.14: (a) Upper part of the experimental single-vortex current-voltage characteristic of junction *E*. (b) Simulated current-voltage characteristic of this junction for  $\alpha = 0.03, \beta = 0$  (open circles) and  $\alpha = 0.02, \beta = 0.0012$  (open squares). The calculated resonance voltages are indicated by vertical dotted lines and marked by the corresponding wave number  $k$ .

By investigating the dependence of the observed fine structure on temperature, number of trapped vortices, and external magnetic field, we have confirmed that the observed effects are due to the interaction of the vortex with the whispering gallery modes of the junction.

At elevated temperatures, no fine structure is noticed in any of the samples due to the increase of the intrinsic damping and the resulting low quality factor of the junction. Decreasing the temperature below 4.2 K, fine structure is observed in all samples *A* to *E*; also the differential resistance of the resonances decreases with temperature. As a typical example, the measured single-vortex current-voltage characteristic of junction *C* is shown in Fig. 4.15a. Obviously no fine structure is resolved at temperatures above  $T = 4.2$  K, whereas at lower temperature the fine structure is clearly visible. The position of the resonance in voltage is almost constant but the differential resistance of the resonance decreases with temperature.

Moreover, we have found that the voltages of the fine-structure resonances scale with the number  $n$  of moving vortices. Therefore, for  $n > 1$  the fine structure is clearly resolved in voltage and also more pronounced because several vortices coherently pump the whispering gallery mode. As an example, the first and second fluxon resonances of junction *C* are shown in Fig. 4.15b. The voltage spacing of steps in the two fluxon case is a factor of 2 larger than in the single fluxon case. The step positions normalized by the number of moving fluxons do not exactly coincide, presumably because of the small change of the dispersion relation due to the presence of more vortices in the junction. No dependence of the fine-structure voltage-step positions on small external magnetic fields was noticed. We have also investigated more narrow annular junctions with a wide idle region both experimentally and theoretically [WFU<sup>+</sup>00]. In this case, the spectrum of the whispering gallery modes (and, thus, of the fine structure) is strongly influenced by the geometry and the electrical properties of the passive region, see Chapter 5. The fine structure recently

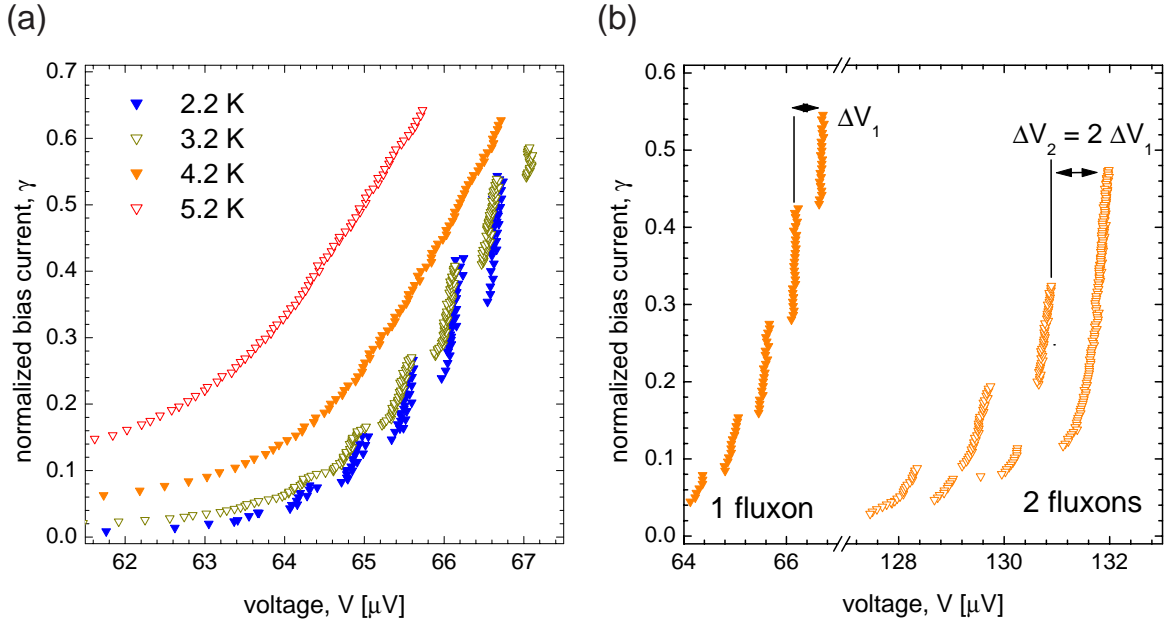


Figure 4.15: (a) Current-voltage characteristic of single-fluxon resonance of junction  $C$  at temperatures between  $T = 5.2$  K and  $T = 2.2$  K. (b) Current-voltage characteristics of first and second vortex resonances of the same junction at  $T = 1.6$  K.

reported in Ref. [MMK<sup>+</sup>98] is consistent with our observations.

Thus, we have developed a consistent picture for the qualitative and quantitative explanation of the Cherenkov-radiation-induced fine structure in effectively two-dimensional annular Josephson junctions.<sup>4</sup>

## 4.8 Conclusion and outlook

We have presented detailed experimental and numerical evidence for the excitation of whispering gallery modes by vortices moving in wide annular Josephson junctions. The vortices appear to whisper (generate radiation) at frequencies between 250 and 450 GHz in the annular whispering gallery of  $100 \mu\text{m}$  diameter. This novel effect has been observed at sufficiently low damping for annular junctions in a wide range of electrical and geometrical parameters. It is very robust with respect to small external perturbations such as variations in bias current density, boundary conditions or junction inhomogeneities. The resonance frequencies have been calculated and quantitative agreement with experimental data and numerical simulations better than one percent has been reached. We have shown that the linear spectrum of the resonator can be sensitively probed by the resonant interaction of plasmon modes with the moving vortex.

<sup>4</sup>The remaining small deviations (on the order of one percent or less) between experiment and theory, are possibly due to the modified plasma spectrum of the junction in the presence of a vortex, the change of the resonance spectrum due to the idle region (see Chapter 5 and [WFU<sup>+</sup>00]) other than the one already taken into account by the rescaling according to Lee et al. [LB92, Lee91], the excitation of large amplitude waves, for which the linearization  $\sin \phi \approx \phi$  is not accurate enough, frequency shifts of the plasma spectrum due to finite damping. These effects could lead to small (less than one percent) corrections to the predicted resonance voltages, but they are not essential for the understanding of the main new effect clearly observed in the experimental data.

The discovery of the fine structure on the single-vortex characteristics of annular junctions has implications for the interpretation of earlier results on Cherenkov radiation in multi-layers [GWTU98, GWU00], fluxon bunching [VLS<sup>+</sup>96], and the temperature dependence of the damping parameters  $\alpha$  and  $\beta$  [DDKP85]. In particular the Cherenkov interaction of the vortex with the whispering gallery modes of the junction due to the finite junction width leads to a similar fine structure as the Cherenkov radiation generated in asymmetric stacks [GWTU98, GWU00]. Therefore, the different sources of fine structure in annular junctions have to be distinguished carefully in experiment. Also the bunching of fluxons [VLS<sup>+</sup>96] may need to be reconsidered in the view of Cherenkov radiation in annular junctions. As pointed out recently in Ref. [GMU00], the bunching of vortices at a particular inter-vortex distance is strongly influenced by the existence of plasma waves in the junction. Furthermore, the determination of the temperature dependence of  $\alpha$  and in particular  $\beta$  [DDKP85], based on the fitting of the form of the single-vortex resonance to perturbation theory, is to be reconsidered. In particular, the fine structure effectively increases the average differential resistance of the resonance, causing an overestimation of the value of  $\beta$ .

In the future work, we plan to perform spatially resolved measurements of the whispering gallery modes by using low temperature scanning electron microscopy (LTSEM) [GK94] or low temperature scanning laser microscopy (LTSLM) [SZT<sup>+</sup>94, SZTD96]. Under the influence of the beam, the quality factor of the junction is modified locally, the effect of which can be monitored by a change in the voltage response of the junction at fixed bias current. This technique allows to image spatially the standing wave patterns in small superconducting structures [GK94]. First promising results using this technique have been presented [Kru98].

We also intend to perform direct measurements of the radiation generated by the resonant interaction of the vortex with the whispering gallery modes of the junction. The radiation can either be detected directly using an SIS detector or measured using an SIS mixer [KSF<sup>+</sup>96]. The major challenge here is to design a coupling circuit between the sample and the detector that is efficient in the frequency range of interest, i.e. 250 - 450 GHz. By choosing the proper junction geometry, the resonance frequencies can be tuned to be accessible with the available equipment. Such a measurement would be the first direct evidence of the generation of Cherenkov radiation by a vortex moving in an annular Josephson junction. Being successful, such measurements could stimulate the use of annular junctions as radiation sources. Due to the Cherenkov-like coupling of the fluxon modes to the linear modes at all the external junction perimeter, the generation of radiation could be very efficient.

An interesting path for future research is the investigation of the transition of whispering gallery modes in symmetric annular junctions to chaotic modes in asymmetric junctions. Geometries of particular interest are the so-called stadium geometry or the Bohigas annular billiard, one being an oval variety of the annular junction and the other being an annular junction where the circle defining the inner perimeter of the junction is offset from the center of the junction. The properties of electromagnetic modes in such junctions can be investigated in detail using the techniques presented in this chapter. Chaotic modes in micro-resonators are currently under active investigation both theoretically and experimentally.

# Chapter 5

## Annular Junctions with Idle Region

Experiments studying the influence of the idle region on the static and dynamic properties of annular Josephson junctions are reported. The dependence of the first critical field of the junction on the width of the idle region is investigated and explained considering a renormalized Josephson length. The excitation of whispering-gallery-type electromagnetic modes by a vortex moving in an annular Josephson junction with large idle region is examined. We calculate analytically the spectrum of the linear modes taking into account the electromagnetic environment of the junction. The experimental data are in good quantitative agreement with analysis and numerical calculations based on the two-dimensional sine-Gordon model.<sup>1</sup>

In literature, many experiments on the static and dynamic properties of long Josephson junctions are qualitatively explained considering the electrical and geometrical parameters of the bare junction only. In many cases, such a simplified approach suffices to qualitatively explain the observations. However, in order to understand experimental results quantitatively, the electromagnetic environment of the junction needs to be considered.

The most important contribution to the electromagnetic environment originates from the fact that the Josephson tunnel junction is usually surrounded by an insulating region, which separates the top and bottom electrodes from one another to avoid shorting out the junction by a direct contact between the two. Such an insulating region is required in any junction fabrication process (see Section 2.3.1), though its physical realization, its size and electrical parameters can be quite diverse. The part of the Josephson junction in which the tunneling of Cooper pairs is possible is called Josephson or active region. In contrast the part in which tunneling is suppressed by a thick insulating barrier is called passive or idle region. The geometry of the active region is determined by the planar dimensions of the tunnel barrier, whereas the dimension of the idle region is determined by the overlap of the

---

<sup>1</sup>Parts of this chapter have been published in ‘Physica B **284-288**, 575 (2000)’ and have been accepted for publication in ‘Journal of Applied Physics’.

Table 5.1: Dimensions and effective Josephson lengths of two sets (*I* and *II*) of annular junctions with mean radius  $\bar{r} = (r_i + r_e)/2 = 55 \mu\text{m}$  and Josephson length  $\lambda_J \approx 10 \mu\text{m}$ .

set	<i>I</i>						<i>II</i>				
$w_j [\mu\text{m}]$	10						6				
#	<i>A</i>	<i>B</i>	<i>C</i>	<i>D</i>	<i>E</i>	<i>F</i>	<i>A</i>	<i>B</i>	<i>C</i>	<i>D</i>	<i>E</i>
$w_p [\mu\text{m}]$	3	5	10	15	20	30	3	5	7	12	22
$w_p/w_j$	0.3	0.5	1.0	1.5	2.0	3.0	0.5	0.83	1.17	2.0	3.67
$\lambda_{\text{eff}}/\lambda_J$	1.16	1.25	1.47	1.65	1.82	2.11	1.25	1.40	1.53	1.82	2.28

top and bottom electrodes outside the active junction region, see Fig. 4.3.

One of the first systematic investigations on the effect of the idle region on the dynamic properties of long Josephson junctions was published by Lee *et al.* [Lee91, LB92]. In this work, the dispersion of the linear modes of a long junction was calculated in dependence on the inductance and the capacitance of the junction and the idle regions. It was found that the Swihart velocity of a junction can be substantially increased by a usually low-capacitance and high-inductance stripline coupled to the junction. Measurements of the Swihart velocity are commonly used to estimate the specific capacitance and inductance of the junction. To estimate those parameters from the measurements, the idle region needs to be considered in the way suggested by Lee *et al.* [Lee91, LB92]. Their results have been experimentally verified for long junctions in Ref. [MCM95].<sup>2</sup>

The static properties of the phase distribution in a long Josephson junction can be probed by measuring its critical-current diffraction pattern. The first experiments investigating the effect of the idle region on such patterns are reported in Ref. [TUK<sup>+</sup>95]. At the same time, a theory explaining the experimental observations by considering a renormalization of the Josephson length was developed by Caputo *et al.* [Cap96], but no systematic comparison between experimental data and theoretical predictions had been performed. Since then, the theoretical understanding of the static properties of the junction has still advanced and is quite complete now, see Ref. [CFK<sup>+</sup>99].

In this chapter, we present experimental results which underline the importance of considering the idle region to understand both static [FWU00a] and dynamic properties [WFKU00] of annular Josephson junctions. In the first section I introduce a model which describes the electrodynamics of an annular junction with idle region. In Section 5.2 I discuss the low field properties of critical-current diffraction patterns of junctions with large idle region and compare the results to the theory by Caputo *et al.*. In Section 5.3 the dynamics of vortex anti-vortex pairs in junctions with a large idle region is considered. In particular the excitation of whispering gallery resonances is observed (compare Chapter 4) and the modification of the characteristic resonance frequencies due to the idle region is discussed. The linear mode spectrum is calculated by considering the idle region as a stripline resonator coupled symmetrically to the annular junction.

We have designed two sets of annular junctions with mean radius  $\bar{r} = (r_i + r_e)/2 = 55 \mu\text{m}$  junction width  $w_j = 10 \mu\text{m}$  and  $6 \mu\text{m}$ , respectively. Within each set, junctions with a passive region width between  $w_p = 3 \mu\text{m}$  and  $30 \mu\text{m}$  are studied. The available samples are listed

<sup>2</sup>The results by Lee *et al.* were also used in Chapter 4 to renormalize the current-voltage characteristics, in order to reconstruct the single-vortex resonances of a bare junction, i.e. one without idle region.

in Table 5.1. The junctions were fabricated at Hypres Inc. [Hyp] using Nb-Al/ $\text{AlO}_x$ -Nb technology with a nominal critical-current density of  $1000 \text{ A/cm}^2$ . The fabrication process, the electrical parameters and the film thicknesses used in junction fabrication are identical to the ones stated in Section 4.2. For reference their values are listed again in Table 5.2 .

## 5.1 The model

The physics of an effectively two-dimensional annular Josephson junction is well described by the normalized perturbed sine-Gordon equation in polar coordinates (4.1), as discussed in detail in Sections 2.1.1 and 4.1. Here, the idle region is considered as a stripline coupled in parallel to the junction. Its electrodynamics is described in terms of a wave equation for the component of the vector potential in the passive region  $\psi$ , which is perpendicular to the plane of the junction

$$\left( \tilde{\nabla}^2 - \frac{1}{\mathcal{V}^2} \frac{\partial^2}{\partial \tilde{t}^2} \right) \psi = 0. \quad (5.1)$$

The factor  $1/\mathcal{V}^2$  is introduced to take into account the different phase velocities  $c_p$  and  $c_j$  in the passive and active regions of the junction, respectively.  $\mathcal{V}$  is defined as

$$\mathcal{V} = \frac{c_p}{c_j} \quad (5.2)$$

with

$$c_{p,j} = \sqrt{\frac{t_{j,p}}{\epsilon_{j,p} d'_{j,p}}}. \quad (5.3)$$

In the respective junction region the magnetic thickness  $d'_{j,p}$  is given by [Wei69]

$$d'_{j,p} = \lambda_L \coth(d_b/\lambda_L) + \lambda_L \coth(d_t/\lambda_L) + t_{j,p}, \quad (5.4)$$

where  $d_{b,t}$  are the top and bottom thicknesses of the superconducting electrodes,  $t_{j,p}$  are the thicknesses of the insulator and  $\epsilon_{j,p}$  are its dielectric constants, the respective values of which are quoted in Table 5.2. In the thick film limit, Eq.(5.4) can be approximated as  $d'_{j,p} = t_{j,p} + 2\lambda_L$ . In this way the electrodynamics of both the junction region and the passive region can be expressed in the same normalized units.

To assure the continuity of the fields  $\phi$  and  $\psi$  at the interface between the two regions, we require

$$\phi|_{\tilde{r}_i, \tilde{r}_e} = \psi|_{\tilde{r}_i, \tilde{r}_e}. \quad (5.5)$$

The jump of the magnetic field at the boundary is proportional to the ratio of the specific inductances  $\lambda$  of the two regions

$$\left. \frac{\partial \phi}{\partial \tilde{r}} \right|_{\tilde{r}_i, \tilde{r}_e} = \lambda \left. \frac{\partial \psi}{\partial \tilde{r}} \right|_{\tilde{r}_i, \tilde{r}_e}. \quad (5.6)$$

Table 5.2: Bottom and top electrode thickness  $d_{b,t}$ , London penetration depth  $\lambda_L$ , barrier thickness  $t_{j,p}$  and dielectric constant  $\epsilon_{j,p}$  of both active and passive junction regions.

	$d_b$ [nm]	$d_t$ [nm]	$\lambda_L$ [nm]	$t_{j,p}$ [nm]	$\epsilon_{j,p}$
junction region (j)	100	400	90	2	10
passive region (p)	100	300	90	200	3.5



The inductance ratio  $\lambda$  is defined as

$$\lambda = \frac{L_j^*}{L_p^*} \quad (5.7)$$

with the specific inductance  $L_{j,p}^*$  given by

$$L_{j,p}^* = \mu_0 d'_{j,p} . \quad (5.8)$$

In zero external magnetic field, neglecting self-field contributions due to the bias current, the boundary conditions at the outer junction edge are given by

$$\left. \frac{\partial \psi}{\partial \tilde{r}} \right|_{\tilde{r}_{ip}, \tilde{r}_{ep}} = 0 . \quad (5.9)$$

Using the above equations the statics and dynamics of long Josephson junctions with idle can be accurately described.

## 5.2 Critical-current diffraction patterns

The maximum possible superconducting current, that is the critical current  $I_c$ , of a Josephson junction depends sensitively on the externally applied magnetic field [Jos64, BP82, AR63]. In Chapter 3, it has been shown that the critical current diffraction patterns of relatively small annular junctions  $\tilde{r}_\epsilon \leq 1$  are well described by an analytical expression calculated using a linear phase approximation [Nap97]. In this limit, excellent agreement between the experimental data and the theoretical prediction was found. For much longer junctions  $\tilde{r}_\epsilon \gg 1$  the experimental data, in particular in the low field range, are not well described in the linear phase approximation. The description of the full critical-current diffraction pattern of long junctions in a large field range is a complicated problem and is usually approached using numerical calculations [PRS91]. However, the dependence of the critical-current on a small applied magnetic field can be well understood in the following way. In weak magnetic fields, a long junction behaves like a weak superconductor and shows the Meissner effect [Sch70]. In this regime the critical current decreases proportional to the external field [OS67]. This behavior exists until a critical field  $H_{c1}$  is reached. At this field flux quanta in form of Josephson vortices penetrate into the junction [OS67]. Neglecting the idle region, the first critical field of a long linear Josephson junction is given by [Sch70]

$$H_{c1} = \frac{\Phi_0}{\pi \Lambda \lambda_J} , \quad (5.10)$$

where  $\Lambda = \lambda_L \tanh(d_b/2\lambda_L) + \lambda_L \tanh(d_t/2\lambda_L) + t_j$  is the effective magnetic thickness of the junction [Wei69] and

$$\lambda_J = \sqrt{\frac{\Phi_0}{2\pi j_c \mu_0 d'_j}} \quad (5.11)$$

is the Josephson length. In first experiments, it was qualitatively found that  $H_{c1}$  of a junction with idle region scales proportional to some effective Josephson length [ML97, TUK+95]. In the following, we consider the dependence of the first critical field of a long annular junction on the width of the idle region and compare our experimental results [FWU00a, Fra99] to predictions by Caputo *et al.* [Cap96, CFK+99].

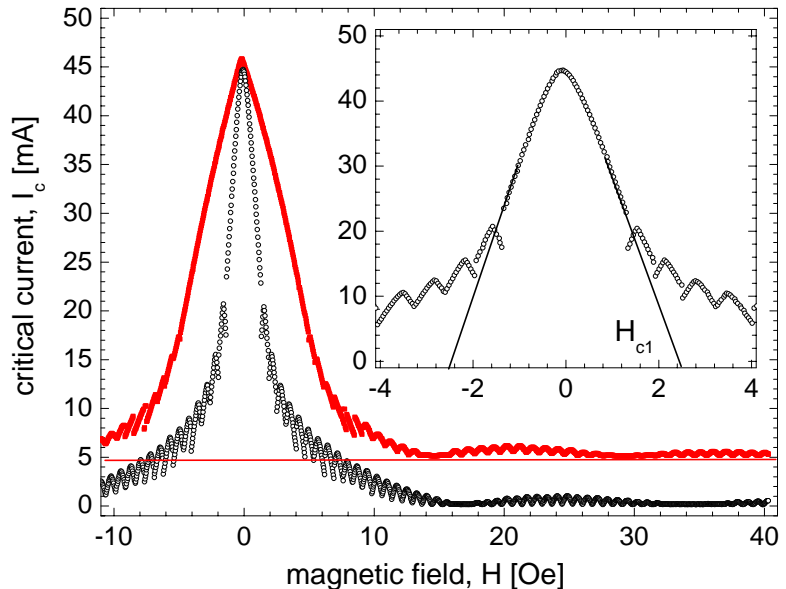


Figure 5.1: Critical-current diffraction patterns of junctions  $IA$  (solid squares, offset by  $\Delta I_c = 0.5$  mA) and  $IF$  (open circles). The inset illustrates the definition of the first critical field  $H_{c1}$ .

In measurements of the critical current versus the externally applied in-plane magnetic field of the annular samples listed in Table 5.1, we found a strong influence of the width of the passive region  $w_p$  on the pattern. The critical-current diffraction patterns of the junction with the most narrow (junction  $IA$ ) and the widest idle region ( $IF$ ) are shown in Fig 5.1 to illustrate the effect. From the experimental data, the first critical field is determined by linearly extrapolating the branch starting at the maximum zero-field critical current to  $I_c = 0$ , see inset of Fig. 5.1. Obviously, we observe a large decrease of  $H_{c1}$  with increasing width of the idle region  $w_p$ . In Fig 5.2a, the values of  $H_{c1}$  determined for both sets of junctions are plotted versus  $w_p$ . Considering the ratio of the idle width  $w_p$  to the junction width  $w_j$ , we find that  $H_{c1}$  scales universally for both sets of junctions with this quantity, see Fig 5.2b. Moreover, a small increase of the maximum zero-field current with  $w_p$  is noticed. In the high-field range, we also observe a modulation of the pattern with a large period, depending on the geometry and the characteristic magnetic field of the junction, as discussed in detail in Chapter 3.

The observed scaling of the first critical field  $H_{c1}$  can be explained by a rescaling of the Josephson length  $\lambda_J$  in dependence on the idle width  $w_p$ , as first pointed out by Caputo *et al.* in Refs. [Cap96, CFK<sup>+</sup>99]. In his work, Caputo calculated the effective size of a Josephson vortex  $\lambda_{\text{eff}}$  in a long junction with various geometries and sizes of the idle region. The calculations are based on the analytical and numerical evaluation of the static limit of Eqs. (4.1) and (5.1)

$$\begin{aligned}\tilde{\nabla}^2\phi - \sin\phi &= 0, \\ \tilde{\nabla}^2\psi &= 0,\end{aligned}\tag{5.12}$$

with the boundary conditions stated in Section 5.1. Considering a long linear junction of width  $w_j$  with a symmetric idle region of width  $w_p$ , the size of the vortex is found by reducing the set of 2D partial differential equations (5.12) to an 1D non-local integro-differential equation [CFK<sup>+</sup>99]. It is found that the solutions to the non-local equations can be mapped to the solutions of a junction with an effective renormalized Josephson length

$\lambda_{\text{eff}}$ . In the limit of  $w_p/\lambda_J \leq 5$ , the effective Josephson length is given by [Cap96]

$$\lambda_{\text{eff}} = \lambda_J \sqrt{1 + \frac{2w_p}{w_j} \lambda}. \quad (5.13)$$

Equation (5.13) can be interpreted by considering the effective inductance of the junction given by the parallel combination of the inductances of the junction and the stripline. The factor 2 appears because the junction is coupled symmetrically on both sides to an idle region of width  $w_p$ . The result (5.13) was verified in Refs. [Cap96, CFK<sup>+</sup>99] by extensive numerical simulations for a large range of junction parameters. The size of the vortex was evaluated by direct numerical calculations of the phase distribution inside the junction and also by a variation of the free energy of the vortex. Moreover, the critical-current diffraction patterns were simulated and it was shown that  $H_{c1}$  decreases inversely proportional to  $\lambda_{\text{eff}}$  [CFK<sup>+</sup>99].

Therefore our measurements of the dependence of the first critical field on the width of the passive region can be analyzed in terms of the effective Josephson length  $\lambda_{\text{eff}}$ . In Fig. 5.3, the first critical field for the two sets of annular junctions I and II is plotted versus the reciprocal normalized effective Josephson length calculated from Eq. (5.13) using an inductance ratio of  $\lambda = 0.5$ . Obviously, the data scales linearly with  $\lambda_J/\lambda_{\text{eff}}$ , proving that the observed effect can be explained by an inductance-dependent renormalization of the Josephson length as stated in Eq. (5.13). All data in Fig.5.3 fit with a relative standard deviation of about 10 % to this linear dependence.

Even though the relation (5.13) was derived in Ref.[Cap96] for linear junctions only, we found that it describes well the data of annular Josephson junctions, as can be seen from Fig. 5.3. The reason is that the universal scaling of the Josephson length in a quasi-one-dimensional Josephson junction ( $w_j < \lambda_J$ ) coupled to an idle region persists regardless of the exact geometry of the junction. The increase of  $\lambda_{\text{eff}}$  with  $w_p$  is also manifested in the fact that the pattern shows a linear dependence of  $I_c$  on  $H$  in the low field range ( $H < H_{c1}$ ) for small  $w_p$ , whereas the feature becomes more and more rounded with increasing  $w_p$  indicating that the effective size of the junction becomes smaller. As predicted by Caputo *et al.*, we also observe a small increase of the zero-field critical current with increasing  $w_p$ ,

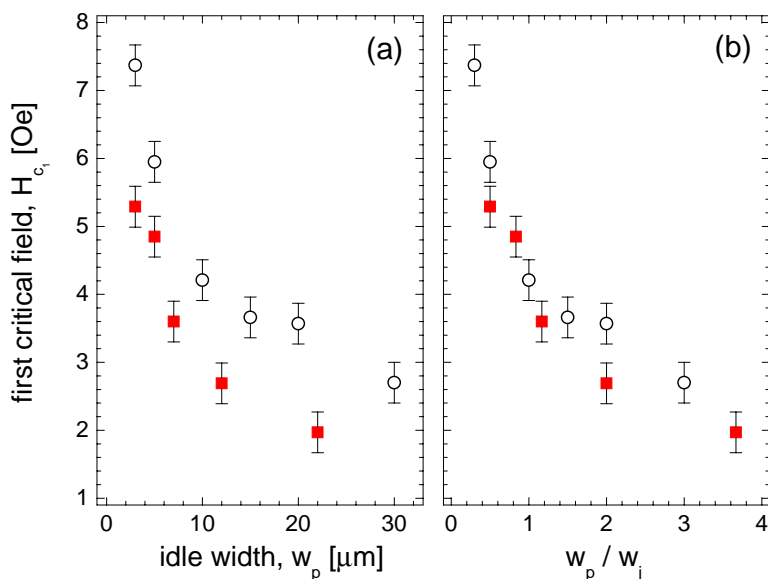


Figure 5.2: (a) First critical field  $H_{c1}$  of junctions in set I (solid squares) and set II (open circles) versus the width of the idle region  $w_p$ . (b)  $H_{c1}$  versus the ratio  $w_p/w_j$ . The error bars indicate the systematic error in the determination of  $H_{c1}$ .

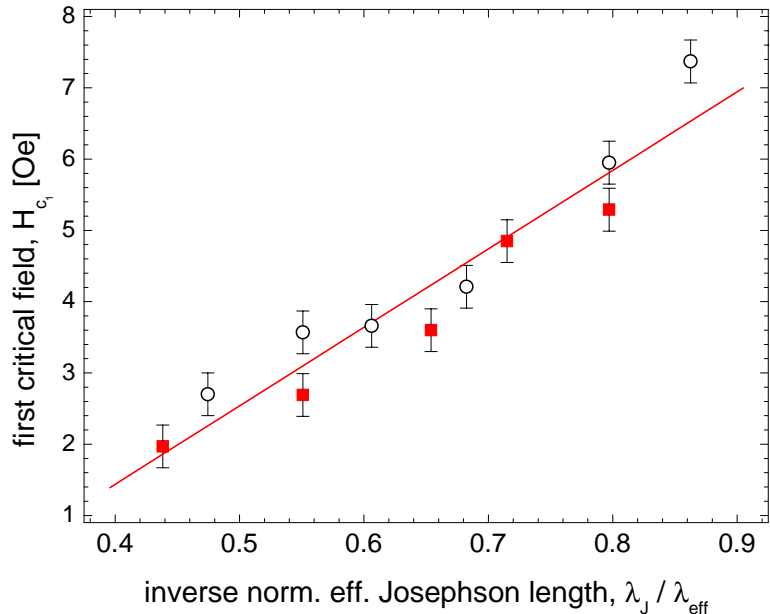


Figure 5.3: First critical field  $H_{c_1}$  versus the inverse normalized effective Josephson length  $\lambda_J/\lambda_{\text{eff}}$  (set I: solid squares, set II: open circles). A fit to the data is indicated by the straight line.

due to the more homogeneous current distribution in the junction induced by the larger Josephson length.

In conclusion we state that the features of the measured critical-current diffraction patterns of annular junctions with large idle region are well described by the theory developed by Caputo *et al.*. We point out that the idle region can substantially increase the effective Josephson length of the junction. The effect is particularly strong for narrow junctions with large idle. For typical sample fabrication technologies and junction width  $w_j \approx 3 \mu\text{m}$ ,  $w_p \approx 2.5 \mu\text{m}$  and  $\lambda = 0.6$  the increase of  $\lambda_J$  is about a factor of  $\sqrt{2}$  which is approximately 40 percent larger than the one predicted considering just the bare junction. Therefore, the idle region has to be considered specifically, when describing the physics of Josephson junctions with an 1D sine-Gordon model.<sup>3</sup>

### 5.3 Whispering gallery modes

In Chapter 4, the excitation of whispering gallery modes in an annular Josephson junction due to the Cherenkov-like interaction between vortices and plasmon modes has been discussed in detail. In that chapter, junctions with a small idle region were considered. In fact, we used a special renormalization to take into account the modification of the effective phase velocity in the junction due to the small idle region. The quantitative comparison between experimental data and predictions was performed for the widest junctions, where the effect of the idle is the smallest. Here, I consider annular junctions with idle regions up to six times larger than the junction itself. These samples have been designed with the intention to investigate the effect of the coupling between a linear resonator and the junction on its whispering gallery resonances. In this case, the electrodynamic properties of the sample are strongly influenced by the idle region.

As shown in Chapter 4, the resonant interaction between a vortex and the whispering

<sup>3</sup>The discussion of these effects considering also linear long junctions can be found in Refs. [FWU00a, Fra99].

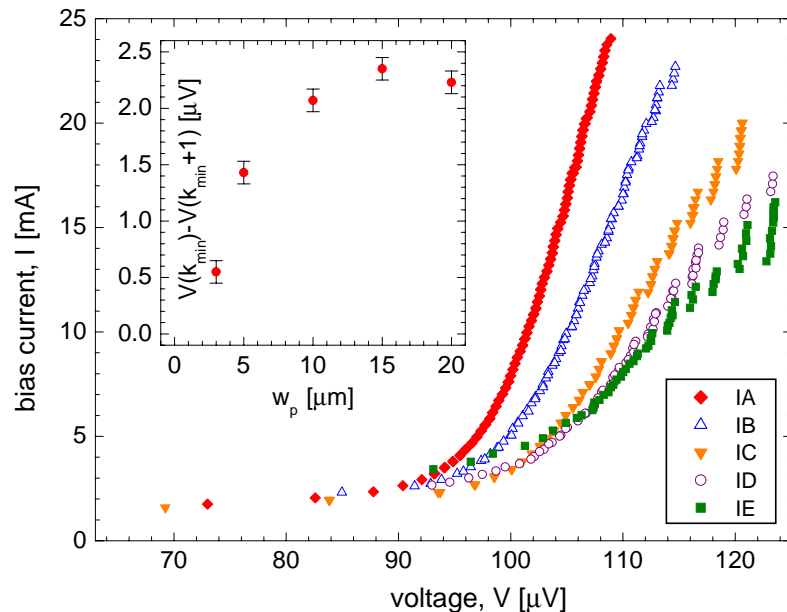


Figure 5.4: Current-voltage characteristics of vortex–anti-vortex resonances in junctions  $IA$  to  $IE$  at 4.2 K. In the inset the voltage separation between the two highest resonances is plotted versus  $w_p$ .

gallery modes is manifested by fine-structure resonances on the current-voltage characteristic. The resonance voltages are given by the condition [KYSV98]

$$V = \Phi_0 \frac{\omega_p \tilde{\omega}_k}{2\pi k}, \quad (5.14)$$

where  $\tilde{\omega}_k$  are the characteristic frequencies of the annular resonator modes. These characteristic frequencies depend strongly on the geometry and the electrical parameters of the junction and its idle region.

### 5.3.1 Experimental observation

We have investigated the current-voltage characteristics of vortex–anti-vortex pairs [WFKU00, Fra99] in the two sets of annular junctions described in the introduction to this chapter. Each junction is initially prepared in a flux free state, i.e. with a maximum critical current at zero field. Then vortex–anti-vortex pairs are nucleated when decreasing the bias current from the whirling state. Once a pair is generated, the two vortices of opposite polarity propagate in opposite directions along the ring. Such a state is stable since the vortices exchange neither momentum nor energy during collisions. The presence of the pair is manifested by a resonance on the current-voltage characteristic of the junction at a voltage which is proportional to the number of propagating vortices. As shown in Chapter 4, multiple vortices interact with the whispering gallery modes almost independently, the main effect being that the voltage separation between resonances scales with the number  $n$  of vortices. Moreover, the amplitude of the excited whispering mode is increased proportional to the number of vortices pumping the mode, leading to more pronounced resonances. As an additional feature, we expect that the counter propagating vortex and anti-vortex generates a standing wave pattern due to the superposition of whispering gallery modes with opposite wave vector.

In both sets of samples, we have observed a clear fine structure on the vortex–anti-vortex resonance at 4.2 K. The current-voltage characteristics of the junctions with a fixed junction width of  $w_j = 10 \mu\text{m}$  (set  $I$ ) are shown in Fig. 5.4. Evidently, both the resonance

voltages and their spacing depend strongly on the width of the idle region. The shift of the asymptotic resonance voltages cannot be explained by a simple rescaling of the effective phase velocity due to the idle region using the approach by Lee et al. [Lee91, LB92]. This indicates that the characteristic frequencies of the whispering gallery modes are sensitively dependent (in an essentially non-linear way) on both the geometry and the electrical parameters of the junction and the idle region. In the inset the voltage difference between the two highest-voltage (i.e. lowest wave number) fine-structure steps is plotted versus the idle region width  $w_p$ , indicating the large variation (more than a factor of two) of the separation between resonance frequencies. These observations can be explained considering the linear modes of the junction being coupled to the idle region.

### 5.3.2 Whispering gallery modes in the presence of an idle region

The whispering gallery mode spectrum is calculated by linearizing the wave equations (4.1, 5.1) coupled via the boundary conditions (5.5, 5.6) between the junction regions [WFKU99]. At the external junction boundary, the zero-field boundary condition (5.9) is considered. In polar coordinates the equations to study are

$$\frac{1}{\tilde{r}} \frac{\partial}{\partial \tilde{r}} \tilde{r} \frac{\partial \phi}{\partial \tilde{r}} + \frac{1}{\tilde{r}^2} \frac{\partial^2 \phi}{\partial \varphi^2} - \frac{\partial^2 \phi}{\partial t^2} - \phi = 0, \quad (5.15)$$

$$\frac{1}{\tilde{r}} \frac{\partial}{\partial \tilde{r}} \tilde{r} \frac{\partial \psi}{\partial \tilde{r}} + \frac{1}{\tilde{r}^2} \frac{\partial^2 \psi}{\partial \varphi^2} - \frac{1}{\mathcal{V}^2} \frac{\partial^2 \psi}{\partial t^2} = 0. \quad (5.16)$$

The solutions for each individual part of the resonator can be cast in the form of linear combinations of Bessel functions of the first and second kind as discussed in Section 4.5

$$\begin{aligned} \psi &= c_1 J_k(\tilde{\omega} \tilde{r} / \mathcal{V}) + c_2 Y_k(\tilde{\omega} \tilde{r} / \mathcal{V}) & \text{for } \tilde{r}_{ip} \leq \tilde{r} < \tilde{r}_i \\ \phi &= c_3 J_k(\tilde{\omega} \tilde{r}) + c_4 Y_k(\tilde{\omega} \tilde{r}) & \text{for } \tilde{r}_i \leq \tilde{r} \leq \tilde{r}_e \\ \psi &= c_5 J_k(\tilde{\omega} \tilde{r} / \mathcal{V}) + c_6 Y_k(\tilde{\omega} \tilde{r} / \mathcal{V}) & \text{for } \tilde{r}_e < \tilde{r} < \tilde{r}_{ep} \end{aligned} \quad (5.17)$$

where  $\tilde{\omega} = \sqrt{\tilde{\omega}^2 - 1}$  and  $c_i$  are constants which are fixed by the boundary conditions. Applying the boundary conditions to the set of solutions (5.17) we find a set of linear equations

$$\hat{A} \vec{C} = 0, \quad (5.18)$$

where  $\vec{C} = (c_1, c_2, \dots, c_6)$  is a vector and  $\hat{A}$  is a matrix defined as

$$\hat{A} = \begin{pmatrix} J'_k(\tilde{\omega} \tilde{r}_{ip} / \mathcal{V}) & Y'_k(\tilde{\omega} \tilde{r}_{ip} / \mathcal{V}) & 0 & 0 & 0 & 0 \\ J_k(\tilde{\omega} \tilde{r}_i / \mathcal{V}) & Y_k(\tilde{\omega} \tilde{r}_i / \mathcal{V}) & -J_k(\tilde{\omega} \tilde{r}_i) & -Y_k(\tilde{\omega} \tilde{r}_i) & 0 & 0 \\ 0 & 0 & -J_k(\tilde{\omega} \tilde{r}_e) & -Y_k(\tilde{\omega} \tilde{r}_e) & J_k(\tilde{\omega} \tilde{r}_e / \mathcal{V}) & Y_k(\tilde{\omega} \tilde{r}_e / \mathcal{V}) \\ \lambda J'_k(\tilde{\omega} \tilde{r}_i / \mathcal{V}) & \lambda Y'_k(\tilde{\omega} \tilde{r}_i / \mathcal{V}) & -J'_k(\tilde{\omega} \tilde{r}_i) & -Y'_k(\tilde{\omega} \tilde{r}_i) & 0 & 0 \\ 0 & 0 & -J'_k(\tilde{\omega} \tilde{r}_e) & -Y'_k(\tilde{\omega} \tilde{r}_e) & \lambda J'_k(\tilde{\omega} \tilde{r}_e / \mathcal{V}) & \lambda Y'_k(\tilde{\omega} \tilde{r}_e / \mathcal{V}) \\ 0 & 0 & 0 & 0 & J'_k(\tilde{\omega} \tilde{r}_{ep} / \mathcal{V}) & Y'_k(\tilde{\omega} \tilde{r}_{ep} / \mathcal{V}) \end{pmatrix}. \quad (5.19)$$

Non-trivial solutions to Eq. (5.18) exist for

$$\det \hat{A} = 0, \quad (5.20)$$

which yields the dispersion equation, i.e. the whispering gallery mode spectrum  $\tilde{\omega}(k)$ , of the Josephson junction with idle.

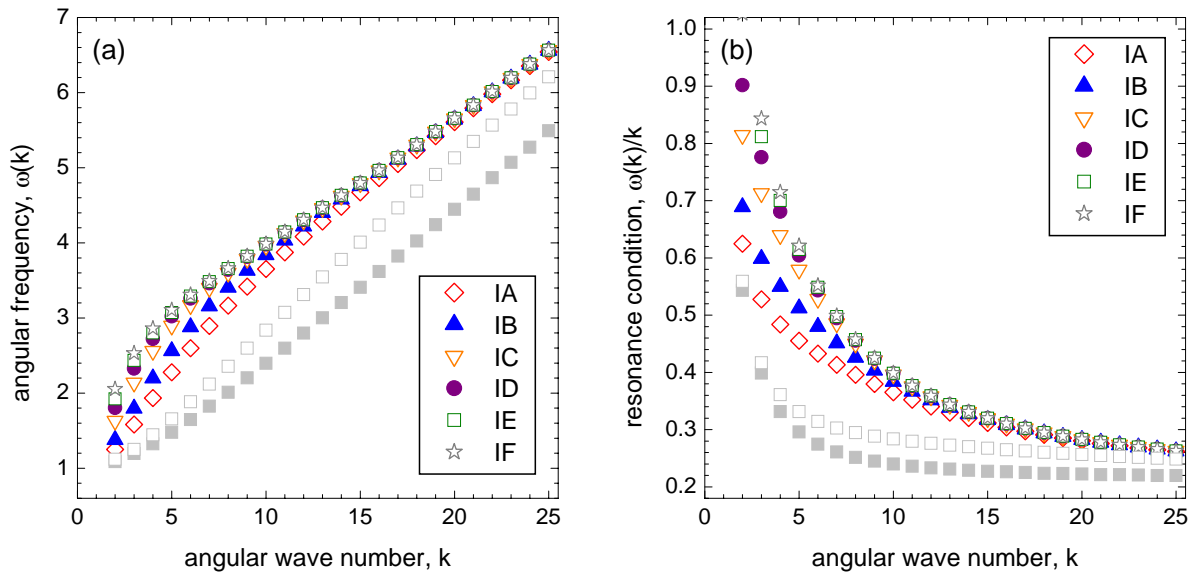


Figure 5.5: (a) Normalized mode spectra for junctions  $IA$  to  $IF$ . Also plotted are the spectra of a junction without idle  $w_p = 0$  (solid gray squares) and of a junction with very small idle  $w_p = 0.5 \mu\text{m}$  (open gray squares). (b) Normalized resonance frequencies  $\tilde{\omega}/k$  for junctions  $IA$  to  $IF$ . Also plotted are the resonance frequencies for a junction without idle  $w_p = 0$  (solid gray squares) and for a junction with very small idle  $w_p = 0.5 \mu\text{m}$  (open gray squares).

Thus the mode spectrum of the system is determined by a complicated transcendental equation (5.20). Exact analytical solutions for the variables  $\tilde{\omega}$  and  $k$  cannot be found and approximate solutions are difficult to determine. Therefore, we have developed the following numerical technique to calculate the mode spectrum.

Since the evaluation of  $\det \hat{A}$  would result in a large polynomial of Bessel functions which is inefficient to solve numerically, we first substitute the geometrical parameters  $\tilde{r}_{ip}$ ,  $\tilde{r}_i$ ,  $\tilde{r}_e$ ,  $\tilde{r}_{ep}$  and the electrical parameters  $\lambda$ ,  $\mathcal{V}$  into the matrix  $\hat{A}$ . Then, for a fixed angular wave number  $k$ , the elements of the matrix  $\hat{A}$  are evaluated for a discrete set of values  $\omega_i$ . Then the determinant is evaluated to find the discrete function  $\det \hat{A}_k(\omega_i)$ , the zeros of which determine the characteristic frequencies of the linear modes. The function is interpolated and its zeros are found iteratively using the Newton's method with a guessed initial value for the zero. The first zero of the function  $\det \hat{A}_k(\omega)$  corresponds to the eigenfrequency of the fundamental radial mode of the resonator. In general, the  $\rho$ -th zero of  $\det \hat{A}_k(\omega)$  determines the eigenfrequency of the radial mode  $\rho$  with the angular wave number  $k$ . The guessing of the initial values for the iterative procedure of determining the zeros was automated and the convergence of the numerical method was checked. To verify the accuracy of the procedure and to exclude errors, the mode spectrum of a junction with arbitrary geometrical parameters of the idle region but with  $\lambda = 1$  and  $\mathcal{V} = 1$  was compared to the results determined from the direct calculation of a spectrum of a junction without idle, but the same outer dimensions, using the approach presented in Section 4.5. Excellent agreement between the two methods was found.

Using the procedure described above, we have determined the normalized linear mode spectrum for the first set of samples, as shown in Fig. 5.5a. The parameters  $\lambda \approx 0.5$ ,  $\mathcal{V} \approx 12$  and  $\lambda_J \approx 12 \mu\text{m}$  have been determined from the geometrical dimensions and

electrical properties of the samples. Obviously, the frequencies of the modes depend on the width of the idle region. At a fixed wave number  $k$ , the characteristic frequency  $\omega_k$  increases with the width of the idle region. The characteristic frequencies differ strongly for small  $k$  because, in this case, the modes have substantial amplitudes both in the Josephson and in the idle region. In the limit of large  $k$  however, the characteristic mode frequencies of all junctions converge to the same value because the modes concentrate at the outer edge of the junction and hence, only the idle region parameters are important. For further comparison we have also calculated the spectra for a junction without idle  $w_p = 0$  (gray solid squares) and for a junction with very small idle  $w_p = 0.5 \mu\text{m}$  (gray open squares). Obviously, in the limit of large  $k$  the characteristic frequencies of the bare junction are smaller than of those of junctions with idle. Even a small idle attached to the junction (open gray squares) shifts the characteristic frequencies to higher values because the higher order angular modes are concentrated at the outer edge of the junction.

The normalized resonance frequencies, corresponding to the mode spectra shown in Fig. 5.5a, are plotted in Fig. 5.5b versus the angular wave number  $k$ . Evidently, the resonance frequencies depend on both the wave number  $k$  and the width of the idle region of the junction. The slope, i.e. the change of the resonance frequency with the wave number  $k$ , of the curves plotted in Fig. 5.5b is proportional to the voltage separation between individual resonances on the current-voltage characteristics of the junction. As can be seen, the slope of the data is the largest for the junctions with the largest idle region and decreases with decreasing idle size. This is in qualitative agreement with the experimental observations in Fig. 5.2, where large (small) step spacing is observed for large (small) idle regions. These calculated resonance frequencies are used to quantitatively fit the experimental data to the calculated mode spectrum.

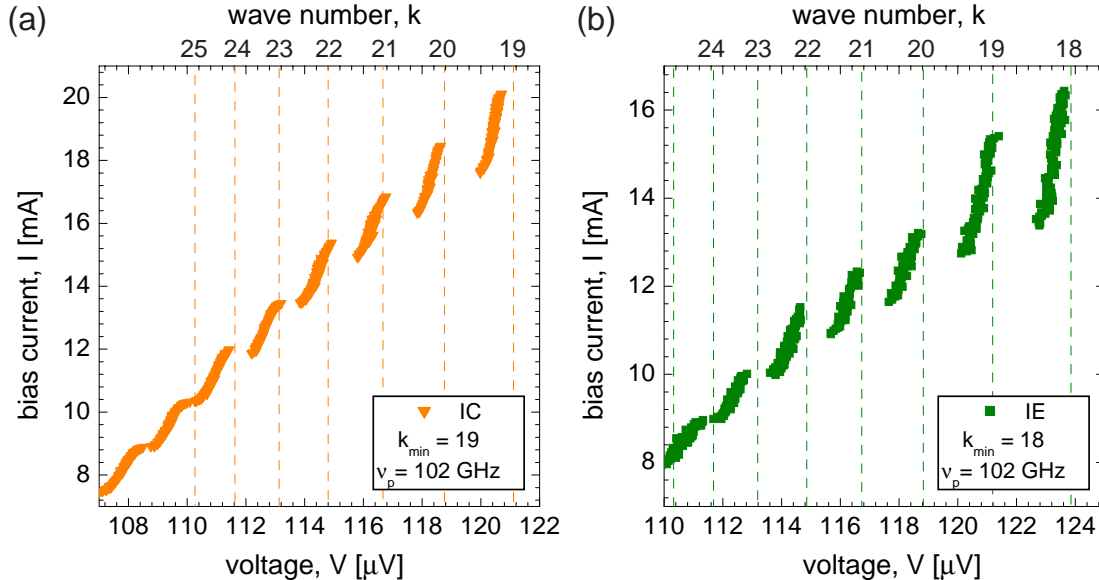


Figure 5.6: Fits to experimental data of junction  $IC$  (a) and junction  $IE$  (b). The calculated resonance frequencies are indicated by vertical dotted lines. The minimum wave number  $k_{\min}$  associated with the highest voltage step and the plasma frequency  $\nu_p = \omega_p/2\pi$  used for the fit are indicated in each plot.



### 5.3.3 Results and discussion

The experimental data are fitted to the calculated resonance frequencies using Eq. (5.14). In the fitting procedure, the plasma frequency  $\omega_p/2\pi$  was chosen such that the absolute voltage of the highest resonance is well approximated. The wave number  $k_{\min}$  was adjusted to fit the sequence of all the resonance steps with a good accuracy. In Fig. 5.6, the experimental data of junctions *IC* and *IE* are compared with the calculated resonance frequencies indicated by vertical dotted lines. For junction *IC* the lowest excited mode number is  $k_{\min} = 19$ , whereas it is  $k_{\min} = 18$  for junction *IE*. The data are fitted consistently with the same plasma frequency  $\omega_p/2\pi \approx 102$  GHz, the value of which is in good agreement with the one evaluated from the critical-current density of the junction. Overall, the agreement between the calculated step positions and the experimental findings is excellent. Here, we point out that the relative accuracy of the fits is better than 1 percent. The remaining uncertainties are due to the effects already discussed in Section 4.7. As for the samples discussed in Chapter 4, we checked the dependence of the fine structure on temperature, number of fluxons and external field. The results pointed out before could be reproduced for these samples.

Finally, we have calculated numerically the current-voltage characteristics and the phase distributions of a junction with a geometry similar to the samples of set I, but without idle region [WFKU00]. Similar calculations but for different junction geometries have also been presented in Section 4.6. The calculated current-voltage characteristic for this sample is shown in Fig. 5.7a. A fine structure is clearly visible. The phase profile of the junction at the highest voltage resonance is plotted in Fig. 5.7b. The wave number of the observed mode is approximately  $k_{\min} = 18$  at the highest resonance, which is in good agreement with the results of the analysis of our experimental data. Of course, the increase of the wave number  $k$  of the excited mode from step to step while reducing the bias current is

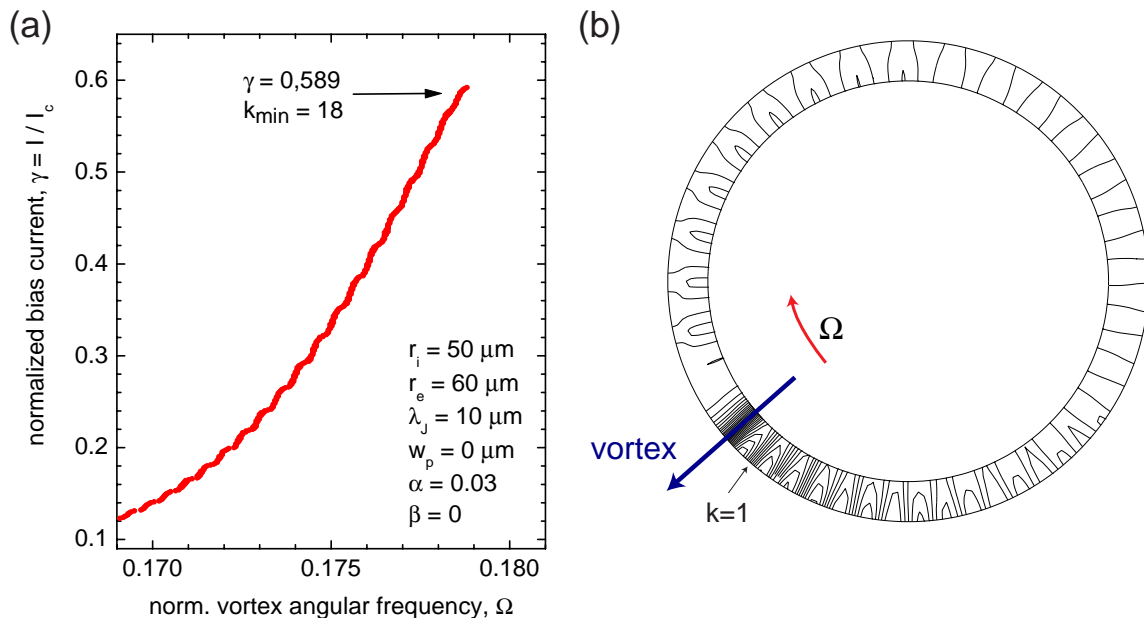


Figure 5.7: (a) Simulated current-voltage characteristic for a bare junction. (b) Phase profile at the bias point indicated in (a). The number of periods in the small amplitude phase modulation corresponds to the wave number  $k_{\min} = 18$ .

also observed in these simulations.

In summary, we have shown that the linear mode spectrum of an annular Josephson junction resonator is determined by both the properties of the junction and the idle region surrounding the junction. The mode spectrum has been sensitively probed by studying its interaction with Josephson vortices moving at relativistic velocities. The dependence of the observed phenomena on the geometry and the electrical properties of the idle region has been interpreted qualitatively. Fitting the experimental data to the theoretically expected mode spectra, we found excellent agreement with an accuracy of better than 1 percent.

In terms of the use of an annular Josephson junction as a source of radiation [KYSV98], we make the important observation that the spectrum of radiation generated by the moving vortex in the junction is tunable by the idle region. Moreover, the idle region may be specifically designed to achieve good impedance matching between the junction and any coupling circuits to enhance the power of the emitted radiation.

## Part III

# CLASSICAL AND QUANTUM PARTICLE PROPERTIES OF JOSEPHSON VORTICES

In the first part of this thesis, I have considered the static and dynamic properties of two-dimensional large area annular Josephson junctions. The observed effects were analyzed and explained in terms of the spatial distribution of the phase difference in the junction and its temporal evolution, describing both the properties of Josephson vortices (non-linear excitations) and plasmons (linear excitations). In this second part, I examine the properties of a Josephson vortex in quasi-one-dimensional long annular Josephson junctions. The dynamics of a Josephson vortex can be described in terms of a particle of effective mass  $m_f$  with a coordinate  $q$  subject to external forces [MS78]. This approach can be used because the Josephson vortex is a topological solitary excitation of the junction, which is stable with respect to small perturbations. In fact the action of small external forces on the vortex, e.g. due to the bias current or external magnetic field, only changes the dynamics of the vortex, not its particle properties. Therefore, the dynamics of a soliton in a sine-Gordon system is well described by perturbation theory [MS78].

Here, I study the dynamics of a Josephson vortex in the presence of a spatially inhomogeneous external force  $F(q)$ , due to the bias current or the magnetic field applied to the junction, or due to different types of spatial inhomogeneities of the junction itself. Equivalently, the vortex can be viewed as a particle of mass  $m_f$  moving in a potential landscape  $U(q)$ , associated with these external forces  $F(q) = -\partial U(q)/\partial q$ . Under certain conditions, the potential  $U(q)$  can form wells in which the vortex is spatially localized if its kinetic energy is less than the depth of the well. Here, I focus on the study of the escape of the vortex from such a potential well. At high temperatures, the vortex is activated from the well due to thermal fluctuations. This process is described by the transition state theory, which considers the transition of a system from one state into another via a potential barrier [HTB90].

Many processes of this type exist in physics, chemistry and biology. The field was pioneered by Kramers, who considered such transitions both in the weak and in the moderate to strong damping regime [Kra40]. A comprehensive review on reaction rate theory including thermal activation processes is published in Ref. [HTB90]. Josephson junctions are interesting experimental systems to investigate thermal activation. In long junctions and arrays of small junctions, the height of the activation barrier, the temperature and the damping can be changed over a wide range, which is an attractive feature for the study of thermal activation. The study of the activation of the phase with particular focus on the transition from discrete to continuous multi-dimensional systems is suggested in Ref. [DMS99]. The multi-dimensional activation of the phase has already been studied for linear long junctions [CTC<sup>+</sup>96]. Here, I consider the Josephson vortex as a collective excitation of an annular

junction. In this limit, its dynamics can be described by a single collective coordinate. In Chapter 6, I investigate experimentally the thermal activation of a vortex from metastable states in potential wells of various physical origins.

In literature, the process of nucleation and annihilation of kinks in a damped sine-Gordon chain, which is a model system for many physical nucleation processes, is actively investigated theoretically and discussed controversially [BL79, BL81, BHL83, Büt89, HMS88, BC95, CB98]. The thermal nucleation of kink–anti-kink pairs may also be studied in long Josephson junctions.

In the limit of zero temperature, the thermal activation process is exponentially suppressed and the Josephson vortex may tunnel through a potential barrier and thus escape quantum mechanically from the well [KI96, SBJM97]. This process corresponds to the macroscopic quantum tunneling of a Josephson vortex. Macroscopic quantum effects in Josephson systems have been studied actively both theoretically and experimentally in the past fifteen years. Initially, the research was inspired by the fundamental question whether quantum mechanics is valid at the macroscopic level or not. The discussion of this issue was largely stimulated by the works of Leggett and Garg [LG85]. The role of the damping, inherent to any physical system, in macroscopic quantum effects was first considered by Caldeira and Leggett [CL81, Leg84, LCD<sup>+</sup>87]. This work has substantially advanced the understanding of these phenomena.

Experimentally, macroscopic quantum effects have been investigated in detail in superconducting Josephson junctions and their circuits. The electronic and electromagnetic properties of a Josephson junction are governed by the phase difference  $\phi$  between the macroscopic wave functions of the junction electrodes. It has been shown both in a phenomenological approach [CL81, Cal83] and from microscopic theory [AES82, ESA84, SZ90] that the quantum mechanics of the charge carriers and the electromagnetic fields in the junction can be accurately described in terms of the collective variable  $\phi$ . In the limit of low damping and small thermal fluctuations, the quantum effects of the phase  $\phi$  are observed for suitable system parameters [SZ90]. Quantum effects in Josephson junctions are considered as being macroscopic because a large number of electrons and field quanta contribute to the effects described by the collective variable  $\phi$ .

A large number of experiments, proving the quantum properties of the phase, have been successfully performed. Macroscopic quantum tunneling (MQT) has been studied in current biased Josephson junctions [DMC85, MDC87] and rf-SQUIDS [SSAL85, HRL96, RHL95]. Also, macroscopic energy level quantization (ELQ) has been examined experimentally both below [MDC87] and above [SPRR97] the cross-over temperature. Experiments observing the collective quantum transport of vortices in arrays of small Josephson junctions have been successfully performed, including the observation of quantum localization [OVM96, vOM96] and of the Aharonov-Casher effect<sup>4</sup> [EWSM93]. The quantum properties of single Josephson vortices in continuous long Josephson junctions have been predicted theoretically, but not observed experimentally until now. Besides the observation of quantum tunneling [KI96, SBJM97], a number of other quantum effects like interference, dephasing and resonant tunneling have been discussed theoretically in literature [SHVBJ95, HSBJ95, SBJM97]. In Chapter 7, I discuss the state of our experimental efforts to observe quantum properties of Josephson vortices. I investigate the possibilities to examine macroscopic quantum tunneling from two types of potentials, a microresistor [KI96]

---

<sup>4</sup>The interpretation of this particular experiment in terms of the Aharonov-Casher effect is still adversely discussed.

and a magnetic-field induced well, and compare the two cases. Moreover, the possibility of observing the quantization of the energy levels of the vortex in the potential well are discussed. Possible experimental methods to observe ELQ, including the irradiation of the junction with microwaves and the generation of a non-equilibrium thermal distribution in the potential well, are discussed.

In the past fifteen years, large efforts have been made to experimentally discover the theoretically predicted macroscopic quantum coherence (MQC) [LG85] in rf-SQUIDS. Currently, there are promising new experiments searching for MQC in similar systems [CCC<sup>+</sup>99, BHF97, MOL<sup>+</sup>99, OMT<sup>+</sup>99]. Only during the past few months first indications of macroscopic quantum coherence in systems, the dynamics of which is governed by the superconducting phase, have emerged [FPC<sup>+</sup>00]. In the charge regime, it has recently been shown experimentally that coherent quantum effects can be observed in superconducting circuits. In this regime, the dynamics of the system is determined by the number of charges on the superconducting electrodes rather than by the phase difference between them. In the first successful experiment of its type, the Rabi-oscillations of a Cooper pair, tunneling onto and off a superconducting electron box embedded in a mesoscopic circuit of Josephson junctions, have been observed [NPT99]. This effect is considered a macroscopic quantum effect - even though only a single Cooper pair is involved in the process - because the macroscopic wave function describing the system is modified due to the addition of a single extra Cooper pair.

Recently, the research in coherent effects in solid state systems has gained additional momentum, due to the new and exciting prospects of using quantum coherent systems for information processing in quantum computers [Llo93, DiV95b]. In Chapter 8, I discuss our proposal [WKL<sup>+</sup>00] to use a heart-shaped Josephson junction subject to an external magnetic field as a macroscopic two-state system which, in the quantum limit, can serve as a qubit for quantum information processing.

# Chapter 6

## Thermal Activation of Josephson Vortices

Experiments indicating the thermal activation of a Josephson vortex from a potential well are reported. We consider a pinning potential induced by the magnetic dipole interaction between a vortex and an external magnetic field or by a microresistor embedded in the junction barrier. The thermal activation process of the vortex is characterized by measuring the distribution of the depinning currents. The measured current distributions are in good agreement with the theory of thermal activation.<sup>1</sup>

The dynamics of a small Josephson junction is described by a single macroscopic variable, which is the phase difference across the junction. Its dynamic equation is formally equivalent to the equation of motion of a driven and damped particle in a sinusoidal potential. Applying a bias current to the junction, metastable states of the phase are formed. The phase can escape both by thermal activation and by quantum tunneling from these states. The escape of the phase is associated with the switching of the junction from a zero-voltage state to a finite-voltage state, which allows the experimental investigation of this process.

In a long Josephson junction, the phase difference across the junction has a spatial dependence which allows the existence of particle-like collective excitations, i.e. Josephson vortices. In this chapter, I investigate the thermal activation of Josephson vortices from pinning potentials of different physical origins. In Section 6.1, I introduce the concept of thermal activation and then briefly consider the thermal activation of the phase in a small Josephson junction and relate it to the activation of a Josephson vortex in a long junction. Different physical realizations of pinning potentials for the vortex are thoroughly analyzed in Section 6.2. The experimental techniques and the measurement setup developed to

---

<sup>1</sup>Parts of this chapter have been published in ‘Journal of Low Temperature Physics **118**, 543 (2000)’ and in ‘Physica B **284-288**, 585 (2000)’.

perform activation measurements of Josephson vortices are discussed in Section 6.3. The experimental results are presented in Section 6.4. Finally, the results are summarized and a conclusion is presented in Section 6.5.

## 6.1 Introduction

In physics, chemistry and biology, there are a large variety of different processes in which a system makes a transition between two distinct states by traversing a potential barrier. In many of these processes, thermal fluctuations govern the rate at which the system overcomes the barrier. The theory of these processes has been actively developed since the days of Arrhenius [Arr89] with important results found by Kramers [Kra40]. The state of the art of thermal activation and transition state theory is presented in a recent review by Hänggi *et al.* [HTB90].

### 6.1.1 Fundamentals of thermal activation

If the dynamics of a physical system can be described by a generalized coordinate  $q$ , its thermal activation can be modeled in terms of a particle of effective mass  $m$  moving in an external potential  $U(q)$  with a metastable minimum, see Fig. 6.1a. In the classical regime and at zero temperature, the particle cannot escape from the potential, even for an arbitrarily small potential barrier  $U_0$ . However, in the presence of thermal fluctuations it can be activated across a potential barrier of finite height. At low temperatures and low damping, the particle may also escape from the well by quantum tunneling, provided that the potential barrier is small enough. This case is considered in Chapter 7. At sufficiently high temperatures, the particle escapes predominantly from the well due to thermal processes and quantum processes only lead to negligibly small corrections. This situation is considered in detail in this chapter.

In the following, we consider a particle in the local minimum of the potential depicted in Fig. 6.1a. The properties of the potential can be characterized by the height of the potential barrier  $U_0$ , by its curvature ( $\partial^2 U / \partial q^2 = U''$ ) at the bottom of the well, which determines the *small amplitude oscillation frequency*

$$\omega_0 = \sqrt{\frac{U''(0)}{m}}, \quad (6.1)$$

and by the curvature of the top of the barrier

$$\omega_b = \sqrt{-\frac{U''(q_b)}{m}}, \quad (6.2)$$

which parameterizes the width of the potential hindering the decay process.  $\omega_b$  is also called the *unstable barrier frequency* [Wei99]. We consider the case that  $U_0$  is larger than the thermal energy  $k_b T$  and  $\hbar \omega_0 \ll U_0$ . In particular, we are interested in situations, where the potential  $U(q)$  is smaller than  $U(0)$  for all values of  $q > q_{\text{ex}}$ , where  $q_{\text{ex}}$  is the exit point of the particle from the potential well, see Fig. 6.1b. In this regime the escape rate of a particle from a metastable potential well can be parameterized in the form

$$\Gamma = A \exp(-B), \quad (6.3)$$

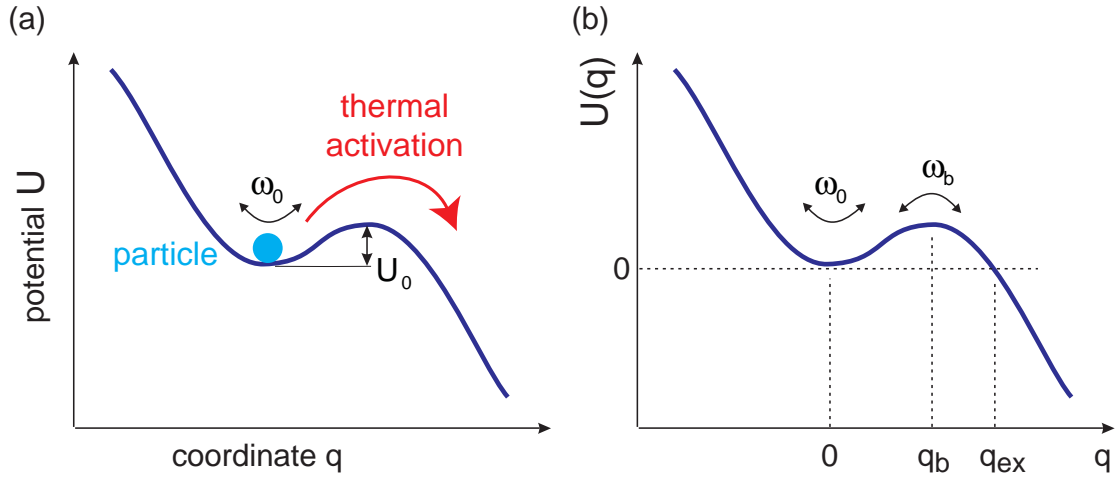


Figure 6.1: (a) A particle of mass  $m$  localized at the bottom of the metastable potential well of depth  $U_0$ . The small amplitude oscillation frequency  $\omega_0$  is proportional to the square-root of the curvature of  $U(q)$  at  $q = 0$ . The particle escapes from the well by a thermally activated process. (b) Potential  $U(q)$ , with minimum at  $q = 0$ , maximum at  $q = q_b$ , and exit point at  $q = q_{ex}$ .  $\omega_b$  characterizes the width of the potential.

where  $B$  is a dimensionless measure for the massiveness of the barrier and  $A$  characterizes the attempt frequency of the particle towards the barrier.

At high temperatures, i.e. sufficiently large thermal fluctuations, a particle trapped in the potential well can escape from the well by a thermally activated process. The rate of the process depends on the temperature  $T$ , the barrier height  $U_0$  and the damping  $a$ . From transition state theory [HTB90], we know that the rate of thermal escape from the well is given by

$$\Gamma_{\text{th}}^{TST} = \frac{\omega_0}{2\pi} \exp\left(-\frac{U_0}{k_b T}\right). \quad (6.4)$$

Equation (6.4), being similar to the Arrhenius law, is found under the assumption that the particle in the potential well is in thermal equilibrium and that a particle which once has crossed the barrier top never falls back into the well (no diffusion). The form of Eq. (6.4) can be understood considering the exponential decrease of the density of thermal states in the well with increasing energy. The factor  $\exp(-U_0/k_b T)$  reflects the fraction of states which, at thermal equilibrium, are at an energy higher than the potential barrier height  $U_0$ . This is also the reason why Eq. (6.4) is independent of the barrier width.

### Damping regimes

In his classical work, Kramers considered the effect of frequency-independent damping on the thermal escape [Kra40]. The escape of a particle from the well in the presence of damping  $a$  is determined by a Langevin equation

$$m\ddot{q} + ma\dot{q} + U'(q) = \xi(t), \quad (6.5)$$

where  $\xi(t)$  is the  $\delta$ -correlated Gaussian white noise associated with a thermal reservoir at temperature  $T$ . Considering a steady flux of thermalized particles from the well, the escape



rate in the *moderate to strong damping* regime is found to be

$$\Gamma_{\text{th}} = \rho_a \frac{\omega_0}{2\pi} \exp\left(-\frac{U_0}{k_b T}\right), \quad (6.6)$$

where  $\rho_a$  is the friction dependent transmission coefficient of the barrier

$$\rho_a = \sqrt{1 + \left(\frac{a}{2\omega_b}\right)^2} - \frac{a}{2\omega_b}. \quad (6.7)$$

In the limit  $a \rightarrow 0$ , the transition state theory result is recovered. In the limit of *strong damping*, the inertia term in the Langevin equation (6.5) can be neglected and the transmission coefficient is found as

$$\rho_a = \frac{\omega_b}{a}. \quad (6.8)$$

In the limit of very *weak damping*, the thermal population of the well is depleted in the range of  $k_b T$  below the top of the barrier because particles decay quicker from that region than they are resupplied due to thermalization. This effect gives rise to a reduced escape rate at low damping with the transmission coefficient

$$\rho_a = \frac{aI}{k_b T} \frac{\omega_0}{2\pi}, \quad (6.9)$$

where  $I$  is a numerical value depending on the particular potential under consideration; for a cubic potential,  $I = 36U_0/5\omega_0$ . Using these results, it is found [Wei99] that the escape process is well described by Kramers formula according to Eqs. (6.6) and (6.7) if

$$\frac{a}{\omega_b} \geq \frac{5k_b T}{36U_0}. \quad (6.10)$$

In the following, the thermal activation of the phase in a small Josephson junction and the thermal activation of a vortex are considered.

### 6.1.2 Activation of the phase in a small junction

In the Stewart-McCumber equivalent circuit model [Ste68, McC68], the electrostatics of a small junction is described by an equation of motion for the phase  $\phi$ , see Chapter 1. Eq. (1.16) can be rewritten in the form

$$C \left(\frac{\Phi_0}{2\pi}\right)^2 \ddot{\phi} + \frac{1}{R} \left(\frac{\Phi_0}{2\pi}\right)^2 \dot{\phi} + I_c \frac{\Phi_0}{2\pi} \sin(\phi) - I \frac{\Phi_0}{2\pi} = 0. \quad (6.11)$$

This is equivalent to the equation of motion

$$m_\phi \ddot{\phi} + m_\phi \frac{1}{RC} \dot{\phi} + \frac{\partial U^\phi(\phi)}{\partial \phi} = 0 \quad (6.12)$$

of a particle of mass  $m_\phi = C(\Phi_0/2\pi)^2$  moving in the presence of damping ( $1/RC$ ) along the generalized coordinate  $\phi$  in the potential

$$U^\phi(\phi) = \frac{I_c \Phi_0}{2\pi} \left(-\frac{I}{I_c} \phi - \cos(\phi)\right) \quad (6.13)$$

$$= E_J(-\gamma\phi - \cos(\phi)), \quad (6.14)$$

where  $E_J = \Phi_0 I_c / 2\pi$  is the Josephson coupling energy and  $\gamma = I/I_c$  is the normalized bias current, see for example Ref. [FD74]. The potential (6.14) is called a *washboard potential*. At zero bias current, the potential is sinusoidal. Increasing the bias current, the potential is tilted proportional to  $I$  and metastable wells are formed. At the current  $I = I_c$ , the metastable well vanishes, see for example Ref. [MDC87].

At a fixed bias current  $\gamma$ , the rate at which the phase  $\phi$  is activated from the potential well depends on the small amplitude oscillation frequency  $\omega_0^\phi$  and the barrier height  $U_0^\phi$ . The small amplitude oscillation frequency

$$\omega_0^\phi = \sqrt{U''^\phi(\phi_0)/m_\phi} = \omega_p (1 - \gamma^2)^{1/4} \quad (6.15)$$

is related to the mass  $m_\phi$  and the curvature  $U''^\phi(\phi_0)$  of the potential well at its minimum located at

$$\phi_0 = \arcsin(\gamma). \quad (6.16)$$

The potential barrier height is found by calculating

$$U_0^\phi = U^\phi(\phi_b) - U^\phi(\phi_0) = 2E_J \left[ \sqrt{1 - \gamma^2} - \gamma \arccos(\gamma) \right], \quad (6.17)$$

where the coordinate of the maximum of the potential is given by

$$\phi_b = \pi - \arcsin(\gamma). \quad (6.18)$$

Considering the typical experimental situation for which  $E_J \gg k_b T$ , thermal activation is important only for bias currents  $I$  close to the critical current  $I_c$ , or equivalently for  $\gamma \rightarrow 1$ . Thus,  $U_0^\phi$  can be approximated as

$$U_0^\phi = E_J \frac{4\sqrt{2}}{3} (1 - \gamma)^{3/2} + \mathcal{O}(1 - \gamma)^{5/2}. \quad (6.19)$$

Sometimes the cubic expansion

$$U^\phi(\phi) = E_J \left( \frac{1}{2} \sqrt{1 - \gamma^2} \phi^2 - \frac{1}{6} \gamma \phi^3 \right) \quad (6.20)$$

of Eq. (6.14) is used. We note that Eq. (6.20) is of the form

$$U^\phi(\phi) = \frac{1}{2} m_\phi \omega_0^{\phi 2} \phi^2 - \text{const.} \phi^3, \quad (6.21)$$

where the constant is proportional to the barrier height. In this approximation the height of the potential barrier is found by evaluating Eq. (6.20) at the maximum  $\phi_b$

$$U_0^\phi = E_J \frac{2}{3} \frac{(1 - \gamma^2)^{2/3}}{\gamma^2}. \quad (6.22)$$

In Fig. 6.2, the bias current dependence of the approximations (6.19) and (6.22) are compared with the exact barrier height (6.17). For  $\gamma$  close to unity, both expressions are close to the exact value. For smaller values of  $\gamma$  however, Eq. (6.19) approximates the exact barrier height more accurately.

The third order expansion of the potential around its minimum is a useful approximation for rate calculations in both the thermal and the quantum regime because, for the relevant

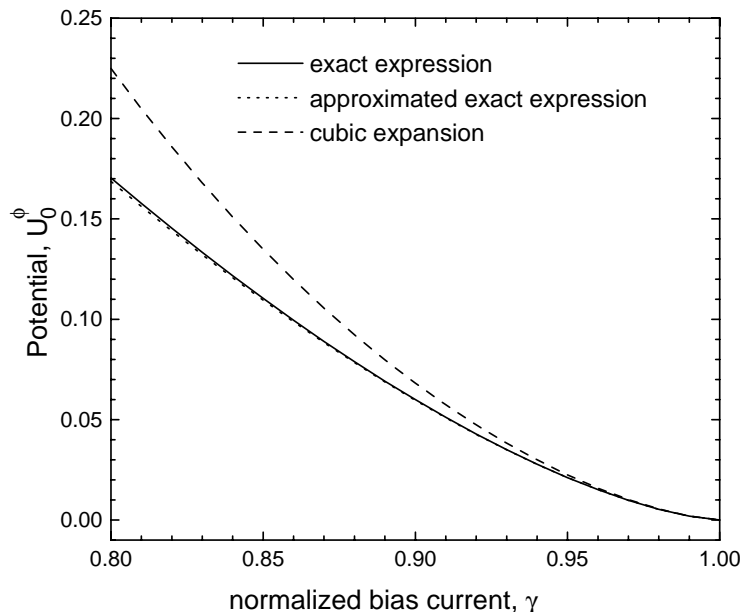


Figure 6.2: Comparison of exact potential barrier height (6.17) [solid line] with the cubic approximation (6.22) [dashed line] and the linearized exact expression (6.19) [dotted line] for  $E_J = 1$ .

junction parameters (see Section 6.2.3), the activation rate is only large for  $\gamma$  very close to unity. Furthermore, in the cubic approximation, the potential is symmetric in the sense that  $\omega_0 = \omega_b$ , which simplifies its analysis.

The thermal activation of the phase in a small junction has been investigated experimentally by measuring the statistics of the switching currents [FD74]. Using the model described above, the experimental data can be accurately explained.

### 6.1.3 Activation of a vortex in a long junction

As pointed out in Chapter 2, a long Josephson junction can be modeled by a parallel connection of small Josephson junctions which are inductively and resistively coupled to one another, see Fig. 2.1. If the activation of the phase in a long junction is to be investigated, the spatial dependence  $\phi(x)$  has to be considered explicitly. For a junction in zero external field and without trapped vortices, the activation of the phase is similar to the one for a small junction. To qualitatively understand the important effects, we consider a parallel connection of five junctions, see Fig. 6.3b. The thermal fluctuations act on each individual phase of the system independently. However, the junctions are coupled inductively to each other. The strength of the coupling is inversely proportional to the separation between individual junctions, to the specific inductance linking the junctions and to the critical-current density. If the junctions are coupled strongly via a small inductance, the phases can overcome the potential barrier only simultaneously. The exact dynamics of the phase in the process of activation depends strongly on the coupling and the damping. In short systems with only a few junctions coupled in parallel, the edges may also play an important role. Activation processes in such systems have been recently investigated theoretically in Refs. [DMS99, DMS00]. The case of only two coupled junctions has also been investigated experimentally [HLL89]. In the limit of a continuous long Josephson junction, the coupling of the phases in the lateral direction is strong. The phase is activated effectively as a rigid string if the energy required to form a kink in the phase is larger than its activation energy, see Fig. 6.3c. The activation of the phase in a linear long Josephson junction has been investigated in dependence on the external field both theoretically and experimentally in

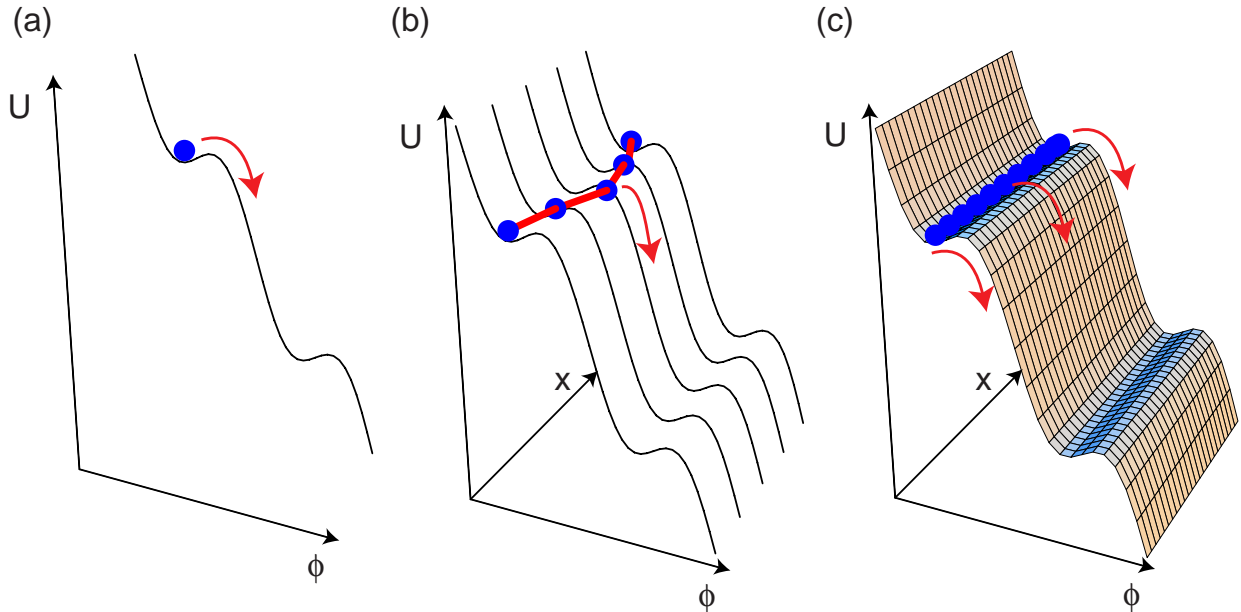


Figure 6.3: (a) Effective potential  $U(\phi)$  for the phase in a small junction. The stable coordinate of the phase is indicated by a solid disc. (b) Potential of the phase in five inductively coupled Josephson junctions. The coupling (acting like springs) between the phases is indicated by the thick lines interconnecting neighboring phases. (c) Effective potential  $U(\phi, x)$  for a long junction. The phase is rigidly coupled.

Ref. [CTC<sup>+</sup>96].

Here, I investigate the thermal activation of a Josephson vortex trapped in an annular junction. A Josephson vortex corresponds to a kink of  $2\pi$  in the phase difference along the junction. In zero external field and at zero bias current, the potential energy of such a kink can be visualized as shown in Fig. 6.4a. In one half of the junction, the phase is localized in the potential minimum at  $\phi = 0$ , whereas in the other half of the junction the phase is localized at  $\phi = 2\pi$ . The rest energy of this excitation corresponds to the integral of  $U(\phi, x)$  along the vortex line  $\phi(x)$ . The dynamics of the vortex in an ideal and uniform quasi-one-dimensional annular junction is governed by the perturbed sine-Gordon equation (2.19) with the periodic boundary conditions (2.45). The Josephson vortex

$$\phi_f(\tilde{x}, \tilde{t}) = 4 \arctan \left[ \exp \left( \frac{\tilde{x} - q(\tilde{t})}{\sqrt{1 - u^2}} \right) \right] \quad (6.23)$$

behaves as a topologically stable, particle-like object of mass  $\tilde{m}_f$  and coordinate  $q(\tilde{t})$  moving at a velocity  $u = \dot{q}$  under the action of external forces, see Section 2.1.1. The external forces acting on a vortex in a *homogeneous* junction are modeled by the usual perturbation terms in the sine-Gordon equation (2.19). Any other forces (e.g. due to an applied magnetic field) can be cast in form of an additional general space and time dependent perturbation  $f(\tilde{x}, \tilde{t})$ .

Using perturbation theory [MS78], the vortex dynamics can be described in terms of an equation of motion for its center of mass coordinate  $q(\tilde{t})$ , as pointed out already in Section 2.1. Considering small vortex velocities, i.e. the non-relativistic limit ( $u = \dot{q} \ll 1$ ), the equation of motion (2.38) has the simple form

$$\tilde{m}_f \ddot{q} + \tilde{m}_f a \dot{q} + \frac{\partial \tilde{U}(q)}{\partial q} = 0, \quad (6.24)$$

where the bias current is considered as an external potential and the two dissipative terms in Eq. (2.38) are taken into account by a single effective term proportional to  $a = \alpha + \beta/3$ . Equation (6.24) describes the damped motion of a particle of effective mass  $\tilde{m}_f$  in the external potential  $\tilde{U}(q)$ .

The energy of a vortex in a Josephson junction is determined by the hamiltonian (2.29), where  $\tilde{\mathcal{H}}^{\text{SG}}$  is the pure sine-Gordon part and  $\tilde{\mathcal{H}}^P$  describes the energy of the perturbations. In the static case ( $\dot{q} = 0$ ), the rest energy of the vortex is  $\tilde{\mathcal{H}}_f^{\text{SG}} = 8$  which is equivalent to the normalized rest mass of the vortex  $\tilde{m}_f = 8$ . The energy of the vortex in SI units can be found by multiplying all energies calculated in normalized units by the natural energy scale of the long junction  $\mathcal{E}_0$ , see Eq. (2.27).  $\mathcal{E}_0$  corresponds to the Josephson coupling energy of the junction in the area  $\lambda_J w$ . Thus the rest energy of the vortex in SI units is given by

$$\mathcal{H}_f^{\text{SG}} = 8\mathcal{E}_0, \quad (6.25)$$

and hence its rest mass is

$$m_f = \frac{8\mathcal{E}_0}{c_0^2}, \quad (6.26)$$

where  $c_0 = \lambda_J \omega_p$  is the Swihart velocity. Typical scales for the energy  $\mathcal{E}_0$  and the mass  $m_f$  of the vortex in an experimental situation are discussed in Section 6.2.3.

Any external force acting on the vortex can be expressed in terms of the potential  $\tilde{U}(q)$ . For example, the energy gain of the junction due to the bias current is calculated using the perturbation hamiltonian

$$\tilde{\mathcal{H}}^\gamma = - \int_0^\ell \gamma \phi d\tilde{x}. \quad (6.27)$$

Substituting the vortex solution (6.23) into Eq. (6.27) we find the equation for the contribution of the bias current to the potential energy of the vortex in dependence on its coordinate  $q$

$$\tilde{U}^\gamma(q) = -2\pi\gamma q. \quad (6.28)$$

Any other spatially inhomogeneous perturbation described by  $f(\tilde{x})$  induces a force on the vortex and results in a pinning of the vortex in space which can be of different physical origins. A pinning center for a Josephson vortex in a long junction can be realized by introducing a microshort [MS78] or a microresistor [GF84, MU90] in the junction barrier. Pinning may also occur due to the interaction of the vortex with the junction leads [MDP<sup>+</sup>98] or its interaction with parasitic magnetic flux trapped in the superconducting films. Alternatively, a vortex can be pinned by its magnetic dipole interaction with an external magnetic field [GJLS91a, UMT97]. Here, we solely consider the microresistor (or microshort) and the magnetic dipole interaction as the origin of the pinning.

Thus, a combination of the potential due to the bias current and any other pinning potential allows for the existence of metastable vortex states in the junction. The activation of the vortex from these states is observable experimentally. The potential energy of the vortex due to different types of spatial inhomogeneities  $f(\tilde{x})$  is calculated and discussed in detail in Section 6.2.

## 6.2 Vortex pinning potentials

The thermal activation rate of a Josephson vortex from a metastable state in a potential depends sensitively on the potential barrier height  $U_0$  and the characteristic oscillation

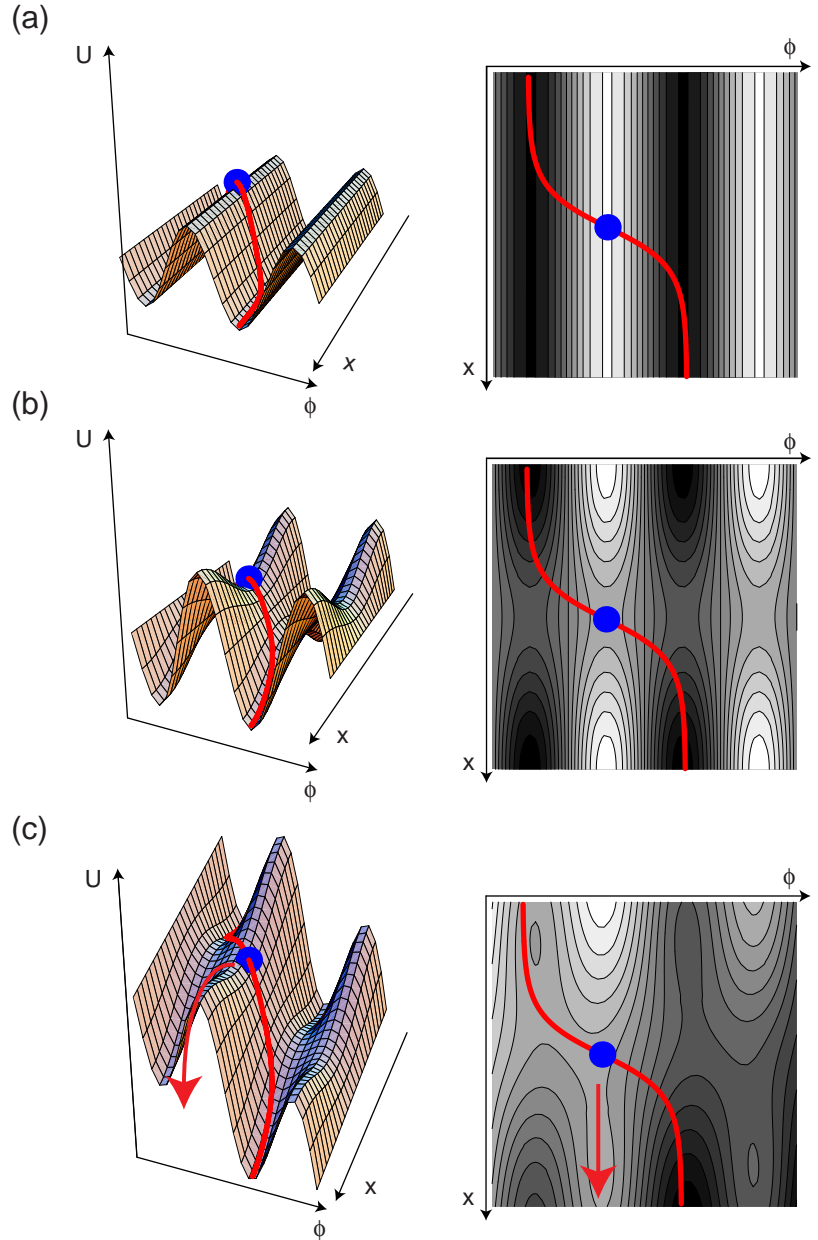


Figure 6.4: (a) Potential energy profile  $U(\phi, x)$  of a long Josephson junction in zero field and without applied bias current, left. A contour plot of the same potential is shown on the right, white corresponds to high energy, black to low energy. A vortex trapped in the junction is indicated by the thick line. The center of mass coordinate of the vortex is indicated by a solid disc. (b) Potential energy in the presence of a periodic magnetic field. (c) Potential energy in the presence of a magnetic field and a bias current  $\bar{\gamma}$  close to unity.

frequencies  $\omega_0$  and  $\omega_b$ . In this section, I discuss properties of vortex potentials induced by an in-plane external magnetic field and a microresistor in combination with a bias current homogeneously applied to the junction. A sketch of a typical annular junction as used in experiment is shown in Fig. 6.5.

### 6.2.1 Magnetic-field induced potential

In Section 2.1.1, we derived the sine-Gordon equation of a linear junction in a homogeneous external field  $H$  and found that the magnetic field drops out of the equation ( $\partial H/\partial x = 0$ ), but determines the boundary conditions. In the case of an annular junction, the magnetic field is effectively space-dependent

$$\frac{\partial H}{\partial x} = \frac{\partial}{\partial x} H \cos\left(\frac{2\pi x}{l}\right) = -H \frac{2\pi}{l} \sin\left(\frac{2\pi x}{l}\right), \quad (6.29)$$

where  $l$  is the circumference of the junction. Here, the coordinate  $x$  is measured counterclockwise around the annular junction with  $x = 0 = l$  at the point where the magnetic field points in the same direction as the outward normal on the junction circumference (see Fig. 6.5b). Reconsidering Eq. (2.5) we find the additional term

$$-H \frac{\mu_0 \Lambda}{L^*} \frac{2\pi}{l} \sin\left(\frac{2\pi x}{l}\right) \quad (6.30)$$

on the right hand side of the sine-Gordon equation (2.6). Rewriting the sine-Gordon equation as done in Section 2.1.1, we can express the magnetic field dependent perturbation term in Eq. (2.15) as

$$f^h(x) = -\frac{2\pi}{\Phi_0} H \mu_0 \Lambda \lambda_J^2 \frac{2\pi}{l} \sin\left(\frac{2\pi x}{l}\right) \quad (6.31)$$

or in normalized units

$$f^h(\tilde{x}) = -h \Delta \frac{2\pi}{\ell} \sin\left(\frac{2\pi \tilde{x}}{\ell}\right), \quad (6.32)$$

with the normalized junction circumference  $\ell = l/\lambda_J$ , and the normalized magnetic field  $h = H/H_0$ , where

$$H_0 = \frac{\Phi_0}{2\pi \mu_0 \Lambda \lambda_J}. \quad (6.33)$$

We have introduced the arbitrary coefficient  $\Delta$  into Eq. (6.32) as a geometry dependent magnetic field coupling coefficient [MM96a], to take into account deviations in the effective field, e.g. due to field focusing or similar effects. From the structure of Eq. (6.32), we see that, in the sine-Gordon equation, the magnetic field interaction has the character of a spatially modulated bias current, the amplitude of which is proportional to the external field. The same result, but with an ambiguous field normalization, has been derived before in Refs. [GJLS91a, MM96a].<sup>2</sup>

According to the lagrangian formalism discussed in Section 2.1.2, it is easy to see the the potential due to the magnetic field  $\tilde{U}^h$  is of the form

$$\tilde{U}^h = \int_0^\ell \phi_{\tilde{x}} \Delta h \cos\left(\frac{2\pi \tilde{x}}{\ell}\right) d\tilde{x}. \quad (6.34)$$

This magnetic-field induced potential in the presence of a trapped vortex is illustrated in Fig. 6.4b in the limit of  $\ell \gg 1$ . The magnetic field induces a modulation of the potential energy of the vortex in dependence on the coordinate  $x$  along the junction. At zero bias current, the vortex center of mass coordinate is at the minimum of the potential energy. Substituting the vortex solution  $\phi_f$  into Eq. (6.34) and integrating, we find in the limit of  $\ell \gg 1$

$$\tilde{U}^h(q) = -2\pi \operatorname{sech}\left(\frac{\pi^2}{\ell}\right) \Delta h \cos\left(\frac{2\pi q}{\ell}\right), \quad (6.35)$$

which is the potential energy  $\tilde{U}^h = -\vec{\mu} \cdot \vec{h}$  of the effective normalized magnetic moment of the vortex  $|\vec{\mu}| = 2\pi \operatorname{sech}(\pi^2/\ell)$  in the normalized external magnetic field  $\vec{h}$ , see Fig. 6.5b. The factor  $\operatorname{sech}(\pi^2/\ell)$  describes the spread of the magnetic moment in space. In the limit

---

<sup>2</sup>Here we note that the characteristic field  $H_0$  is inversely proportional to  $\lambda_J$  instead of  $r_e$  as in Chapter 3, where a small junction was assumed. The different cases remind of the difference in the first critical field of a long and a short linear junction.

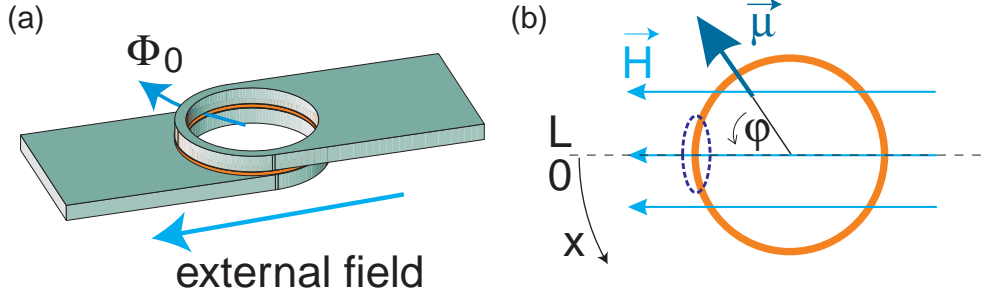


Figure 6.5: (a) External magnetic field applied in the plane of the annular Josephson junction. (b) Dipole interaction between the external magnetic field and the magnetic moment associated with the vortex.

of  $\lambda_J \rightarrow 0$  (or equivalently  $\ell \rightarrow \infty$ ), the magnetic moment of the vortex is effectively local and given by  $|\vec{\mu}| = 2\pi$ .

Thus, the normalized potential of a vortex in an annular junction in the presence of a bias current and an in-plane external homogeneous field is given by

$$\tilde{U}^{\gamma h}(q) = \tilde{U}^\gamma + \tilde{U}^h = -2\pi\gamma q - 2\pi \operatorname{sech}\left(\frac{\pi^2}{\ell}\right) \Delta h \cos\left(\frac{2\pi q}{\ell}\right). \quad (6.36)$$

This potential is plotted in Fig. 6.4c. The applied bias current tilts the potential both in the direction of  $\phi$  and in the direction of  $x$ . The energy profile is plotted for a bias current close to the critical one. It can be seen that the vortex can now be activated from the magnetic-field induced well by thermal fluctuations, resulting in a propagation of the vortex along the  $x$ -direction. For the purpose of the following analysis it is convenient to introduce the normalizations

$$\bar{q} = 2\pi q/\ell, \quad (6.37)$$

$$\bar{h} = 2\pi \operatorname{sech}\left(\frac{\pi^2}{\ell}\right) \Delta h, \quad (6.38)$$

for the vortex coordinate  $q$  and the magnetic field  $h$ , resulting in a simplified expression for Eq. (6.36)

$$\tilde{U}^{\gamma h}(\bar{q}) = -\ell\gamma\bar{q} - \bar{h} \cos(\bar{q}). \quad (6.39)$$

The characteristic terms of the potential (6.39) are the  $\cos \bar{q}$ -like oscillating term proportional to the external field and periodic in the circumference and the term proportional to the bias current and linear in the coordinate. This type of potential is known as the washboard potential, see Sec.6.1.2. In the range of  $\gamma < \gamma_c^h$ , the potential has distinct minima and maxima. At the critical bias<sup>3</sup>

$$\gamma_c^h = \frac{\bar{h}}{\ell} \quad (6.40)$$

the potential has a set of saddle points. For  $\gamma > \gamma_c^h$ , these disappear and the potential decreases monotonically with  $\bar{q}$ . The coefficient of the linear term in Eq. (6.39) can be expressed in terms of  $\gamma_c$  and we can rewrite Eq. (6.39) as

$$\tilde{U}^{\gamma h}(\bar{q}) = \bar{h} (-\bar{\gamma}\bar{q} - \cos(\bar{q})), \quad (6.41)$$

<sup>3</sup>The critical bias can be found by solving  $U'(\bar{q}) = 0$  and finding the condition at which no solutions to this equation exist.



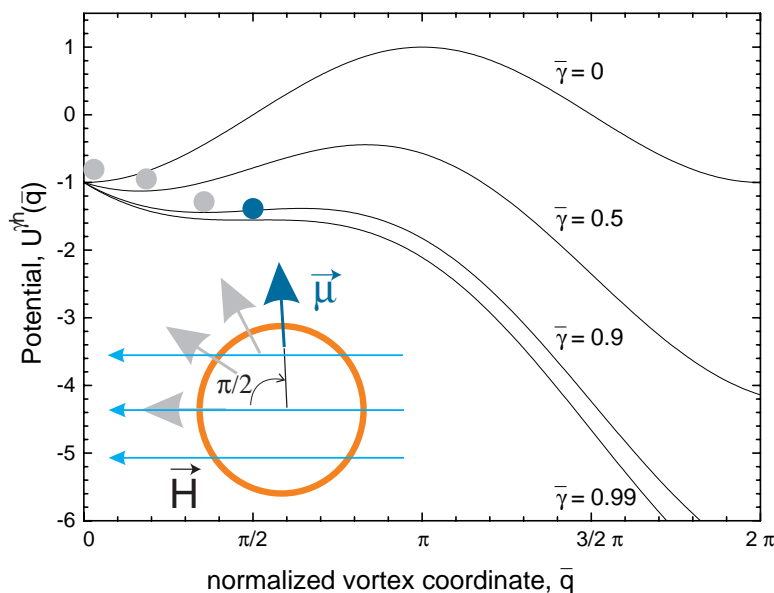


Figure 6.6: Potential  $\tilde{U}^{\gamma^h}(\bar{q})$  (6.41) for  $\bar{h} = 1$  and  $\bar{\gamma} = 0, 0.5, 0.9, 0.99$ . The minimum of the potential (i.e. the lowest energy position of the vortex) is indicated by a solid circle. In the inset, the position of the vortex with respect to the external field is shown for the different values of  $\bar{\gamma}$ .

where the bias current is now expressed relative to the critical bias  $\gamma_c^h$  as

$$\bar{\gamma} = \gamma / \gamma_c^h. \quad (6.42)$$

In Eq. (6.41),  $\bar{h}$  corresponds to the normalized interaction energy between the vortex and the external magnetic field. The potential (6.41) is plotted in Fig. 6.6 for  $\bar{h} = 1$  and  $\bar{\gamma} = 0, 0.5, 0.9, 0.99$ . As the bias current is increased from  $\bar{\gamma} = 0$ , we observe that the washboard potential is tilted proportionally to  $\bar{\gamma}$ . At the same time, the position of the minimum in the potential shifts from the position where the magnetic moment of the vortex is aligned with the field to the position where it is perpendicular to the external field  $\bar{\gamma} = 1$ . For  $\bar{\gamma} \geq 1$ , the vortex is depinned and rolls down the potential surface.

We note that the equation of motion for the center of mass coordinate  $\bar{q}$  of a vortex in an annular junction subject to an in-plane external field is identical to the dynamic equation of the phase  $\phi$  in a small Josephson junction [GJLS91b, UMT97].

### Characteristic properties of the potential

In order to calculate the thermal activation rate (6.6) of the vortex from the magnetic-field induced potential (6.41), the oscillation frequency  $\omega_0$  at the bottom of the well and the barrier height  $U_0$  need to be determined in dependence on the bias current.

As pointed out before, the dynamics of the phase  $\phi$  in a small junction and the dynamics of a Josephson vortex described by the coordinate  $\bar{q}$  in a long annular junction subject to an external magnetic field are formally equivalent. Thus, we can establish a mapping between the two different physical systems. The characteristic features of the two potentials are compared in Table 6.1. As a result, one can use the theoretical results obtained before for small junctions to analyze the thermal activation of a vortex in the long junction case.

Table 6.1: Mapping between a vortex in a magnetic-field induced potential and the potential for the phase in a small junction.

quantity	vortex	phase
generalized coordinate	$\bar{q}$	$\phi$
potential $U$	$U(\bar{q}) = \bar{h}\mathcal{E}_0(-\bar{\gamma}\bar{q} - \cos(\bar{q}))$	$U(\phi) = E_J(-\gamma\phi - \cos(\phi))$
potential scale	$\bar{h}\mathcal{E}_0$	$E_J$
normalized bias current	$\bar{\gamma} = \frac{I}{I_c} \frac{\ell}{\hbar}$	$\gamma = \frac{I}{I_c}$
potential barrier height	$U_0 = \bar{h}\mathcal{E}_0 \frac{4\sqrt{2}}{3}(1 - \bar{\gamma})^{3/2}$	$U_0 = E_J \frac{4\sqrt{2}}{3}(1 - \gamma)^{3/2}$
small oscillation frequency	$\omega_0 = \omega_p \sqrt{\frac{\bar{h}}{\tilde{m}_f}} (1 - \bar{\gamma}^2)^{1/4}$	$\omega_0 = \omega_p (1 - \gamma^2)^{1/4}$

Following the calculations in Section 6.1.2 and identifying  $\bar{q} \rightarrow \phi$ ,  $\bar{h} \rightarrow E_J$ ,  $\tilde{m}_f \rightarrow m_\phi$ , and  $\bar{\gamma} \rightarrow \gamma$ , we find the small amplitude oscillation frequency of the vortex of mass  $\tilde{m}_f = 8$  at  $\bar{q}_0$  as

$$\tilde{\omega}_0^{\gamma h} = \sqrt{\frac{\tilde{U}^{\gamma h''}(\bar{q}_0)}{\tilde{m}_f}} = \sqrt{\frac{\bar{h}}{\tilde{m}_f}} (1 - \bar{\gamma}^2)^{1/4}. \quad (6.43)$$

Similarly, the approximated barrier height  $\tilde{U}_0^{\gamma h}$  is found as

$$\tilde{U}_0^{\gamma h} \approx \bar{h} \frac{4\sqrt{2}}{3} (1 - \bar{\gamma})^{3/2}. \quad (6.44)$$

## 6.2.2 Microresistor (microshort) potential

A microresistor or a microshort in a long Josephson junction is formed by a locally increased or decreased thickness of the tunnel barrier. An increase (decrease) in the barrier thickness  $t_j$  leads to an exponential decrease (increase) of the Josephson current density  $j'_c$  with respect to the surrounding region with current density  $j_c$ , see Fig. 6.7a. We consider the microresistor (microshort) as one of the possibilities to construct a pinning potential for the vortex.

In the sine-Gordon equation (2.19), the microresistor (microshort) is modeled by the perturbation term [MS78]

$$f^\epsilon(\tilde{x}) = \epsilon \delta(\tilde{x}) \sin \phi \quad (6.45)$$

where  $\epsilon = (j'_c - j_c)b/j_c\lambda_J$  is the normalized strength of the inhomogeneity.  $\epsilon$  depends on the width  $b/\lambda_J$  and on the modulation of the critical-current density  $(j'_c - j_c)/j_c$  at the microshort ( $j'_c - j_c > 0$ ) or microresistor ( $j'_c - j_c < 0$ ), as shown in Fig. 6.7a. The microresistor (short) contributes to the sine-Gordon hamiltonian (see Section 2.1.2) as

$$\tilde{\mathcal{H}}^\epsilon = - \int_0^\ell \epsilon \delta(\tilde{x}_0) (1 - \cos(\phi)) d\tilde{x}, \quad (6.46)$$

where the microresistor is spatially localized at the coordinate  $\tilde{x}_0$ . Substituting the vortex solution (6.23) into Eq. (6.46) and integrating, we find the effective potential for the vortex [MS78, Ma188, MU90]

$$\tilde{U}^\epsilon(q) = - \frac{2\epsilon}{\cosh^2 q}. \quad (6.47)$$

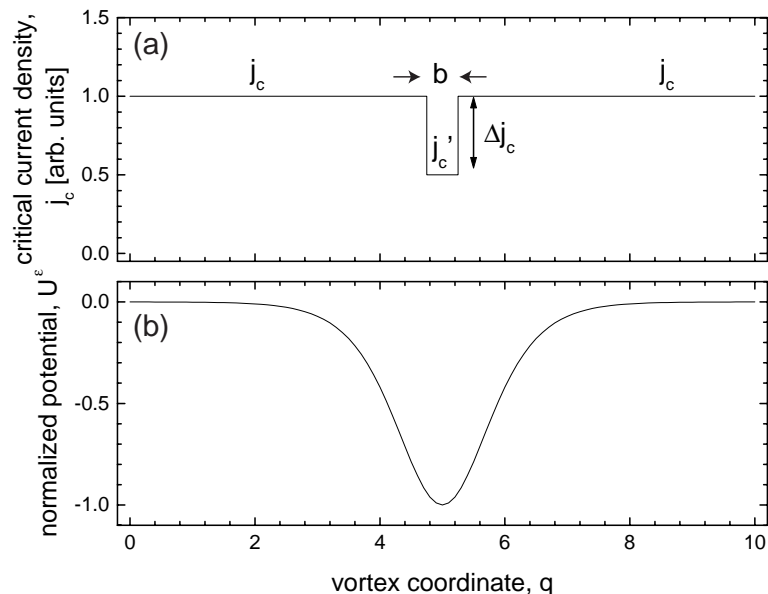


Figure 6.7: (a) Critical-current density vs. vortex coordinate for a junction of normalized length  $\ell = 10$ . The critical current is suppressed by  $\Delta j_c$  over a length of  $b$ , forming a microresistor. (b) Attractive interaction potential for the vortex in a microresistor potential with  $\Delta j_c = 0.5$  and  $b/\lambda_J = 0.5$ .

As an example, the potential profile for a microresistor potential with  $\epsilon = 0.5$  at zero bias current is plotted in Fig. 6.7b. We note that the width of the potential well scales with the Josephson length. Equation (6.47) describes the vortex potential even for inhomogeneities which are not  $\delta$ -shaped. In fact, Eq. (6.47) is a good approximation to the potential for microresistors with  $b < \lambda_J$ , since in this limit  $b$  only changes the amplitude of the potential but not its shape.

### Characteristic properties of the potential

Again, we are interested in the properties of the potential due to the bias current and the microresistor

$$\tilde{U}^{\gamma\epsilon}(q) = \tilde{U}^\gamma + \tilde{U}^\epsilon = -2\pi\gamma q - \frac{2\epsilon}{\cosh^2 q}, \quad (6.48)$$

which has been analyzed in Ref. [KI96], with the intention to study thermal activation and macroscopic quantum tunneling. Here, I recapitulate some of those results and introduce a normalization, which is more convenient for the analysis of the experimental data presented in Section 6.4.3.

The critical bias, i.e. the bias at which the minimum of the potential (6.48) vanishes, is given<sup>4</sup> by

$$\gamma_c^\epsilon = \frac{4}{3\sqrt{3\pi}}\epsilon. \quad (6.49)$$

Introducing the normalized bias current

$$\bar{\gamma} = \frac{\gamma}{\gamma_c^\epsilon}, \quad (6.50)$$

<sup>4</sup>First the coordinate  $q_c$  at which the saddle point of the potential would appear at the critical bias is calculated. At this position, the first derivative of the potential is calculated. Finally, the equation  $U'(q_c) = 0$  is solved for  $\gamma$  resulting in the value of the critical bias  $\gamma_c$ .

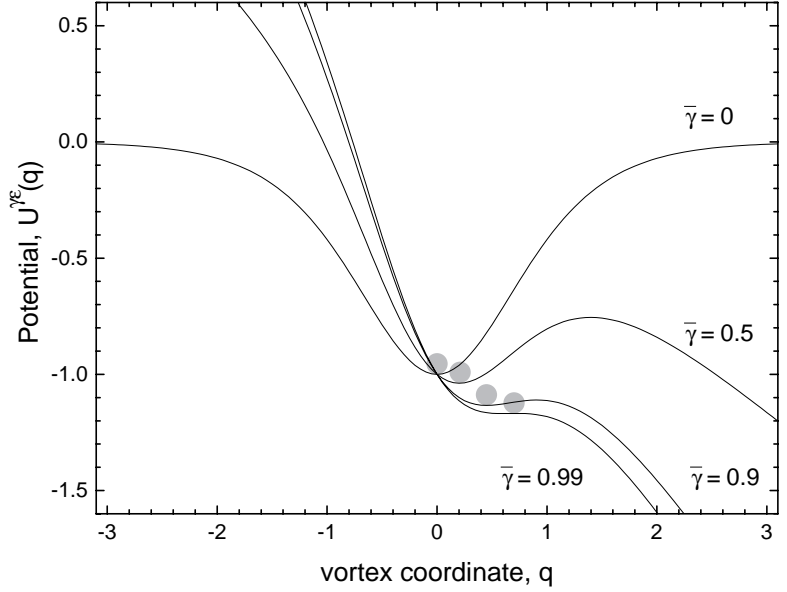


Figure 6.8: Potential  $\tilde{U}^{\gamma\epsilon}(q)$  (6.51) for  $\epsilon = 0.5$  and  $\bar{\gamma} = 0, 0.5, 0.9, 0.99$ .  $\tilde{U}^{\gamma\epsilon}(q)$  is plotted in the range  $q = [-3, 3]$ . The minimum of the potential (i.e. the lowest energy position of the vortex) is indicated by a solid circle.

Eq. (6.48) can be rewritten as

$$\tilde{U}^{\gamma\epsilon}(q) = 2\pi\gamma_c^\epsilon \left( -\bar{\gamma}q - \frac{3\sqrt{3}}{4} \frac{1}{\cosh^2 q} \right). \quad (6.51)$$

In Fig. 6.8, the potential (6.51) is plotted for different values of  $\bar{\gamma}$ . At  $\bar{\gamma} = 0$ , the half width of the potential is about  $\lambda_J$ . As the bias current is increased, the potential barrier to the right of the vortex is decreased and at  $\bar{\gamma} = 1$  a saddle-point is formed. Here, the center of mass coordinate of the vortex is only shifted by  $\Delta q = \text{arcsech}(\sqrt{2/3}) \approx 0.66$  to the right as the bias current is increased to  $\bar{\gamma} = 1$ , whereas for the magnetic-field induced potential the vortex moves a distance of  $\Delta q = \ell/4$  before it reaches the saddle point.

A cubic approximation to Eq. (6.47) yields a potential barrier height of

$$\tilde{U}_0^{\gamma\epsilon} = \pi\gamma_c^\epsilon \frac{4\sqrt{2}}{3} (1 - \bar{\gamma})^{3/2} \quad (6.52)$$

and a small amplitude oscillation frequency of

$$\tilde{\omega}_0^{\gamma\epsilon} = \sqrt{\frac{\pi\gamma_c^\epsilon}{\sqrt{2}}} (1 - \bar{\gamma})^{1/4}. \quad (6.53)$$

The approximate potential barrier height (6.52) is compared to a numerically exact calculation of  $\tilde{U}_0^{\gamma\epsilon}$  in Fig. 6.9. Good agreement is found for the values of  $\bar{\gamma}$  of interest.

Introducing the normalized parameter

$$\bar{\epsilon} = \frac{4}{3\sqrt{3}}\epsilon, \quad (6.54)$$

$\tilde{U}_0^{\gamma\epsilon}$  has the simple form

$$\tilde{U}_0^{\gamma\epsilon} = \bar{\epsilon} \frac{4\sqrt{2}}{3} (1 - \bar{\gamma})^{3/2}. \quad (6.55)$$

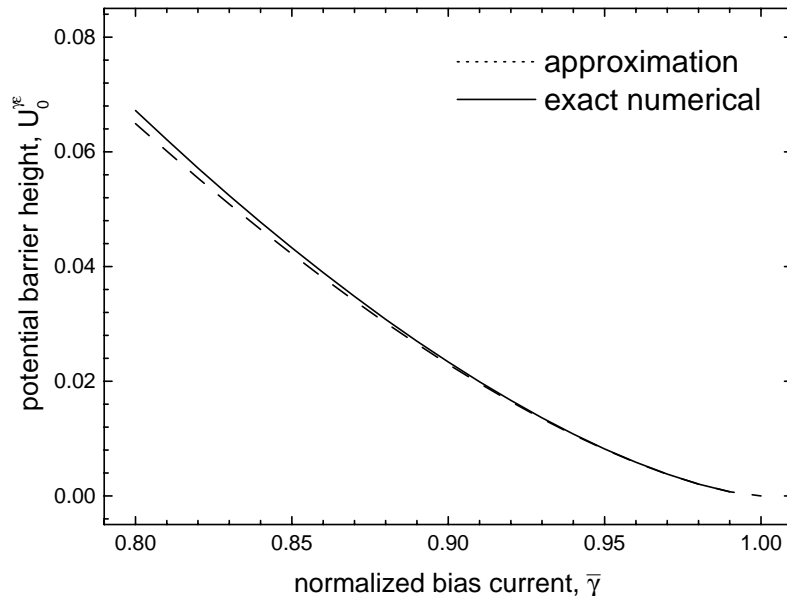


Figure 6.9: Approximated potential barrier height (6.52) [dashed line] and exact numerical calculation of  $\tilde{U}_0^{\gamma\epsilon}$  (solid line) versus  $\bar{\gamma}$  for  $\epsilon = 0.5$ .

Noting that  $2^{-1/4}(1 - \bar{\gamma})^{1/4} \approx (1 - \bar{\gamma}^2)^{1/4}$  for  $\bar{\gamma} \rightarrow 1$  we can also rewrite the small amplitude oscillation frequency as

$$\tilde{\omega}_0^{\gamma\epsilon} = \sqrt{\frac{8\bar{\epsilon}}{\tilde{m}_f}}(1 - \bar{\gamma}^2)^{1/4}. \quad (6.56)$$

Thus, comparing Eqs. (6.55) and (6.56) with Eqs. (6.44) and (6.43), we find that the microshort and magnetic-field induced potentials have the same type of dependence on the bias current close to  $\bar{\gamma} = 1$ . We note that for the microresistor  $\omega_0$  is a factor of  $\sqrt{8} \approx 2.83$  larger with respect to the barrier height as in comparison with the case of the magnetic-field induced potential, see Eq. (6.43).

### 6.2.3 Scaling of parameters

The characteristic properties  $\tilde{U}_0$  and  $\tilde{\omega}_0$  of the different pinning potentials described above scale in a similar way with the junction parameters and the bias current. No matter what the specific properties of a certain potential are, its characteristic energy scale is given by

$$\mathcal{E}_0 = \frac{\Phi_0 j_c \lambda_J w}{2\pi}, \quad (6.57)$$

see Section 2.1.2. From Eq. (6.57) it is evident that the height of the potential barrier  $\tilde{U}_0 \mathcal{E}_0$  and the mass of the vortex  $8\mathcal{E}_0/\bar{c}^2$  are proportional to  $\sqrt{j_c} w$ , where  $w$  is the junction width and  $j_c$  the critical-current density of the junction. For typical junction parameters (see Table 6.2), we find that the potential barrier height scales with  $\mathcal{E}_0 \approx w \times 1.0 \times 10^{-20} \text{ J}/\mu\text{m}$ , where the junction width  $w$  is given in  $\mu\text{m}$ . Because we consider thermal activation processes, it is convenient to relate this energy to the thermal energy  $k_b T$ . Thus for the parameters discussed above,  $\mathcal{E}_0/k_b$  is approximately  $w \times 900 \text{ K}/\mu\text{m}$ .<sup>5</sup> For the same junction parameters, we find the vortex rest mass  $m_f = 7 \times w \times 10^{-34} \text{ kg}/\mu\text{m}$ . For a  $w = 0.1 \mu\text{m}$  junction,  $m_f$  is approximately 0.1 percent of the rest mass of a single electron.

At zero bias current, the thermal escape of the vortex is strongly suppressed at the typical operating temperatures ( $T < 9.2 \text{ K}$ ) of our devices due to the large energy barrier,

<sup>5</sup>An energy of 1 Kelvin corresponds to approximately  $86 \mu\text{eV}$ .

Table 6.2: Typical electrical and geometrical junction parameters.

quantity	unit	approximate value	meaning
$j_c$	[A/cm <sup>2</sup> ]	100	critical-current density
$C^*$	[mF/m <sup>2</sup> ]	30	specific capacitance
$d'$	[nm]	182	magnetic thickness
$r$	[ $\mu$ m]	50	mean junction radius
$\lambda_J$	[ $\mu$ m]	38	Josephson length
$\ell$		8.3	normalized junction length
$\lambda_L$	[nm]	90	London penetration depth
$t_j$	[nm]	2	barrier thickness
$\epsilon_j$		8	barrier dielectric constant

which is more than 100 times larger than the thermal energy  $k_b T$ . However, by applying a bias current to the junction, the potential barrier height can be reduced to arbitrarily small values, such that thermal escape may be observed for bias currents close to  $\gamma_c$ , when the barrier height is comparable to the thermal energy.

The value of  $\mathcal{E}_0/k_b$  quoted above for a long Josephson junction is identical to the Josephson coupling energy  $E_J/k_b$  in a small junction with the area of  $w \times \lambda_J$  and electrical parameters identical to those of the long junction. Thus, the thermal activation processes are observable in similar parameter ranges for both systems.

The small amplitude oscillation frequency

$$\omega_0 = \tilde{\omega}_0 \omega_p. \quad (6.58)$$

is proportional to the plasma frequency  $\omega_p$ , which scales the rate of the activation process as stated in Eq. (6.6). Typically  $\omega_p/2\pi$  is around 50 GHz, again, calculated for the junction parameters in Table 6.2, and scales  $\propto \sqrt{j_c}$ . In comparison to the small junction case, the vortex attempt frequency is somewhat reduced ( $\tilde{\omega}_0 < 1$ ) for typical pinning potential parameters. The vortex attempt frequency in the narrow potential of the microresistor is larger than for the relatively broad potential in the magnetic-field case. We also note that the small amplitude oscillation frequency is independent of the junction width  $w$ . This can be easily understood considering Eq. (6.43) and noting that both the potential and the mass of the fluxon depend in the same way on  $w$ , such that the effect of  $w$  on  $\omega_0$  cancels.

During sample fabrication,  $\mathcal{E}_0$  and  $\omega_0$  can be adjusted by the junction width  $w$  and the critical-current density  $j_c$ .  $w$  may be varied between several microns down to  $0.3 \mu\text{m}$  and  $j_c$  between  $10 \text{ A/cm}^2$  and  $1 \text{ kA/cm}^2$ . The scaling of  $\mathcal{E}_0$  and  $\omega_0$  with  $j_c$  and  $w$  is discussed above. All other electrical sample parameters in Table 6.2 are fairly constant for a given fabrication procedure and thus, cannot be varied much.<sup>6</sup>

Besides the identical scaling of all considered potentials with  $\mathcal{E}_0$ , we also find a similar scaling of the potential barrier height and the small amplitude oscillation frequency with the normalized bias current for  $\bar{\gamma} \rightarrow 1$ . This is a result of the cubic approximation, which is valid for  $\bar{\gamma} \rightarrow 1$  for all potentials discussed here. The potential barrier height

$$\tilde{U}_0 = \tilde{u}_0 \frac{4\sqrt{2}}{3} (1 - \bar{\gamma})^{3/2} \quad (6.59)$$

<sup>6</sup>The capacitance and the inductance of the junction might be influenced in some useful way by modifying the idle region.

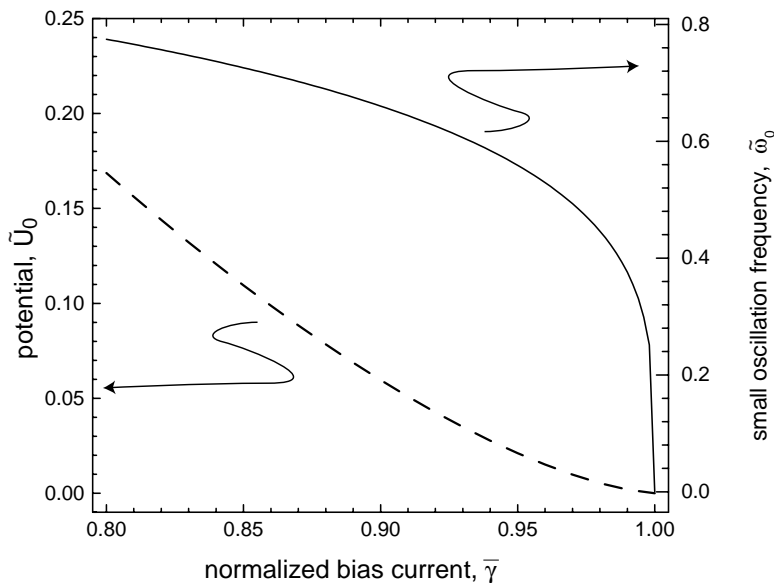


Figure 6.10: Universal dependence of  $\tilde{U}_0$  (dashed line) and  $\tilde{\omega}_0$  (solid line) on  $\bar{\gamma}$  for  $\tilde{u}_0 = \tilde{\Omega}_0 = 1$ .

scales universally with  $\bar{\gamma}$  for both the microresistor and the magnetic-field induced potential as shown in Fig. 6.10. The same scaling prevails for the potential of the phase in a small junction. Ideally, the potential barrier  $\tilde{U}_0$  can be made arbitrarily small by biasing close to the critical bias current ( $\gamma \rightarrow \gamma_c$ ). Hence, in this parameter regime, the height of the potential barrier can be tuned in a wide range depending on  $\tilde{u}_0$ ,  $w$  and  $j_c$ .

Also, the characteristic attempt frequency

$$\tilde{\omega}_0 = \tilde{\Omega}_0 (1 - \bar{\gamma}^2)^{1/4} \quad (6.60)$$

scales with the bias current identically for all discussed potentials. Its dependence on the bias current is weak for small  $\bar{\gamma}$  and drops sharply to zero for  $\bar{\gamma} \rightarrow 1$ , as can be seen in Fig. 6.10. Thus, the thermal activation rate increases strongly towards the critical bias, due to the reduction of the barrier height, but then falls off again due to the reduction of the attempt frequency.<sup>7</sup>

The major differences between the vortex pinning potentials are due to the prefactors  $\tilde{u}_0$  and  $\tilde{\Omega}_0$ . For the magnetic-field induced potential the barrier height  $\tilde{u}_0^h = \bar{h}$  can be varied in experiment by the external magnetic field. In practice, the lower limit may be given by  $h \approx 0.01$  because of the residual (non-magnetic field induced) pinning forces due to imperfections of the junction but also due to the limited accuracy of the field bias. The requirements on the current and voltage resolution of the experimental setup are also more stringent for measurements of small depinning currents at very low fields, setting a practical lower limit on the values of the fields that can be employed. The upper limit of  $h$  for which the above analysis is valid is approximately 0.5. Above this threshold value, the magnetic field penetration into the junction will lead to forces on the vortex which are not linear in the field. This modifies the simple perturbative vortex dynamics discussed above. The microresistor potential has a maximum amplitude of  $\epsilon = -1$  for a completely suppressed critical current. Because the potential involves a spatial modification of the junction barrier, its amplitude cannot be modified in situ in an experiment, but only

<sup>7</sup>Obviously, this statement is only true in the limits of the validity of the thermal rate calculations, see Section 6.1.1.

during junction fabrication. In the case of a microshort ( $\epsilon > 0$ ), the potential barrier can in principle be arbitrarily large, though in practice this type of inhomogeneity is more difficult to fabricate. Comparing the calculated attempt frequencies for similar values of the depinning current for the two discussed potentials, we find that  $\omega_0$  is somewhat larger (typically less than a factor of 2) for the microresistor potential (also see Sec. 7.1.1). This fact can be qualitatively understood, noticing that the potential well is more localized for the microresistor than for the magnetic field case. Thus, the curvature at the bottom of the microresistor well is larger, leading to a higher attempt frequency.

### 6.3 Experimental technique

The thermal activation rate of a vortex from a potential well can be determined by measuring its lifetime in a metastable state at fixed bias current. With no bias current applied to the junction, the vortex is prepared at the bottom of the well at  $t = 0$ . Then, at time  $t_0$ , the bias current is rapidly increased to the desired value  $I < I_c$ . The increase in current has to be much faster than the typical activation rate but slower than the relaxation rate of the vortex in the well, to assure the preparation of the vortex in the ground state. Then, the life time  $\Delta t = t_{sw} - t_0$  is determined by measuring the time  $t_{sw}$  at which the junction switches from the zero-voltage state to a finite-voltage state. Repeating this measurement many times, the activation rate is determined by the inverse average value of  $\Delta t$ . This scheme requires a fast and accurate control of the bias current. However, the band pass of the experimental setup is typically limited by the low-pass filtered bias leads needed to avoid electromagnetic interference. Therefore, we chose a method which was pioneered in measurements of switching currents of small Josephson junctions [FD74, WWVF84, MDC87].

#### 6.3.1 Measurement method

A typical current-voltage characteristic of a vortex trapped in an annular junction subject to some pinning potential is shown in Fig. 6.11a. In this case, the vortex is not depinned ( $V = 0$ ) until the switching (or depinning) current  $I_0$  is reached. The depinning process has a statistical nature, due to the presence of thermal fluctuation. Therefore, one observes a distribution of depinning currents  $I_0$  (see Fig. 6.11b) instead of a single value  $I_0$  upon performing the measurement many times. We measure the escape of the vortex from the potential well, by sweeping the bias current at a fixed rate  $dI/dt$  with a triangular waveform in time, see Fig. 6.11c. In each cycle of the current sweep, the depinning current  $I_0$  is recorded. Statistically analyzing these data, we find the distribution of the depinning currents [FD74].

With this technique, the temporal rate of escape can be associated with the rate of escape at a certain value of bias current. Thus, the experiment can be done in the current domain instead of the time domain, which is the experimentally most feasible approach. It can be shown [FD74] that the probability distribution of the switching currents  $P(I)$  is related to the escape rate  $\Gamma(I)$  as

$$P(I) dI = \left| \frac{dI}{dt} \right|^{-1} \Gamma(I) \left( 1 - \int_0^I P(I') dI' \right) dI, \quad (6.61)$$

i.e. the probability of the vortex to be activated in the current interval  $dI$  centered around the current  $I$  is given by the rate of activation at that current  $\Gamma(I)$  multiplied by the inverse



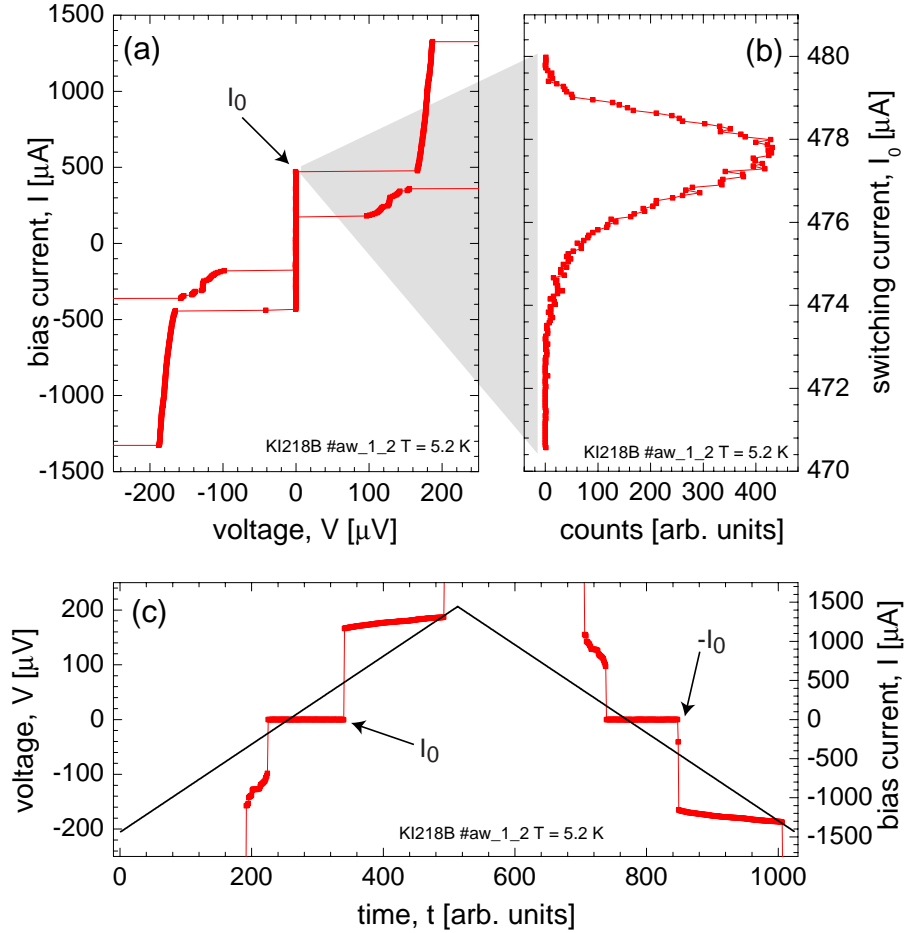


Figure 6.11: (a) Typical experimental current-voltage characteristic of a single-vortex resonance with pinning. The switching (depinning) current  $I_0$  is indicated. (b) Probability distribution of the switching current  $I_0$ . The counts reflect the relative probability of the depinning current  $I_0$  in the interval  $I_0 \pm \Delta I/2$ . (c) Current and voltage versus time for the characteristic shown in (a). The bias current is a triangular waveform with period  $T$ , the voltage is in correspondence to (a).

of the current sweep rate  $|dI/dt|$  and the probability that the vortex was not already activated at a lower current. The integral equation (6.61) can be solved explicitly for switching-current distribution

$$P(I) = \left| \frac{dI}{dt} \right|^{-1} \Gamma(I) \exp \left( - \left| \frac{dI}{dt} \right|^{-1} \int_0^I \Gamma(I') dI' \right). \quad (6.62)$$

Thus, the probability distribution  $P(I)$  is dependent only on the activation rate  $\Gamma(I)$  and the bias current sweep rate  $|dI/dt|$ . The shape, the mean value  $\langle I \rangle$  and the standard deviation  $\sigma_I$  of the switching-current distribution are characteristic for the activation process in the given potential. The bias current dependent activation rate  $\Gamma(I)$  can be found from a measured  $P(I)$  distribution by inverting Eq. (6.62). The details of the calculation of a switching-current distribution  $P(I)$  from a given rate  $\Gamma(I)$  and the inverse problem for data analysis are discussed later in this section.

### 6.3.2 Experimental setup and data acquisition

All presented measurements have been performed in an insertable He-4 cryostat [Swa86], the temperature of which can be stabilized between the base-temperature 1.5 K of the cryostat and well above the critical temperature  $T_c \approx 9.2$  K of our niobium samples. The cooling is done by pumping on a small helium volume ( $10 \text{ cm}^3$ ), the so-called 1K-pot, which is mounted in the vacuum chamber of the cryostat. The 1K-pot is continuously refilled with a capillary with an adjusted flow impedance, for optimizing the cooling power. For temperature control, a  $60 \Omega$  manganin wire heater is installed below the 1K-pot. The temperature is measured using a calibrated carbon-glass resistor. Using a PID controller [Lak], the temperature can be stabilized to better than 5 mK at temperatures below 2 K and to better than 1 mK at all other temperatures of interest.

The sample is mounted on the cold finger in the inner vacuum chamber of the cryostat. A cryoperm shield is integrated into the vacuum can to effectively screen residual magnetic fields. A superconducting coil is mounted on the 1K-radiation shield, delivering a homogeneous field of 0.05 Oe/mA in the plane of the sample. All sample wires are carefully twisted in pairs and filtered using commercial  $\pi$ -filters with a -3 dB cut-off at 700 kHz at room temperature. Additionally, a symmetric RC-filter stage with a cut-off at 30 kHz mounted on the 1K-pot was used.

The sample is current biased using a custom-made low-noise battery-powered current source. The current can be swept at frequencies up to 100 Hz using an analog internal triangular waveform generator or, alternatively, an external generator [Hew]. The measured voltages are amplified using custom-made bipolar or FET preamplifiers. The monitor signals of the analog electronics are read out differentially using a 100 kS/s 16-bit AD converter. The current biasing can be controlled by 16-bit DA converters on the same board [Natb]. All measurements are done using custom-made software to control the AD-DA converters and any other required instruments [Nata].

The switching-current measurements are performed using two different measurement schemes, one relying on triggered high resolution AD-conversion, the other one using a time-of-flight technique. In both schemes, the bias current is swept synchronized to a symmetric triangular waveform of adjustable amplitude and frequency, see Fig. 6.12a. Each switching event is recognized by feeding the preamplified voltage signal from the sample, see Fig. 6.12d, to a custom-made trigger circuit with adjustable threshold and window. The trigger detects the switching of the sample from the zero-voltage state to a finite-voltage state which corresponds to the activation of the vortex from the potential well, see Fig. 6.12c. The trigger provides a TTL output signal when the switching is detected. This TTL signal is used to trigger the AD-conversion of the current-monitor signal, yielding the switching current of the junction. The current resolution attainable with this technique is limited by the resolution of the AD converter. In a typical measurement of a switching-current distribution with a mean value of  $\langle I \rangle = 0.5$  mA a sweep-frequency independent resolution of 15 nA can be achieved with a 16 bit ADC.

In the time-of-flight technique, the time delay  $\Delta\tau$  between the zero-crossing of the bias current (Fig. 6.12b) and the TTL signal of the voltage trigger (c) is measured using a counter with a 20 GHz stabilized clock [Sta]. Knowing the current sweep rate, the switching current can be calculated as  $I_c = \Delta\tau dI/dt$ . This technique offers current resolution of

$$\nu_s I_s 0.1 \frac{\text{pA}}{\text{mA Hz}}, \quad (6.63)$$

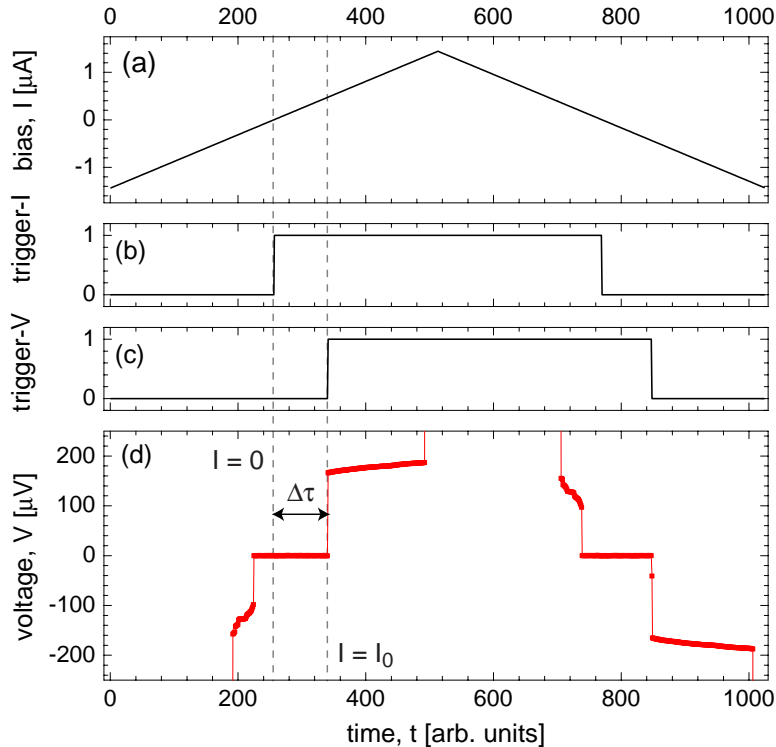


Figure 6.12: (a) Triangular current ramp. (b) Trigger signal on current,  $V_{\text{trig}} = 1$  for  $I > 0$ . (c) Trigger signal on voltage,  $V_{\text{trig}} = 1$  for  $V > 0$  (d) Measured voltage profile. The time between the two rising trigger edges is measured to determine the critical current in the time-of-flight technique.

that depends on the sweep rate. The sweep frequency  $\nu_s$  is given in Hz and the sweep amplitude  $I_s$  in mA. At a typical sweep frequency of 100 Hz and a typical sweep amplitude of 1 mA, the maximum current resolution of  $10^{-11}$  A = 10 pA is in principle attainable with this technique. At 100 Hz, this resolution is 3 orders of magnitude better than the one of the 16 bit ADC. Only at sweep frequencies above 100 kHz the resolution of the ADC is comparable or better than that of the time-of-flight technique.

To verify that the time-of-flight method and the method using an AD-converter for data acquisition give the same results, I have measured the switching-current distributions of an annular junction with a trapped vortex at 4.2 K. The acquired histograms (symbols) and fits to theory (solid lines) are plotted in Fig.6.13. The two distributions are virtually identical and the effective escape temperature  $T_{\text{esc}}$  and the critical current  $I_c$  determined from these histograms (see next section) are equal to better than 0.1%, proving the feasibility of both measurement schemes.

### 6.3.3 Data evaluation: probability distributions, activation rates and escape temperature

To determine the probability distribution  $P(I)$ ,  $N$  individual switching currents  $\{I_i\} = \{I_1, I_2, \dots, I_N\}$  are measured. Typically,  $10^4$  to  $10^6$  current values are acquired. Using these data, a histogram is calculated by dividing the current range of interest between  $I_{\text{min}}$  and  $I_{\text{max}}$  in  $M$  intervals of width  $\Delta I$  and counting the number of switching events  $n$  in each current interval (bin). A typical histogram is shown in Fig. 6.13.

To achieve the best possible resolution for the histogram based on a given data set  $\{I_i\}$ , the bin width  $\Delta I$  is chosen to be an integer multiple  $m$  of the discretization  $\delta I$  of the data

$$\Delta I = m \delta I. \quad (6.64)$$

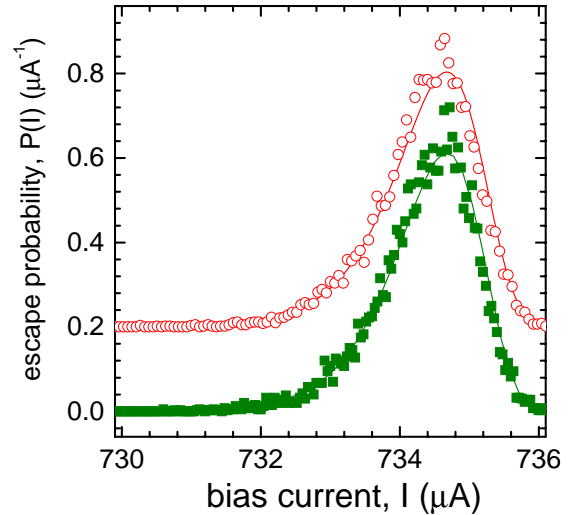


Figure 6.13: The same switching-current distribution acquired with AD-converter (solid squares) and with the time-of-flight technique (open circles). Solid lines are fits to theory. For better visibility the second set of data is offset by  $0.2 \mu\text{A}^{-1}$ .

The discretization  $\delta I$  is due to the digital data acquisition system, which discretizes the analog data either using an AD-converter or a counter. The minimum value of  $\delta I$  depends on the maximum resolution of the AD-converter or equivalently, the time base of the counter, as pointed out in the previous section.

Each bin  $j$  of the histogram is labeled by the current value corresponding to the middle of the interval  $\Delta I$  that the bin spans. The number of events  $n_j$  in each bin is normalized by the total number of counts in the histogram, reflecting the relative probability of an event occurring in the current interval  $\Delta I$ . It is useful to normalize this quantity by the width of the bin  $\Delta I$ , giving the probability of a switching event occurring in an arbitrary current interval  $dI$

$$P(I) dI = \frac{n_j}{N \Delta I} dI. \quad (6.65)$$

Thus, the probability distribution  $P(I)$  is normalized such that  $\int P(I) dI = 1$ .

The activation rate  $\Gamma(I)$  is related to  $P(I)$  as

$$\Gamma(I) = \frac{dI/dt}{\Delta I} \ln \frac{\int_I^\infty P(I') dI'}{\int_{I+\Delta I}^\infty P(I') dI'}, \quad (6.66)$$

which is found by solving Eq. (6.62) for  $\Gamma(I)$  [FD74]. Thus, the activation rate at the bias current  $I$  can be calculated from the measured discrete probability distribution  $P(I)$  according to

$$\Gamma(I_k) = \frac{dI/dt}{\Delta I} \ln \frac{\sum_{j \geq k} P_j \Delta I}{\sum_{j \geq k+1} P_j \Delta I}. \quad (6.67)$$

The experimentally determined dependence of the activation rate (6.67) on the bias current can then be compared to the theoretical predictions for the rate of the process under consideration.

The nature of an escape process can be effectively characterized by assuming that it is of thermal origin and calculating its effective escape temperature  $T_{\text{esc}}$ . According to Eq. (6.6), the thermal escape rate of a fluxon from a potential well of depth  $\tilde{U}_0 \mathcal{E}_0$  is given by

$$\Gamma_{\text{th}} = \rho_a \frac{\tilde{\omega}_0 \omega_p}{2\pi} \exp\left(-\frac{\tilde{U}_0 \mathcal{E}_0}{k_b T_{\text{esc}}}\right). \quad (6.68)$$

Table 6.3: Parameters relevant for the calculation of histograms.

quantity	unit	description
$N$		total number of switching currents
$dI/dt$	[A/s]	sweep rate of current
$I_i$	[A]	$i$ th individual switching current
$P(I)$		probability distribution of switching currents
$\Delta I$	[A]	width of bin in $P(I)$ histogram
$P_j$		probability for $j$ th interval of histogram

Knowing the dependence of  $\tilde{U}_0$  and  $\tilde{\omega}_0$  on the bias current  $I$ , *any two experimentally relevant parameters* can be determined from the data with good accuracy. All other parameters have to be supplied to the model and should be confirmed independently in experiment. Usually, the effective escape temperature  $T_{\text{esc}}$  and the critical current in absence of fluctuations  $I_c$  are determined from the measured switching current distribution  $P(I)$ .

For the purpose of the experimental data analysis, we transform Eq. (6.68) to the form

$$\ln \frac{2\pi\Gamma}{\rho_a \tilde{\omega}_0 \omega_p} = \frac{\mathcal{E}_0}{k_b T_{\text{esc}}} \tilde{U}_0. \quad (6.69)$$

Substituting the approximated potential barrier height

$$\tilde{U}_0 = \tilde{u}_0 \frac{4\sqrt{2}}{3} (1 - \bar{\gamma})^{3/2} \quad (6.70)$$

into Eq. (6.69), we find an expression for the activation rate which is to first order linear in  $\bar{\gamma}$

$$\left( \ln \frac{2\pi\Gamma}{\rho_a \tilde{\omega}_0 \omega_p} \right)^{2/3} = \left( \frac{\mathcal{E}_0}{k_b T_{\text{esc}}} \tilde{u}_0 \frac{4\sqrt{2}}{3} \right)^{2/3} (1 - \bar{\gamma}). \quad (6.71)$$

The dependence of the left hand side of Eq. (6.71) on the bias current is only logarithmically weak and can be neglected in the first approximation. Hence, the left hand side of Eq. (6.71) is evaluated using the data  $\Gamma(I)$  calculated from the measured probability distribution  $P(I)$  and the dependence of  $\tilde{\omega}_0 \omega_p$  on the bias current using an estimated value of  $I_c$ .<sup>8</sup>

In a next step, the experimental data obtained in that way can be fitted to the right hand side of Eq. (6.71), which is a linear function of the bias current. Using a fitting function of the type  $f(\bar{\gamma}) = c_{\text{const}} - c_{\text{lin}} \bar{\gamma}$ , both  $T_{\text{esc}}$  and  $I_c$  can be determined as

$$T_{\text{esc}} = \frac{1}{c_{\text{lin}}^{3/2}} \frac{\mathcal{E}_0}{k_b} \tilde{u}_0, \quad (6.72)$$

$$I_c = j_c A \gamma_c = \frac{c_{\text{const}}}{c_{\text{lin}}}. \quad (6.73)$$

Using the calculated value of  $I_c$ , we recursively iterate the fitting procedure starting with the calculation of the left hand side of Eq. (6.69) to improve the accuracy of the fit. Due to the weak dependence of the procedure on  $I_c$ , the iterations converge quickly to the final

<sup>8</sup>E.g.  $I_c$  can be approximated by  $\langle I_0 \rangle$  in the first iteration.

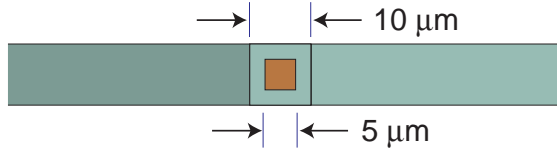


Figure 6.14:  $5 \times 5 \mu\text{m}^2$  square Josephson junction with  $2.5 \mu\text{m}$  wide idle region and  $10 \mu\text{m}$  wide bias lines.

accurate value. If the experimental data are appropriate, the determined  $T_{\text{esc}}$  is identical to the thermal bath temperature  $T$ .

For the purpose of data analysis, a program has been implemented [Wol] which calculates histograms from raw data and determines current dependent activation rates from them. Moreover, the experimental data can be fitted to extract any two relevant parameters, e.g.  $T_{\text{esc}}$  and  $I_c$ . It is also possible to calculate thermal and quantum switching-current distributions on the basis of supplied junction parameters and the temperature. The program has been adjusted to work with data for the activation of the phase in a small junction, of a vortex from a field induced potential and of a vortex from a microresistor potential.

## 6.4 Experimental results

First, I present experimental results on the thermal activation of the phase in a small square Josephson junction and prove that the newly developed experimental setup, the measurement technique and the data analysis provide reliable results. Next, the thermal activation measurements of vortices are presented and the results are discussed in detail.

### 6.4.1 Small junction

The switching-current distributions of a  $5 \times 5 \mu\text{m}^2$  square Josephson junction fabricated at Hypres Inc. [Hyp] with a nominal current density of  $j_c = 1 \text{ kA}/\text{cm}^2$  have been measured at temperatures between 1.6 and 7.5 Kelvin. The sample geometry is shown in Fig. 6.14. Due to the fabrication technology, the junction is surrounded by a symmetric  $2.5 \mu\text{m}$  wide idle region. The general geometrical and electrical properties of this junction and its idle region correspond to those discussed already in detail in Section 4.2. The sample is biased via two long superconducting lines of  $10 \mu\text{m}$  width.

#### Sample properties

To electrically characterize the sample, its current-voltage characteristics have been measured at temperatures between 1.6 and 10 Kelvin, see Fig 6.15a. From these data, we have evaluated the critical current  $I_c$ ,<sup>9</sup> the current jump at the gap  $I_g$ , the normal resistance  $R_n$  and the subgap resistance  $R_{sg}$  according to the procedure described in Ref. [DEK<sup>+</sup>99]. In Fig. 6.15b, the dependence of  $I_c$  (solid squares) and  $I_g$  (open circles) on the temperature are plotted. The critical current can be fitted well to the Ambegaokar-Baratoff dependence [AB63a, AB63b] with  $T_c \approx 8.55 \text{ K}$  and  $I_c \approx 310 \mu\text{A}$ . The current jump at the gap voltage also follows well the Ambegaokar-Baratoff dependence with  $T_c \approx 8.75 \text{ K}$  and  $I_g \approx 474 \mu\text{A}$ , though there are small deviations in the intermediate temperature range. These deviations are due to the modified quasiparticle density of states at the gap, which is a result

<sup>9</sup>In these measurements, a single realization of the switching current  $I_0$  is identified with the critical current  $I_c$ .

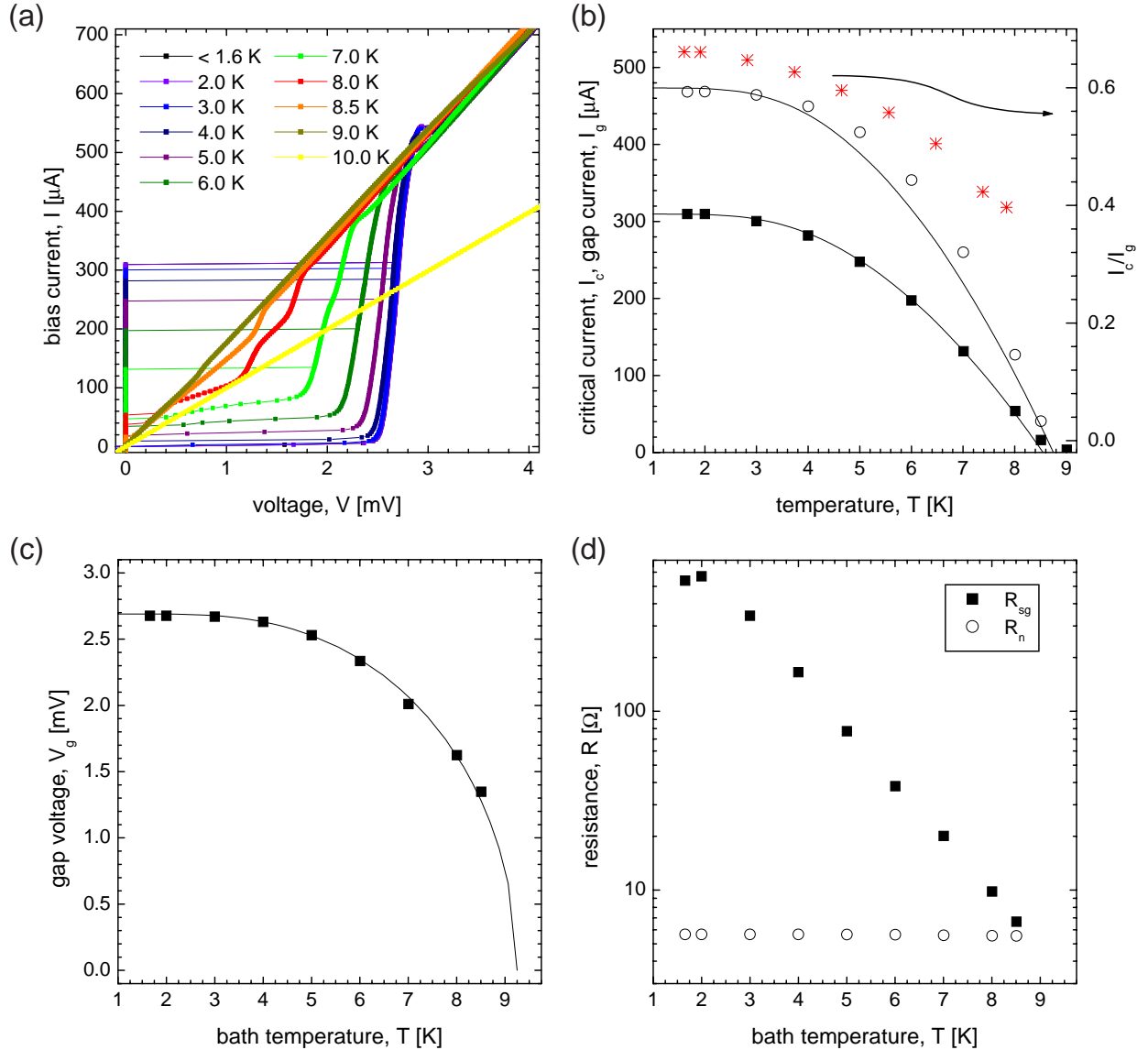


Figure 6.15: (a) Current-voltage characteristic of a  $5 \times 5 \mu\text{m}^2$  square Josephson junction in the temperature range between  $T = 1.6$  K and  $T = 10$  K. (b) Experimental critical current  $I_c$  (solid squares) and gap current  $I_g$  (open circles) vs. temperature. The solid lines are fits according to the Ambegaokar-Baratoff theory [AB63a, AB63b]. Crosses indicate the ratio  $I_c/I_g$ . (c) Gap voltage  $V_g$  (solid squares) and fit according to theory [Müh59] (solid line). (d) Normal resistance  $R_n$  (open circles) and subgap resistance  $R_{sg}$  (solid squares) on a logarithmic scale.

of the proximity induced superconductivity in the non-oxidized aluminum of the barrier [GHG<sup>+</sup>95, ZLZ<sup>+</sup>99]. This is also well seen from the double-gap structure in the current-voltage characteristics at 7, 8, and 8.5 K in Fig. 6.15a. Also plotted in Fig 6.15b is the ratio  $I_c/I_g$ , which for low temperatures is approximately 0.66 indicating a good junction quality and no (or only a small) reduction of the critical current due to trapped flux or self-fields. The dependence of the gap voltage  $V_g$  on temperature also fits well the theoretical expectations [Müh59], see Fig. 6.15c.

The subgap and the normal resistance are determined from the current-voltage characteristics. The subgap resistance needs to be known in order to estimate the influence of

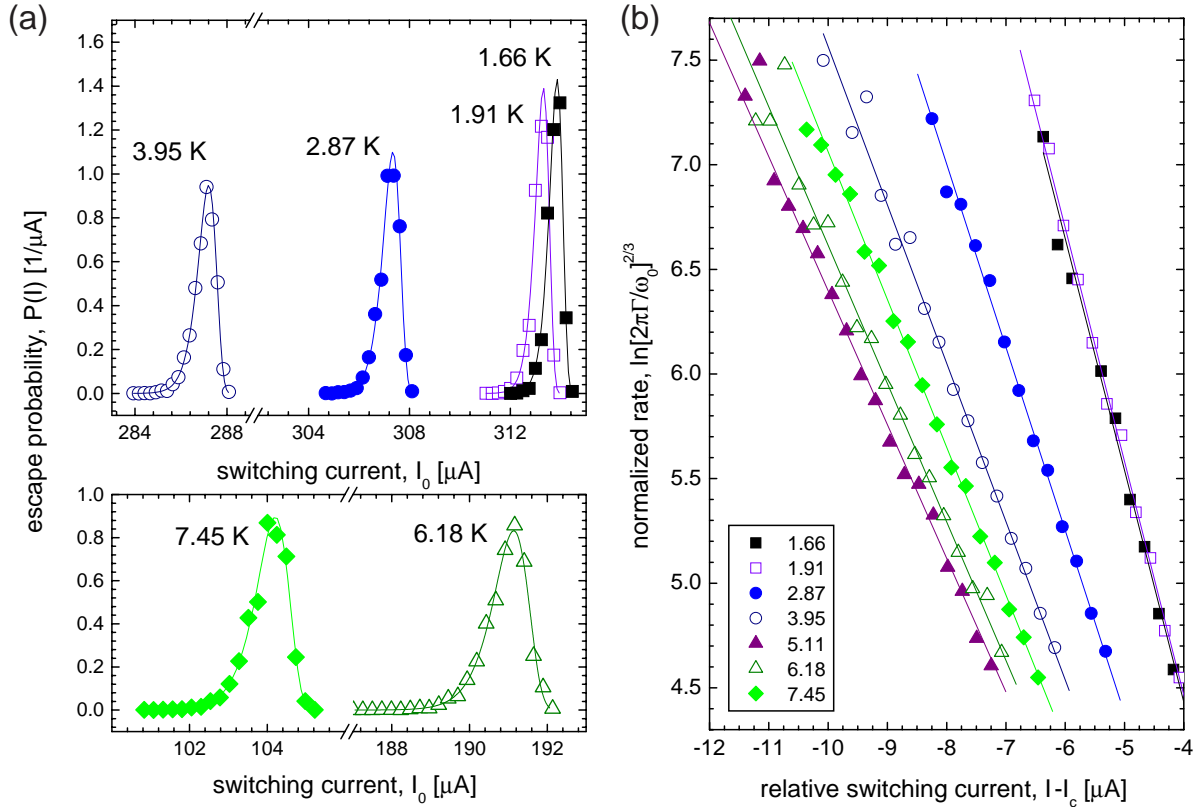


Figure 6.16: (a) Measured switching-current distributions (symbols) and fits (solid lines) at temperatures between 1.66 and 7.45 K. (b) Normalized experimental activation rates (symbols) in dependence on the reduced bias current  $I - I_c$ . Fits to the experimental data are indicated by solid lines.

damping on the thermal activation of the phase. In Fig. 6.15d, both  $R_n$  (open circles) and  $R_{sg}$  (solid squares) are plotted vs. temperature on a logarithmic scale. In good approximation  $R_{sg}$  decreases exponentially with temperature from about  $660 \Omega$  at 2 Kelvin to  $6.6 \Omega$  at 8.5 Kelvin reflecting the exponential suppression of the quasiparticle tunnel current with decreasing  $T$ , whereas  $R_n \approx 6.6 \Omega$  is temperature independent as expected.

### Thermal activation of the phase

At each of the temperatures  $T = 1.66, 1.91, 2.87, 3.95, 5.11, 6.18,$  and  $7.45$  K, we measured  $10^4$  switching currents with a bias current sweep rate of  $dI/dt = 0.16$  A/s. The data were digitized using a 12-bit AD-converter<sup>10</sup> and histograms were calculated using the discretization of the data acquisition as bin width. The measured normalized switching-current distributions are plotted in Fig. 6.16a. With increasing temperature, the width of the distributions increase while the maximum current decreases. This observation is in agreement with the qualitative expectations.

Using the analysis described in Section 6.3.3, the effective temperature  $T_{\text{esc}}$  of the thermal escape and the critical current  $I_c$  in absence of thermal fluctuations are determined. The thermal activation rate of the phase from the potential (6.14) close to the critical

<sup>10</sup>For these initial measurements, no higher resolution ADC or counter was available in our lab.



current  $I_c$  is given by

$$\Gamma(I) = \rho_a \frac{\omega_0^\phi(I)}{2\pi} \exp\left(-\frac{U_0^\phi(I)}{k_b T}\right), \quad (6.74)$$

which is evaluated by substituting the expressions (6.15) and (6.19) into Kramers formula (6.6). According to the scheme outlined in Section 6.3.3, we first calculate the quantity

$$\Gamma^{\text{norm}}(I) = \left(\ln \frac{2\pi \Gamma^{\text{exp}}(I)}{\rho_a \omega_0^\phi(I)}\right)^{2/3} \quad (6.75)$$

using the rate  $\Gamma^{\text{exp}}(I)$  (6.67) determined from the probability distribution  $P(I)$  of the measured data. We use the mean value of the switching-current distribution  $\langle I_0 \rangle$  as a first estimate of  $I_c$  to calculate the current-dependent small amplitude oscillation frequency  $\omega_0^\phi(I_c, I)$ . For the calculation of the plasma frequency  $\omega_p(I_c, C)$ , the total capacitance of the junction is determined as  $C = 2\text{pF}$ .<sup>11</sup> The effect of the exact value of  $C$  on the experimental results is discussed in some detail later. Additionally, we set  $\rho_a = 1$  and consider the damping dependence of the activation at the end of this section. The resulting experimental  $\Gamma^{\text{norm}}(I)$  data are plotted with a current offset of  $-I_c$  in Fig. 6.16b. As a first observation, we find that the data are approximately linear in the bias current. Thus, we conclude that the cubic approximation of the potential is valid for this experiment. Next, the experimental data  $\Gamma^{\text{norm}}(I)$  are fitted to the expression

$$\left(\frac{E_J}{k_b T_{\text{esc}}} \frac{4\sqrt{2}}{3}\right)^{2/3} \frac{1}{I_c} (I_c - I). \quad (6.76)$$

The solid lines in Fig. 6.16b are linear fits of the form  $f(I) = c_{\text{const}} - c_{\text{lin}} I$  to the data (symbols). From the two fit parameters  $c_{\text{const}}$  and  $c_{\text{lin}}$ , we determine  $I_c$  and  $T_{\text{esc}}$  as

$$I_c = \frac{c_{\text{const}}}{c_{\text{lin}}}, \quad (6.77)$$

$$T_{\text{esc}} = \frac{1}{k_b} \frac{\Phi_0}{2\pi} \frac{4\sqrt{2}}{3} \frac{1}{c_{\text{const}}^{1/2} c_{\text{lin}}}. \quad (6.78)$$

The resulting escape temperatures for different bath temperatures  $T$  are plotted in Fig. 6.17a (solid squares). For comparison, the curve  $T_{\text{esc}} = T$  (solid line) is also plotted in the same figure. The error bars associated with  $T_{\text{esc}}$  are calculated from the root mean squared statistical error of the fit to the experimental data. Obviously, we find good agreement between the physical bath temperature  $T$  and the experimentally determined escape temperature  $T_{\text{esc}}$ .

In Fig. 6.17b, the mean value of the switching current  $\langle I_0 \rangle$  (solid squares) is compared to the fitted value of the critical current  $I_c$  (open triangles). Clearly, the value of  $I_c$  corresponding to the value of current at which the potential barrier disappears (for  $T = 0$ ) is larger than  $\langle I_0 \rangle$  due to the presence of the thermal fluctuations. Both sets of data fit well to the Ambegaokar-Baratoff temperature dependence with  $T_c = 8.7\text{ K}$  and  $I_c^{(0)} = 320\ \mu\text{A}$  for the critical current  $I_c$  and  $T_c = 8.55\text{ K}$  and  $\langle I_0 \rangle^{(0)} = 310\ \mu\text{A}$  for the mean switching current

<sup>11</sup>The total junction capacitance was estimated from the maximum voltages of single-vortex resonances in long junctions on the same chip. This is one of the most accurate techniques to determine  $C$  [Lee91, LB92]. Hypres Inc. [Hyp] quotes a specific capacitance  $C^* = 38\text{ fF}/\mu\text{m}^2$  for their samples, which is in good agreement with our measurements that give  $C^* = 40\text{ fF}/\mu\text{m}^2$ .

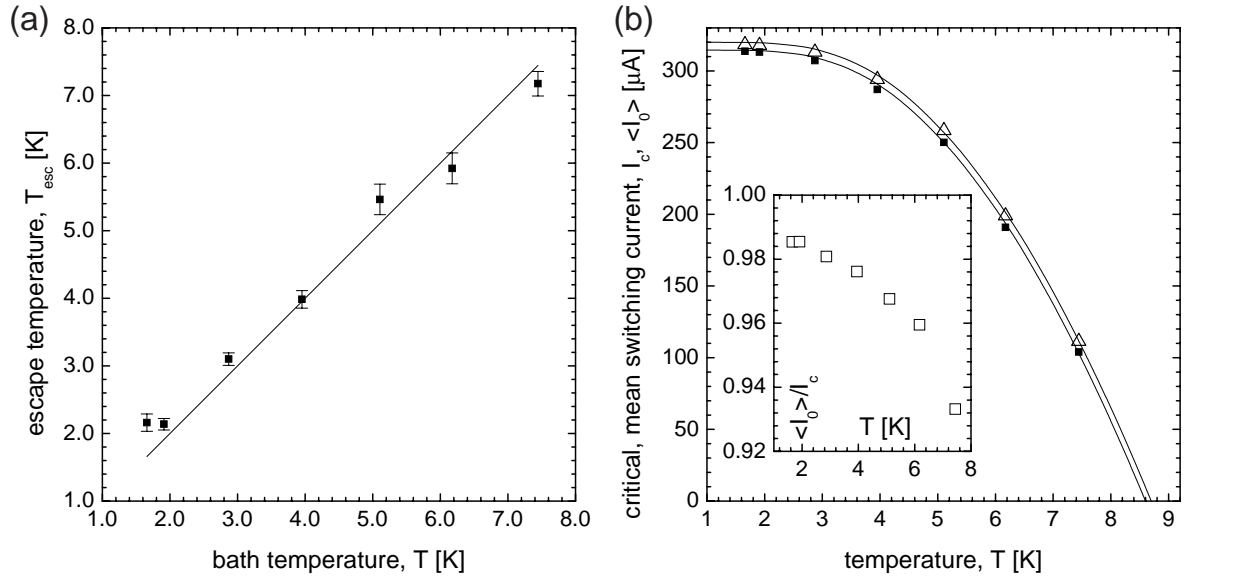


Figure 6.17: (a) Fitted escape temperature  $T_{\text{esc}}$  (squares) vs. thermal bath temperature  $T_{\text{bath}}$ . The solid line indicates the expected dependence  $T_{\text{esc}} = T$ . (b) Mean switching current  $\langle I_0 \rangle$  (solid squares) and critical current  $I_c$  (open triangles) vs. temperature. Solid lines are fits to the Ambegaokar-Baratoff dependence of the critical current on the temperature. In the inset  $\langle I_0 \rangle / I_c$  is plotted vs.  $T$ .

$\langle I_0 \rangle$ . Moreover, we observe that the ratio  $\langle I_0 \rangle / I_c$  plotted in the inset of Fig. 6.17b is close to unity for all temperatures, which is another evidence for the validity of the cubic approximation to the activation potential. A clear suppression of the mean switching current  $\langle I_0 \rangle$  with respect to the fluctuation-free critical current  $I_c$  is observed. The suppression is stronger for higher temperatures.

To cross-check the data evaluation procedure, the values of  $T_{\text{esc}}$  and  $I_c$  determined from the fits have been used to calculate the switching-current distribution  $P(I)$  by numerically integrating Eq. (6.62) using the rate (6.74). The resulting calculated distributions are shown in Fig. 6.16a by solid lines. Excellent agreement between data and simulations is found.

Here, we note that the only parameters supplied to the self-consistent evaluation of  $T_{\text{esc}}$  and  $I_c$  are the total junction capacitance  $C$  and the current sweep rate  $dI/dt$ . The latter is accurately controlled in experiment. To check the influence of the capacitance  $C$  on the result, we have repeated the data analysis doubling and dividing by two the value of  $C$  quoted above. We find that, due to the logarithmically small effect of the value of  $C$  on the normalized rate (6.75), the resulting changes in  $T_{\text{esc}}$  or  $I_c$  are less than 1 % at all measured temperatures and thus, can be neglected with respect to the other experimental errors.

Finally, we consider the damping dependence of the transmission coefficient  $\rho_a$ , which was initially neglected. We note that, similar to the influence of the capacitance, it has only a logarithmically weak effect on Eq. (6.75). For a worst case estimate, we consider the highest temperature, i.e. the highest damping  $a = 1/R_{sg}C$ , and the attempt frequency at the most frequent switching current  $\omega_0^\phi(\langle I_0 \rangle)$ .<sup>12</sup> We estimate  $\rho_a \approx 0.86$  using Eq. (6.7). For the lowest temperature  $T = 1.66$  K, the transmission coefficient  $\rho_a \approx 0.998$  is almost unity. The correction resulting from transmission coefficients  $0.85 < \rho_a < 1$  to the quantities of

<sup>12</sup> $\omega_b = \omega_0$  in the cubic approximation.

interest here is much smaller than 1% and thus, is neglected in this analysis.

In summary, the switching-current distributions of a small junction have been evaluated self-consistently to find the critical current  $I_c$  and the effective temperature  $T_{\text{esc}}$  of the thermal escape of the phase. The parameters  $dI/dt$  and  $C$  have been accurately determined in separate measurements, allowing for a data analysis with no free parameters. The determined escape temperatures are, within the experimental errors, identical with the respective thermal bath temperatures. At low temperatures ( $< 3\text{K}$ ), a small deviation of  $T_{\text{esc}}$  to larger values is observed, possibly indicating the existence of residual electromagnetic noise.

Thus, we have shown that our measurement setup and our data analysis scheme are well suited for switching-current measurements (in the range of a few  $100\ \mu\text{A}$ ) in the thermal activation regime.

### 6.4.2 Magnetic-field induced vortex potential

We have performed measurements of the thermal activation of a single vortex trapped in an annular Josephson junction subject to an in-plane external field. The magnetic dipole interaction of the vortex with the external field giving rise to an effective pinning potential is described in detail in Section 6.2.1. We have performed systematic measurements on the most narrow junction ( $A$ ) of the set of samples listed in Table 4.1, which have been examined with respect to their static and dynamic properties in Chapters 3 and 4.

#### Sample properties

We consider sample  $A$ , which has a mean radius of  $\bar{r} = 48.5\ \mu\text{m}$  and a width of  $w = 3\ \mu\text{m}$ . The current-voltage characteristics and the critical-current diffraction patterns of the junction without trapped flux are plotted in Figs. 6.18 a and b at temperatures between 1.66 and 8.5 Kelvin. The critical-current diffraction pattern is regular and symmetric indicating a good junction quality and a homogeneous bias current distribution. From the diffraction patterns, we have determined the magnetic thickness of the junction as  $\Lambda \approx 200\ \text{nm}$ , see Chapter 3. The normal resistance of the junction  $R_n \approx 0.65\ \Omega$  is temperature independent and its subgap resistance scales exponentially with  $T$ , see Fig. 6.18c. The low subgap resistance indicates good barrier quality and small quasiparticle damping at low temperatures. In Fig. 6.18d, the critical current  $I_c$  of the junction<sup>13</sup> at zero field (solid squares) is plotted versus temperature. Good agreement with the theoretically expected Ambegaokar-Baratoff dependence (solid line) is found with  $T_c = 9.05\ \text{K}$  and  $I_c^{(0)} = 1.53\ \text{mA}$ . We have estimated the critical-current density of the sample as  $j_c = I_c/A \approx 1.6 \times 10^2\ \text{A/cm}^2$ , with the junction area given by  $A = 2\pi\bar{r}w$ . The current jump at the gap  $I_g$ , evaluated according to Ref. [DEK<sup>+</sup>99], is indicated in the same plot by open circles. Its temperature dependence is not well described by the Ambegaokar-Baratoff dependence, probably due to a strong proximity effect [GHG<sup>+</sup>95, ZLZ<sup>+</sup>99] which is consistent with the large knee-structure observed at the gap-voltage in Fig. 6.18a. In the full temperature range, the ratio  $I_c/I_g$  (stars in Fig. 6.18d) is comparable to the value found for the small junction in the previous section. This indicates that the critical current is not substantially reduced by self-field effects or trapped flux.

---

<sup>13</sup>In these measurements, a single realization of the switching current  $I_0$  is identified with the critical current  $I_c$ .

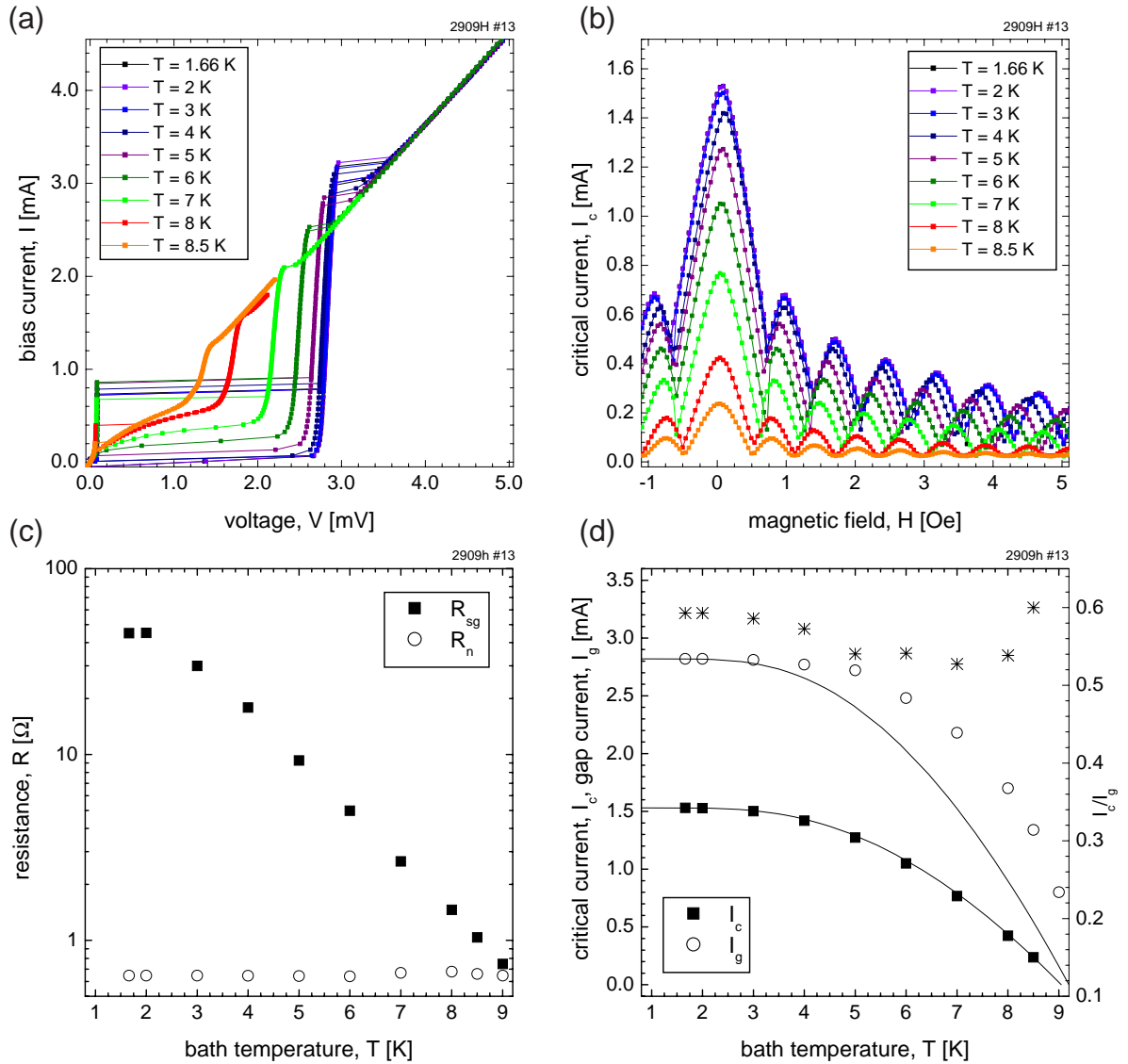


Figure 6.18: (a) Current-voltage characteristic of sample *A* at different temperatures. (b) Critical-current diffraction patterns at the same temperatures. (c) Normal resistance  $R_n$  and subgap resistance  $R_{sg}$  vs. temperature. (d) Critical-current  $I_c$  and gap current  $I_g$  vs. temperature. Solid lines are comparison to Ambegaokar-Baratoff theory. Stars indicate the ratio  $I_c/I_g$ .

As shown in Chapter 4, the junctions can be prepared in a single-vortex state, which is identified by its current-voltage characteristic and critical-current diffraction pattern. The single-vortex resonances at zero field are plotted in Fig. 6.19a for the same set of temperatures. The maximum voltage of the step is  $V_{\max} \approx 85 \mu\text{V}$  at low temperatures, from which we estimate an approximate specific junction capacitance of  $C^* \approx 25 \text{ fF}/\mu\text{m}^2$ . From the shape of the current-voltage characteristic, the effective damping parameters  $\alpha$  and  $\beta$  can be deduced by a fit to perturbation theory, see Section 2.2. The critical-current diffraction patterns in Fig. 6.19b are further evidence for a single vortex being trapped in the junction, see Section 3.2.2.

In the following, I analyze the switching-current distributions of this junction with a trapped vortex for fields smaller than 0.5 Oe, i.e. in the regime in which the critical current

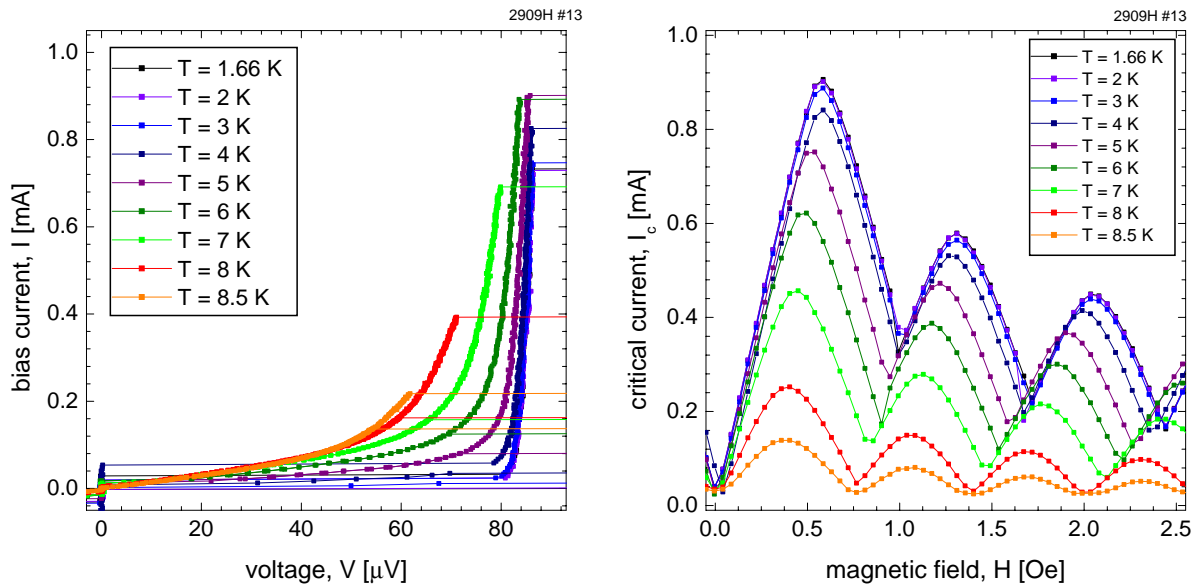


Figure 6.19: (a) Single-vortex current-voltage characteristic of sample *A* at different temperatures. (b) Critical-current diffraction patterns at the same temperatures.

depends approximately linearly on the external field, see Fig. 6.19b. In this regime, the switching of the junction from zero voltage to finite voltage is associated with the activation of the vortex from the field induced potential well.

### Thermal activation measurements

We have performed switching-current measurements at the temperatures  $T = 2, 4$  and  $6$  K in an in-plane external field between  $0.058$  and  $0.464$  Oe aligned parallel to the junction bias leads, see Fig. 6.5a. The field was generated with a current biased cylindrical coil with a field coefficient of  $0.058$  Oe/mA. At each temperature and field value,  $10^4$  switching currents were measured using the technique described in Section 6.3. The data were acquired using a 16-bit AD converter, resulting in a substantially better current resolution as in comparison with the measurements described in the previous section.

As a typical set of data, the switching-current distributions  $P(I)$  for  $H = 0.232$  Oe at  $T = 2, 4$  and  $6$  K are plotted in Fig. 6.20. The histograms have been calculated from the raw data grouping switching currents into bins of width  $\Delta I = 120$  nA, which corresponds to  $m = 4$  times the intrinsic data discretization of  $\delta I \approx 30$  nA. In Fig. 6.20 a to c, the distributions are plotted in a range of  $5 \mu\text{A}$  around the maximum of the distribution, to allow a qualitative comparison of the histograms. The narrowing of the distribution with decreasing temperature due to the reduced thermal fluctuations is clearly observed, while the area under the histogram corresponding to the total switching probability  $\int P(I)dI = 1$  is conserved.

For further data evaluation, the normalized activation rate

$$\Gamma^{\text{norm}}(I) = \left( \ln \frac{2\pi \Gamma^{\text{exp}}(I)}{\rho_a \tilde{\omega}_0^{\gamma^h} \omega_p} \right)^{2/3} \quad (6.79)$$

is calculated using the same procedure as discussed in the last section, but considering the attempt frequency  $\tilde{\omega}_0^{\gamma^h}$  which is specific for the magnetic-field induced vortex potential. In

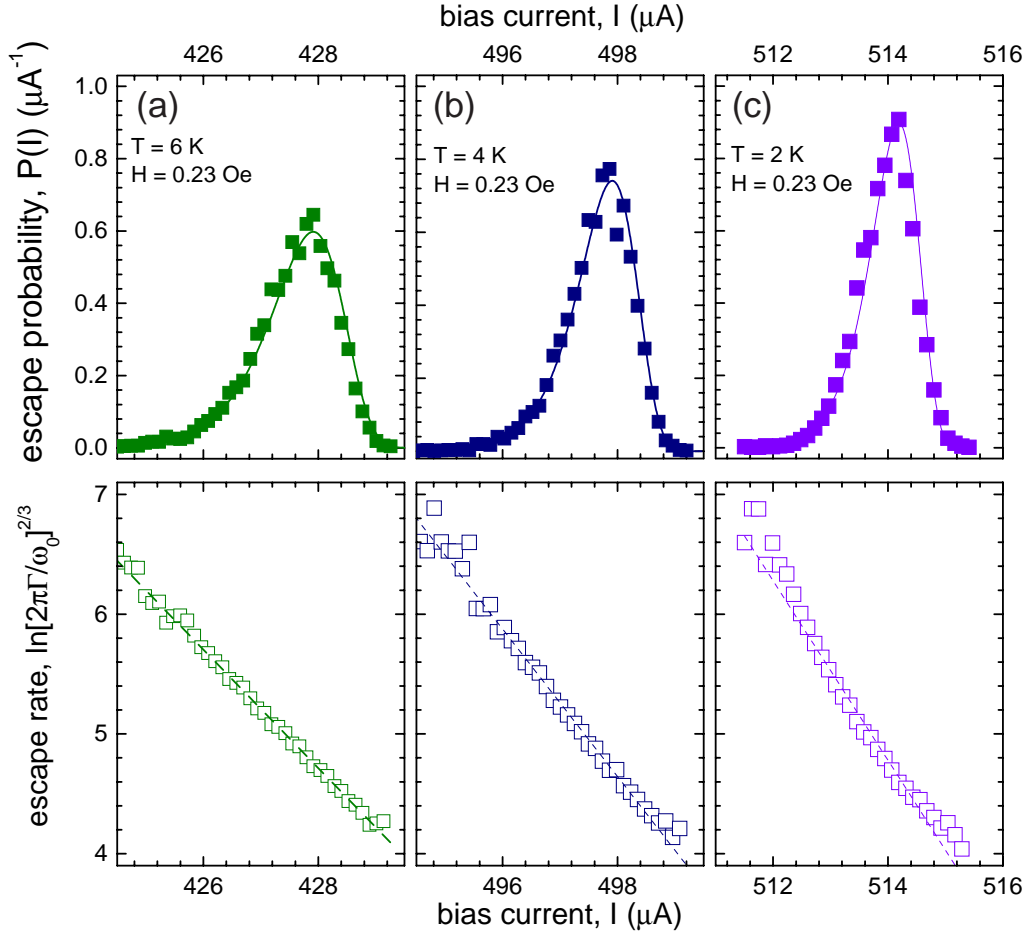


Figure 6.20: Measured switching-current distributions (symbols) at  $H = 0.23\text{ Oe}$  and (a)  $T = 6\text{ K}$ , (b)  $T = 4\text{ K}$  and (c)  $T = 2\text{ K}$ . Experimental normalized activation rates  $\Gamma^{\text{norm}}(I)$  (open symbols) and fits (dashed lines) to extract the escape temperature  $T_{\text{esc}}$  and the depinning current  $I_c^h$ . The calculated probability distributions  $P(I)$  are indicated by solid lines.

Fig. 6.20, we observe a linear dependence of  $\Gamma^{\text{norm}}(I)$  on the bias current indicating the validity of the cubic approximation of the potential. We note that the slope of the data depends on the bath temperature  $T$ . Linear fits to  $\Gamma^{\text{norm}}(I)$  are indicated by dashed lines in the same plots. The data were fitted using the square root of the number of events  $n_j$  registered in each bin as weighting factors, reflecting the Poisson statistics of the probability distribution. From the fits, both the constant and linear term including the errors associated with the fit are determined. Obviously, at high temperatures, the data are fitted well. At the lowest however instead, we observe a deviation of the data from the linear dependence at low and at high bias currents. This deviation indicates an excess of switching current events at these bias currents. This effect can be explained by a gaussian broadening of the switching-current distribution due to spurious non-thermal electromagnetic noise in the measurement setup.

Comparing the data extracted from the fits to the expected dependence of the normalized activation rate on the current given by

$$\left( \frac{\mathcal{E}_0}{k_b T_{\text{esc}}} \ell \gamma_c^h \frac{4\sqrt{2}}{3} \right)^{2/3} \left( 1 - \frac{I}{I_c \gamma_c^h} \right), \quad (6.80)$$

we can extract both the escape temperature  $T_{\text{esc}}$  and the depinning current  $I_c^h = I_c \gamma_c^h$ , where  $I_c$  is the critical current of the junction at zero field and without trapped flux. Using the constant and linear coefficients (see previous section) determined from the fits to the data, we find both quantities as

$$I_c^h = \frac{c_{\text{const}}}{c_{\text{lin}}}, \quad (6.81)$$

$$T_{\text{esc}} = \frac{1}{k_b} \frac{\Phi_0}{2\pi} \frac{4\sqrt{2}}{3} \frac{1}{c_{\text{const}}^{1/2} c_{\text{lin}}}, \quad (6.82)$$

where we have substituted the definitions of  $\mathcal{E}_0$ ,  $\ell$  and  $\gamma_c^h$ . The determined expressions are identical to those found for the small junction but with the reduced critical current  $I_c^h = \gamma_c^h I_c$ , see Section 6.4.1. The attempt frequency  $\omega_0^{\gamma^h}$  can be rewritten as

$$\omega_0^{\gamma^h} = \sqrt{\frac{\Phi_0}{2\pi} \frac{I_c \gamma_c^h}{C}} \sqrt{\frac{\ell}{\tilde{m}_f}} \left( 1 - \left( \frac{I}{I_c \gamma_c^h} \right)^2 \right)^{1/4}. \quad (6.83)$$

We notice the reduction of the attempt frequency by the factor  $\sqrt{\ell/\tilde{m}_f}$  in comparison with the small junction case with reduced critical current  $I_c^h$ . Thus, for the accurate data analysis, not only the junction capacitance  $C$  but also the Josephson length  $\lambda_j$  (inductance  $L^*$ , current density  $j_c$ ) and the junction geometry are parameters to be supplied to the model. All other parameters can be determined self-consistently from the data.

The escape temperatures calculated from the experimental data according to Eq. (6.82) are shown in Fig. 6.21a for the different bath temperatures and magnetic fields in the range of  $H = 0$  Oe to 0.5 Oe. The error bars indicate the uncertainty in the value of  $T_{\text{esc}}$  calculated from the errors in  $c_{\text{const}}$  and  $c_{\text{lin}}$ . We observe a clear scaling of  $T_{\text{esc}}$  with the bath temperature  $T$ . At high temperatures 4 and 6 Kelvin, the experimentally determined values of  $T_{\text{esc}}$  are within 0.5 K of the thermal bath temperatures  $T$  (indicated by dashed horizontal lines) for all values of the magnetic field. The measured escape temperature corresponds to the thermal bath temperature with a relative accuracy of about 10 %. At the lowest temperature however, the fitted  $T_{\text{esc}}$  is notably higher than the bath temperature. As noticed already in Fig. 6.20c, the measured current distribution is not as well described by the theory at 2 Kelvin as it is at the higher temperatures. One of the reasons is the residual electromagnetic noise in the biasing circuits of the junction, which is broadening the switching-current distributions. This effect is noticed in the more narrow distributions at low temperatures and at small fields. Thus, the experimental setup used in this particular measurement allows for accurate analysis of switching-current distributions with a full width of approximately 0.5  $\mu\text{A}$  at half of the maximum height of the probability distribution. Better results should be achieved with improved filtering and analog electronics.

At every bath temperature, we observe a systematic increase of the escape temperature with decreasing magnetic field. These effects suggest a dependence of the escape process on the potential barrier height. They may possibly be explained by a change of the vortex shape due to the external field, which is not taken into account in the collective coordinate model. In the model, we have considered the effect of the magnetic field in terms of a perturbation, which only acts as an external force on the rigid vortex but does not change its shape.

Another possible reason for the observed increase in the effective escape temperature may be the existence of an additional magnetic-field independent pinning force acting on the

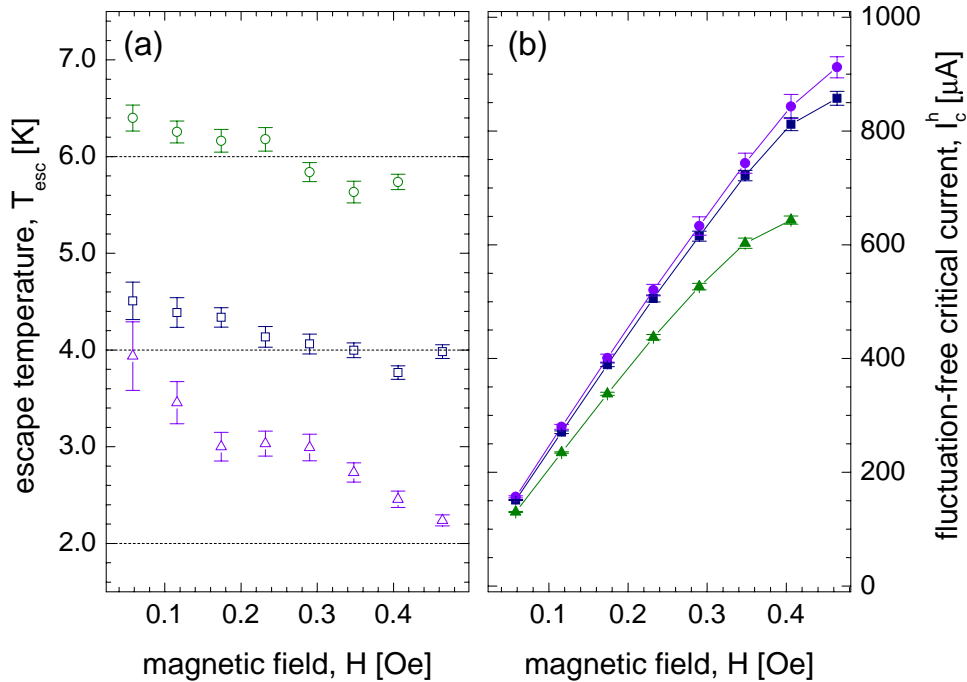


Figure 6.21: (a) Escape temperatures  $T_{\text{esc}}$  (open symbols) and (b) depinning current  $I_c^h$  (closed symbols) in dependence on the externally applied magnetic field at temperatures  $T = 2$  (triangles), 4 (squares), and 6 (circles) K. In (a) the respective bath temperatures are indicated by dashed horizontal lines.

vortex. A possible origin of such a force could be the interaction of the vortex with the bias leads. We are planning experiments in which the coordinate at which the vortex is depinned may be changed by varying the angle at which the magnetic field is applied to the sample. In this way, the pinning of the vortex at the edges of the bias leads may be avoided. The pinning at the junction edges was analyzed qualitatively using low temperature scanning electron microscopy [MDP<sup>+</sup>98].

Recently, we have shown theoretically [FCC<sup>+</sup>00] that a localized magnetic-field independent contribution to the pinning potential can lead to an effective enhancement of the activation rate at low fields. In this regime, the modified escape temperature is given by

$$T_{\text{esc}}^* = T_{\text{esc}} \left( 1 - \frac{2}{3} \frac{I_c^*(0)}{I_c^h(H)} \right)^{-1}, \quad (6.84)$$

where  $I_c^*(0)$  is the depinning current of the vortex in zero field. For an ideal junction  $I_c^* = 0$ . For  $I_c^* \neq 0$  however, the effective escape temperature is increased at low  $H$ . In Fig. 6.22, the measured escape temperatures at 4 and 6 Kelvin are fitted to Eq. (6.84) considering a residual critical current of 20 percent of the critical current at the lowest measured field. Thus, the residual field-independent pinning may explain the increase of the measured escape temperature at low fields. The data for the lowest temperature is not well explained by this model, strengthening the suggestion that electromagnetic noise has influenced those measurements.

The depinning currents  $I_c^h(H)$  are plotted versus the magnetic-field in Fig. 6.21b. The dependence is qualitatively similar to the one shown in Fig. 6.19b, however the  $I_c^h$  values are clearly larger than the mean switching currents  $\langle I_0 \rangle$ . Calculating the ratio  $\langle I_0 \rangle / I_c^h$  we find



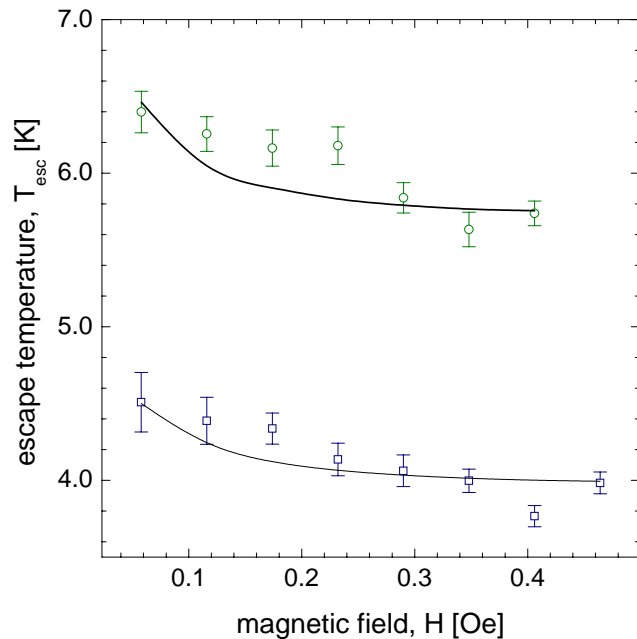


Figure 6.22: Escape temperatures at  $T = 4$  K (open squares) and 6 K (open circles) with fit (solid lines) according to Eq. (6.84).

values between 0.96 for high temperatures and low fields up to 0.99 for low temperatures and high fields. As for the small junctions, the reduction of the transmission coefficient  $\rho_a$  due to damping can be neglected. The worst case analysis for temperatures close to  $T_c$  yields a reduction of  $\rho_a$  to about 0.85. For lower temperatures,  $\rho_a$  quickly approaches unity for the high subgap resistance samples used here. Nevertheless, an experiment may be set up to observe the effect of the damping, e.g. by decreasing  $\rho_a$  to values smaller than 0.5, by working in the high temperature limit or with junction specifically prepared to have a low subgap resistance.

### 6.4.3 Vortex in a microresistor potential

In the set of measurements described in this section, we observe the thermal activation of a vortex pinned at a microresistor. The properties of the potential well considering an ideal microresistor are discussed in Section 6.2.2.

#### Sample properties

We have designed annular Josephson junctions with a width of  $3\ \mu\text{m}$  and a mean radius of  $\bar{r} = 18.5\ \mu\text{m}$ . The junction contains a microresistor in the location indicated in Fig. 6.23a. The microresistor is realized by a  $b = 3\ \mu\text{m}$  wide break in the upper trilayer electrode which is then filled by depositing  $t_p = 200\ \text{nm}$   $\text{SiO}_x$  [GF84, VDKS88]. The whole ring is covered by the wiring layer. In Fig. 6.23b, a cross-section along the length of the junction is plotted in the region of the microresistor.

The current-voltage characteristics of the sample without trapped flux are plotted in Fig. 6.24 at different temperatures. Also shown are the critical-current diffraction patterns which were acquired with the field applied in parallel to the junction bias leads, see Fig. 6.23a. The critical-current patterns are regular and symmetric. No observable change in the patterns due to the microresistor is noticed. From the patterns, we determine a magnetic-field penetration depth of  $\Lambda \approx 200\ \text{nm}$ .

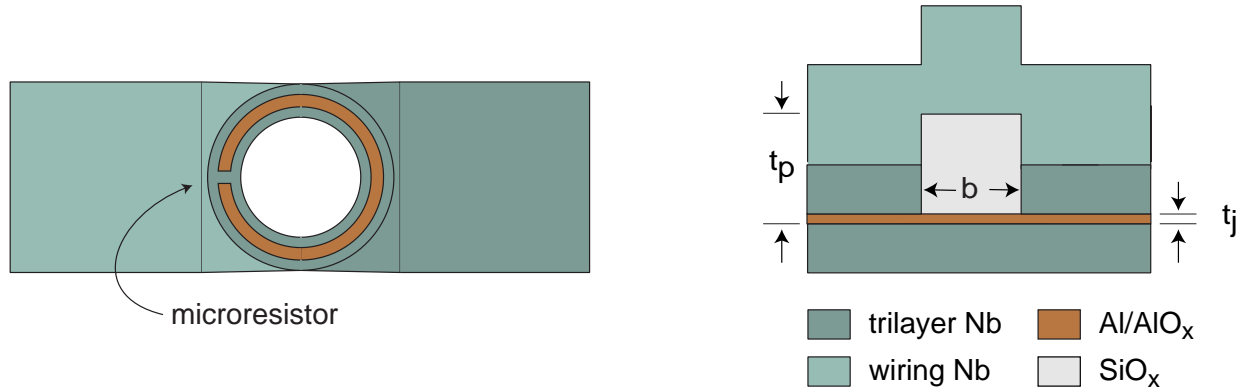


Figure 6.23: (a) Top view of an annular junction with a microresistor realized by a break in the top trilayer electrode in the position indicated by an arrow. (b) Cross-section along the junction length in the region of the microresistor.

Using the usual methods, we have determined the critical current  $I_c$ , the gap current  $I_g$ , the normal resistance  $R_n$  and the subgap resistance  $R_{sg}$  from the current-voltage characteristics. As observed for all other samples, the  $I_c(T)$  dependence fits well to the Ambegaokar-Baratoff theory with  $I_c^{(0)} = 3.4$  mA and  $T_c = 9.05$  K, see Fig. 6.25a. The ratio  $I_c/I_g$  is approximately 0.6 indicating good junction quality and no, or only negligible, suppression of the critical current by trapped flux or self-field effects. Considering the junction area  $A = w(2\pi\bar{r} - b)$ , we find a critical-current density of  $j_c \approx 1.00$  kA/cm<sup>2</sup>. The normal resistance of the sample is approximately  $R_n \approx 0.53 \Omega$ . The subgap resistance changes exponentially with temperature between  $R_{sg} = 75 \Omega$  at 2 K and  $R_{sg} = 0.85 \Omega$  at 8.5 K.

Single vortices could be trapped reproducibly in the junction. The low-current and low-voltage part of the junction characteristics with a single trapped vortex are plotted in Fig. 6.26a. At low temperatures, we observe a rich fine structure on the single-vortex resonances. In the dynamic state, the vortex generates plasma excitations in the junction due to the interaction with the microresistor. The high-voltage part of the fine structure may be explained by the geometric whispering gallery resonances of junction [WUK<sup>+</sup>00]. The lower voltage resonances are similar to those discussed in Ref. [Ust96, UT97]. From the maximum voltage of the single-vortex resonance  $V_{\max} \approx 187 \mu\text{V}$ , we have estimated the effective capacitance of the junction as  $C^* = 40$  fF/ $\mu\text{m}^2$ .

In comparison with the critical-current diffraction pattern without trapped vortex (see Fig. 6.24b), the pattern with a single trapped vortex is drastically modified. As usual, the critical current around zero field is suppressed in the presence of the vortex. However, we observe a peculiar dependence of the depinning current  $I_c$  on  $H$  at very small fields. In the positive field direction  $I_c$  is reduced, whereas in the negative direction  $I_c$  is increased. This effect can be understood qualitatively by considering the sum of the magnetic-field induced potential and the microresistor potential. For one field direction, the depth of the well is increased whereas for the other one, the depth is effectively decreased leading to a change of the depinning current. The dependence of the depinning current on the magnetic-field amplitude and on the direction is to be studied further. Here, we only consider the  $H = 0$  case.

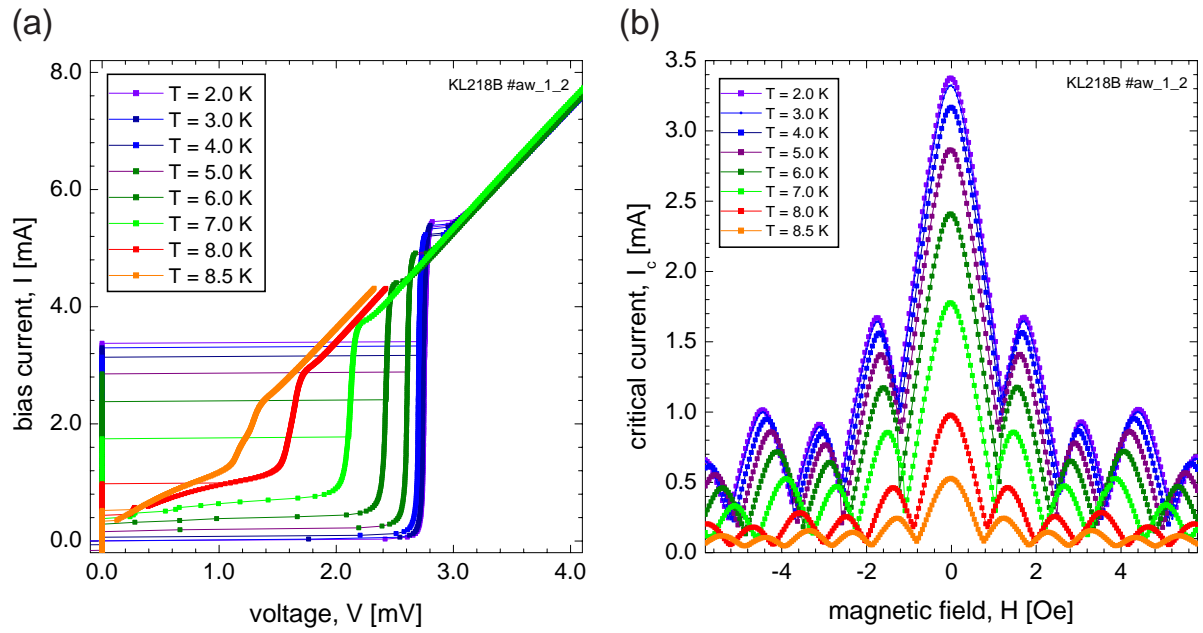


Figure 6.24: (a) Current-voltage characteristics of the sample at temperatures between 2.0 and 8.5 Kelvin. (b) Critical-current diffraction patterns without trapped flux at the same temperatures as in (a).

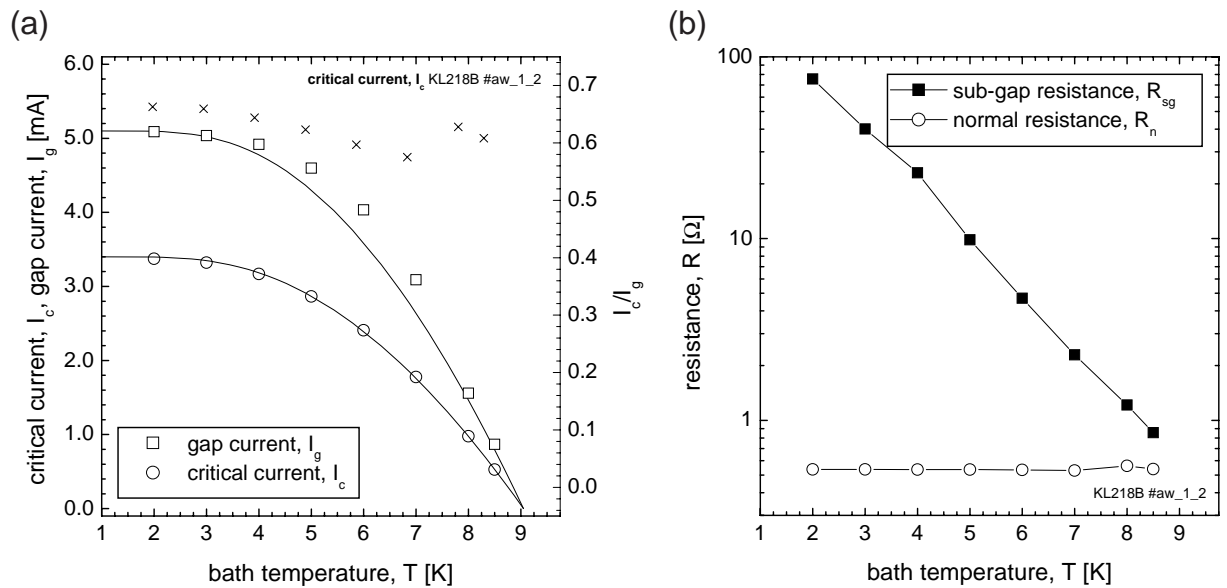


Figure 6.25: (a) Critical current  $I_c$  (open circles), gap current  $I_g$  (open squares) and the ratio  $I_c/I_g$  (stars) vs. temperature. The solid lines are fits to the Ambegaokar-Baratoff  $I_c(T)$  dependence. (b) Normal  $R_n$  (open circles) and subgap resistance  $R_{sg}$  (solid squares) on a logarithmic scale vs. temperature.

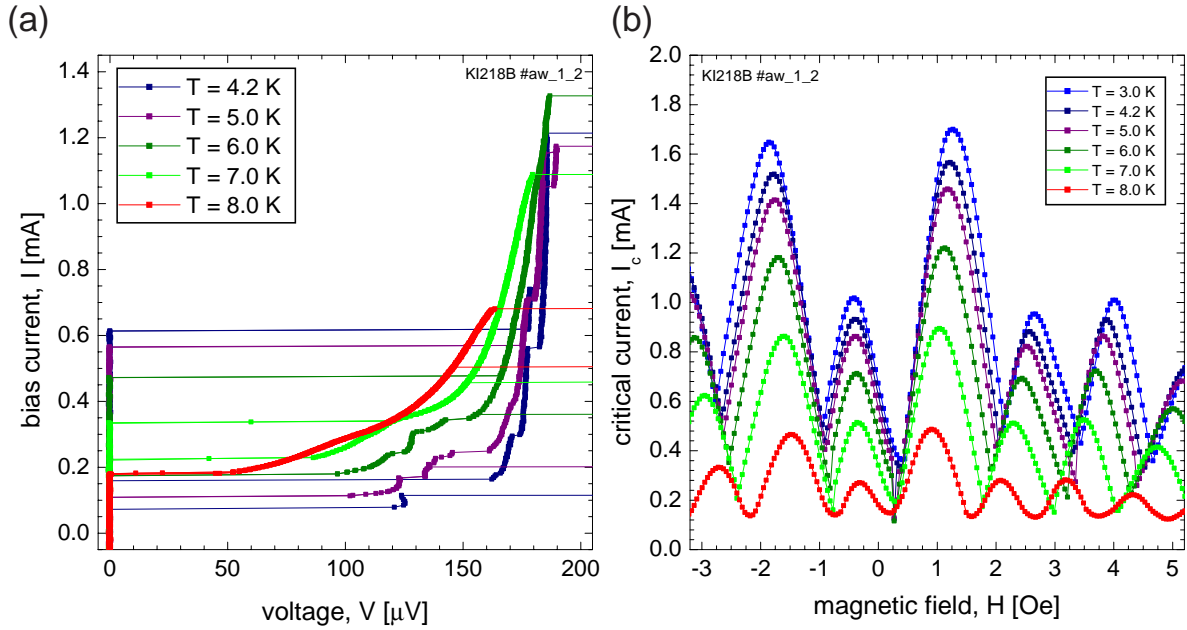


Figure 6.26: (a) Current-voltage characteristics of single-vortex resonances at various temperatures. (b) Critical-current diffraction patterns with trapped vortex.

### Thermal activation measurements

We have measured the thermal activation of a single vortex from the microresistor potential in the sample discussed above at temperatures between 2 and 8 Kelvin. At each temperature,  $10^4$  switching currents have been acquired using the time-of flight technique discussed in Section 6.3. The current sweep rate was adjusted to 0.8 A/s. Two typical switching-current distributions at  $T = 2$  K and at  $T = 6$  K are plotted in the lower part of Fig. 6.27. As before, we observe the broadening of the switching-current distribution with increasing temperature. For a quantitative analysis we calculate the normalized activation rate

$$\Gamma^{\text{norm}}(I) = \left( \ln \frac{2\pi \Gamma^{\text{exp}}(I)}{\rho_a \tilde{\omega}_0^\epsilon \omega_p} \right)^{2/3}, \quad (6.85)$$

using the measured switching-current distributions. The experimentally found dependence of  $\Gamma^{\text{norm}}(I)$  is plotted in the upper part of Fig. 6.27. Again, we observe that  $\Gamma^{\text{norm}}(I)$  is linear in the bias current  $I$ , indicating that the cubic approximation of the microresistor pinning potential is valid. Fitting these data linearly, we determine the two coefficients  $c_{\text{lin}}$  and  $c_{\text{const}}$ . Comparing the fit to the expected current dependence of the normalized activation rate

$$\Gamma^{\text{norm}}(I) = \left( \frac{\mathcal{E}_0}{k_b T_{\text{esc}}} \pi \gamma_c^\epsilon \frac{4\sqrt{2}}{3} \right)^{2/3} \left( 1 - \frac{I}{I_c \gamma_c^\epsilon} \right), \quad (6.86)$$

we have determined the depinning current  $I_c^\epsilon = I_c \gamma_c^\epsilon$  and the escape temperature  $T_{\text{esc}}$  as

$$I_c^\epsilon = \frac{c_{\text{const}}}{c_{\text{lin}}}, \quad (6.87)$$

$$T_{\text{esc}} = \frac{1}{k_b} \frac{\Phi_0 \pi 4\sqrt{2}}{2\pi \ell} \frac{1}{3} \frac{1}{c_{\text{const}}^{1/2} c_{\text{lin}}}. \quad (6.88)$$

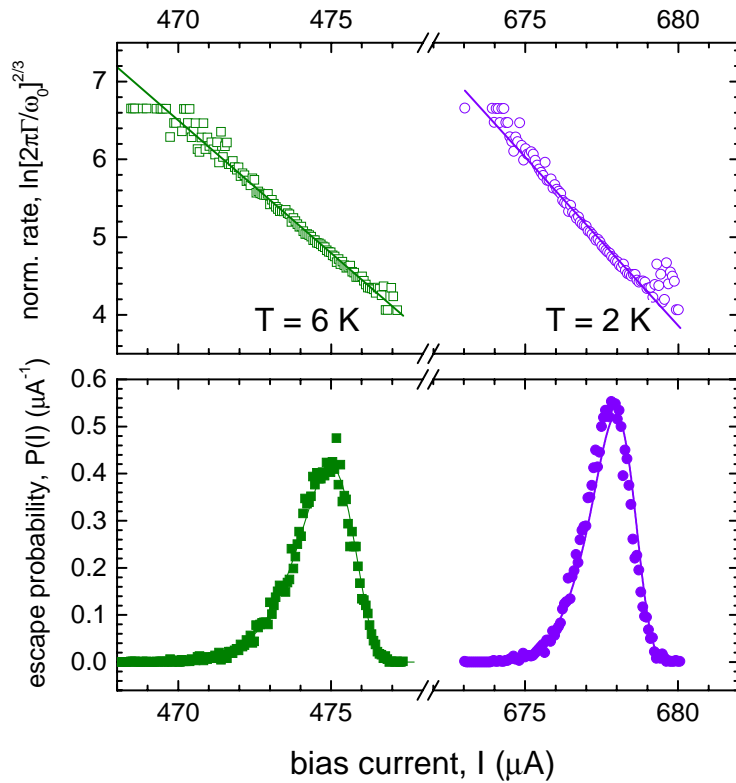


Figure 6.27: Normalized activation rate  $\Gamma^{\text{norm}}(I)$  and switching-current distributions  $P(I)$  at  $T = 2$  K (circles) and  $T = 6$  K (squares). Solid lines are fits to the data.

In Fig. 6.28a, the depinning current  $I_c^\epsilon$  is plotted versus the bath temperature. Due to the temperature dependence of the pinning potential  $\epsilon$ ,  $I_c^\epsilon$  follows well the expression

$$I_c^\epsilon(T) \propto j_c(T)\gamma_c^\epsilon(T) \propto j_c(T)^{3/2}\sqrt{\lambda_L(T)} \quad (6.89)$$

with  $T_c = 9.4$  K and  $I_c^\epsilon(T = 0) = 692 \mu\text{A}$ , see solid line in Fig. 6.28a. The error bars indicate the statistical error of  $I_c^\epsilon$  which is determined from the fit to  $\Gamma^{\text{norm}}(I)$ . The value of the mean switching current  $\langle I_0 \rangle$  with respect to  $I_c^\epsilon$  is plotted in Fig. 6.28. We clearly observe a reduction of  $\langle I_0 \rangle / I_c^\epsilon$  with increasing temperature due to the increasing thermal fluctuation.

The effective escape temperature  $T_{\text{esc}}$  calculated from the data according to Eq. (6.88) is in good approximation linear in the bath temperature  $T$ . However, we find from our measurements that  $T_{\text{esc}}$  is systematically about 65 % smaller than the bath temperature of the cryostat. To compare the escape temperature with the bath temperature we have multiplied  $T_{\text{esc}}$  by a constant factor of  $t^* = 1.55$ . The resulting dependence is plotted in Fig. 6.28b. The error bars represent the statistical errors due to the fit and the uncertainty in the normalized junction length  $\ell$ , see Eq. (6.88). Considering the renormalized escape temperature  $t^*T_{\text{esc}}$  the agreement with the bath temperature is satisfactory. At low temperatures, we observe a slight increase of  $t^*T_{\text{esc}}$ , due to residual electromagnetic noise in the bias circuitry. This effect was observed also in the measurements described in the previous sections. At high bath temperatures, we also observe a slight increase of  $t^*T_{\text{esc}}$  with respect to the expected values. Here, we point out that the analysis of the switching-current distributions in this large temperature range is less accurate because the strong temperature dependence of the superconducting parameters  $j_c(T)$  and  $\lambda_L(T)$  has to be considered. We have implemented these temperature dependencies into the data analysis. However, at

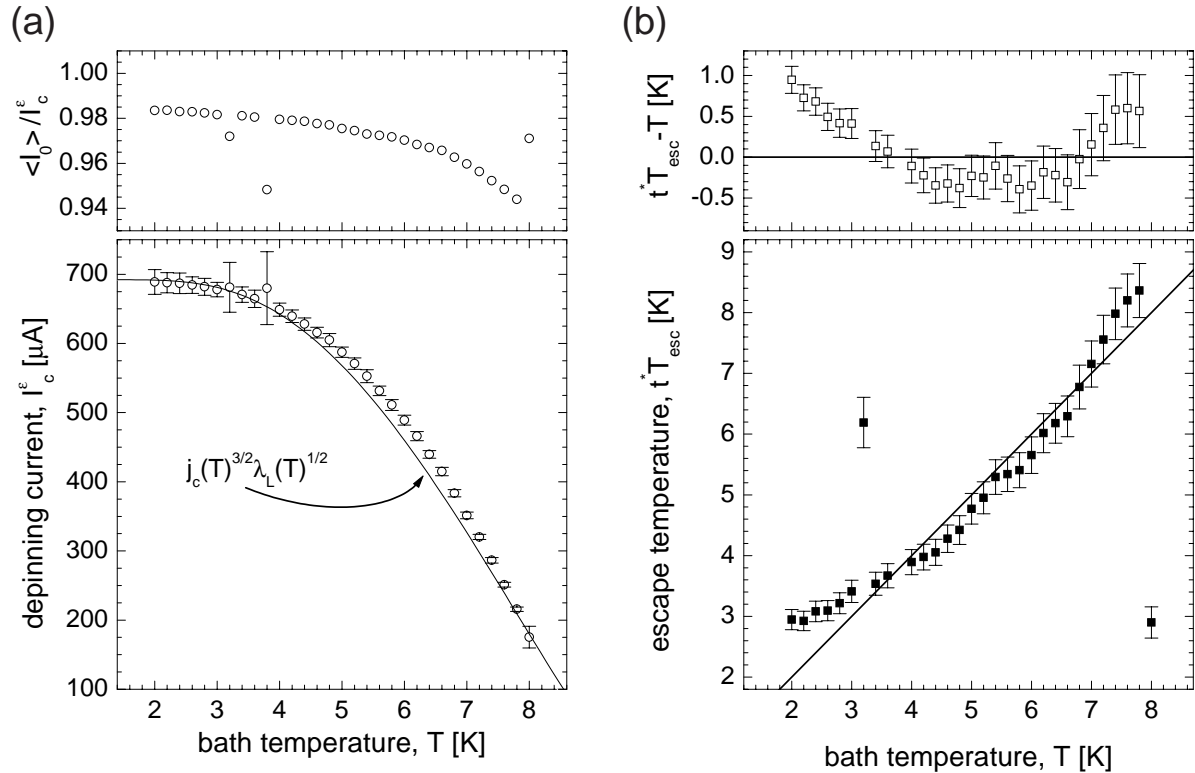


Figure 6.28: (a) The fluctuation-free depinning current  $I_c^\epsilon$  versus  $T$ . The solid line is a fit to Eq.(6.89); also plotted is  $\langle I_0 \rangle / I_c^\epsilon$ . (b) Escape temperature  $t^* T_{\text{esc}}$  versus bath temperature  $T$ . The dependence  $t^* T_{\text{esc}} = T$  is indicated by a solid line. Also plotted is the difference  $t^* T_{\text{esc}} - T$  versus  $T$ .

high temperatures ( $T > 6$  K) the errors in the estimated parameters are larger than at low temperatures.

In the remainder of this section, I discuss possible reasons for the reduced  $T_{\text{esc}}$  as determined from the measured data. According to Eq. (6.88),  $T_{\text{esc}}$  is proportional to  $1/\ell \propto \lambda_J$ . Thus, a bad estimation of  $\lambda_J$  may result in an incorrect value of  $T_{\text{esc}}$ . In the calculations discussed above, we have neglected the effect of the idle region on  $\lambda_J$  (compare Chapter 5). Considering the renormalized Josephson length  $\lambda_{\text{eff}}$  as in Eq. (5.13) with  $2w_p/w_j \approx 1.7$  and an inductance ratio  $\lambda \approx 0.5$  (see Eq. 5.7), we find  $\lambda_{\text{eff}} \approx 1.4\lambda_J$ . The phenomenological factor  $t^* \approx 1.55$  is close to the factor of the enhancement of the effective Josephson length, due to the presence of an idle region. Thus, the renormalization of  $\lambda_J$  due to the idle region does partially explain the observed effect.

Moreover, we note that in our samples the microresistor is realized by a 200 nm thick  $\text{SiO}_x$  layer deposited on top of the tunnel barrier to suppress the critical current. The model discussed in Section 6.2.2 considers solely this local suppression of  $j_c$ . However, this particular realization of a microresistor also modifies the effective inductance and capacitance of the junction. The junction inductance is increased at the microresistor by the factor  $L_p^*/L_j^* = (2\lambda_L + t_p)/(2\lambda_L + t_j) \approx 2$ , which increases the magnetic energy of the junction. The effective potential for the vortex due to the inductance change can then be expressed as

$$\tilde{U}^L(q) = - \int_0^\ell \epsilon_L \delta(\tilde{x}_0) \frac{1}{2} \phi_{\tilde{x}}(\tilde{x} - q)^2 d\tilde{x} = 2\epsilon_L \frac{1}{\cosh^2 q}, \quad (6.90)$$

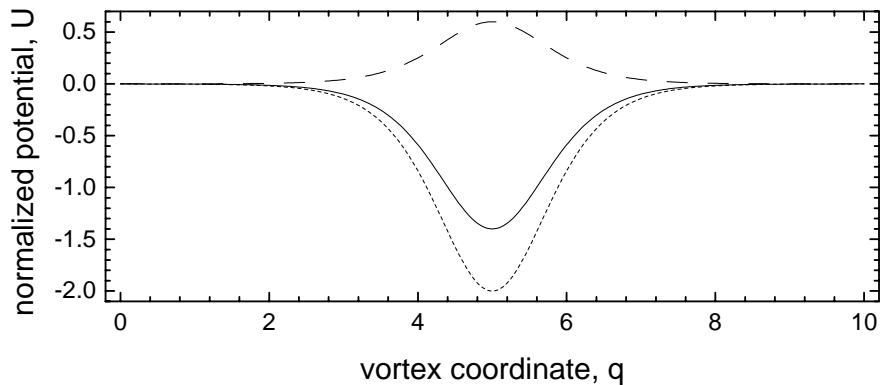


Figure 6.29: Effective static vortex potential  $U(q)$  due to an ideal microresistor with  $\epsilon = -1$  (dotted line) and an ideal inductance change (dashed line) with  $\epsilon_L = 0.5$ . The solid line is the sum of the two potentials.

where  $\epsilon_L = (L_p^*/L_j^* - 1)b/\lambda_J$  is the strength of the ‘microinductor’. For the junction parameters considered here, the depth of the pure microresistor vortex-potential is effectively reduced due to the increase of the magnetic energy of the junction at the resistor. To illustrate the effect, the pure microresistor potential and the same potential including the inductance change are plotted in Fig. 6.29 for  $\epsilon = -1$  and  $\epsilon_L = 0.5$ . Due to the identical shape of the pure microresistor potential and the pure microinductor potential, the combined potential can be described as a localized potential with the effective strength  $\epsilon_{\text{eff}} = \epsilon + \epsilon_L$ . Thus, within this consideration, the modification of the potential due to the microinductor can be treated consistently in our model by considering  $\epsilon_{\text{eff}}$  instead of  $\epsilon$ .

In addition, at the microresistor the junction capacitance is reduced by a factor of 100 due to the 200 nm thick  $\text{SiO}_x$  barrier. The capacitance decrease results in an increase of the effective plasma frequency by a factor of 10 at the microresistor. Thus, the attempt frequency of the vortex may be strongly enhanced, depending on the average distance between the vortex and the microresistor. In a crude approximation, assuming an increased average attempt frequency, one expects a reduction of the width of the switching-current distribution, which is in qualitative agreement with the experimental observation of a reduced escape temperature.

The modifications in the vortex potential due to the inductance and capacitance change in the region of the microresistor may be taken into account quantitatively. However, this would involve a more complicated data analysis. In the future, we plan experiments in which both the width of the resistor and the thickness of the insulator are to be varied in order to quantify the observed effects for different parameters of the microresistor potential.

## 6.5 Summary and conclusion

I have investigated experimentally the thermal activation of a single Josephson vortex from a metastable state. An experimental setup has been developed to measure the switching-current distributions of Josephson junctions at temperatures between 1.5 K and 9.2 K. A data analysis scheme to extract the characteristic quantities of the thermal escape process from the switching-current distributions has been implemented. The setup and the data

analysis have been tested successfully by measuring the thermal activation of the phase in a small Josephson junction. Within the experimental accuracy, the measured escape temperature is identical to the thermal bath temperature for these samples. No free parameters are used in the data analysis.

The thermal escape of a single Josephson vortex from a magnetic-field induced and a microresistor induced potential has been considered. The dynamics of the Josephson vortex in the potential well has been described in terms of a quasiparticle of mass  $m_f$  with generalized coordinate  $q$ . The characteristic properties of the potentials in dependence on the bias current and the electrical and geometrical parameters of the samples have been investigated. The measured switching-current distributions are well described considering the thermal activation of the vortex from a metastable state. The activation from the magnetic-field induced potential has been analyzed self-consistently, without any free parameter. For the microresistor however, an additional fitting parameter is required to relate the effective escape temperature to the bath temperature. Within the experimental errors the effective vortex escape temperature is identical to the bath temperature, indicating that the escape process is well described by the used models.

In future experiments, the activation of vortices is to be investigated for a variety of pinning potentials. The characteristics of the potential can be modified by shaping the junction in an external field (see Chapter 8) and by implementing different types of microresistors and microshorts or other local modifications of the junction properties. Using the measurement technique discussed in this chapter, we intend to investigate the activation of the phase considering the transition from discrete Josephson junction arrays with varying inter-junction coupling to continuous long junctions. Such experiments allow to systematically examine the multi-dimensional activation of the phase as suggested in Ref. [DMS99]. Only few experiments on such systems have been performed until now [CTC+96].

Moreover, we intend to perform activation measurements of vortices at lower temperatures. Using a newly acquired  $^3\text{He}$  cryostat, temperatures between 2 K and 250 mK can be achieved. In this temperature range, the fluctuation-free critical current of Nb Josephson tunnel junctions is almost temperature-independent allowing for a more accurate analysis of data. Performing similar measurements at even lower temperatures in a  $^3\text{He}$ - $^4\text{He}$  dilution refrigerator, we intend to observe the quantum properties of Josephson vortices as discussed in Chapters 7 and 8.



# Chapter 7

## Quantum Properties of Josephson Vortices in Annular Junctions

The main objective of our experiments with Josephson vortices in annular junctions is the observation of macroscopic quantum effects. As suggested in theoretical works [KI96, SBJM97], the Josephson vortex may tunnel through a potential barrier out of a metastable state. Here, we propose to form the pinning potential for the vortex using the external magnetic field [WKL<sup>+</sup>00]. In contrast to the microresistor pinning potential suggested earlier in literature [KI96], our approach allows to modify the cross-over temperature between quantum and thermal regime in situ during experiment. We discuss the important experimental conditions to observe macroscopic quantum tunneling of the vortex and show that these can be met using the experimental setup developed for vortex activation measurements. We also discuss the feasibility of observing the energy level quantization of vortex states in the potential well.

### 7.1 Macroscopic quantum tunneling

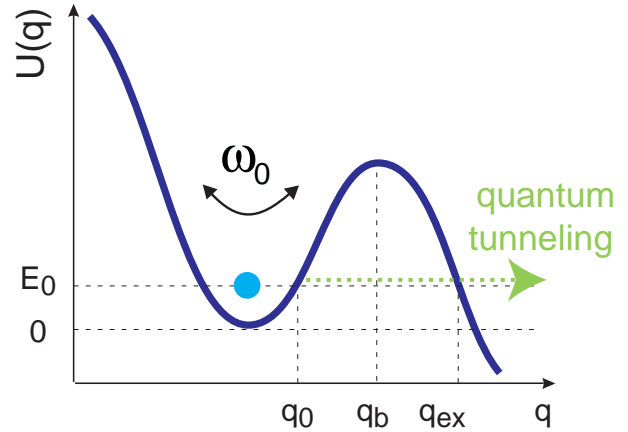
The thermal activation of a vortex from a potential well is exponentially suppressed as the thermal bath temperature  $T$  is decreased, see Eq. (6.6). At low temperatures, the quantum tunneling through the potential barrier becomes the dominating process. The theory of macroscopic quantum tunneling of a single Josephson vortex from a microresistor potential has been recently developed in Refs. [KI96, SBJM97]. Here, we adopt this theory to discuss the case of a vortex in a magnetic-field induced potential well. The magnetic-field induced potential has the considerable advantage that the potential barrier may be varied in situ during the experiment.

The rate of escape of a particle of mass  $m$  from a metastable state in a potential well  $U(q)$  can be calculated in the quasi-classical Wentzel-Kramers-Brillouin (WKB) approximation [LL79] as

$$\Gamma_{\text{qu}} = \text{const.} \omega_0 \left( \frac{U_0}{\hbar\omega_0} \right)^{1/2} \exp \left( -2 \int_{q_0}^{q_{\text{ex}}} \frac{1}{\hbar} \sqrt{2m(U(q) - E_0)} dq \right), \quad (7.1)$$

where  $q$  is the particle coordinate,  $q_0$  is the entrance point into the potential barrier and  $q_{\text{ex}}$  the exit point, defined by the intersection between the ground-state energy level  $E_0$  of the particle in the well and the potential, see Fig. 7.1. For sufficiently simple potentials, e.g.

Figure 7.1: Sketch of a potential well. The energy of the ground state of the particle is  $E_0$ ; the entrance and exit points of the particle in the potential barrier are indicated by  $q_0$  and  $q_{ex}$ .



the quadratic plus cubic potential in Eq. (6.21), the WKB approximation (7.1) is explicitly solved [Leg84]

$$\Gamma_{\text{qu}} = \omega_0 \left( \frac{60U_0}{\hbar\omega_0} \right)^{1/2} \left( \frac{18}{5\pi} \right)^{1/2} \exp \left( -\frac{36}{5} \frac{U_0}{\hbar\omega_0} \right). \quad (7.2)$$

The tunneling of the particle in the presence of damping can be described using the Caldeira-Leggett theory [CL81, Cal83, Leg84]. In this approach, the damping is phenomenologically modeled as a coupling of the particle degree of freedom to an infinite number of harmonic oscillators in the environment. It was shown [CL81, Cal83, Leg84] that the quantum mechanical tunneling rate of a particle out of a cubic potential in the presence of the damping  $a$  can be expressed as

$$\Gamma_{\text{qu}} = A \exp(-B) \quad (7.3)$$

with

$$A = \sqrt{60}\omega_0 \left( \frac{B}{2\pi} \right)^{1/2} (1 + \mathcal{O}(a)), \quad (7.4)$$

$$B = \frac{36U_0}{5\hbar\omega_0} (1 + 1.74a + \mathcal{O}(a^2)), \quad (7.5)$$

where the damping has been considered up to the first order in the exponent. According to Eq. (7.3), the quantum tunneling rate is reduced due to the increase of the exponential factor  $B$  in dependence on the normalized damping coefficient  $a$ .

This model can be adopted to describe the quantum tunneling of a vortex out of a magnetic-field induced potential well. It is useful to consider the WKB approximation in the normalized units of the sine-Gordon equation. Rewriting Eq. (7.1), we find

$$\Gamma_{\text{qu}} = \text{const.} \tilde{\omega}_0 \omega_p \left( \frac{\mathcal{E}_0 \tilde{U}_0}{\hbar\omega_p \tilde{\omega}_0} \right)^{1/2} \exp \left( -2 \int_{q_0}^{q_{ex}} \frac{\mathcal{E}_0}{\hbar\omega_p} \sqrt{2\tilde{m}_f(\tilde{U}(q) - \tilde{E}_0)} dq \right), \quad (7.6)$$

where we can identify  $\hbar\omega_p/\mathcal{E}_0$  as the normalized Planck constant [KI96]

$$g^2 = \frac{\hbar\omega_p}{\mathcal{E}_0} = \alpha_f 16\pi \left( \frac{d't}{w^2\epsilon_j} \right)^{1/2}, \quad (7.7)$$

with  $\alpha_f = e^2/(4\pi\epsilon_0\hbar c) = 1/137$  being the fine structure constant. The quantum character of the vortex scales with  $g^2$ , being inversely proportional to the junction width  $w$

Table 7.1: Typical electrical and geometrical junction parameters.

quantity	unit	approximate value	meaning
$j_c$	[A/cm <sup>2</sup> ]	100	critical-current density
$C^*$	[fF/ $\mu\text{m}^2$ ]	30	specific capacitance
$d'$	[nm]	200	magnetic thickness
$\bar{r}$	[ $\mu\text{m}$ ]	50	mean junction radius
$w$	[ $\mu\text{m}$ ]	3.0, 0.3	junction width

and proportional to the square root of the magnetic thickness  $d'$  and the inverse junction capacitance  $t_j/\epsilon_j$ . Since the junction capacitance and its magnetic thickness are mainly determined by the material properties, the remaining crucial parameter is the junction width  $w$ . Thus, quantum effects of vortices should be more pronounced in narrow long junctions than in wide ones. For a junction of width  $w = 3\ \mu\text{m}$  and typical electrical parameters (see Table 7.1), the normalized Planck constant is  $g^2 \approx 1.0 \times 10^{-3}$ . We also note that  $g^2$  is proportional to the inverse ratio of the vortex energy and the plasmon energy.

### 7.1.1 Calculated switching-current distributions: Cross-over from thermal activation to quantum tunneling

Quantum tunneling of a vortex from the magnetic-field induced potential well may be detected by measuring the switching-current distribution at low temperatures. With decreasing temperature, the thermal activation is exponentially suppressed and the  $P(I)$  distribution is dominated by quantum effects. To estimate the possibility to observe quantum tunneling, we have calculated numerically switching-current distributions. In the calculations, we have used sample parameters (see Table 7.1) similar to those of the thermal activation experiments presented in Section 6.4.2. In particular, I discuss two different junction widths, i.e.  $w = 3.0\ \mu\text{m}$  which can still be fabricated using standard photolithographic techniques, and  $w = 0.3\ \mu\text{m}$  which is the most narrow high quality long Josephson junction ever fabricated [KWF<sup>+</sup>99].

Using the expressions for the magnetic-field induced barrier height  $\tilde{U}_0^{\gamma h}$  (6.44) and the small amplitude oscillation frequency  $\tilde{\omega}_0^{\gamma h}$  (6.43), the switching-current distributions in the thermal regime are calculated by evaluation of Eq. (6.62) with the rate (6.6). For simplicity, we have used a transmission coefficient of  $\rho_a = 1$ . The probability distributions are calculated for a  $w = 0.3\ \mu\text{m}$  wide junction in a normalized field of  $\bar{h}/2\pi = 0.4$  of intermediate strength at a current sweep rate of  $dI/dt = 0.04\ \text{A/s}$ . The current sweep rate corresponds to approximately  $4j_c 2\pi r w \times 100\ \text{Hz}$ . In practice, the amplitude of the current sweep should not be increased substantially above the critical current of the junction due to the increased probability of trapping flux at large currents. The calculated switching-current distributions are plotted in Fig. 7.2 for bath temperatures between 500 mK and 10 mK.<sup>1</sup> As expected we observe a strong reduction of the distribution width with decreasing temperature. At the same time, the mean switching current  $\langle I_0 \rangle$  approaches  $I_c^h$  due to the decrease of thermal fluctuations. The  $P(I)$  distribution for the escape of the vortex from the well due to quantum tunneling at zero temperature is shown in the same plot. The rate expression (7.3) with vanishing damping  $a = 0$  was used for the calculation. For better

<sup>1</sup>Experimentally, temperatures in this range can be achieved with <sup>3</sup>He-<sup>4</sup>He dilution refrigerator technology [Pob95].

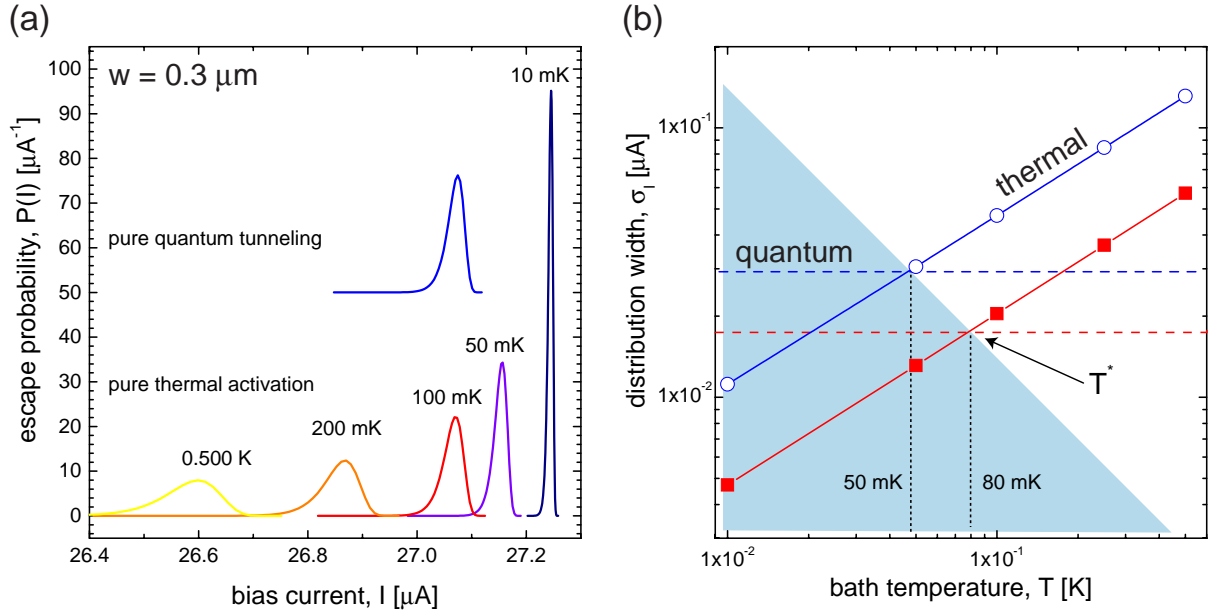


Figure 7.2: (a) Simulated thermal escape probability  $P(I)$  for different thermal bath temperatures  $T$ . The quantum escape  $P(I)$  distribution at  $T = 0$  is shown with an offset of  $50 \mu\text{A}^{-1}$ . (b) Variance  $\sigma_I$  of the thermal distribution in dependence on  $T$  for  $w = 3.0 \mu\text{m}$  (open circles) and  $w = 0.3 \mu\text{m}$  (solid squares). The variance of the temperature-independent quantum distributions are shown by horizontal dashed lines. The cross-over temperature  $T^*$  for the narrow junction is indicated by an arrow. The shaded area indicates the region in which quantum tunneling dominates.

visibility, the distribution is offset by 50 units in  $P(I)$ . Obviously, the quantum probability distribution is similar to the thermal distribution at about 100 mK. Thus, at temperatures below 100 mK we expect a substantial broadening of  $P(I)$  due to quantum tunneling of the vortex out of the metastable state.

In Fig. 7.2b, the standard deviation  $\sigma_I$  of  $P(I)$  is plotted versus temperature for both the temperature-dependent thermal activation (solid squares) and the temperature-independent quantum tunneling (dashed horizontal line). The intersection between the two corresponds to the *cross-over temperature*  $T^*$ . For these particular sample parameters ( $w = 0.3 \mu\text{m}$ ), this external field and this current sweep rate, we find a cross-over temperature of about 80 mK. At temperatures  $T > T^*$ , the switching-current distribution is dominated by thermal activation, whereas for  $T < T^*$  quantum tunneling is the main escape process. In experiment, this cross-over should be observable as a saturation of the width  $\sigma_I$  of the switching-current distribution at low temperatures. Equivalently, this corresponds to a saturation of the escape temperature  $T_{\text{esc}}$  at small  $T$ . Similar experiments have been performed considering the quantum tunneling of the phase in point-like junctions [MDC87].

Additionally, the distribution widths  $\sigma_I$  are plotted in Fig. 7.2b for a  $3 \mu\text{m}$  wide junction (open circles). For this junction width  $T^* = 50 \text{ mK}$ , which is substantially lower than for the more narrow junction. This is expected because the normalized Planck constant, determining the quantum character of a vortex, is smaller for wide junctions. We also note that the cross-over appears at an approximately twice larger absolute distribution width  $\sigma_I$ . At the same time, the mean value of the switching current is roughly proportional to the junction width, such that the relative current resolution  $\sigma_I / \langle I_0 \rangle$  required for an

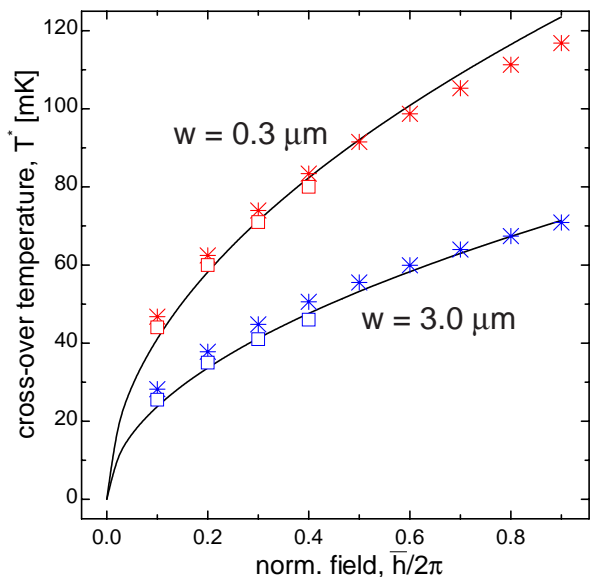


Figure 7.3: Cross-over temperature  $T^*$  in dependence on the external field for the junction widths  $w = 0.3 \mu\text{m}$  (upper data set) and  $w = 3.0 \mu\text{m}$  (lower data set). The data calculated from Eq. (7.8) are indicated by stars, the data found from numerically calculated  $P(I)$  curves are indicated by open symbols. Both curves are compared to a  $\sqrt{h}$  dependence (solid lines).

experiment with a wider junction is higher. Varying the junction width  $w$ , we can adjust the temperature range in which quantum escape dominates, see shaded area in Fig. 7.2b. The more narrow the junction, the smaller is  $\sigma_I$  and the higher is  $T^*$ .

Analytically, the cross-over temperature can be defined as the temperature at which the thermal and the quantum escape rates are equal. Neglecting the prefactors but considering damping, the cross-over temperature for a cubic potential is given by [HGIW85]

$$T^* = \frac{\hbar\omega_0}{2\pi k_b} \left( \sqrt{1+a^2} - a \right), \quad (7.8)$$

where  $a$  is the damping constant. The influence of the damping parameter  $a$  on the quantum switching-current distribution has been considered. For temperatures below 1 K the damping parameter  $a$  is typically<sup>2</sup> less than  $10^{-2}$ . In this regime, the reduction of the tunneling rate, leading to a narrowing of the switching-current distribution due to ohmic dissipation, is negligibly small. However, in an experiment, the effective dissipation may be substantially larger due to fluctuations in the environment [TLvdW<sup>+</sup>99].

Substituting the attempt frequency  $\tilde{\omega}_0^{\gamma^h}\omega_p$  into Eq. (7.8) with  $a = 0$ , we find

$$T^* = \frac{\hbar\omega_p}{2\pi k_b} \sqrt{\frac{\hbar}{\tilde{m}_f}} \left[ 1 - \left( \frac{I}{I_c^h} \right)^2 \right]^{1/4}, \quad (7.9)$$

where we identify three different contributions to the cross-over temperature. First, the cross-over temperature is proportional to the plasma frequency  $\omega_p \propto j_c^{1/2}$ , the value of which is determined during fabrication. Second,  $T^*$  is proportional to the square root of the external field  $H$  which can be modified easily during experiment. Finally,  $T^*$  depends on the ratio of  $I/I_c^h$ . This effect can be estimated by considering the most probable switching current  $\langle I_0 \rangle$  and calculating the expression  $[1 - (\langle I_0 \rangle / I_c^h)^2]^{1/4}$ , the bias current dependence of which is plotted in Fig. 6.10.

We have evaluated the cross-over temperature  $T^*$  from numerically determined switching-current distributions in dependence on the external field for the junction parameters discussed above, see Fig. 7.2. We compare those values (open squares) to the ones calculated

<sup>2</sup>See, for example, Master's thesis of A. Franz [Fra99].

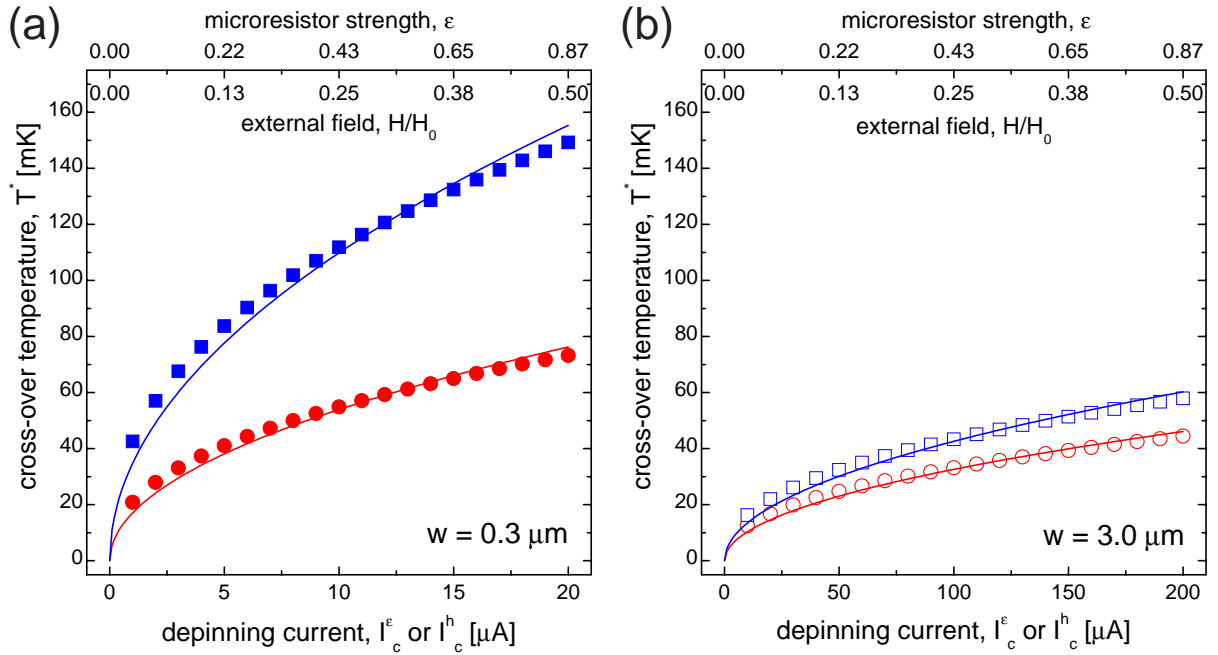


Figure 7.4: Vortex escape cross-over temperature  $T^*$  in dependence on the depinning current  $I_c^h$  and  $I_c^\epsilon$  for the magnetic-field induced potential (circles) and the microresistor potential (squares). The corresponding potential parameters  $H/H_0 = h$  and  $\epsilon$  are quoted on the top axes. The  $\sqrt{I_c^h}$  and  $\sqrt{I_c^\epsilon}$  are indicated by solid lines. (a) Data for  $w = 0.3 \mu\text{m}$ . (b) Data for  $w = 3.0 \mu\text{m}$ .

analytically (stars) from Eq. (7.8) using the same parameters and the mean switching current  $\langle I_0 \rangle$ . The data are shown in Fig. 7.3 for  $w = 0.3 \mu\text{m}$  (upper data set) and for  $w = 3.0 \mu\text{m}$  (lower data set). Good agreement is found between the analytical and numerical calculations. In particular the increase of the cross-over temperature with the applied magnetic field is well described by Eq. (7.9). The data are compared to the expected  $\sqrt{h}$  dependence, see solid lines in Fig. 7.3, and good agreement is found.

We note that the cross-over temperature  $T^*$  is substantially smaller for the wider junction than for the more narrow one. The increase in  $w$  leads to a larger barrier height due to the increase of  $\mathcal{E}_0$ . At the same time, the activation takes place at currents closer to the critical current, i.e.  $\langle I_0 \rangle / I_c^h$  is closer to unity. Thus, the attempt frequency  $\omega_0$  is reduced, resulting in a smaller tunneling rate and, hence, a smaller cross-over temperature, see Eq. (7.9). Thus it is most likely to observe the quantum escape of a vortex from a magnetic-field induced potential well, using narrow junctions and large fields.

Additionally, we have compared the cross-over temperature of the escape from the magnetic-field induced potential to the one from the microresistor potential. To perform the comparison, we have numerically calculated switching-current distributions in the quantum regime adjusting the potential depth (parameterized by  $h$  and  $\epsilon$ , respectively), such that the fluctuation-free depinning currents  $I_c^h$  and  $I_c^\epsilon$  are identical for both potentials. Then,  $T^*$  was estimated according to Eq. (7.8), using the numerically found mean depinning current  $\langle I_0 \rangle$ . The resulting values of  $T^*$  are shown in Fig. 7.4 for the sample parameters quoted in Table 7.1. At the same depinning current ( $I_c^h = I_c^\epsilon$ ), the cross-over temperature is substantially larger for the escape from the microresistor potential than for the escape from the magnetic-field induced potential, see Fig. 7.4. This is understood noting that the

small amplitude oscillation frequency of the vortex is higher in the spatially more localized potential. For the wider junctions ( $w = 3.0 \mu\text{m}$ ) however, the difference in the cross-over temperature is smaller because in this regime  $T^*$  is governed by the factor  $\langle I_0 \rangle / I_c$ , which is closer to unity for wider junctions, see Fig. 7.4b. All data obey with good accuracy a scaling according to  $\sqrt{I_c^h}$  or  $\sqrt{I_c^\epsilon}$  respectively, see solid lines in Fig. 7.4.

In conclusion, the higher cross-over temperatures can be realized using microresistor potentials. In the magnetic-field induced potential however, the dependence of the cross-over temperature on the magnetic field allows to verify the quantum nature of the saturation of the switching-current distribution more directly because the dependence of  $T^*$  on  $H$  can be tested experimentally using a single sample. In this way, electromagnetic noise (being independent of  $H$ ) can be excluded as the origin of a broadened switching-current distribution. To perform the same tests for the microresistor potential, the cross-over temperatures of different samples with different strengths of the microresistor have to be compared.

### 7.1.2 Experimental requirements

To experimentally observe the quantum tunneling of a vortex, the sample has to be cooled to temperatures of approximately 100 mK or below. These temperatures can be achieved using a  $^3\text{He}$ - $^4\text{He}$  dilution refrigerator. Since the cooling power of a dilution-refrigerator is small at these temperatures, constraints on the possible critical current and resistance of the sample do exist. In Fig. 7.5a, the cooling power of an ‘Oxford 300’ bottom loading dilution refrigerator is plotted versus temperature. Obviously, the available cooling power decreases strongly with decreasing temperature according to a power law. For comparison, the power dissipated in an annular Josephson junction with  $j_c \approx 160 \text{ A/cm}^2$  and  $w = 3 \mu\text{m}$  at  $T = 2 \text{ K}$  is plotted on a logarithmic scale versus bias current in Fig. 7.5b. If the junction is biased on the fluxon resonance, the dissipated power is below  $0.1 \mu\text{W}$  which can be easily handled by the dilution refrigerator at base temperature. As the junction switches to the gap voltage, the dissipated power increases suddenly to above  $1.0 \mu\text{W}$  and continues to increase to about  $20 \mu\text{W}$  in the normal state. Biased at the gap voltage, a junction of these parameters dissipates more power than the refrigerator can support at 10 mK. At 50 mK the dissipated power is balanced with the cooling power of the cryostat. Both axis in Fig. 7.5b scale linearly with the critical-current density  $j_c$  and the junction width  $w$ . Thus, reducing  $w$  effectively reduces dissipation, whereas increasing  $j_c$  to increase the cross-over temperature is only possible at the cost of increased dissipation.

Above we have considered an infinitely large heat conductance between the sample and the cryostat. However, the sample is usually prepared on an insulating  $\text{SiO}_x$  wafer which has a poor thermal conductivity. The heat generated in the sample should be small enough to allow for sufficient cooling through the substrate and wiring. This can be achieved by biasing the junction only at currents which generate voltages across the junction identical to or smaller than the maximum voltage of the single-vortex resonance. This is only possible for the field range in which the junction switches from  $V = 0$  to the vortex resonance. For larger fields (approximately  $h > 0.5$ ), the junction switches directly to the gap voltage. To avoid extra heating in this situation, a circuit which reduces the bias current immediately after the junction has switched to a finite voltage state [MDC87] and, thus, minimizes the dissipated power, has to be used. Alternatively, the junction may be thermalized by setting the bias current to 0 for a certain time after each switching event. Thus, one has to choose

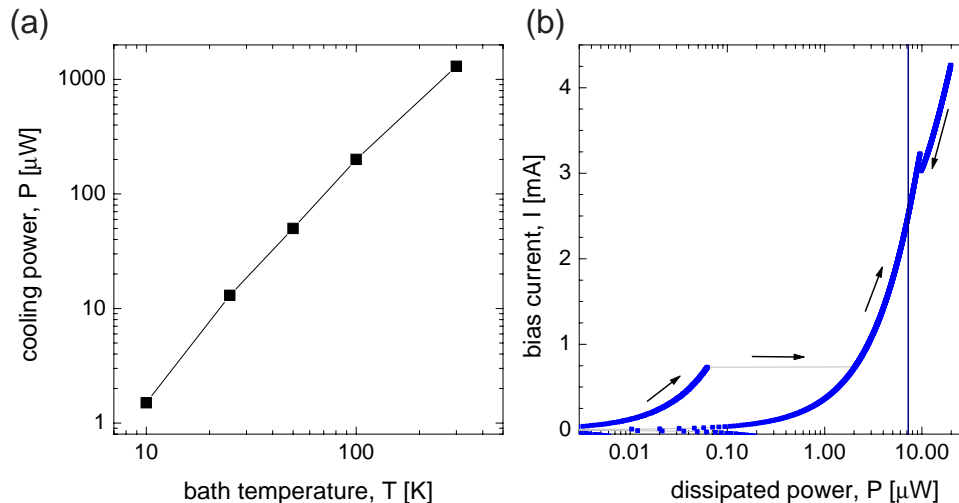


Figure 7.5: (a) Cooling power  $P$  versus temperature  $T$  for an ‘Oxford 300’ dilution refrigerator. (b) Dissipated power  $P$  in dependence on the bias current  $I$  for a typical  $3\ \mu\text{m}$  wide junction with a trapped fluxon. The vertical line indicates the average power dissipated in a cycle with a constant current sweep rate.

sample parameters such that the cross-over temperature is large enough to be measured conveniently and, at the same time, assuring a proper thermalization of the sample after each switching event.

Another important issue is the attainable current resolution. As estimated in numerical simulations, one needs to properly resolve a quantum switching-current distribution with  $\sigma_I \approx 0.02\ \mu\text{A}$  for a  $0.3\ \mu\text{m}$  wide junction. The equipment limited current resolution using the time-of-flight techniques is conservatively estimated approximately to  $100\ \text{pA}$ . However, the most narrow distributions measured accurately for a  $3\ \mu\text{m}$  wide junctions has a  $\sigma_I$  of  $0.5\ \mu\text{A}$ . With the currently available setup described in Section 6.3, we expect to attain a well resolved switching-current distributions with  $\sigma_I$  down to  $0.05\ \mu\text{A}$  for  $0.3\ \mu\text{m}$  wide junctions, since the relative accuracy of our measurement setup scales with the current range required. To attain even better resolution, we need to avoid interference due to electromagnetic pickup in the sample wires and decrease the noise in the current read-out electronics. Measures to be implemented include:

- installation of current sources and preamplifiers at room-temperature on the top of the cryostat to avoid external wiring
- use of isolation amplifiers to decouple current-control and voltage-readout from the sample bias circuit
- better grounding

An electrically hermetic sample holder, acting as a Faraday-cage, has been designed and fabricated. Its function is to shield the sample from high frequency radiation in the environment. The biasing leads are fed into the sample box through custom-made in-wall low-pass filters. We have tested the performance of different filter technologies including copper powder filters [MDC87] and miniature coaxial lines [Zor95]. For both types of filters,



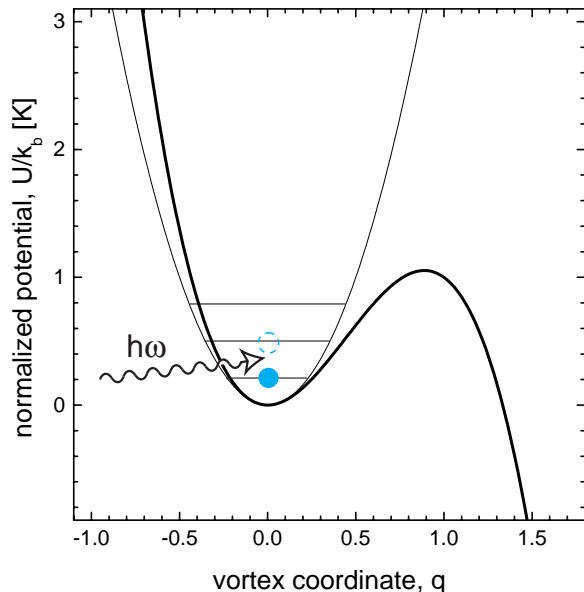


Figure 7.6: Quadratic approximation to energy levels in a cubic potential. Applying external radiation of frequency  $\omega = \Delta E/\hbar$  excites the vortex from the ground state to the excited state.

we have measured an attenuation of approximately -50 dB in the frequency range between 2 and 20 GHz.<sup>3</sup> Thin-film on-chip circuits may also serve as effective filters [VOJ<sup>+</sup>95].

Using these techniques, we are optimistic to achieve the current resolution required to perform a quantum tunneling experiment with a Josephson vortex in the near future.

## 7.2 Energy level quantization

The energy levels of a quantum particle trapped in a potential well are quantized. If at low temperatures the lifetime-broadened width of an individual energy level is smaller than the energy separation between neighboring levels, the discrete energy levels of the particle may be observed in an experiment. The energy level quantization has been observed in small junctions [MDC87, SPRR97] and in rf-SQUIDS [RHL95]. We expect to observe the quantization of the energy levels of a Josephson vortex trapped in a magnetic-field induced metastable state in an annular junction.

We consider the vortex trapped in a potential well as depicted in Fig. 7.6. We assume that the barrier separating the ground state from the continuum is large enough to suppress quantum tunneling and small enough to allow thermal activation. At low temperatures and in thermal equilibrium, the vortex occupies the ground state of the well with the largest probability. The population of higher levels is exponentially suppressed. Using a harmonic approximation of the well around its classical minimum, the energy levels in the well are determined by

$$E_n = \left(n + \frac{1}{2}\right)\hbar\omega_0, \quad (7.10)$$

where  $n$  is the quantum number of the harmonic oscillator with the characteristic frequency  $\omega_0$ . Considering the vortex in the magnetic-field induced potential, the separation in energy

---

<sup>3</sup>The network analyzer used for the characterization of filters has a frequency band between 45 MHz and 20 GHz.

between individual levels is determined by the small amplitude oscillation frequency

$$\omega_0 = \sqrt{\frac{U''(0)}{m_f}} \quad (7.11)$$

of the vortex at the minimum of the well, see Eq. (6.43). Thus the energy level spacing is given by

$$\Delta E = \hbar \omega_p \sqrt{\frac{\hbar}{\tilde{m}_f}} \left[ 1 - \left( \frac{I}{I_c^h} \right)^2 \right]^{1/4}. \quad (7.12)$$

Obviously, the energy level separation is proportional to the plasma frequency of the junction and to the square-root of the external field  $H$ . Moreover, it depends on the relative bias current  $I/I_c^h = \bar{\gamma}$  as shown in Fig. 6.10. We note that the energy level separation is independent of the junction width. The number  $n$  of energy levels in the well can be estimated within the harmonic approximation by calculating the quantity  $U_0/\hbar\omega_0$ . For the vortex in a magnetic-field induced potential, the number  $n$  of levels is given by

$$n \approx \frac{1}{g^2} \frac{16}{3} \sqrt{\hbar} \frac{1}{2^{1/4}} \left( 1 - \frac{I}{I_c^h} \right)^{5/4}. \quad (7.13)$$

The energy level quantization can be observed by measuring the thermal activation of the vortex from a quantized energy level. At low temperatures and in thermal equilibrium, the vortex occupies the ground state of the well. Excited states have a small occupation if the energy level separation is larger than the thermal energy. To observe the activation from different energy levels for  $\Delta E > k_b T$ , a non-equilibrium distribution of vortex-states in the well is required. This can be achieved by irradiating the vortex with a microwave, which induces the resonant transition of the vortex from the ground state to the first excited state. Due to the inharmonic potential well, the electromagnetic radiation is only resonant with a single pair of energy levels. Depending on the bias current, the probability of the vortex to be activated is large if its energy level is close to the top of the barrier and small if it is far away from the barrier giving rise to a modulation of the  $P(I)$  distribution. Experiments observing this effect have been performed successfully for small Josephson junctions [MDC87].

Here, we consider a vortex trapped in a typical annular junction (see Table 7.1) of width  $0.3 \mu\text{m}$  in order to estimate the experimental parameters required for the observation of energy level quantization. At temperatures  $T < 1 \text{ K}$ , the thermal activation of the vortex from a well induced by a magnetic field of  $h \approx 0.5$  takes place in the current range of  $0.95 < I/I_c^h < 1.00$ . For these bias currents, less than 10 levels are present in the well. We find a level separation  $\Delta E$  on the order of a few 100 mK, which corresponds to a required excitation frequency between 10 and 20 % of the junction plasma frequency of 50 GHz.

Alternatively, a non-thermal distribution of states can also be realized by using very high current-sweep rates [SPRR97]. If the activation rate of the vortex from an excited state is larger than the relaxation rate from level to level, a non-thermal distribution of states is realized. Again, this distribution of states can be measured by performing an activation measurement in which the quantized energy levels lead to a modulation of the  $P(I)$  distribution. Such experiments have been performed with small Josephson tunnel junctions, where the energy level quantization well above the cross-over temperature has been observed [SPRR97].

As pointed out before, to resolve the different energy levels in experiment, the width  $W_{if}$  of the transition between the initial state  $i$  and the final state  $f$  has to be less than the level spacing  $\Delta E_{if} = E_f - E_i$ . The width  $\Delta E_j$  of each individual level  $j$  is inversely proportional to the lifetime  $\tau_j$  of that state. According to Refs. [EDM86, MDC87], the lifetime  $\tau_j$  at low temperatures can be estimated accurately by considering the ground-state fluctuations of the effective resistance of the junction. As pointed out in the same reference, the ratio  $W_{01}/\Delta E_{01}$  is proportional to the damping  $a$  of the oscillation in the well. According to that approximation, it should be possible to resolve the energy levels of the vortex, since the ohmic contribution to  $a$  is less than  $10^{-2}$  at  $T < 4.2$  K for typical samples. However, the effective damping  $a$  may be strongly modified by the external biasing circuitry [EDM86].

### 7.3 Summary and conclusion

We have considered the macroscopic quantum tunneling of a Josephson vortex from a field induced potential well. By varying the magnetic field, we can conveniently modify the pinning potential for the vortex during experiment. We expect that the quantum tunneling of the vortex from the potential well should dominate thermal activation at temperatures below 100 mK, depending on the magnetic field amplitude and the width of the junction. To achieve a high cross-over temperature, it is favorable to use narrow junctions which have already been developed in our group [KWF<sup>+</sup>99]. In general, the measurement setup developed for vortex activation measurements is suitable to observe quantum tunneling of the vortex. However, we still need to reduce electromagnetic interference by improving the filtering and shielding of the sample. A number of filter designs have been realized and tested for this purpose. If the quantum tunneling of the vortex is not substantially suppressed by fluctuation-induced dissipation, we are optimistic to observe this effect in experiments in the near future. As an intermediate step, we plan to observe the energy level quantization of the vortex in the magnetic-field induced potential well. This quantum effect is easier to observe experimentally because it can be investigated by measuring switching-current distributions of a non-equilibrium population of vortex states in the thermal regime.

# Chapter 8

## A Vortex in a Double-Well Potential:

### A Path towards Macroscopic Quantum Coherence and Quantum Computation

A method for engineering a magnetic-field induced double-well potential for a Josephson vortex by shaping a long junction is discussed. The two lowest energy states of the vortex in the double-well potential can be identified by performing a depinning current measurement. In the quantum limit, the vortex states in the double-well potential may serve as a macroscopic quantum mechanical two-state system. An experiment to observe the coherent oscillation of the vortex between the two states is suggested. Such a coherent two-state system may be used as a qubit in a quantum computation scheme.<sup>1</sup>

## 8.1 Introduction

The quest for new quantum coherent two-state systems has been stimulated by the ideas of using quantum mechanical systems to perform computation [Llo93, DiV95b]. In *quantum computers*, quantum mechanical variables such as spins, photons or atoms are used to store and process information.<sup>2</sup> The basic unit of information in a quantum computer is called a *qubit* [Sch95]. In contrast to a classical bit, a qubit can also be in a quantum mechanical superposition of its two basis states 0 and 1, thus storing the information much more efficiently. In a quantum computer, information is processed by coherent interactions between different qubits. It has been shown theoretically that a quantum computer can solve certain computationally complex problems [Cle99] much more efficiently than any classical

---

<sup>1</sup>Parts of this chapter have been published in ‘Journal of Low Temperature Physics **118**, 543 (2000)’

<sup>2</sup>For recent reviews on the theoretical foundations of quantum computing, see Refs. [BD00, Ste97].

computer, the most prominent example being the factoring of large numbers [LP92]. Most of today's secure communication schemes rely on encryption of data using protocols like RSA, in which a product of two large prime numbers is used to encode the data. The security of the RSA scheme is due to the fact that the product of two prime numbers is very difficult to factorize by any classical computer. In fact, it can be shown that the time needed to do this calculation depends exponentially on the size of the number. On a quantum computer however, this calculation can be done with an exponential speed-up in comparison with a classical computer, using the Shor algorithm [Sho94]. A number of other algorithms, including searching entries in a data-base [Gro97], have been developed. Moreover, it has been shown that any task that can be solved on a classical computer can also be solved on a quantum computer [DiV95b]. The first very basic quantum algorithms have been implemented and tested experimentally and the principle of their operation has been demonstrated [CVZ<sup>+</sup>98, JMH98]. In these experiments, the possibility to solve certain tasks more efficiently than on a classical computer has been demonstrated. Thus, quantum computing may be a useful means to process information.

By now, qubits have been implemented in different physical systems including cavity electrodynamics [THL<sup>+</sup>95], ion traps [MMK<sup>+</sup>95] and spins [GC97]. Also first algorithms have been shown to perform well in quantum computers containing a small number of qubits [CVZ<sup>+</sup>98, JMH98]. However, most experimental realizations proposed so far rely on the use of microscopic quantum systems as the quantum variable. These systems have the advantage that they can be isolated effectively from the environment, thus reducing decoherence. On the other hand, the physical properties of microscopic systems are given by nature and, therefore, the design of a prospective quantum computer is less flexible. Macroscopic quantum systems however are interesting candidates to *design* a quantum computer.

The macroscopic systems proposed for use as qubits are based on nano-structured electronic circuits using either quantum dots or tunnel junctions as their basic elements. All macroscopic systems suffer from the drawback that they are more difficult to isolate from the environment and therefore they are more prone to decoherence. On the other hand, the fact that they can be designed and implemented in a chip-based technology using modern lithography techniques creates more flexibility in the design and the scaling of the quantum computer. At the same time, these macroscopic systems are much closer in fabrication and operation to conventional computers than any of the microscopic realizations, which is a considerable advantage.

The use of superconductors in the design of macroscopic qubits has two main advantages: the coherence of the superconducting condensate and the reduced number of degrees of freedom in the superconducting state. The first will help to design qubits and the second to reduce decoherence. Superconducting qubits proposed so far fall into two main classes, i.e. charge qubits and flux qubits [Ave00]. In charge qubits, the charge states of an electron box [BVJ<sup>+</sup>98] are used as the basis states of the qubit. The superposition of states and the existence of coherent Rabi-oscillations of such a qubit have been recently verified experimentally in a ground-breaking experiment [NPT99, NT00]. Moreover, schemes to couple and operate this type of qubit have been devised [MSS99]. In flux qubits, circuits of somewhat larger Josephson junctions are used to design two-state systems, the dynamics of which is governed by the superconducting phase difference across the junction rather than by the charge. The rf-SQUID qubit [BHF97] follows the classical approach of using a SQUID as a macroscopic quantum coherent system [LCD<sup>+</sup>87]. Even though the quantum mechanical

properties of the rf-SQUID are thoroughly investigated [SSAL85, RHL95, HRL96, HRL00], its coherent oscillation between two states could not be verified experimentally until now [BvWdBO83, Tes90, Col95]. The failure of observing the macroscopic quantum coherence in rf-SQUIDS is attributed to the insufficient decoupling of the system from the environment. A proposal trying to circumvent parts of these problems is the persistent current qubit [MOL<sup>+</sup>99, OMT<sup>+</sup>99]. In this proposal, the qubit is implemented using a loop of three junctions, in which two opposite circulating currents are the basis states. Due to the design of the system using three junctions, it is predicted theoretically that it may be much less prone to decoherence than the rf-SQUID [OMT<sup>+</sup>99]. The principles of operation of the persistent current qubit in a quantum computer are developed [OMT<sup>+</sup>99] and decoherence is considered in some detail [OMT<sup>+</sup>99, TLvdW<sup>+</sup>99]. Other proposals using multi-junction loops are under development. In particular the use of  $\pi$ -junctions [WvHL<sup>+</sup>93], which have an unconventional current phase relation, may be interesting to design qubits [IGF<sup>+</sup>99, BGI99]. The combination of conventional and  $\pi$ -junctions in a single circuit allows to design new types of qubits, which are decoupled more effectively from the environment [IGF<sup>+</sup>99].

Our interest in this subject is related to the possibility of using macroscopic quantum states of Josephson vortices for quantum computation. We suggest that two distinct states of a fluxon trapped in a field-controlled double-well potential inside a narrow long junction can be used for designing a qubit [WKL<sup>+</sup>00]. We propose that by varying the external magnetic field and the junction shape, one is able to form an arbitrarily-shaped potential for a fluxon in a junction [WKL<sup>+</sup>00]. The amplitude of this potential can be varied in experiment by tuning the magnetic field. Under sufficient decoupling from the environment and provided that the temperature and dissipation in the junction are low enough, the superposition of two macroscopically distinct quantum states is expected to be observed, also see Ref. [KI96]. The superposition of the states may be observed by measuring the energy splitting of the degenerate ground state of the system. We propose a scheme to measure the coherent transition, i.e. the Rabi-oscillation of the vortex between the two degenerate states in the time domain. The preparation of the initial state for a quantum coherence measurement may be achieved by turning the magnetic field in the plane of the junction, and the final state of the vortex can be read out by performing an escape measurement [WKU00].

In Section 8.2, we introduce the idea to engineer the magnetic dipole potential of a vortex by shaping the junction. The basic quantum mechanics of a Josephson vortex in a double-well potential are discussed in Section 8.3. We point out in Section 8.4 how the vortex states may be manipulated classically by adjusting the bias current and the field applied to the junction. How to use these ideas to perform a macroscopic quantum coherence measurement is presented in Section 8.5. In the last two sections of this chapter, we discuss how to manipulate states of our *vortex-qubit* to perform computation and point out relevant decoherence mechanisms.

## 8.2 Engineering the vortex potential

As pointed out already in Section 6.2.1, the magnetic dipole energy of a vortex in an external magnetic field depends on the angle between its magnetic moment, which is essentially perpendicular to the junction perimeter, and the external field. In the simple case of an annular junction, the potential is sinusoidal, see Eq. (6.35). By shaping the junction, it is possible to form magnetic-field induced potentials which are more complex and therefore

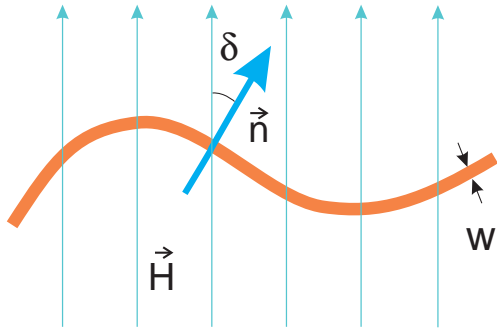


Figure 8.1: Arbitrary junction geometry in a homogeneous external field  $\vec{H}$ . The angle  $\delta$  between  $\vec{n}_J$  and  $\vec{H}$  determines the potential energy of the vortex.

more interesting [WKL<sup>+</sup>00]. In principle, long Josephson junctions can be fabricated in any shape allowing to form almost arbitrary fluxon potentials by simply varying the junction geometry, see Fig. 8.1.

However, we note that there are constraints on the shape of the potential that can be generated in this way because the geometry-dependent part of the potential is effectively averaged over the vortex size ( $\propto \lambda_J$ ). Thus, for an arbitrary but closed junction shape, the vortex dipole energy is given by

$$\tilde{U}^h(q) = \int_0^\ell \Delta \phi_{\tilde{x}}(\tilde{x} - q) \vec{n}_J(\tilde{x}) \cdot \vec{h} d\tilde{x}, \quad (8.1)$$

where  $\vec{n}_J$  is the unit vector normal to the junction perimeter and  $\phi_{\tilde{x}}(\tilde{x} - q)$  is the normalized magnetic field associated with the vortex.  $\vec{h} = \vec{n}_h h$  is the normalized external field,  $\Delta$  is the coupling coefficient between field and vortex, and  $\ell$  is the normalized junction circumference. For the explicit calculation of  $\tilde{U}^h$ , it is useful to note that Eq. (8.1) is a convolution of the vortex magnetic field profile  $\phi_{\tilde{x}}(\tilde{x} - q)$  with the junction shape  $\vec{n}_J(\tilde{x}) \cdot \vec{n}_h$ . Since a convolution corresponds to a multiplication in Fourier space,  $\tilde{U}_h$  is given by

$$\tilde{U}^h(q) = \Delta h \mathcal{FT}^{-1} \{ \mathcal{FT}[\phi_{\tilde{x}}(\tilde{x})] \cdot \mathcal{FT}[\vec{n}_h \cdot \vec{n}_J(\tilde{x})] \} (q), \quad (8.2)$$

which can be solved either analytically or numerically, depending on the junction geometry. Since the vortex size scales with  $\lambda_J$ , we note that all features of the potential disappear for  $\lambda_J \rightarrow \infty$  or equivalently for  $\ell \rightarrow 0$ . Thus, we have to properly choose the junction geometry and  $\lambda_J$  to design the wanted potential.

The challenging goal in our experiments with quantum fluxons is the demonstration of macroscopic quantum coherence. To realize a coherence experiment, one needs to design a suitable two-state system. A possible realization of a macroscopic two-state system is a vortex in a double-well potential. We suggest to use a heart-shaped Josephson junction like the one shown in Fig. 8.2a for this purpose [WKL<sup>+</sup>00]. If the magnetic field  $\vec{H}$  is applied along the symmetry axis of the junction, two stable potential minima are formed for the fluxon at locations ‘*l*’ (left) and ‘*r*’ (right). At these two positions, the vortex magnetic moment  $\vec{\mu}$  is parallel to  $\vec{H}$  minimizing the vortex dipole energy, see Fig 8.2b. The barrier height between the wells can be conveniently controlled by the field amplitude and its angle with the symmetry axis of the junction. The corresponding potential profile at  $h = 1$ , calculated from Eq. (8.1) for the junction shape shown in Fig. 8.2a and the normalized junction length  $\ell \approx 27$ , is plotted in units of  $\mathcal{E}_0$  in Fig. 8.2c. If the barrier separating the two states is sufficiently large, the vortex is classically localized in one of the potential minima. It should be possible to detect the vortex in either of those states by measuring its position using a SQUID as a flux meter or by performing an activation measurement, as discussed in Section 8.4.

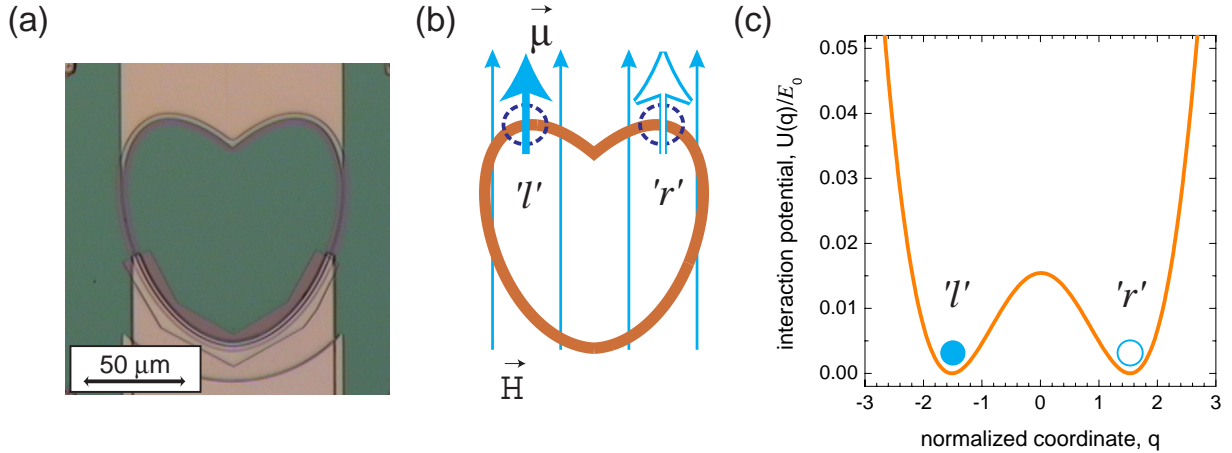


Figure 8.2: (a) Photograph of a  $0.3 \mu\text{m}$  wide heart-shaped junction fabricated in Nb- $\text{AlO}_x$ -Nb technology. (b) Sketch of a heart-shaped junction with magnetic field applied along its symmetry axis. Two energetically identical vortex states are indicated by arrows in positions ' $l'$ ' and ' $r'$ '. (c) Normalized magnetic field interaction potential  $\tilde{U}^h(q)$  at  $h = 1$  calculated according to Eq. (8.1).

First experiments with samples of the geometry shown in Fig. 8.2 have been performed [WKL<sup>+</sup>00]. We have shown that it is possible to trap single Josephson vortices in these junctions. From the current-voltage characteristics of the samples, we infer a high junction quality. The critical-current diffraction patterns show some geometry-dependent peculiarities which are to be investigated in more detail [Kem00]. To further investigate the classical dynamics of Josephson vortices, a new sample design was developed, which allows to engineer double-well potentials [Kem00]. The junction design is based on three joined sections of circles with two different radii  $R$  and  $r$ , see inset of Fig. 8.3. The centers of the circles are on the same baseline and the two small sections are joined forming an angle of  $2\beta$  between the respective tangents. For a fixed  $H$ , the barrier height  $U_0$  and the spatial separation  $\Delta q$  of the classical states of the vortex can be varied smoothly by changing  $r$ ,  $R$  and  $\lambda_J$  in the sample design. A typical sample geometry is shown in Fig. 8.3.

Cooling a heart shaped Josephson junction to sufficiently low temperatures, we expect that the vortex is observed to tunnel back and forth between the two equivalent states ' $l'$ ' and ' $r'$ ' depicted in Fig. 8.2c. The rate  $\Gamma_{a/s}$  of the transition depends on the massiveness of the barrier (i.e. its height *and* its width), which can be tuned by the external magnetic field. In the quantum limit, the two distinct fluxon states in the double-well potential form a degenerate two-state system.

We discuss the quantum mechanics of a fluxon in the double-well potential of a sample of the type shown in Fig. 8.3. We choose a radius  $R = 70 \mu\text{m}$  and an angle  $\beta = 37^\circ$  to fix the junction geometry. The total length of the junction is then  $l = 413 \mu\text{m}$ . To keep the Josephson energy low, the junction width is set to  $w = 0.3 \mu\text{m}$ . The critical-current density  $j_c = 500 \text{ A/cm}^2$ , the magnetic thickness  $d' = 182 \text{ nm}$  and the specific capacitance  $C^* = 30 \text{ mF/m}^2$  are chosen close to expected junction fabrication parameters. The characteristic field is  $H_0 \approx 1 \text{ Oe}$ . The resulting potential for an externally applied normalized magnetic field  $h = 1$  is plotted in Fig. 8.3. The potential barrier height is  $U_0 \approx 1 \text{ K}$  and the distance between the minima is  $\Delta q \approx 1.5 \lambda_J$ .



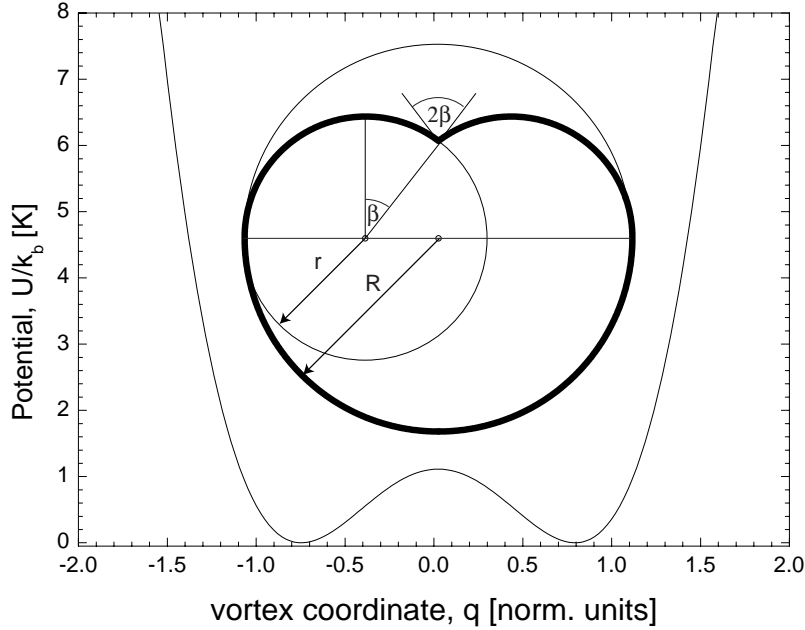


Figure 8.3: Double-well potential  $U(q)/k_b$  (at  $\hbar = 1$ ) for the junction geometry sketched in the inset.

### 8.3 The quantum mechanics of a Josephson vortex in a double-well potential

The transition rate  $\Gamma_{a/s}$  for a particle of mass  $m$  from one minimum of a generic double-well potential to the other is calculated in the quasi-classical WKB approximation as [LL79]

$$\Gamma_{a/s} = \text{const.} \omega_0 \exp \left( - \int_{q_0}^{q_1} \frac{1}{\hbar} \sqrt{2m(U(q) - E_0)} dq \right), \quad (8.3)$$

where  $\omega_0$  is the small amplitude oscillation frequency in one of the wells,  $U(q)$  is the potential energy of the particle in dependence on its coordinate  $q$  and the constant is of the order of one.<sup>3</sup> The integral is evaluated between the entrance  $q_0$  and the exit point  $q_1$  of the particle in the potential barrier, determining the massiveness of the barrier, see shaded area in Fig. 8.4a.  $q_0$  and  $q_1$  are defined by the intersection of the ground state energy level  $E_0 = \hbar\omega_0/2$  of the particular well with the potential  $U(q)$ . The quasi-classical WKB approximation Eq. (8.3) is valid if the condition  $U_0 > \hbar\omega_0/2$  is satisfied [Lik86].

Using a quadratic approximation of  $U(q)$  around  $U_0$ , we can explicitly integrate Eq. (8.3). Considering the case of a Josephson vortex and using the same normalization as in Section 7.1, we find

$$\Gamma_{a/s} = \text{const.} \tilde{\omega}_0 \omega_p \exp \left( - \frac{\mathcal{E}_0}{\hbar \omega_p} \frac{\pi}{4} 2\tilde{m}_f (\tilde{U}(q) - \tilde{E}_0) \Delta q \right), \quad (8.4)$$

where  $\Delta q = q_1 - q_0$  is the width of the potential barrier and  $\tilde{U}_0$  is its height. From Eq. (8.4), we can determine the approximate height and width of the potential barrier to achieve an experimentally observable transition rate  $\Gamma_{a/s}$  between the two states as

$$(\tilde{U}_0 - \tilde{E}_0) \Delta q = \frac{\hbar \omega_p}{\mathcal{E}_0} \frac{2}{\pi \tilde{m}_f} \ln \left( \frac{\tilde{\omega}_0 \omega_p}{\Gamma_{a/s}} \right). \quad (8.5)$$

<sup>3</sup>Note the difference of a factor of 2 in comparison with Eq. (7.1).

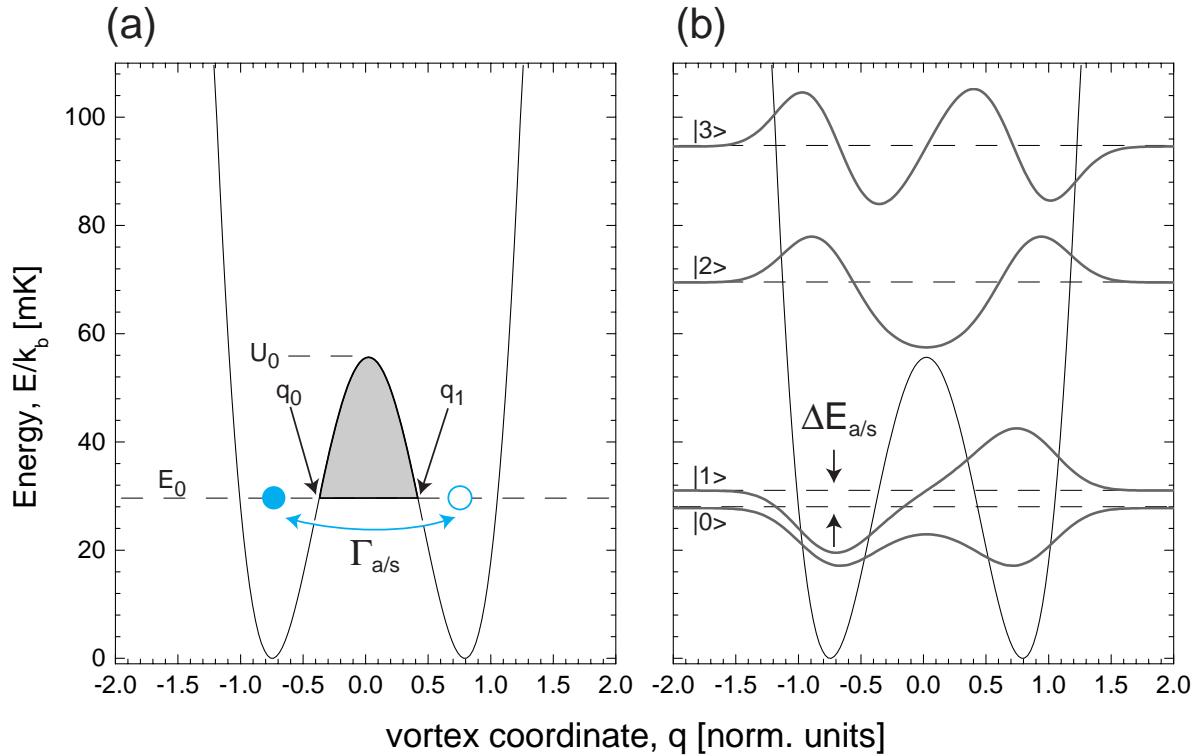


Figure 8.4: (a) Double-well potential for the sample geometry shown in Fig 8.3.  $E_0$  is the ground state energy of the individual well. The two states are separated by a barrier of height  $U_0$  and width  $\Delta q = q_1 - q_0$ .  $\Gamma_{a/s}$  is the transition rate between the two states. (b) Numerically calculated wave functions for the four lowest energy eigenstates  $|0\rangle \dots |3\rangle$  of the potential. The energy of each state is indicated by a dashed horizontal line. The splitting  $\Delta E_{a/s}$  of the ground state energies due to the coupling is indicated.

With values of  $(\tilde{U}_0 - \tilde{E}_0)\Delta q \approx 10^{-2}$  to  $10^{-3}$ , we can realize transition rates  $\Gamma_{a/s}$  between several 100 kHz to close to the plasma frequency of several 10 GHz for the sample parameters discussed above. Typically the distance  $\Delta q$  between the two states is of the order of unity. Therefore, we are able to tune the transition rate freely in this range by controlling the barrier height with the external field.

The tunnel coupling between the ground states of the individual wells lifts the degeneracy and leads to a splitting of the ground state energy level into a symmetric  $|0\rangle = 2^{-1/2}(|l\rangle + |r\rangle)$  and an anti-symmetric  $|1\rangle = 2^{-1/2}(|l\rangle - |r\rangle)$  one, as shown in Fig. 8.4b. The energy splitting is proportional to the transition rate

$$\Delta E_{a/s} = \hbar \Gamma_{a/s}. \quad (8.6)$$

In terms of temperature, the level splitting is  $\Delta E_{a/s}/k_b = \Gamma_{a/s} \hbar/k_b = 7.610^{-12} \Gamma_{a/s} \text{ K}$ , e.g. at a transition rate of  $\Gamma_{a/s} = 1 \text{ GHz}$ , a splitting of the ground level of about 7.6 mK would appear.

To support the analytical calculations of the transition rates, we have also solved numerically the quantum mechanical problem of a vortex in a double-well potential. The system is described by the stationary Schrödinger equation

$$\hat{H}\psi_j = E_j\psi_j \quad (8.7)$$

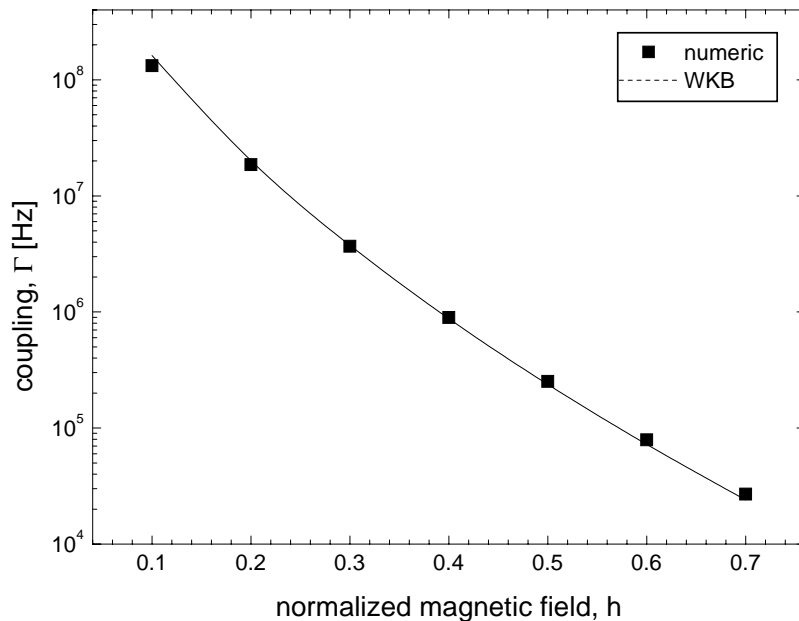


Figure 8.5: Transition rate  $\Gamma_{a/s}$  calculated analytically using the WKB approach (solid line) and solving the Schrödinger equation numerically (solid squares) for the discussed junction geometry.

with the hamiltonian  $\hat{H}$  which we solve numerically for its eigenvalues  $E_j$  and eigenfunctions  $\psi_j$ , see Appendix A. In Fig. 8.4b, the wave functions for the first four eigenstates of the potential are plotted. Each wave function is offset by the corresponding eigenenergy of the state. The two lowest symmetric and anti-symmetric eigenstates are separated by an energy corresponding to  $\Delta E_{a/s}$ . These states can be viewed as a symmetric and anti-symmetric combination of the eigenstates of each individual well which are weakly coupled via the tunneling transition between the wells. The two spatially localized states  $|l\rangle$  and  $|r\rangle$  can be viewed as a linear combination of the energy eigenstates  $|0\rangle$  and  $|1\rangle$ .

For the potential plotted in Fig. 8.4, we have analyzed the dependence of the transition rate on the magnetic field amplitude. Using the WKB approximation, we have calculated analytically the quantum transition rate  $\Gamma_{a/s}$  of the vortex between the two states. For the junction parameters described above, the calculated rate (solid line) is plotted versus the normalized external field in Fig. 8.5. We find that for these parameters we can tune the transition rate by roughly four orders of magnitude between 10 kHz and 100 MHz when varying the external field in the range of  $h = 0.01 \dots 0.50$ .

In Fig. 8.5, the WKB calculation is compared to the results of a direct numerical solution of the stationary Schrödinger equation (solid squares). The agreement between the two independent approaches is good. In both calculations, we have set the constant prefactor in Eq. (8.3) to unity.

In Figs. 8.6a-c, the numerically calculated eigenenergies and eigenfunctions of the hamiltonian are plotted for different values of the magnetic field. From this set of figures, a number of further features can be extracted. We note that the potential  $U(q)$  scales with the magnetic field amplitude. As a result, not only the barrier height  $U_0$  separating the two states but also the attempt frequency  $\omega_0$  changes with  $h$ . Also the energies of the excited states scale with  $h$ . As shown in Figs. 8.6a-c, the excited states ( $|2\rangle$ ,  $|3\rangle$ ) move closer to the two low energy states as the barrier height is lowered by the magnetic field. If the separation between the excited states and the ground states is comparable or smaller than the bath temperature, these states will be thermally populated. If an ideal two-state system is to be considered, the excitation of higher energy states leads to decoherence of the ground state.

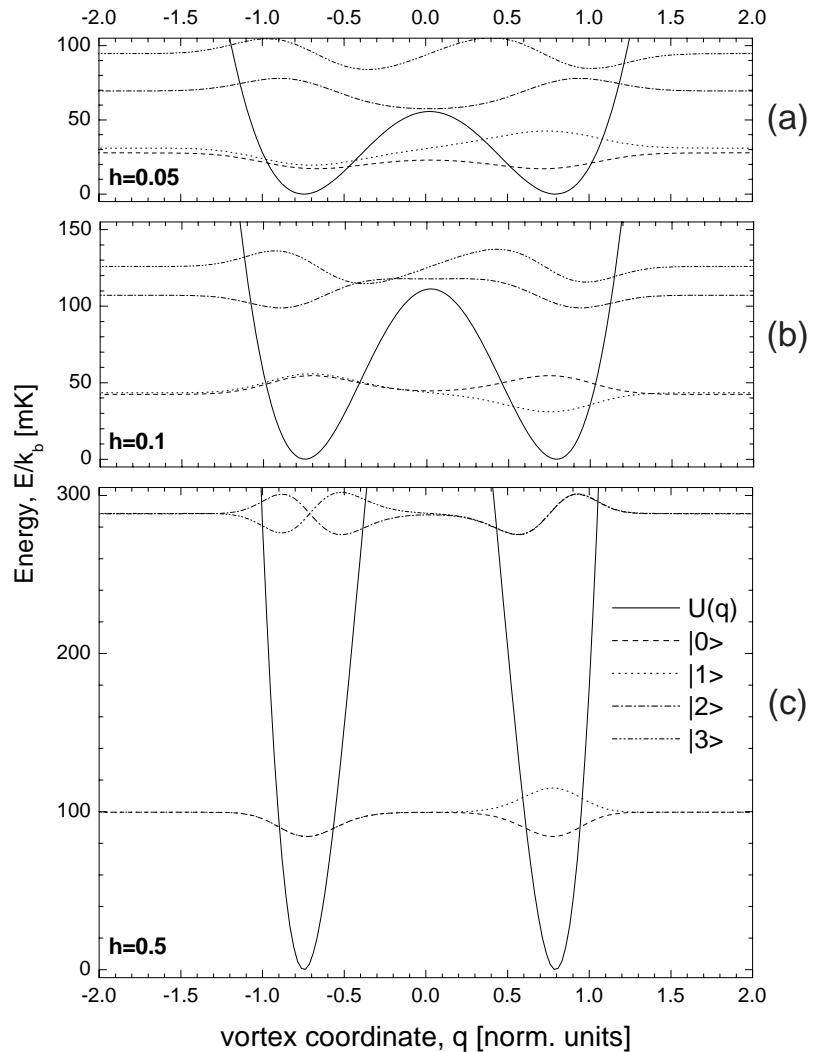


Figure 8.6: Eigenenergies  $E_j$  and eigenfunctions  $\psi_j$  plotted for different values of the magnetic field  $h = 0.05, 0.1, 0.5$ . The eigenfunctions are normalized and leveled at the energy of the corresponding state. The potential for each magnetic field is also shown.

## 8.4 Manipulation of a fluxon in a double-well

Up to now, we have discussed the potential energy of a vortex at zero bias current and with a magnetic field applied parallel to the symmetry axis of the junction. Both tilting the magnetic field and applying a bias current will change the potential energy of the vortex. First, we discuss purely classical effects of changing the potential. The quantum mechanical implications are considered in Sections 8.5 and 8.6, where we propose a measurement scheme to perform a macroscopic quantum coherence experiment with a single Josephson vortex [WKU00]. Using appropriate manipulations of the bias current and of the magnetic field, the classical state of the vortex (either ‘ $l$ ’ or ‘ $r$ ’) can be determined by measuring its depinning current.

In the classical regime, we consider the case where the potential barriers separating different vortex states are large. Therefore, quantum tunneling of the vortex is suppressed. We also consider small thermal fluctuations such that the vortex is effectively localized at the minimum of its potential well.

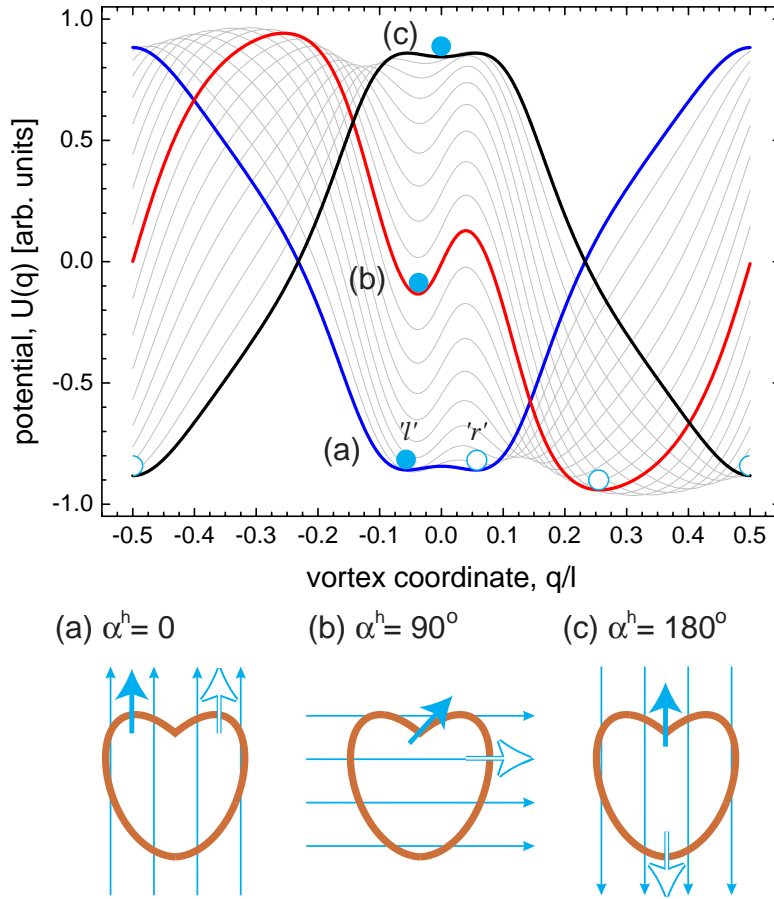


Figure 8.7: Vortex potential  $U(q)$  in dependence on the angle of the external magnetic field (a)  $\alpha^h = 0$ , (b)  $\alpha^h = 90^\circ$  and (c)  $\alpha^h = 180^\circ$ . The coordinate axis is normalized by the length  $\ell$  of the junction. The stable and metastable vortex positions are indicated by a solid (' $l$ '-state) and an open disc (' $r$ '-state). The locations of the vortices in space are indicated in a sketch for the different directions of the applied field.

### Magnetic field angle

The magnetic dipole potential of the vortex in dependence on the angle  $\alpha^h$  of the applied field with respect to the symmetry axis of the junction is discussed here first. The double-well potential is perfectly symmetric, as discussed in the previous sections, only if the external magnetic field is aligned to the symmetry axis of the junction, see Fig. 8.7a. In this case, the vortex potential has two minima, which we identify with the possible classical states ' $l$ ' and ' $r$ ' of the vortex. The two states are indicated by a solid and an open disc, see Fig. 8.7. The spatial location of a vortex in either state ' $l$ ' (solid arrow) or state ' $r$ ' (open arrow) in the junction for  $\alpha^h = 0$  is indicated in the sketch (a) of Fig. 8.7.

As the field is turned, both the position and the energy of the potential minima change. For small angles  $\alpha^h$ , both minima shift to the right, while the energy of state ' $l$ ' remains almost constant and the energy of state ' $r$ ' is slightly increased. As the field angle is further increased, a vortex in state ' $l$ ' is pinned at the cusp of the heart. To overcome the cusp, the magnetic moment of the vortex would need to turn with respect to the external field, which is energetically not favorable. In contrast, a vortex in state ' $r$ ' can freely adjust its position as to align its magnetic moment in parallel to the external field, see sketch (b) of Fig. 8.7. Further increasing the angle  $\alpha^h$  leads to a larger misorientation angle of the pinned ' $l$ '-state vortex with respect to the field, effectively increasing its potential energy, see the potential energy profile for  $\alpha^h = 90$  (curve b) in Fig. 8.7. Moreover, we note that the potential barrier height, separating the metastable state ' $l$ ' from the state ' $r$ ', increases in amplitude to a maximum value as  $\alpha^h$  approaches 90 degrees. In contrast, the state-' $r$ '

vortex is perfectly aligned to the external field and rests in a deep potential well (open disc on curve b).

Turning the field to  $\alpha^h = 180^\circ$  leads to an inversion of the potential with respect to the  $\alpha^h = 0$  case. Due to the smooth change of the field, the ‘*l*’-state vortex now is a metastable state at high energy, whereas the ‘*r*’-state vortex is at the lowest potential energy. In the position indicated by the solid arrow in Fig. 8.7c, the magnetic moment of the vortex is locally reduced due to the averaging along the junction. Shifting the vortex to the left or to the right from that position would increase its energy. Thus by turning the field, we have separated the two equivalent states of the double-well potential into a metastable state and a stable state at diametrically opposite locations in the junction.

### Bias current

As discussed in Section 6.2.1, the vortex potential is effectively tilted proportional to the bias current applied to the junction. Here, we discuss the depinning of the vortex from the two metastable states ‘*l*’ and ‘*r*’ in dependence on the bias current and the direction of the external field.

In absence of thermal fluctuations and quantum tunneling, the depinning current is proportional to the maximum slope of the potential barrier separating the initial vortex state from other states. Obviously, the depinning current depends on the direction of the applied bias current. Thus, the vortex in state ‘*l*’ is depinned at a lower bias current than the vortex in state ‘*r*’, see Fig.8.8a. This is true for any angle of the applied magnetic field. The vortex will be retrapped in a lower energy state if the potential barrier separating that state from the running state is larger than the potential energy of the vortex in the moment of the escape. In such a case, a vortex initially prepared in state ‘*l*’ can only switch to the running state via state ‘*r*’. Thus, only a single depinning current would be measured in experiment. If however the kinetic energy of the vortex is large enough to overcome the potential barrier of state ‘*r*’, two distinct depinning currents, depending on the initial state of the vortex, should be observable in experiment.

Since we would like to distinguish the vortex states ‘*l*’ and ‘*r*’ by measuring the depinning current, we have to construct a potential for which the vortex will not be retrapped in a lower energy potential minimum. Such a potential can be realized by turning the magnetic field to a sufficiently large angle, after having prepared the vortex in either the ‘*l*’ or the ‘*r*’ state. Here, we consider the depinning of a vortex from the potential for  $\alpha^h = 90^\circ$  in the heart-shaped junction discussed before. In Fig. 8.8, the potential profiles for different values of applied bias current are plotted. At zero bias current, the ‘*l*’-state is metastable and the ‘*r*’-state is stable (curve a). Increasing the bias current, the potential is tilted and the vortex is first activated from the ‘*l*’-state (curve b). The vortex is not retrapped in the lower potential well because its potential energy is sufficiently high to overcome the barrier.<sup>4</sup> At a substantially higher bias current, the vortex in the ‘*r*’-state would also escape from the well (curve c). For all three bias currents, the positions of the vortex at the moment of activation are indicated in the sketches of the heart-shaped junction in Fig. 8.8.

Due to the large difference in depinning current, it is possible to distinguish the states ‘*l*’ and ‘*r*’ by a depinning measurement. Experiments to prove the feasibility of this scheme for distinguishing vortex states are currently in progress [Kem00].

---

<sup>4</sup>Only in the case of very high damping, the vortex could be retrapped in a neighboring metastable minimum.

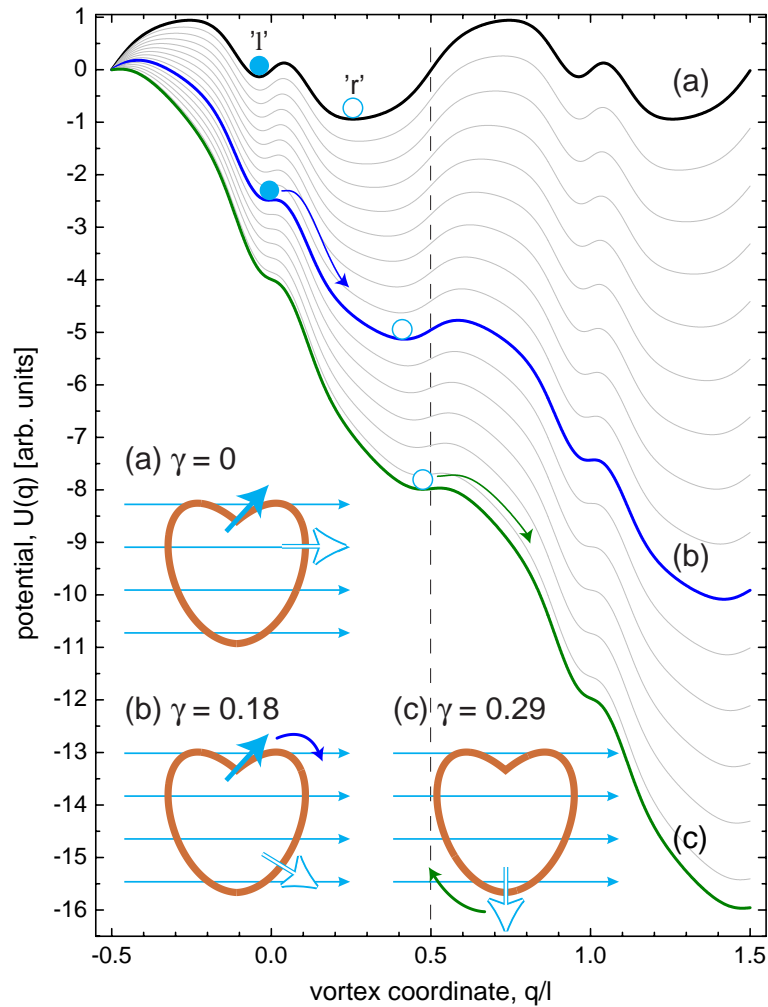


Figure 8.8: Vortex potential  $U^{\gamma h}(q)$  for  $\alpha^h = 90^\circ$  and different values of bias current. The coordinate axis is normalized by the length  $\ell$  of the junction. The stable and metastable vortex positions are indicated by a solid (' $l$ '-state) and an open disc (' $r$ '-state). The spatial positions of the metastable vortex-states are indicated in the insets for three characteristic bias currents (a)  $\gamma = 0$ , (b)  $\gamma = 0.18$  and (c)  $\gamma = 0.29$

## 8.5 A macroscopic quantum coherence experiment

In this section, I describe our scheme to perform a macroscopic quantum coherence measurement with a Josephson vortex in a heart-shaped Josephson junction. The idea is based on a time resolved measurement of the Rabi-oscillation [CTDL99] of a Josephson vortex between the two degenerate states of the double-well potential. The measurement scheme consists of four steps: the preparation of the state, the coherent oscillation, the freezing of the state and the readout.

In the first step, we prepare the vortex in either state ' $l$ ' or ' $r$ ' by applying a large off-axis field to the junction. The large field amplitude suppresses the tunneling of the vortex and the field direction distorts the potential such that one of the states is at lower energy. Then, the field is aligned to the axis of the junction forming a perfectly symmetric double-well potential, but with the vortex being localized in one known state.

In the next step, the field is reduced at time  $t = 0$  to allow the quantum mechanical coupling between the two states  $|l\rangle$  and  $|r\rangle$ . The size of the barrier determines the coupling and, thus, the oscillation frequency of the vortex between the two states. At time  $t = t_1$ , the state of the vortex is frozen by increasing the magnetic field and thus, suppressing the quantum tunneling between the two states. This constitutes the measurement of the quantum mechanical superposition state of the vortex at time  $t = t_1$ . The probability to

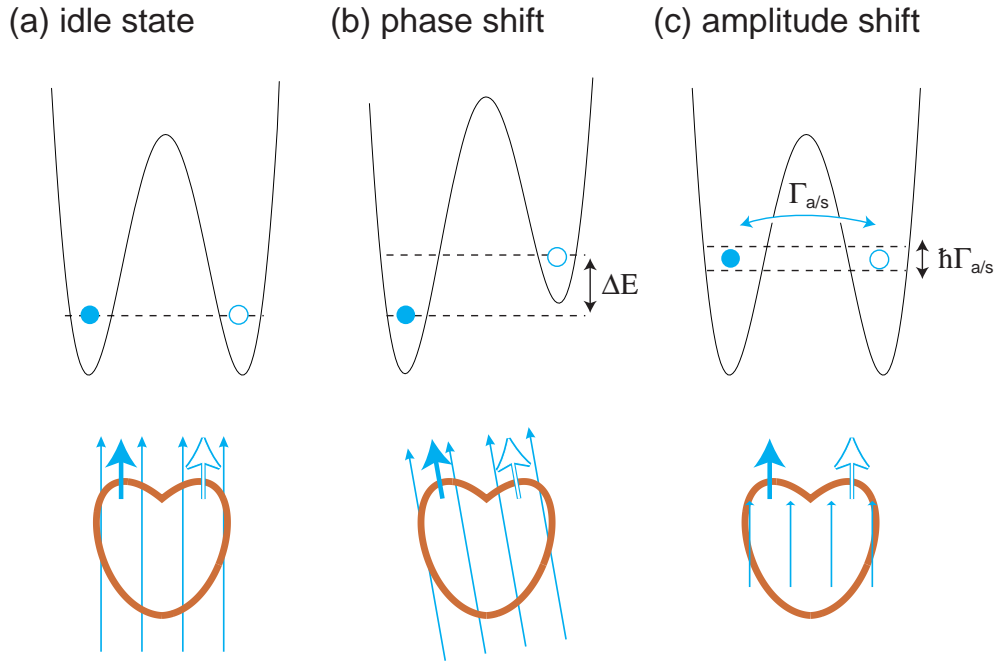


Figure 8.9: Single-qubit operations: (a) idle state, (b) phase shift and (c) amplitude shift. The first row shows the effective vortex-potential for the field amplitude and direction shown in the sketches of the second row.

find the vortex in either state ‘ $l$ ’ or state ‘ $r$ ’ is determined by the oscillation frequency  $\Gamma_{a/s}$  and the time  $t_1$ . The final state of the vortex can be determined in an escape measurement as described in the previous section.

By varying the time  $t_1$ , it should be possible to measure the probability of the vortex ending up in state ‘ $l$ ’ or ‘ $r$ ’ versus time. To observe Rabi-oscillations [CTDL99], the quantum mechanical system has to evolve coherently in time. The coherence time  $\tau_{\text{coh}}$  has to be much larger than the period of the expected oscillations. If  $\tau_{\text{coh}}$  is much smaller than  $1/\Gamma_{a/s}$ , the vortex would be observed in either one of the states with equal probability  $P = 1/2$  all the time. Therefore, a measurement of the Rabi-oscillation implies a measurement of the macroscopic quantum coherence.

## 8.6 Quantum computation using the vortex-qubit

In this section, I lay out the general principles to operate a vortex-qubit in the ways necessary to perform quantum computation. We note that the general operations that need to be performed on the qubits are identical for any physical realization of a quantum computer. Only the implementation of the operations differs strongly for different physical systems. In general, it is necessary to address an individual qubit and control its state, measure the qubit for reading out its state, couple qubits to each other and decouple all of them from the environment to perform calculations.

It has been shown [DiV95b] that the functions necessary to perform quantum computation can be separated in two classes: single-qubit and two-qubit operations. Single-qubit operations include the preparation of the qubit state, the generation of superposition states, the adjustment of the phase difference between states and reading out the state. Two-



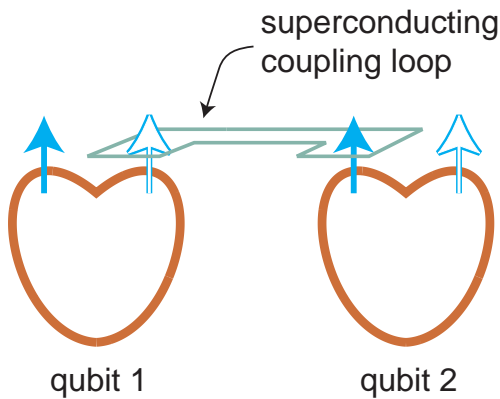


Figure 8.10: Coupling of two vortex-qubits via an inductive loop.

qubit operations can be realized by an arbitrary interaction between any two qubits. It was pointed out in Ref. [Llo95] that any interaction between two qubits and the possibility to perform arbitrary single qubit operations suffice to construct a *universal quantum logic gate*.

All required single-bit operations can be realized in the vortex qubit in the following way. In the *idle state* (see Fig. 8.9a), a large magnetic field is applied in parallel to the symmetry axis of the junction. The ground states of both wells are decoupled because of the large field-controlled energy barrier between them. Both states  $|l\rangle$  and  $|r\rangle$  evolve according to their energy as  $|l, r\rangle \propto \exp iE_{l,r}t/\hbar$  with no phase shift in time. To induce a *phase shift* between the two states, we keep the magnetic field at a high level to suppress tunneling and tilt it. The tilting results in a relative shift in energy between the two ground states of the well, see Fig. 8.9b. The two states now evolve in time accumulating a phase shift proportional to the energy difference  $\Delta E = E_r - E_l$  between the two states. Finally, an *amplitude shift* between the two states can be induced by decreasing the external magnetic field and, thus, lowering the barrier as to induce the coupling between the two states. The vortex starts to oscillate back and forth at the rate  $\Gamma_{a/s}$ , see Fig. 8.9c. Increasing the barrier again after an appropriate time  $\Delta t$ , an amplitude shift between the states  $|l\rangle$  and  $|r\rangle$  is induced. Using these operations one can perform an arbitrary transformation of the single-qubit state. Naturally, any of these operations requires the coherence of the quantum mechanical system. These single-qubit operations can be expressed in terms of Pauli-matrices, effectively treating the vortex-qubit in analogy to a spin 1/2 system, see for example [IGF<sup>+</sup>99]. After any number of operations, the qubit may be read out using a switching current measurement of the type described in detail in Section 8.4.

As pointed out before, any interaction between two qubits may be used to form a universal quantum logic gate. Similar to previous proposals for superconducting qubits, we suggest to use inductances to couple individual qubits. By placing a superconducting loop close to two neighboring vortex-qubits in the way depicted in Fig. 8.10, one can achieve a coupling between two qubits. In this case, the flux coupled into the superconducting loop depends on the state of qubit 1, i.e. more flux is coupled in state  $|r\rangle$  than in state  $|l\rangle$ . The flux coupled into the loop leads to a magnetic field coupling to qubit 2 via the loop. The magnetic field changes the effective vortex potential of qubit 2, modifying its quantum mechanical state.

Thus, in the quantum limit, a vortex trapped in a heart-shaped Josephson junction can serve as a qubit in a quantum computation scheme. The major open question is the effect of the environment on the coherence of this quantum two-state system.

## 8.7 Decoherence

The degree of coherence of a quantum system is characterized by the coherence time  $\tau_{\text{coh}}$ . For times  $t < \tau_{\text{coh}}$ , any two-state quantum system prepared in a superposition state remains in the same state with a large probability. Due to decoherence, the quantum state decays into an incoherent mixed state after the average time  $\tau_{\text{coh}}$ .

The ratio of  $\tau_{\text{coh}}$  to the typical time to perform a single or a two-qubit operation  $\tau_{\text{op}}$  is the figure of merit in practical quantum computation [DiV95a]. The larger this ratio, the more operations can be performed before the qubit is decohered and all information are lost. Error correction schemes have been developed to allow the operation of a quantum computer in the presence of weak decoherence [Ste99]. To use these schemes, the quality factor<sup>5</sup>  $\tau_{\text{coh}}/\tau_{\text{op}}$  of the system has to be on the order of  $10^5$  or larger. Consequently, decoherence is the most important issue in realizing a useful quantum computer [Ste99].

The coherence of any macroscopic quantum two-state system is strongly affected by both dissipation and fluctuations. A general approach to calculate the coherence time is to estimate the decay of a pure quantum state into a mixed state in the presence of a perturbation due to the environment, see for example Ref. [TLvdW<sup>+</sup>99]. In general, any degree of freedom in the environment can couple to the qubit, leading to decoherence. The characteristic coherence time for a specific interaction with the environment depends on the strength of the coupling. Various decoherence mechanisms have been discussed in detail for the persistent current qubit [TLvdW<sup>+</sup>99]. The decoherence due to charge fluctuations in the environment, quasiparticle tunneling in the junctions (ohmic dissipation), interaction with nuclear spins, spontaneous emission of radiation, and spurious interactions with other qubits discussed in Ref. [TLvdW<sup>+</sup>99] is generally relevant for any realization of a magnetic-flux qubit. Thus, all of these effects need to be considered for the vortex-qubit. Since up to now, no specific calculations for the vortex-qubit have been performed, we only discuss the relative importance of the different sources of decoherence mentioned above.

The decoherence of the vortex-qubit due to quasiparticle damping in the junction can be estimated in the framework of the Caldeira-Leggett theory for macroscopic two-state quantum systems [LCD<sup>+</sup>87]. The case of a vortex in a double-well potential formed by two nearby microresistors has been treated in Ref. [KI96]. Within the limits of the Caldeira-Leggett theory, it was found that it should be possible to observe macroscopic quantum coherence in that system. Here, we adopt the same methods to the case of the magnetic-field induced potential of heart-shaped junctions.

The effect of dissipation on the coherent quantum mechanical oscillation of a particle in a double-well potential is described by the dissipation amplitude

$$K = \tilde{m}_f a \frac{(\Delta q)^2}{2\pi g^2}, \quad (8.8)$$

where  $a$  is the damping coefficient,  $\Delta q$  is the spatial separation between the two states and  $g^2$  is the normalized Planck constant [LCD<sup>+</sup>87]. The conditions to observe macroscopic quantum coherence are then given by [LCD<sup>+</sup>87, LG85]

$$K \ll 1, \quad (8.9)$$

$$k_b T \ll \frac{\hbar \Gamma_{a/s}}{K}. \quad (8.10)$$

---

<sup>5</sup>The quality factor is defined as the number of operations that can be performed within the coherence time of the system.

For a typical magnetic-field induced double-well potential, we have estimated  $\Delta q \approx 1$  and  $g^2 \approx 10^{-2}$  for a  $0.3 \mu\text{m}$  wide junction and a conservatively estimated intrinsic damping parameter of  $a \approx 10^{-3}$ , resulting in a value of  $K \approx 0.1$  which is marginally within the range of the criterion Eq. (8.9). From the second criterion, we find the condition  $T < 80 \text{ mK}$  for a transition rate of  $\Gamma = 1 \text{ GHz}$ , which is possible to maintain in a real experiment. Since  $K$  depends quadratically on the spatial distance between the states  $\Delta q$ , we can drastically increase the possibility to observe quantum coherence by designing a sample with a smaller value of  $\Delta q$ . The damping due to quasiparticle tunneling may also be substantially smaller at millikelvin temperatures. A reduction of the parameter  $K$  by proper design of the experiment may facilitate the observation of macroscopic quantum coherence in this system.

As pointed out in Ref. [TLvdW<sup>+</sup>99], the fluctuations of the charges and of the nuclear magnetic moments in the environment (substrate, electrodes, etc.) may lead to additional dissipation. These effects can be considered in the framework of the Caldeira-Leggett model using the *fluctuation-dissipation theorem*. The vortex-qubit may also decohere due to the *spontaneous emission* of radiation during the oscillation of the vortex magnetic dipole between the two states of the qubit. The decoherence time is inversely proportional to the spontaneous emission rate. Rough estimates show that for the heart-shaped junctions the coherence time has an upper bound due to spontaneous emission of about approximately one second, which is very safe with respect to other decoherence mechanisms.

## 8.8 Summary and conclusions

We have pointed out the possibilities of using a vortex trapped in a double-well potential as a macroscopic quantum coherent two-state system. We have shown how to manipulate the states of the vortex and how these manipulations may be used to perform quantum computation. Possible decoherence mechanisms in this system have to be investigated theoretically and experiments trying to observe the coherent oscillation of a vortex between the ground states of a double-well potential need to be performed.

It is important to note that, up to now, there has been only a single experiment that has succeeded in observing the coherent phenomenon of Rabi-oscillations in a solid state environment [NPT99]. The various mechanisms of decoherence in solid state systems are not well understood and only relatively few experiments probing these phenomena have been performed until now. Therefore, it is an interesting and challenging task to further investigate quantum coherent effects in solid state systems.

The research directed towards the realization of a quantum computer currently leads to many new insights into the physics of coherent quantum systems. The efforts to manipulate and control quantum states are common to the rather new and exciting interdisciplinary field of physics called *quantum information processing*. Eventually, the knowledge gained about the manipulation of quantum systems may pioneer fascinating new applications like the *quantum computer*.



# Appendix A

## Numerical solution of the stationary Schrödinger equation

The hamiltonian of a particle in a potential can be written as

$$\hat{H} = \frac{\hat{p}^2}{2m_f} + \hat{U} \quad (\text{A.1})$$

$$= -\frac{\hbar^2}{2m_f} \frac{\partial^2}{\partial q^2} \psi + U(q) \quad (\text{A.2})$$

with the momentum operator  $\hat{p} = -i\hbar\partial/\partial q$  and the potential  $\hat{U} = U(q)$ . The eigenfunctions  $\psi_j$  and the eigenenergies  $E_j$  of  $\hat{H}$  are determined according to a procedure similar to the one described in Ref. [PFTV86]. Accordingly, the wave function is discretized on an equally spaced grid of size  $N$ . The hamiltonian  $\hat{H}$  is discretized on the same grid, resulting in a  $N \times N$  matrix. Discretizing  $\hat{U}$  results in a matrix with the potential evaluated at the grid-points on the diagonal and no other non-zero values. The momentum operator is discretized using the well-known four-point finite difference method to calculate the second derivative of  $\psi$

$$\psi'' = \frac{\psi_{i-1} - 2\psi_i + \psi_{i+1}}{\Delta x^2}. \quad (\text{A.3})$$

As a result,  $\hat{H}$  can be written as a tri-diagonal matrix

$$\hat{H} = \begin{pmatrix} U_0 - \frac{2}{2m\Delta_x^2} & \frac{1}{2m\Delta_x^2} & 0 & \dots & 0 \\ \frac{1}{2m\Delta_x^2} & \ddots & \ddots & \ddots & \vdots \\ 0 & \ddots & \ddots & \ddots & 0 \\ \vdots & \ddots & \ddots & \ddots & \frac{1}{2m\Delta_x^2} \\ 0 & \dots & 0 & \frac{1}{2m\Delta_x^2} & U_N - \frac{2}{2m\Delta_x^2} \end{pmatrix}, \quad (\text{A.4})$$

the eigenvalues  $E_j$  and eigenvectors  $\psi_j$  of which can be easily determined with standard techniques.<sup>1</sup>

---

<sup>1</sup>Calculations have been performed using Mathematica [Wol].

# Appendix B

## List of symbols

<i>symbol</i>	<i>description</i>
<i>physical constants</i>	
$e$	electron charge
$\epsilon_0$	vacuum permittivity
$\hbar$	Planck constant
$k_b$	Boltzmann constant
$\mu_0$	vacuum permeability
$\Phi_0$	magnetic flux quantum
<i>arabic letter symbols</i>	
$a$	damping constant
$A$	junction area
$\vec{A}$	vector potential
$b$	width of microresistor
$c_0$	Swihart velocity
$\bar{c}_0$	Swihart velocity considering idle region
$C$	total junction capacitance
$C^*$	specific capacitance
$d_{t,b}$	electrode thickness, top, bottom
$d'$	magnetic thickness
$E$	electric field
$E_J$	Josephson coupling energy
$E_i, E_f$	initial, final state energy
$E_0$	ground state energy
$E_j$	$j$ th energy eigenvalue of hamiltonian
$\mathcal{E}_0$	long junction energy scale
$g^2$	normalized Planck constant
$h$	normalized magnetic field
$\bar{h}$	renormalized magnetic field
$H, H_r, H_\phi$	magnetic field, radial and angular components
$H_0$	characteristic magnetic field of annular junction
$H_{c1}$	first critical field
$\hat{\mathcal{H}}$	hamiltonian operator
$\tilde{\mathcal{H}}$	normalized hamiltonian

<i>symbol</i>	<i>description</i>
$\mathcal{H}_f^{\text{SG}}$	unperturbed vortex rest energy
$\tilde{\mathcal{H}}^{\text{SG}}$	normalized unperturbed sine-Gordon hamiltonian
$\tilde{\mathcal{H}}^{\text{P}}$	normalized perturbation hamiltonian
$\tilde{\mathcal{H}}^\gamma$	normalized bias current perturbation hamiltonian
$I$	bias current
$I_c$	critical current
$I_c^h, I_c^e$	depinning current in magnetic-field, microresistor potential
$\langle I \rangle$	mean value of switching current distribution
$I_0$	single switching current
$dI/dt$	bias-current sweep rate
$j$	bias current density
$j_c$	critical current density
$J_k$	Bessel function of the first kind of order $k$
$k$	angular wave number
$\tilde{k}$	normalized wave vector
$K$	dissipation amplitude for quantum tunneling
$l$	length of a long junction
$\ell$	normalized length of long junction
$L_{\text{eff}}$	effective annular junction length
$L$	inductance
$L^*$	specific inductance
$\mathcal{L}, \tilde{\mathcal{L}}$	lagrangian, normalized lagrangian
$m_f, \tilde{m}_f$	vortex rest mass, normalized vortex rest mass
$n^{\text{CP}}$	Cooper pair density
$n, \bar{n}$	number of vortices, antivortices trapped in the junction
$\vec{n}_r, \vec{n}_\phi, \vec{n}_z$	radial normal vector, angular normal vector, normal vector on the junction plane
$P(I)$	switching-current probability distribution
$q$	normalized vortex center of mass coordinate, generalized coordinate
$\bar{q}$	renormalized vortex coordinate
$q_0, q_b, q_{ex}$	coordinate of potential minimum, maximum and exit point from the potential
$r$	radius of annular junction
$r_i$	inner junction radius
$r_e$	external junction radius
$\bar{r}$	mean junction radius
$r, \varphi$	polar coordinates
$\tilde{r}, \tilde{\varphi}$	normalized polar coordinates
$R$	junction resistance
$R_n$	normal junction resistance
$R_{sg}$	subgap junction resistance
$R_s$	electrode surface resistance
$t, \bar{t}$	time, normalized time
$t_{j,p}$	barrier thickness in junction and passive region

<i>symbol</i>	<i>description</i>
$T$	temperature
$T_c$	critical temperature of superconductor
$T_{\text{esc}}$	effective thermal escape temperature
$T^*$	cross-over temperature
$T_{\text{kin}}$	kinetic energy
$u$	normalized vortex velocity
$U^\phi$	potential for the phase in small junction
$U_0^\phi$	potential barrier height for the phase in small junction
$\tilde{U}^\gamma, \tilde{U}^h, \tilde{U}^\epsilon$	normalized vortex potential due to bias current, due to magnetic field, due to microshort
$\tilde{U}^{\gamma h}, \tilde{U}^{\gamma \epsilon}$	normalized magnetic-field induced, microresistor potential with bias current
$U_{\text{pot}}$	potential energy
$v$	linear vortex velocity
$V$	voltage
$V_g$	gap voltage
$V_{\text{max}}$	maximum single-vortex resonance voltage
$\mathcal{V}$	ratio of Swihart velocities in active and passive region
$w$	width of a long junction
$x, y, z; \tilde{x}, \tilde{y}, \tilde{z}$	spatial coordinates, normalized spatial coordinates
$Y_k$	Bessel function of the second type of order $k$
<i>greek letter symbols</i>	
$\alpha$	normalized quasiparticle damping coefficient
$\alpha_f$	fine structure constant
$\alpha_\rho$	numerical constant in analytical approximation to whispering gallery mode frequencies
$\alpha^h$	angle of magnetic field vs. symmetry axis of junction
$\beta$	normalized surface impedance coefficient
$\delta$	ratio of inner to outer junction radius
$\Delta$	superconducting energy gap
$\Delta E_{a/s}$	energy splitting of ground state in double-well potential
$\epsilon$	normalized strength of microresistor
$\bar{\epsilon}$	renormalized strength of microresistor
$\epsilon_{j,p}$	relative dielectric constant, junction and passive region
$\gamma$	normalized bias current
$\gamma_c^h, \gamma_c^\epsilon$	normalized depinning current in magnetic-field induced or microresistor potential
$\bar{\gamma}$	relative normalized depinning current
$\Gamma$	escape rate
$\Gamma_{\text{th}}$	thermal activation rate
$\Gamma_{\text{qu}}$	quantum escape rate
$\Gamma_{a/s}$	tunnel rate in double-well potential
$\lambda$	ratio of magnetic thicknesses of active and passive junction region
$\lambda_{\text{eff}}$	effective Josephson length considering the idle region
$\lambda_J$	Josephson length



<i>symbol</i>	<i>description</i>
$\lambda_L$	London penetration depth
$\Lambda$	magnetic thickness
$\nu_p$	Josephson plasma frequency
$\tilde{\omega}$	normalized angular frequency
$\bar{\omega}$	renormalized angular frequency
$\omega_p$	angular Josephson plasma frequency
$\omega_{\rho,k}, \omega_k$	frequency of whispering gallery mode with angular wave number $k$ and radial wave number $\rho$ , same for $\rho = 0$
$\omega_0, \omega_0^\phi, \omega_0^h, \omega_0^\epsilon$	small amplitude oscillation frequency, for the phase in small junction, for a vortex in magnetic-field induced, or microresistor potential
$\omega_b$	unstable barrier frequency
$\Omega, \tilde{\Omega}$	angular vortex rotation frequency, the same quantity normalized
$\phi$	superconducting phase difference
$\phi_f$	fluxon solution of sine-Gordon equation
$\Phi$	magnetic flux
$\psi_j$	$j$ th eigenfunction of hamiltonian
$\Psi$	superconducting macroscopic wave function, order parameter
$\rho$	junction resistance per unit length
$\rho_s$	electrode surface resistance per unit length
$\rho_a$	transmission coefficient
$\sigma_I$	standard deviation of switching-current distribution
$\theta$	superconducting phase
$\xi$	ratio of Swihart velocities without and with idle



# Bibliography

- [AB63a] V. Ambegaokar and A. Baratoff. Tunneling between superconductors. *Phys. Rev. Lett.*, 10:486, 1963.
- [AB63b] V. Ambegaokar and A. Baratoff. Tunneling between superconductors: Errata. *Phys. Rev. Lett.*, 11:104, 1963.
- [Abd94] F. Abdullaev. *Theory of Solitons in Inhomogeneous Media*. Wiley, 1994.
- [AES82] V. Ambegaokar, U. Eckern, and G. Schön. Quantum dynamics of tunneling between superconductors. *Phys. Rev. Lett.*, 48:1745, 1982.
- [Alf95] G.L. Alfimov. On small perturbations of stationary states in a nonlinear nonlocal model of a Josephson junction. *Phys. Lett. A*, 198:105, 1995.
- [AOSU95] Yu. M. Aliev, K. N. Ovchinnikov, V. P. Silin, and S. A. Uryupin. Nonlocal Josephson electrostatics in layered structures. *JETP*, 80(3):551, 1995.
- [AR63] J.R. Anderson and J.M. Rowell. Probable observation of the Josephson superconducting tunnel effect. *Phys. Rev. Lett.*, 10:230, 1963.
- [Arr89] S. Arrhenius. *Z. Phys. Chem. (Leipzig)*, 4:226, 1889.
- [AS93a] Yu. M. Aliev and V. P. Silin. Nonlocal Josephson electrostatics. *JETP*, 77(1):142, 1993.
- [AS93b] Yu. M. Aliev and V. P. Silin. Travelling  $4\pi$ -kink in nonlocal Josephson electrostatics. *Phys. Lett. A*, 177:259, 1993.
- [Ave00] D. V. Averin. Quantum computation and quantum coherence in mesoscopic Josephson junctions. *J. Low Temp. Phys.*, 118(5/6):781, 2000.
- [BC95] M. Büttiker and T. Christen. Nucleation of weakly driven kinks. *Phys. Rev. Lett.*, 75:1895, 1995.
- [BD00] C. H. Bennett and D. P. DiVincenzo. Quantum information and computation. *Nature*, 404:247, 2000.
- [BGI99] G. Blatter, V. B. Geshkenbein, and L. B. Ioffe. Engineering superconducting phase qubits. *condmat/9912163*, 1999.
- [BHF97] M.F. Bocko, A.M. Herr, and M.J. Feldman. Prospects for quantum coherent computation using superconducting electronics. *IEEE Trans. Appl. Supercond.*, 7:3638, 1997.
- [BHL83] M. Büttiker, E.P. Harris, and R. Landauer. Thermal activation of extremely underdamped Josephson-junction circuits. *Phys. Rev. B*, 28(3):1268, 1983.

- [BL79] M. Büttiker and R. Landauer. Nucleation theory of overdamped soliton motion. *Phys. Rev. Lett.*, 43:1453, 1979.
- [BL81] M. Büttiker and R. Landauer. Nucleation theory of overdamped soliton motion. *Phys. Rev. A*, 23:1397, 1981.
- [BP82] A. Barone and G. Paterno. *Physics and Applications of the Josephson Effect*. Wiley, 1982.
- [Büt89] M. Büttiker. *Transport and fluctuations in the driven and damped sine-Gordon chain*, chapter 6. Manchester University Press, 1989.
- [BVJ<sup>+</sup>98] V. Bouchiat, D. Vion, P. Joyez, D. Esteve, and M. H. Devoret. Quantum coherence with a single cooper pair. *Physica Scripta*, T76:165, 1998.
- [BvWdBO83] D. W. Bol, R. van Weelder, and R. de Bruyn Ouboter. On the conditional transition probabilities at low temperatures in a superconducting loop enclosed with a low-capacitance superconducting point contact. *Physica B*, 122:1, 1983.
- [Cal83] A.O. Caldeira. Quantum tunneling in a dissipative system. *Ann. of Phys.*, 149:374, 1983.
- [Cap96] J.G. Caputo. Effect of geometry on fluxon width in a Josephson junction. *Int. J. Mod. Phys. C*, 7(2):191, 1996.
- [CB98] T. Christen and M. Büttiker. Diffusion controlled initial recombination. *Phys. Rev. B.*, 58:1533, 1998.
- [CCC<sup>+</sup>99] C. Cosmelli, P. Carelli, M. G. Castellano, F. Chiarello, G. Diambri Palazzi, R. Leoni, and G. Torrioli. Measurement of the intrinsic dissipation of a macroscopic system in the quantum regime. *Phys. Rev. Lett.*, 82(26):5357, 1999.
- [CEF<sup>+</sup>99] R. Cristiano, E. Esposito, L. Frunzio, M. P. Lisitskii, C. Nappi, G. Ammendola, A. Barone, and L. Parlato. Magnetic properties of annular Josephson junctions for radiation detection: Experimental results. *Appl. Phys. Lett.*, 74:3389, 1999.
- [CFK<sup>+</sup>99] J.-G. Caputo, N. Flytzanis, V. Kurin, N. Lazarides, and E. Vavalis. Effective sine-gordon model for the static properties of narrow window junctions. *J. Appl. Phys.*, 85(10):7291, 1999.
- [CL81] A.O. Caldeira and A.J. Leggett. Influence of dissipation on quantum tunneling in macroscopic systems. *Phys. Rev. Lett.*, 46(4):211, 1981.
- [Cle99] R. Cleve. An introduction to quantum complexity theory. In C. Macchiavello, G. M. Palma, and A. Zeilinger, editors, *Collected Papers on Quantum Computation and Quantum Information Theory*. World Scientific, 1999.
- [Col95] MQC Collaboration. *Macroscopic quantum coherence in superconducting networks*, chapter Experimental detection of macroscopic quantum coherence with SQUIDs: state of the art and preliminary tests on high quality Josephson junctions, page 39. World scientific, 1995.
- [CPS<sup>+</sup>78] G. Costabile, R.D. Parmentier, B. Savo, D.W. McLaughlin, and A.C. Scott. Exact solution of the sine-Gordon equation describing oscillations in long (but finite) Josephson junctions. *Appl. Phys. Lett*, 32:587, 1978.

- [CTC+96] M.G. Castellano, G. Torrioli, C. Cosmelli, A. Costantini, F. Chiarello, P. Carelli, G. Rotoli, M. Cirillo, and R.L. Kautz. Thermally activated escape from the zero-voltage state in long Josephson junctions. *Phys. Rev B*, 54(21):15417, 1996.
- [CTDL99] C. Cohen-Tannoudji, B. Diu, and F. Laloe. *Quantenmechanik, Teil 1*. deGruyter, Berlin, 1999.
- [CVZ+98] I. L. Chuang, L. M. K. Vandersypen, X. Zhou, D. W. Leung, and S. Lloyd. Experimental realization of a quantum algorithm. *Nature*, 393:143, 1998.
- [DDKP85] A. Davidson, B. Dueholm, B. Kryger, and N.F. Pedersen. Experimental investigation of trapped sine-Gordon solitons. *Phys. Rev. Lett.*, 55(19):2059, 1985.
- [DEK+99] P. N. Dmitriev, A. B. Ermakov, A. G. Kovalenko, V. P. Koshelets, N. N. Iosad, A. A. Golubov, and M. Yu. Kupriyanov. Niobium tunnel junctions with multi-layered electrodes. *IEEE Trans. Appl. Supercond.*, page 3970, 1999.
- [DiV95a] D. P. DiVincenzo. Quantum computation. *Science*, 270:255, 1995.
- [DiV95b] D. P. DiVincenzo. Two-bit gates are universal for quantum computation. *Phys. Rev. A*, 51(2):1015, 1995.
- [DMC85] M.H. Devoret, J.M. Martinis, and J. Clarke. Measurements of macroscopic quantum tunneling out of the zero-voltage state of a current biased Josephson junction. *Phys. Rev. Lett.*, 55(18):1908, 1985.
- [DMS99] T. Dröse and C. Morias-Smith. Crossover in the thermal decay of metastable states in discrete systems. *Phys. Rev. B*, 60(13):9763, 1999.
- [DMS00] T. Dröse and C. Morais-Smith. Metastability in Josephson transmission lines. *Phys. Rev. B*, 61:1506, 2000.
- [DPP86] A. Davidson, N.F. Pedersen, and S. Pagano. The effect of surface losses on soliton propagation in Josephson junctions. *Appl. Phys. Lett.*, 48(19):1306, 1986.
- [EDM86] D. Esteve, M. H. Devoret, and J. M. Martinis. Effect of an arbitrary dissipative circuit on the quantum energy levels and tunneling of a Josephson junction. *Phys. Rev. B*, 34:158, 1986.
- [EFPB96] E. Esposito, L. Frunzio, L. Parlato, and A. Barone. Superconductive tunnel junction detectors: ten years ago, ten years from now. *Nucl. Instrum. Methods Phys. Res. A*, 370:26, 1996.
- [ESA84] U. Eckern, G. Schön, and V. Ambegaokar. The quantum dynamics of a superconducting tunnel junction. *Phys. Rev. B*, 30:6419, 1984.
- [EWSM93] W.J. Elion, J.J. Wachtters, L.L. Sohn, and J.E. Mooij. Observation of the Aharonov-Casher effect of vortices in Josephson junction arrays. *Phys. Rev. Lett.*, 71(14):2311, 1993.
- [FCC+00] M. V. Fistul, M. G. Castellano, M. Cirillo, A. Torrioli, G. Wallraff, and A. V. Ustinov. Escape of a Josephson vortex trapped in an annular Josephson junction. *Physica B*, 284-288:585–586, 2000.
- [FD74] T.A. Fulton and L.N. Dunkelberger. Lifetime of the zero-voltage state in Josephson tunnel junctions. *Phys. Rev. B*, 9:4760, 1974.

- [Fis64] M.D. Fiske. Temperature and magnetic field dependences of Josephson tunneling current. *Rev. Mod. Phys.*, 36:221, 1964.
- [FLS65] R.P. Feynman, R.B. Leighton, and M. Sands. *Lectures in Physics*, volume 3. Addison-Wesley, 1965.
- [FPC<sup>+</sup>00] J. R. Friedman, Vijay Patel, W. Chen, S. K. Tolpygo, and J. E. Lukens. Detection of a Schrödinger's cat state in an rf-SQUID. *condmat/0004283*, 2000.
- [Fra99] A. Franz. Fluxonendynamik in ringförmigen Josephson-Kontakten. Master's thesis, Physikalisches institut III, Universität Erlangen-Nürnberg, 1999.
- [FWU00a] A. Franz, A. Wallraff, and A.V. Ustinov. Magnetic field penetration in a long Josephson junction imbedded in a wide stripline. *J. Appl. Phys.*, 2000. (submitted).
- [FWU00b] A. Franz, A. Wallraff, and A.V. Ustinov. Measurements of the critical current diffraction patterns in annular Josephson junctions. *Phys. Rev. B*, 62(1), 2000. (in print, also cond-mat/9912302).
- [GC97] N. A. Gershenfeld and I. L. Chang. Bulk spin-resonance quantum computation. *Science*, 275:350, 1997.
- [GCN<sup>+</sup>98] C. Gmachl, F. Capasso, E. E. Narimanov, J. U. Nöckel, A. D. Stone, J. Faist, D. L. Sivico, and A. V. Cho. High-power directional emission from microlasers with chaotic resonators. *Science*, 280:1556, 1998.
- [GF84] Yu. S. Galpern and A. T. Filippov. *Zh. Eksp. Teor. Fiz.*, 86:1527, 1984.
- [GHG<sup>+</sup>95] A.A. Golubov, E.P. Houwman, J.G. Gijsbertsen, V.M. Krasnov, J. Flokstra, J. B. le Grand, and P.A.J. de Korte. Proximity effect in superconductor-insulator-superconductor Josephson tunnel junctions: Theory and experiment. *Phys. Rev. B*, 49:1073, 1995.
- [GJC94] N. Grønbech-Jensen and M. Cirillo. Phase locking of Fiske modes in sine-Gordon systems. *Phys. Rev. B*, 50(17):12851, 1994.
- [GJLS91a] N. Grønbech-Jensen, P.S. Lomdahl, and M.R. Samuelson. Phase locking of long annular Josephson junctions coupled to an external rf magnetic field. *Phys. Lett. A*, 154(1,2):14, 1991.
- [GJLS91b] N. Grønbech-Jensen, P.S. Lomdahl, and M.R. Samuelson. Bifurcation and chaos in dc-driven long Josephson junctions. *Phys. Rev. B*, 43(16):12799, 1991.
- [GK94] R. Gross and D. Koelle. Low temperature scanning electron microscopy of superconducting thin films and Josephson junctions. *Rep. Prog. in Phys.*, 57(7):651, 1994.
- [GMU00] E. Goldobin, B. A. Malomed, and A. V. Ustinov. Bunching fluxons by the cherenkov radiation in josephson multilayers. 2000. (cond-mat/0002051).
- [Gol] E. Goldobin, Goldexi, <http://www.geocities.com/SiliconValley/Heights/7318/>.
- [Gol91] H. Goldstein. *Klassische Mechanik*. AULA-Verlag Wiesbaden, 11th edition, 1991.
- [Gro97] L. K. Grover. Quantum mechanics helps searching a needle in a haystack. *Phys. Rev. Lett.*, 79:325, 1997.

- [GT95] C. Giovannella and M. Tinkham. *Macroscopic quantum phenomena and coherence in superconducting networks*. World Scientific, 1995.
- [Gur92] A. Gurevich. Nonlocal Josephson electrodynamics and pinning in superconductors. *Phys. Rev. B*, 46(5):3187, 1992.
- [GV95] Z. D. Genchev and V. I. Vaskivskii. Fiske resonances in the I-V curves of a large Josephson junction: The effect of nonlocal electrodynamics. *Phys. Conf. Ser.*, 148:1235, 1995.
- [GWTU98] E. Goldobin, A. Wallraff, N. Thyssen, and A.V. Ustinov. Cherenkov radiation in coupled long Josephson junctions. *Phys. Rev. B*, 57(1):130, 1998.
- [GWU00] E. Goldobin, A. Wallraff, and A.V. Ustinov. Cherenkov radiation from fluxons in a stack of coupled long Josephson junctions. *J. Low. Temp. Phys.*, 119(5/6):589, 2000.
- [Hew] Hewlett-Packard. *HP 3245A universal source*.
- [HG85] H.A. Huggins and M. Gurvitch. Preparation and characteristics of Nb/Al-oxide/Nb tunnel junctions. *J. Appl. Phys.*, 57(6):2103, 1985.
- [HGIW85] P. Hanggi, H. Grabert, G.-L. Ingold, and U. Weiss. Quantum theory of activated events in presence of long-time memory. *Phys. Rev. Lett.*, 55(7):761, 1985.
- [HKUM97] G. Hechtfisher, R. Kleiner, A.V. Ustinov, and P. Müller. Non-Josephson emission from intrinsic junctions in  $\text{BiSr}_2\text{CaCu}_2\text{O}_{8+y}$ : Cherenkov radiation by Josephson vortices. *Phys. Rev. Lett.*, 79(7):1365, 1997.
- [HLL89] S. Han, J. Lapointe, and J. E. Lukens. Thermal activation in a two-dimensional potential. *Phys. Rev. Lett.*, 63(16):1712, 1989.
- [HMS88] P. Hänggi, F. Marchesoni, and P. Sodano. Nucleation of thermal sine-Gordon solitons: Effect of many-body interactions. *Phys. Rev. Lett.*, 60:2563, 1988.
- [HRL96] S. Han, R. Rouse, and J. E. Lukens. Generation of population inversion between quantum states of a macroscopic variable. *Phys. Rev Lett.*, 76(18):3404, 1996.
- [HRL00] S. Han, R. Rouse, and J. E. Lukens. Observation of cascaded two-photon-induced transitions between fluxoid states of a SQUID. *Phys. Rev. Lett.*, 84:1300, 2000.
- [HSBJ95] Z. Hermon, A. Shnirman, and E. Ben-Jacob. Dephasing length and coherence of a quantum soliton in an ideal long Josephson junction. *Phys. Rev. Lett.*, 74(24):4915, 1995.
- [HTB90] P. Hänggi, P. Talkner, and M. Borkovec. Reaction-rate theory: fifty years after Kramers. *Rev. Mod. Phys.*, 62:251, 1990.
- [Hyp] Elmsford, NY 10523, U.S.A.
- [IGF<sup>+</sup>99] L. B. Ioffe, V. B. Geshkenbein, M. V. Feigel'man, A. L. Fauchere, and G. Blatter. Environmentally decoupled sds-wave Josephson junctions for quantum computing. *Nature*, 398:679, 1999.
- [IS90] Yu. M. Ivanchenko and T. K. Soboleva. Nonlocal interaction in Josephson junctions. *Phys. Lett. A*, 147:65, 1990.

- [JEL60] E. Janke, F. Emde, and F. Loesch. *Tables of higher functions*. McGraw-Hill, New York, 1960.
- [JMH98] A. J. Jones, M. Mosca, and R. H. Hansen. Implementation of a quantum search algorithm on a quantum computer. *Nature*, 393:344, 1998.
- [Jos62] B. D. Josephson. Possible new effects in superconductive tunneling. *Phys. Lett.*, 1(7):251, 1962.
- [Jos64] B. D. Josephson. Coupled superconductors. *Rev. Mod. Phys.*, page 216, 1964.
- [Kem00] A. Kemp. in preparation. Master's thesis, Physikalisches Institut III, Universität Erlangen-Nürnberg, 2000.
- [KGS91] H. Kohlstedt, K.H. Gundlach, and A. Schneider. Investigation of the tunnel barrier in Nb-based junctions prepared by sputtering and electron beam evaporation. *IEEE Transactions on magnetics*, 27(2):3149, 1991.
- [KHN<sup>+</sup>97] H. Kohlstedt, G. Hallmanns, I.P. Nevirkovets, D. Guggi, and C. Heiden. Preparation and properties of Nb/Al-AlO<sub>x</sub>/Nb multilayers. *IEEE Trans. Appl. Supercond.*, 3:1993, 2197.
- [KI96] T. Kato and M. Imada. Macroscopic quantum tunneling of a fluxon in a long Josephson junction. *J. Phys. Soc. Jpn.*, 65(9):2963, 1996.
- [KM88] Yu.S. Kivshar and B.A. Malomed. Dynamics of fluxons in a system of coupled Josephson junctions. *Phys. Rev.B*, 37:9325, 1988.
- [KM89] Y.S. Kivshar and B.A. Malomed. Dynamics of solitons in nearly integrable systems. *Rev. Mod. Phys.*, 61(4):763–915, 1989.
- [Kra40] H.A. Kramers. Brownian motion in a field of force and the diffusion model of chemical reactions. *Physica*, 7(4):284, 1940.
- [Kru98] Dietmar Kruse. Relativistische solitonen in josephson-tunnelkontakten. Master's thesis, Physikalisches Institut der Universität Tübingen, Lehrstuhl für Experimentalphysik II, Dezember 1998.
- [KSF<sup>+</sup>96] V. P. Koshelets, S.V. Shitov, L.V. Filippenko, A.M. Baryshev, H. Golstein, T.de Graauw, W. Luinge, H. Schaeffer, and H. vandeStadt. First implementation of a superconducting integrated receiver at 450 GHz. *Appl. Phys. Lett.*, 68:1273, 1996.
- [KSF<sup>+</sup>97] V.P. Koshelets, S.S. Shitov, L.V. Filippenko, A.M. Baryshev, W. Luinge, H. Golstein, H. van de Stadt, J.R. Gao, and T. de Grauw. An integrated 500 GHz receiver with superconducting local oscillator. *To be published in IEEE Trans. Appl. Supercond.*, 1997. Proceedings of ASC 96.
- [Kul67] I.O. Kulik. Wave propagation in a Josephson tunnel junction in the presence of vortices and the electrodynamics of weak superconductivity. *Sov. Phys. JETP*, 24:1307, 1967.
- [KVL<sup>+</sup>96] S. Keil, I.V. Vernik, A. Laub, H. Preßler, R.P. Huebener, N. Thyssen, A.V. Ustinov, and H. Kohlstedt. Magnetic flux pinning in annular Josephson junctions in a barrier parallel dc magnetic field. *Phys. Rev. B*, 54(21):14948, 1996.
- [KWF<sup>+</sup>99] Yu. Koval, A. Wallraff, M. Fistul, N. Thyssen, H. Kohlstedt, and A. V. Ustinov. Narrow log Josephson junctions. *IEEE Trans. Appl. Supercond.*, 9:3957, 1999.



- [KYSV98] V.V. Kurin, A.V. Yulin, Shereshevskii, and N.K. Vdovicheva. Cherenkov radiation of vortices in a two-dimensional annular Josephson junction. *Phys. Rev. Lett.*, 80(15):3372, 1998.
- [Lak] Lakeshore. *LS 340 temperature controller*.
- [LB92] G.S. Lee and A.T. Barfknecht. Geometric and material dispersion in Josephson transmission lines. *IEEE Trans. Appl. Supercond.*, 2(2):67, 1992.
- [LCD<sup>+</sup>87] A. J. Leggett, S. Chakravarty, A. T. Dorsey, M. P. A. Fisher, A. Garg, and W. Zwerger. Dynamics of the dissipative two-state system. *Rev. Mod. Phys.*, 59(1):1, 1987.
- [LDL<sup>+</sup>95] A. Laub, T. Doderer, S.G. Lachenmann, R.P. Huebener, and V.A. Oboznov. Lorentz contraction of flux quanta observed in experiments with annular Josephson tunnel junctions. *Phys. Rev. Lett.*, 75(7):1372, 1995.
- [Lee91] G.S. Lee. Analysis of linear resonances in modern Josephson junction geometries. *IEEE Trans. Appl. Supercond.*, 1(3):121, 1991.
- [Leg84] A. J. Leggett. Macroscopic quantum tunneling and related effects in Josephson systems. In *Percolation, localization, and superconductivity*, New York, 1984. Plenum Press.
- [LG85] A. J. Leggett and A. Garg. Quantum mechanics versus macroscopic realism: is the flux there when nobody looks? *Phys. Rev. Lett.*, 54(9):857, 1985.
- [Lik79] K.K. Likharev. Superconducting weak links. *Rev. Mod. Phys.*, 51(1):101–159, 1979.
- [Lik86] K.K. Likharev. *Dynamics of Josephson Junctions and Circuits*. Gordon and Breach Science Publishers, 1986.
- [LL79] L. D. Landau and E. M. Lifschitz. *Lehrbuch der theoretischen Physik, Band 3, Quantenmechanik*. Verlag Harri Deutsch, 1979.
- [Llo93] S. Lloyd. A potentially realizable quantum computer. *Science*, 261:1569, 1993.
- [Llo95] S. Lloyd. Almost any quantum logic gate is universal. *Phys. Rev. Lett.*, 75:346, 1995.
- [LP92] H. Lenstra and C. Pomerance. A rigorous time bound for factoring integers. *J. of the Am. Math. Soc.*, 5:482, 1992.
- [Mal88] B. A. Malomed. Dynamics of a fluxon in a long Josephson junction with a periodic lattice of inhomogeneities. *Phys. Rev. B*, 38:9242, 1988.
- [MBCF85] S. L. Miller, K. R. Biagi, J. R. Clem, and D. K. Finnemore. *Phys. Rev. B*, 31:2684, 1985.
- [McC68] D.E. McCumber. Effect of ac impedance on dc voltage-current characteristics of superconductor weak-link junctions. *J. Appl. Phys.*, 39(7):3113, 1968.
- [MCM95] R. Monaco, G. Costabile, and N. Martucciello. Influence of the idle region on the dynamic properties of window Josephson tunnel junctions. *J. Appl. Phys.*, 77:2073, 1995.

- [MDC87] J.M. Martinis, M.H. Devoret, and J. Clarke. Experimental tests for the quantum behavior of a macroscopic degree of freedom: The phase difference across a Josephson junction. *Phys. Rev. B*, 35(10):4682, 1987.
- [MDP<sup>+</sup>98] D. Münter, T. Doderer, H. Preßler, S. Keil, and R. P. Huebener. Fluxon pinning through interaction with the superconducting wiring of long annular Josephson junctions. *Phys. Rev. B*, 58:14518, 1998.
- [Min97] R.G. Mints. Nonlocal Josephson electrodynamics. *J. Low Temp. Phys.*, 106(3/4):183, 1997.
- [ML97] S. Maggi and Lacquaniti. Analysis of magnetic field patterns of single Josephson tunnel junctions with large idle regions. *J. Low Temp. Phys.*, 106:393, 1997.
- [MLS<sup>+</sup>91] S. L. McCall, A. F. J. Levi, R. E. Slusher, S. J. Pearton, and R. A. Logan. Whispering mode microdisk lasers. *Appl. Phys. Lett.*, 60:289, 1991.
- [MM96a] N. Martucciello and R. Monaco. Annular Josephson tunnel junctions in an external magnetic field: the statics. *Phys. Rev. B*, 53(6):3471, 1996.
- [MM96b] N. Martucciello and R. Monaco. Static properties of annular Josephson tunnel junctions. *Phys. Rev. B*, 54(13):9050, 1996.
- [MMK<sup>+</sup>95] C. Monroe, D. M. Meekhof, B. E. King, W. M. Itano, and D. J. Wineland. *Phys. Rev. Lett.*, 75:4714, 1995.
- [MMK<sup>+</sup>98] N. Martucciello, J. Mygind, V.P. Koshelets, A.V. Shchukin, L.V. Filippenko, and R. Monaco. Fluxon dynamics in long annular Josephson tunnel junctions. *Phys. Rev. B*, 57(9):5444, 1998.
- [MMS] N. Martucciello, R. Monaco, and C. Soriano. Annular Josephson tunnel junctions in external magnetic field. (preprint).
- [MOL<sup>+</sup>99] J. E. Mooij, T. P. Orlando, L. Levitov, Lin Tian, Caspar H. van der Wal, and Seth Lloyd. Josephson persistent-current qubit. *Science*, 285:1036, 1999.
- [MS78] D.W. McLaughlin and A.C. Scott. Perturbation analysis of fluxon dynamics. *Phys. Rev. A*, 18:1652, 1978.
- [MSM96] N. Martucciello, C. Soriano, and R. Monaco. Annular Josephson tunnel junctions in external magnetic field: the dynamics. *Phys. Rev. B*, 55(22):15157, 1996.
- [MSS99] Yu. Makhlin, G. Schön, and A. Shnirman. Josephson-junction qubits with controlled couplings. *Nature*, 398:305, 1999.
- [MU90] B. A. Malomed and A. V. Ustinov. Pinning of a fluxon chain in a long Josephson junction with a lattice of inhomogeneities: theory and experiment. *J. Appl. Phys.*, 67(8):3791, 1990.
- [Müh59] B. Mühlischlegel. Die thermodynamische Funktion des Supraleiters. *Z. Physik*, 155:313, 1959.
- [Nap97] C. Nappi. Critical-current diffraction pattern of annular Josephson junctions. *Phys. Rev. B*, 55(1):82, 1997.
- [Nata] National Instruments. *LabView*.

- [Natb] National Instruments. *PCI-MIO-16XE-10*.
- [NC97] C. Nappi and R. Cristiano. Annular Josephson junctions as superconductive nuclear particle detectors. *Appl. Phys Lett.*, 70:1320, 1997.
- [NCL98] C. Nappi, R. Cristiano, and M. P. Lisitskii. Fiske steps in annular Josephson junctions with trapped flux quanta. *Phys. Rev. B*, 85(17):11685, 1998.
- [NEIY83] T. Nagatsuma, K. Enpuku, F. Irie, and K. Yoshida. Flux-flow type oscillator for millimeter and submillimeter wave region. *J. Appl. Phys.*, 54(6):3302, 1983.
- [NEYI84] T. Nagatsuma, K. Enpuku, K. Yoshida, and F. Irie. Flux-flow type oscillator for millimeter and submillimeter wave region. II. Modeling. *J. Appl. Phys.*, 56(11):3284, 1984.
- [NEYI85] T. Nagatsuma, K. Enpuku, K. Yoshida, and F. Irie. Flux-flow type oscillator for millimeter and submillimeter wave region. iii. oscillation stability. *J. Appl. Phys.*, 58(1):441, 1985.
- [NPT99] Y. Nakamura, Yu. A. Pashkin, and J. S. Tsai. Coherent control of macroscopic quantum states in a single-cooper-pair box. *Nature*, 198:786, 1999.
- [NT00] Y. Nakamura and J. S. Tsai. Quantum-state control with a single-cooper-pair-box. *J. Low Temp. Phys.*, 118(5/6):765, 2000.
- [OMT<sup>+</sup>99] T. P. Orlando, J. E. Mooij, Lin Tian, van der Wal Caspar H., L. Levitov, Seth Lloyd, and J. J. Mazo. A superconducting persistent current qubit. *Phys. Rev. B*, 60:15398, 1999.
- [OS67] C. S. Owen and D. J. Scalapino. Vortex structure and critical currents in Josephson junctions. *Phys. Rev.*, 164:538, 1967.
- [OVM96] A. Oudenaarden, S.J.K. Vardy, and J.E. Mooij. One-dimensional localization of quantum vortices in disordered Josephson junction arrays. *Phys. Rev. Lett.*, 77(20):4257, 1996.
- [Par93] R.D. Parmentier. *The new superconducting electronics*, page 221. Kluwer, Dordrecht, 1993.
- [Ped82] N.F. Pedersen. *Advances in Superconductivity*, chapter Solitons in long Josephson junctions. Plenum Press, New York, 1982.
- [PFTV86] W. H. Press, B. P. Flannery, S.A. Teukolsky, and W. T. Vetterling. *Numerical Recipes*. Cambridge University Press, 1986.
- [PJFC95] C.P. Poole Jr., H.A. Farach, and R.J. Creswick. *Superconductivity*. Academic Press, 1995.
- [Pob95] F. Pobell. *Matter and methods at low temperatures*. Springer, 2nd edition, 1995.
- [PRS91] S. Pagano, B. Ruggiero, and E. Sarnelli. Magnetic field dependence of critical current in long Josephson junctions. *Phys. Rev. B*, 43:5364, 1991.
- [PU95] N.F. Pedersen and A.V. Ustinov. Fluxons in Josephson transmission lines: new developments. *Supercond. Sci. Technol.*, 8:389, 1995. Review article.
- [Ray14] Lord Rayleigh. *Phil. Mag.*, 27:100, 1914.

- [RHL95] R. Rouse, S. Han, and J. E. Lukens. Observation of resonant tunneling between macroscopically distinct quantum levels. *Phys. Rev. Lett.*, 75(8):1614, 1995.
- [SBJM97] A. Shnirman, E. Ben-Jacob, and B.A. Malomed. Tunneling and resonant tunneling of fluxons in a long Josephson junction. *Phys. Rev. B*, 56(22):14677, 1997.
- [Sch70] K. Schwidtal. Type-I and type-II superconductivity in wide Josephson junctions. *Phys. Rev. B*, 2:2526, 1970.
- [Sch95] B. Schumacher. Quantum coding. *Phys. Rev. A*, 51:2738, 1995.
- [Sho94] P. W. Shor. Polynomial-time algorithms for prime factorization and discrete logarithms on a quantum computer. *Proc. of the 35th Annual Symposium on Foundations of Computer Science 1994, Los Alamitos*, page 124, 1994. (quant-ph/9508027).
- [SHVBJ95] A. Shnirman, Z. Hermon, L. Vaidman, and E. Ben-Jacob. Interference and transmission of quantum fluxons through a Josephson ring. *Phys. Rev. A*, 52:3541, 1995.
- [SPRR97] P. Silvestrini, V.G. Palmieri, B. Ruggiero, and M. Russo. Observation of energy levels quantization in underdamped Josephson junctions above the classical-quantum regime crossover temperature. *Phys. Rev. Lett.*, 79(16):3046, 1997.
- [SSAL85] D. B. Schwartz, B. Sen, C. N. Archie, and J. E. Lukens. Quantitative study of the effect of the environment on macroscopic quantum tunneling. *Phys. Rev. Lett.*, 55(15):1547, 1985.
- [Sta] Stanford Research Systems. *SR 620 universal time interval counter*.
- [Ste68] W.C. Stewart. Current-voltage characteristics of Josephson junctions. *Appl. Phys. Lett.*, 12(8):277, 1968.
- [Ste97] A. Steane. Quantum computing. *Rep. Prog. Phys.*, 61:117, 1997.
- [Ste99] A. M. Steane. Efficient fault-tolerant quantum computing. *Nature*, 399:124, 1999.
- [Swa86] E. T. Swartz. Efficient  $^4\text{He}$  cryostats for storage dewars. *Rev. Sci. Instr.*, 57:2848, 1986.
- [Swi61] J.C. Swihart. Field solution for a thin-film superconducting strip transmission line. *J. Appl. Phys.*, 32:461, 1961.
- [SZ90] G. Schön and A. D. Zaikin. Quantum coherent effects, phase transitions, and dissipative dynamics of ultra small tunnel junctions. *Phys. Rep.*, 198:237, 1990.
- [SZT+94] A. G. Sivakov, A. P. Zhuravel, O. G. Turutanov, I. M. Dmitrenko, J. W. M. Hilgenkamp, G. C. S. Brons, J. Flokstra, and H. Rogalla. Laser scanning imaging and local characterization of superconducting properties in high- $t_c$  thin film multiturn coil. *Physica C*, 232:93, 1994.
- [SZTD96] A. G. Sivakov, A. P. Zhuravel, O. G. Turutanov, and I. M. Dmitrenko. Spatially resolved characterization of superconducting films and cryoelectronic devices by means of low temperature scanning laser microscope. *Appl. Surf. Sci.*, 106:390, 1996.
- [Tes90] C. D. Tesche. Can a noninvasive measurement for magnetic flux be performed with superconducting circuits? *Phys. Rev. Letts.*, 64(20):2356, 1990.

- [THL<sup>+</sup>95] Q. A. Turchette, C. J. Hood, W. Lange, H. Mabuchi, and H. J. Kimble. Measurement of conditional phase shifts for quantum logic. *Phys. Rev. Lett.*, 75:4710, 1995.
- [Tin96] M. Tinkham. *Introduction to Superconductivity*. McGraw-Hill International Editions, 1996.
- [TLvdW<sup>+</sup>99] Lin Tian, L. S. Levitov, Caspar H. van der Wal, J. E. Mooij, T. P. Orlando, S. Lloyd, C. J. P. M. Harmans, and J. J. Mazo. Decoherence of the superconducting persistent current qubit. 1999. cond-mat/9910062.
- [TUK<sup>+</sup>95] N. Thyssen, A. V. Ustinov, H. Kohlstedt, S. Pagano, J. G. Caputo, and N. Flytzantis. Experimental study of fluxon resonances in window-type long Josephson junctions. *IEEE Trans. Appl. Supercond.*, 5:2965, 1995.
- [UDH<sup>+</sup>92] A.V. Ustinov, T. Doderer, R.P. Huebener, N.F. Pedersen, B. Mayer, and V.A. Oboznov. Dynamics of sine-Gordon solitons in the annular Josephson-junction. *Phys. Rev. Lett.*, 69(12):1815, 1992.
- [UMT97] A.V. Ustinov, B. A. Malomed, and N. Thyssen. Soliton trapping in a harmonic potential: experiment. *Phys. Lett. A*, 233:239, 1997.
- [Ust96] A.V. Ustinov. Observation of radiation induced soliton resonances in a Josephson ring. *JETP Lett.*, 64:191, 1996.
- [Ust98] A. V. Ustinov. Solitons in Josephson junctions. *Physica D*, 123:315, 1998.
- [Ust99] A. V. Ustinov. Backbending current-voltage characteristic for an annular Josephson junction in a magnetic field. *Phys. Rev. B*, 60(2):1365, 1999.
- [UT97] A.V. Ustinov and N. Thyssen. Experimental study of fluxon dynamics in a harmonic potential well. *J. of Low Temp. Phys.*, 106:193, 1997.
- [VDKS88] A. N. Vystavkin, F. Drachevskii, Yu. V. P. Koshelets, and I. L. Serpuchenko. First observation of static bound states of fluxons in long Josephson junctions with inhomogeneities. *Sov. J. Low Temp. Phys.*, 14:357, 1988.
- [VDT81] T. Van Duzer and C.W. Turner. *Principles of superconducting devices and circuits*. Edward Arnold, U.K., 1981.
- [VKT<sup>+</sup>96] I.V. Vernik, S. Keil, N. Thyssen, T. Doderer, A.V. Ustinov, H. Kohlstedt, and R.P. Huebener. Fluxon pinning in annular Josephson junctions by an external magnetic field. *Phys. Rev. B*, 1996. (submitted).
- [VKT<sup>+</sup>97] I. V. Vernik, S. Keil, N. Thyssen, T. Doderer, A. V. Ustinov, H. Kohlstedt, and R. P. Huebener. Fluxon pinning in annular Josephson junctions by an external magnetic field. *J. Appl. Phys.*, 81(3):1335, 1997.
- [VLS<sup>+</sup>96] I.V. Vernik, N. Lazarides, M.P. Soerensen, A.V. Ustinov, N.F. Pedersen, and V.A. Oboznov. Soliton bunching in annular Josephson junctions. *J. Appl. Phys.*, 79:7854, 1996.
- [VOJ<sup>+</sup>95] D. Vion, P. F. Orfila, P. Joyez, D. Esteve, and M. H. Devoret. Miniature electrical filters for single electron devices. *J. Appl. Phys.*, 77:2519, 1995.
- [vOM96] A. van Oudenaarden and J.E. Mooij. One-dimensional Mott insulator formed by quantum vortices in Josephson junction arrays. *Phys. Rev. Lett.*, 76(26):4947, 1996.

- [Wal78] Jearl Walker. The amateur scientist: Some whispering galleries are simply sound reflectors, but others are more mysterious. *Scientific American*, 239(4):147, 1978.
- [WBK<sup>+</sup>97] A. Wallraff, D. Bolkhovskiy, V. Kurin, N. Thyssen, and A.V. Ustinov. Effective length of annular long Josephson junctions with finite width: theory and experiment. *Inst. Phys. Conf. Ser.*, 158:531, 1997.
- [Wei69] M. Weihnacht. *Phys. Stat. Sol.*, 32:K169, 1969.
- [Wei99] U. Weiss. *Quantum dissipative systems*. World Scientific, 2nd edition, 1999.
- [WFKU99] A. Wallraff, A. Franz, V. V. Kurin, and A. V. Ustinov. 1999. unpublished.
- [WFKU00] A. Wallraff, A. Franz, V. V. Kurin, and A. V. Ustinov. Influence of the environment on whispering gallery modes in annular Josephson junctions. 2000. (in preparation).
- [WFU<sup>+</sup>00] A. Wallraff, A. Franz, A. V. Ustinov, V. V. Kurin, I. A. Shereshevsky, and N. K. Vdovicheva. Observation of whispering gallery resonances in annular Josephson junctions. *Physica B*, 284-288:575–576, 2000.
- [WKL<sup>+</sup>00] A. Wallraff, Yu. Koval, M. Levitchev, M. V. Fistul, and A. V. Ustinov. Annular long Josephson junction in a magnetic field: Engineering and probing the fluxon potential. *J. Low Temp. Phys.*, 118(5/6):543, 2000. (also cond-mat/9911437).
- [WКУ00] A. Wallraff, A. Kemp, and A. V. Ustinov. 2000. (unpublished).
- [Wol] Wolfram Research Inc. *Mathematica*.
- [WUK<sup>+</sup>00] A. Wallraff, A. V. Ustinov, V. V. Kurin, I. A. Shereshevsky, and N. K. Vdovicheva. Whispering vortices. *Phys. Rev. Lett.*, 84:151, 2000.
- [WvHL<sup>+</sup>93] D. A. Wollmann, D. J. van Haarlingen, W. C. Lee, D. M. Ginsberg, and A. J. Leggett. Experimental determination of the superconducting pairing state in ybco from the phase coherence of ybco-pb dc SQUIDs. *Phys. Rev. Lett.*, 71:2134, 1993.
- [WWVF84] S. Wahsburn, R.A. Webb, R.F. Voss, and S. M. Faris. Effects of dissipation and temperature on macroscopic quantum tunneling. *Phys. Rev. Lett.*, 54(25):2712, 1984.
- [YKN87] Masahiro Yuda, Ken'ichi Kuroda, and Jun'ichi Nakano. Small Nb/Al-Oxide/Nb Josephson junction fabrication using lift-off processes. *Jpn. J. of Appl. Phys.*, 26(3):L166, 1987.
- [ZLZ<sup>+</sup>99] A. Zehnder, Ph. Lerch, S. P. Zhao, Th. Nussbaumer, and E. C. Kirk. Proximity effects in Nb/Al-AlO<sub>x</sub>-Al/Nb superconducting tunneling junctions. *Phys. Rev. B*, 59(13):8875, 1999.
- [Zor95] A. B. Zorin. The thermocoax cable as the microwave frequency filter for single electronic circuits. *Rev. Sci. Instrum.*, 66:4296, 1995.

# Summary

## Fluxon Dynamics in Annular Josephson Junctions: From Relativistic Strings to Quantum Particles

In this thesis, the fascinating and diverse dynamics of Josephson vortices in annular Josephson junctions is investigated experimentally. Annular Josephson junctions consist of a vertical stack of two micron-size annular superconducting electrodes weakly coupled by a thin tunnel barrier. Due to the quantum properties of the superconducting charge carriers, magnetic field penetrates into these structures in a quantized fashion. The dynamics of the charge carriers and of the fields in the junction is described in terms of the spatial and temporal evolution of the phase difference between the wave functions describing the superconducting condensate. The non-linear dynamics of the phase difference is explained using a sine-Gordon model. The annular Josephson junction can be prepared in a state in which a single magnetic flux quantum is topologically trapped between the two superconducting electrodes threading only one of them. A magnetic flux quantum, also called Josephson vortex or fluxon, trapped in the junction has the character of a solitary wave which propagates along the non-linear waveguide formed by the junction. The dynamics of the soliton is controlled by applying a bias current and external fields to the junction and are investigated by performing transport measurements. In different experimental situations, the dynamics of the vortex displays either wave or particle character. The intention of this work is to study properties of the Josephson vortex in these two different regimes. In effectively two-dimensional wide annular junctions, the vortex behaves as a spatially extended solitary wave. In the limit of narrow long junctions, the vortex displays particle character.

The static properties of the spatial distribution of the phase difference across the junction is investigated experimentally. Measurements of the maximum supercurrent supported by the junction in dependence on the externally applied in-plane magnetic field show interesting features depending on the exact junction geometry. The measured critical-current diffraction patterns are explained in terms of the field-dependent interference of the supercurrent, which is formally equivalent to a multi-beam optical diffraction pattern. The experimental data are in excellent quantitative agreement with theoretical expectations. The structure of the pattern is shown to depend sensitively on the field distribution in the junction. In this way, the state of the junction with a single trapped vortex is uniquely identified.

In a second experiment, it is observed that a Josephson vortex revolving at relativistic velocities around a wide annular junction excites linear electromagnetic modes of the

whispering gallery type in the junction. It is demonstrated experimentally that the vortex moves with a group velocity larger than the phase velocity of the linear modes, hence generating radiation in a way that is similar to the Cherenkov mechanism. This radiation is detected by its resonant interaction with the vortex leading to a characteristic fine structure on the current-voltage characteristic of the junction. The dependence of the linear mode frequency spectrum of the junction on the electrical and geometrical parameters of the sample is measured quantitatively by analyzing the resonance voltages.

The effect of the electromagnetic environment on the statics and dynamics of an annular junction is investigated by coupling an annular resonator in parallel to the junction. It is shown that the characteristic frequencies and the length scales of the electromagnetic phenomena in the junction are strongly affected by the resonator. The observed effects are explained accurately by considering the coupling between a non-linear and a linear waveguide. In particular, the whispering gallery frequency spectrum of the coupled resonators is determined from the fine structure on the current-voltage characteristic induced by the resonant interaction between the vortex and the linear modes.

In the second part of the work, the particle properties of single Josephson vortices are investigated in the non-relativistic regime. Making use of the magnetic dipole interaction between the magnetic moment associated with the vortex and a magnetic field applied in the plane of the junction, the vortex is spatially confined in a potential well. The escape of the vortex from the well due to thermal fluctuations is investigated by measuring the statistical distribution of the vortex depinning currents. The experimental results are explained describing the vortex in terms of a particle with an effective mass and a generalized center of mass coordinate, which is thermally activated from the potential well. From the experimental data, the effective temperature of the escape process is determined and good agreement with the thermal bath temperature is found. Similar results are found for a potential well induced by a microresistor implemented into the junction barrier.

Based on the results of the experiments performed on the thermal escape of a single Josephson vortex from a metastable state, the feasibility of observing the quantum escape is quantitatively analyzed. It is suggested that the quantum tunneling of a vortex from a magnetic-field induced potential dominates the thermal escape at temperatures below 100 mK if sub-micron wide annular junctions are employed. Improvements in the current experimental setup are suggested for the future observation of quantum tunneling and energy level quantization of a Josephson vortex in a potential well.

The need for the experimental investigation of decoherence mechanisms in macroscopic quantum systems and the search for coherent two-state systems in relation to applications in quantum computation inspired a proposal of our group presented in this thesis. It is suggested to use quantum vortices in shaped long junctions to investigate macroscopic quantum coherence. A measurement scheme to observe Rabi-oscillations of a vortex relying on the manipulation of a double-well potential by the external field and the bias current is described. Means to manipulate the quantum states of a vortex in a double-well potential are pointed out and decoherence is considered within existing models.



# Curriculum Vitae

## Andreas Joachim Wallraff

- April 29, 1971 Born in Bonn, Germany
- 1981 - 1990 Abitur, Bischöfliches Pius Gymnasium, Aachen
- 1990 - 1991 Zivildienst, Marienhospital Aachen
- 1991 - 1997 Studiengang Diplom Physik at  
Rheinisch-Westfälische Technische Hochschule (RWTH) Aachen  
and  
Imperial College of Science and Technology,  
London, United Kingdom
- October 1994 Imperial College International Diploma in Physics
- 1995-1996 Graduate research at  
Institut für Schicht- und Ionentechnik,  
Forschungszentrum Jülich  
in the 'Low Temperature Superconductivity' group of  
Prof. A. Braginsky under supervision of Dr. A. V. Ustinov  
subject: Fluxon Dynamics and Radiation Emission in Twofold  
Long Josephson Junction Stacks.
- March 1997 Diplom in Physik, RWTH Aachen
- 1997 - 2000 PhD research at  
Physikalisches Institut III,  
Friedrich-Alexander Universität Erlangen-Nürnberg  
in the group of Prof. A. V. Ustinov  
subject: Fluxon Dynamics in Annular Josephson Junctions:  
From Relativistic Strings to Quantum Particles

# List of Publications

1. A. Wallraff, E. Goldobin, and A. V. Ustinov, 'Numerical Analysis of the Coherent Radiation Emission by Two Stacked Josephson Flux-flow Oscillators', *Journal of Applied Physics* **80**, 6523 (1996)
2. A. Wallraff, D. Bolkhovskiy, V. Kurin, N. Thyssen, and A.V. Ustinov, 'Effective length of annular long Josephson junctions with finite width: theory and experiment.' *Institute of Physics Conference Series* No **158**, 531 (1997) (Proceedings of European Conference on Applied Superconductivity EUCAS'97)
3. E. Goldobin, A. Wallraff, B. A. Malomed, and A. V. Ustinov, 'Delocking of flux-flow states in dc-driven magnetically coupled Josephson junctions', *Physics Letters A* **224**, 191 (1997)
4. E. Goldobin, A. Wallraff, A. V. Ustinov, and N. Thyssen, 'Cherenkov radiation in coupled long Josephson junctions', Proceedings of the 6th International Superconductive Electronics Conference (ISEC) 1997, Berlin, Germany, Vol. **3**, p. 219 (1997) published by: *Physikalisch-Technische Bundesanstalt, Braunschweig, Germany*, ISBN 3-9805741-0-5
5. A. V. Ustinov, E. Goldobin, G. Hechtfisher, N. Thyssen, A. Wallraff, R. Kleiner, and P.Müller, 'Cherenkov radiation from Josephson fluxons', *Festkörperprobleme / Advances in Solid State Physics* **38** 521, (1998)
6. E. Goldobin, A. Wallraff, N. Thyssen, and A.V. Ustinov, 'Cherenkov radiation in coupled long Josephson junctions', *Physical Review B* **57**, 130 (1998)
7. Yu. Koval, A. Wallraff, M. Fistul, N. Thyssen, H. Kohlstedt, and A.V. Ustinov, 'Narrow Long Josephson Junctions', *IEEE Transactions on Applied Superconductivity* **9**, 3957 (1999)
8. A. Wallraff, A. V. Ustinov, V. V. Kurin, I. A. Shereshevsky, and N. K. Vdovicheva, 'Whispering Vortices', *Physical Review Letters* **84**, 151 (2000)
9. A. Wallraff, Yu. Koval, M. Levitchev, M. V. Fistul, and A. V. Ustinov, ' Annular Long Josephson Junctions in a Magnetic Field: Engineering and Probing the Fluxon Interaction Potential', *Journal of Low Temperature Physics* **118**, 543 (2000)
10. A. Wallraff, A. Franz, A. V. Ustinov, V. V. Kurin, I. A. Shereshevsky, and N. K. Vdovicheva, 'Observation of whispering gallery resonances in annular Josephson junctions', *Physica B* **284-288**, 575 (2000) (Proceedings of LT22, Helsinki, Finland, 1999)

11. M. V. Fistul, M. G. Castellano, M. Cirillo, G. Torrioli, A. Wallraff, and A. V. Ustinov 'Escape of a Josephson vortex trapped in an annular Josephson junction', *Physica B* **284-288**, 585 (2000) (Proceedings of LT22, Helsinki, Finland, 1999)
12. E. Goldobin, A. Wallraff, and A. V. Ustinov, 'Cherenkov radiation from a fluxon in a stack of coupled long Josephson junctions', *Journal of Low Temperature Physics* **119**, 589 (2000)
13. A. Franz, A. Wallraff, and A. V. Ustinov, 'Measurements of the critical current diffraction patterns in annular Josephson junctions', *Physical Review B* **62**, 119 (2000)
14. A. Franz, A. Wallraff, and A. V. Ustinov, 'Magnetic field penetration in a long Josephson junction embedded in a wide stripline', accepted for publication in *Journal of Applied Physics* (June 2000)